BREAKTHROUGHS IN LOW-PROFILE LEAKY-WAVE HPM ANTENNAS

Prepared by: Robert A. Koslover (PI), Sammuel M. Jalali, and Greg R. Raith



Scientific Applications & Research Associates, Inc.
6300 Gateway Drive
Cypress, CA 90630-4844

17 Oct 2016

Data Item: A001 - Scientific and Technical Report (Final Report)

Prepared for:

Program Officer: Lee Mastroianni
ONR Code 30



OFFICE OF NAVAL RESEARCH
875 North Randolph Street
Suite 1425
Arlington, VA 22203-1995

REPORT DOCUMENTATION PAGE

Form Approved
OMB No. 0704-0188

Public reporting burden for this collection of information is estimated to average 1 hour per response, including the time for reviewing instructions, searching existing data sources, gathering and maintaining the data needed, and completing and reviewing this collection of information. Send comments regarding this burden estimate or any other aspect of this collection of information, including suggestions for reducing this burden to Department of Defense, Washington Headquarters Services, Directorate for Information Operations and Reports (0704-0188), 1215 Jefferson Davis Highway, Suite 1204, Arlington, VA 22202-4302. Respondents should be aware that notwithstanding any other provision of law, no person shall be subject to any penalty for failing to comply with a collection of information if it does not display a currently valid OMB control number. **PLEASE DO NOT RETURN YOUR FORM TO THE ABOVE ADDRESS.**

1. REPORT DATE *(DD-MM-YYYY)*	**2. REPORT TYPE**	**3. DATES COVERED** *(From - To)*
17-10-2016	Final	18 Sep 2013 - 17 Oct 2016

4. TITLE AND SUBTITLE
Breakthroughs in Low-Profile Leaky-Wave HPM Antennas.
Scientific and Technical Report (Final Report)

5a. CONTRACT NUMBER
N00014-13-C-0352

5b. GRANT NUMBER

5c. PROGRAM ELEMENT NUMBER

6. AUTHOR(S)
Koslover, Robert A.; Jalali, Sammuel M.; Raith, Greg R.

5d. PROJECT NUMBER

5e. TASK NUMBER

5f. WORK UNIT NUMBER

7. PERFORMING ORGANIZATION NAME(S) AND ADDRESS(ES)

Scientific Applications &
Research Associates, Inc.
6300 Gateway Drive
Cypress, CA 90630-4844

8. PERFORMING ORGANIZATION REPORT NUMBER

9. SPONSORING / MONITORING AGENCY NAME(S) AND ADDRESS(ES)
Office of Naval Research
875 North Randolph Street
Suite 1425
Arlington, VA 22203-1995

10. SPONSOR/MONITOR'S ACRONYM(S)
Code 30

11. SPONSOR/MONITOR'S REPORT NUMBER(S)

12. DISTRIBUTION / AVAILABILITY STATEMENT
Distribution Statement A. Approved for public release; distribution is unlimited. Other requests for this document shall be referred to the Program Officer listed in the contract.

13. SUPPLEMENTARY NOTES
..

14. ABSTRACT
This report presents the results of a 37-month program to discover, identify, investigate, characterize, quantify, and document the designs ––and to predict performance characteristics of ––novel low-profile leaky-wave High Power Microwave (HPM) antennas. Our primary focus was upon geometries employing forward-traveling, fast-wave, continuous-type leaky-wave apertures conformable to various flat, singly-curved, and multi-curved surfaces. In anticipation of applications in Directed Energy Weapons (DEWs), we sought high aperture-efficiency geometries that yielded narrow-angle beams suitable for delivering high peak power densities against distant targets. New, improved, and more-compact designs for leaky-wave HPM antennas were identified, investigated, and advanced under this program. These antennas may help to solve the difficult packaging and system integration problems associated with HPM-based DEWs.

15. SUBJECT TERMS
Leaky-wave Antennas. High Power Microwave (HPM) Antennas. Low-profile Conformal Antennas.

16. SECURITY CLASSIFICATION OF:			**17. LIMITATION OF ABSTRACT**	**18. NUMBER OF PAGES**	**19a. NAME OF RESPONSIBLE PERSON (Monitor)**
a. REPORT	**b. ABSTRACT**	**c. THIS PAGE**			Lee Mastroianni
Unclassified	Unclassified	Unclassified	SAR	___	**19b. TELEPHONE NUMBER**(incl. area code) (703) 696-3073

Standard Form 298 (Rev. 8-98)
Prescribed by ANSI Std. Z39.18

Table of Contents

List of Figures iii

1. SUMMARY 1

2. INTRODUCTION 3
   2.1. Background 3
   2.2. Nomenclature 3
   2.3. Presentations at Meetings/Symposia 5

3. METHODS, ASSUMPTIONS, AND PROCEDURES 6

4. RESULTS AND DISCUSSION 7
   4.1. Theory 7
      4.1.1. Developing an initial understanding of leaky wire grills 7
      4.1.2. Developing an initial understanding of leaky dielectric windows 11
      4.1.3. Generalization of the Approach → Wave Chain Matrix Theory 13
      4.1.4. Generalization to Finite, Non-uniform (Slowly-varying) Interface Sandwiches 21
      4.1.5. Finite-width Leaky-wave Channels: 2D vs 3D Analyses 24
      4.1.6. Transition from a *Finite-width* to *Open Half-space* in the E-plane 26
      4.1.7. E-plane Transitions with Rounded, More HPM-compatible Edges. 35
      4.1.8. Mutual Coupling 41
      4.1.9. Compensating for Modified Phase-velocities in Leaky-wave Channels 52
      4.1.10. Optimizing Aperture Field Distributions Conformal to Curved Platform Surfaces 54
   4.2. FAWSEA 59
      4.2.1. A Recommended FAWSEA Design 59
      4.2.2. Steering a FAWSEA Beam in the E-plane by Phasing Multiple Channels 68
      4.2.3. Rotation of the Waveguides to Yield a Lower Profile → the FRAWSEA 69
   4.3. CAWSEA 76
      4.3.1. A Recommended CAWSEA Design 76
      4.3.2. Taking Advantage of a Greater Fraction of a Cylindrical Surface → $CAWSEA_{180}$ 83
   4.4. AAWSEA — A Representative Design Example 87
   4.5. BAWSEA 92
      4.5.1. BAWSEA Principles 92
      4.5.2. A Recommended BAWSEA Design (Preliminary) 94
   4.6. PAWSEA and GAWSEA 97
   4.7. Summary of Performance Characteristics for Recommended 4-Channel Designs 99
   4.8. Combinations with Novel Reflectors → High-Gain, Rapid HPM Beam Steering 102
   4.9. An HPM-Capable Cylindrical TM_{01}-driven Leaky Wave Antenna 104
   4.10. Beam Stabilization: Compensation/Suppression of Scanning with Frequency 107

5. CONCLUSIONS 110

6. RECOMMENDATIONS 110

7. REFERENCES 111

List of Figures

Figure 1. Decomposition of a TE_{10} waveguide mode into a pair of plane-waves. 6
Figure 2. Left: Equivalent-circuit representation (Marcuvitz, 1951) of a uniform, infinite wire grill, for TE plane-wave incidence. Right: Extracting the power reflection coefficient. 8
Figure 3. Automated generation of a list of "ideal" wire diameters for an example leaky-wave aperture (L=5m, θ=30°, f=1.3 GHz). 9
Figure 4. A 2D finite-element model, using the 159 wires generated from the theory and using the scripts described in Figure 3. 10
Figure 5. Predicted H-plane pattern, normalized to 0dB, from the 2D finite-element model, using the 159 wires generated from the theory and scripts described in Figure 3. 10
Figure 6. A dielectric window can behave much like a wire grill. 11
Figure 7. Values of ε_r (z) generated for a dielectric-window designed to deliver ~the same leaky-wave performance as the wire grill defined in Figure 3. 12
Figure 8. 2D finite-element model using the varied-dielectric window defined in Figure 7. 12
Figure 9. Predicted H-plane pattern, normalized to 0dB, from the 2D finite-element model, using the varied-dielectric window defined in Figure 7. 13
Figure 10. Some concepts & notation in the wave-matrix formalism (R.E. Collin, 1991). 14
Figure 11. Left: Equivalent circuit of wire grill (from Figure 2). Right: T-network. 15
Figure 12. Coordinates used by R.E. Collin [1991] to represent a dielectric window for TE wave incidence. 17
Figure 13. Comparison of T_{pow} predictions via Wave Matrix theory and 2D FE models. Example TE wave is incident at 30° relative to the normal. For the wire grill, we have set each wire diameter = 0.2cm and the wire separation = 4cm. The dielectric window is displaced 5cm along the normal from the grill, has a thickness of 1cm, and ε_r = 3.0 21
Figure 14. A MatLab function to evaluate R_{pow} for TE wave incidence for a wire-grill & window combination. 22
Figure 15. Theory-generated wire-diameters for a high-performance leaky-grill *with* (shown in red) and *without* (shown in blue) the presence of a dielectric window (see text for parameters). 22
Figure 16. 2D FE model, with 159 wires (see red curve in Figure 15) with diameters set via the combined wave-matrix theory including a dielectric window. (Compare to Figure 4.) 23
Figure 17. Predicted H-plane pattern, normalized to 0dB, from the 2D finite-element model in Figure 16, using the 159 wires generated via wave-matrix theory and Matlab scripts. 23
Figure 18. 2D vs. 3D representations of a leaky-wave antenna channel with identical channel lengths, depths, and leaky wire-grill geometries (and no dielectric windows). 24
Figure 19. Comparison of computed VSWR vs. frequency, 2D vs. 3D representations. (See Figure 18 for representative model geometries). All four plots on same scale. 25
Figure 20. Example channel to free-space transition in 2D, E-plane. (input *E* is vertical.) 26
Figure 21. Parallel-plate joining to an open half-space. (Borrowed from N. Marcuvitz, *Waveguide Handbook*.) 27
Figure 22. Overlay of G_A and B_A from our 2D E-plane normal-incidence FE model (the blue and green curves) on the corresponding plots in the *Waveguide Handbook*, for a parallel-plate to free half-space sudden transition in the E-plane. 27
Figure 23. Comparison of G_A and B_A from FE model (blue & green) to Marcuvitz's simplified (narrow-channel) expressions (red & light blue). 28
Figure 24. Computed reflection (S_{11}, dB) for E-plane transition, *normal incidence*. 28
Figure 25. Left: 3D model, E-plane aperture, incidence 30° to normal. Right: Predicted $|S_{11}|$. 29
Figure 26. 3D FE model, Test #1 of T_{3D0} expression. f=1.0 GHz. FE model-computed effective S_{11} = -1.882 dB, while S_{11} from wave-matrix theory = -2.018 dB. 30
Figure 27. Test #2 of T_{3D0} expression. (Note the more widely-separated wires.) FE model-computed eff. S_{11} = -4.604 dB. S_{11} from wave-matrix theory = -4.728 dB. 31

Figure 28. Left: Script to generate wire diameters vs. position, for a fixed-width channel. Right: Function called by script to compute power-reflection coefficient. 32
Figure 29. Predicted wire diameters vs. position to yield ~optimum leaky aperture. Red: Computed via the new 3D script & function listed in Figure 28. Blue: Computed via earlier 2D script, for same input conditions. 33
Figure 30. Left: Slice of E_x, 3D model of 1"-wide channel with wire-grill based on new 3D analyses. Right: After replacing wire-grill with one based on earlier 2D analyses. 33
Figure 31. H-plane patterns predicted via 3D models of a 1"-wide leaky channel. Left: For antenna with leaky-grill wire diameters derived from the new 3D analyses. Right: For antenna with leaky-grill wire diameters derived from the earlier 2D analyses. 34
Figure 32. Snapshot from a 2D E-plane model of a channel to free-space transition including a curved edge (input *E* is vertical.) 35
Figure 33. Conductance G (left) and susceptance B (right) parts of Y_A, as extracted from our FE models for a curved-edge, TEM channel to free half-space transition. 35
Figure 34. Color-plot of the *FE model-predicted* susceptance vs. both b/λ' and R_{fil}/λ' 36
Figure 35. Color-plot of *equation-based approximation* to FE-model data in Figure 34. 37
Figure 36. Approx. for the effective conductance term at the aperture, for a finite-width guide (E-plane) at a half-space interface. (Compare to left panel in Figure 33.) 37
Figure 37. 3D model, E-plane aperture *with finite radius,* R_{fil} = 3.0 cm. Plate separation b = 6.0 cm, f = 1.0 GHz, and α' = 30° rel. to normal. From this FE-model, $|S_{11}|$ = -8.97 dB. A prediction based on our new approx. for Y_A yields: $|S_{11}|$ = -8.72 dB. 38
Figure 38. Matlab function to compute TEM wave power-reflection coefficient (R_{pow}) for a *wire-grill* across a *fixed-width* channel followed by a short *vacuum-space* and a *rounded transition* to an aperture onto an open half-space. 38
Figure 39. 3D model, wire grill + E-plane aperture *with finite radius,* R_{fil} = 3.0 cm. Plate separation b = 6.0 cm, f = 1.0 GHz, and α' = 30° rel to normal. Grill wire diams = 2mm. Grill wire spacing = 6cm. Grill is 5cm from aperture. From the FE-model, $|S_{11}|$= -4.19 dB. From the function in Figure 38, $|S_{11}|$= -4.65 dB, for a difference of 0.46 dB or about 11%. 39
Figure 40. 3D model, wire grill + E-plane aperture *with finite radius,* R_{fil} = 2.0 cm. Plate separation b = 5.0 cm, f = 1.3 GHz, and α' = 30° rel. to normal. Grill wire diams = 3.0mm. Grill wire spacing = 4.5cm. Grill 5cm from aperture. FE-model→ $|S_{11}|$ = -1.75dB. Function in Figure 38 → $|S_{11}|$ = -1.87 dB, a difference of 0.12 dB, or about 3%. 39
Figure 41. Computed wire diameters vs. position for 3D single-channel 1.5m-long FAWSEA with a flared aperture but no window. See text for more info. 40
Figure 42. 3D single-channel FAWSEA model for f_0=1.3 GHz, with length =1.5m, chan. width =5cm, R_{fil} = 2cm, and wire-grill based on 3D analyses. No window. 40
Figure 43. Predicted H-plane antenna pattern after increasing channel depth of model in Figure 42 by 2.2%. The beam now points at 30.0° and the beamwidth = 9.01°. 41
Figure 44. Mutual coupling between two adjacent channels in a leaky-wave antenna. 41
Figure 45. Examining mutual coupling, five neighboring channels *driven identically.* 42
Figure 46. Parameter definitions in 2D E-plane TEM-wave mutual-coupling study. 43
Figure 47. Computation space in 2D E-plane TEM-wave mutual-coupling study. 43
Figure 48. Computed S_{21} (dB) vs. frequency (all 3,300 cases) 44
Figure 49. Projections of values in Figure 48 vs. key parameters scaled by wavelength. 44
Figure 50. Computed wire diameters vs position for the 3D FAWSEA (with no window) selected for initial use in our mutual-coupling study. 45
Figure 51. Case of one isolated 3D FAWSEA channel (opening onto a conducting plane) 46
Figure 52. Three tightly-spaced channels, all driven. (Channel spacing = 8 cm) 46
Figure 53. Three tightly-spaced channels, one side-channel driven. Chan. spacing 8 cm. 47
Figure 54. Three tightly-spaced channels, center-channel driven. Chan. spacing: 8 cm. 48

Figure 55. Selected curves from Figure 48, showing falling S_{21} as chan. separation rises. 48
Figure 56. Three channels, with only center-channel driven. Chan. spacing = 10 cm. 49
Figure 57. Three channels, with only center-channel driven. Chan. spacing = 12 cm. 49
Figure 58. Three channels, with only center-channel driven. Chan. spacing = 14 cm. 50
Figure 59. Three channels, all driven. Channel spacing = 14 cm. 50
Figure 60. Three channels, only one side channel driven. Channel spacing = 14 cm. 51
Figure 61. |E| (kV/cm) in vicinity of the aperture for the Figure 59 design, if P_{src} ~1 GW. 51
Figure 62. Three channels, all driven, R_{fil} increased to 4cm. Channel spacing = 14 cm. 52
Figure 63. |E| (kV/cm) in vicinity of the aperture for the Figure 62 design, if P_{src} ~1 GW. 52
Figure 64. Concept of a *virtual* perfectly-conducting wall for the phase-velocity computation. (Note: this is an H-plane view; E is normal to the page) 53
Figure 65. Listing of custom MatLab function 'DeltaXtra' that computes $\delta_{xtra.}$ 53
Figure 66. Computed δ_{xtra} vs wire diameter for various wire spacings, scaled to the free-space λ, for $\theta_{inc}=30^{o}$. 54
Figure 67. Snapshots, projected plane-waves onto cylinder, sphere, & cylinder + ogive. 57
Figure 68. Predicted gains vs. frequency, computed using the projected aperture fields on the example surfaces in Figure 67. 58
Figure 69. Perspective views of the subject antenna in one- and four-channel variants. 59
Figure 70. Single FAWSEA channel, cross-section taken at junction to feed. Units are cm. 60
Figure 71. Single channel side view, including wires and tapered backplane. Units are cm. 60
Figure 72. List of wire radii vs. position index. Wire spacing is fixed at 5.25 cm, center-to-center. All 36 wires are parallel and lie in the same plane, 9.1 mm below the "zero-reference plane" in Figure 70. 61
Figure 73. A half-channel, sliced along its symmetry plane for use in 3D RF modeling. 61
Figure 74. Four channel FAWSEA cross-section (not tapered). Units are cm. 62
Figure 75. Half of a 4-chan FAWSEA sliced along its symmetry plane, for 3D RF modeling. 62
Figure 76. Computed Effective VSWR vs. Frequency 63
Figure 77. Computed Gain vs. Frequency 63
Figure 78. Predicted Aperture Efficiency vs. Frequency. 64
Figure 79. Peak values of E_{max} vs. frequency on exposed exterior window surfaces, for total input power = 1 GW. 64
Figure 80. Predicted beam tilt relative to aperture normal, vs. frequency. 65
Figure 81. Principal-plane pattern cuts at $f=f_0$. 65
Figure 82. Selected 3D far-field patterns for a single-channel FAWSEA. 66
Figure 83. Selected 3D far-field patterns for a four-channel FAWSEA. 67
Figure 84. An example 14-channel Phase-Steerable HPM-Capable FAWSEA 68
Figure 85. The output beam can be steered effectively via relative phasing the inputs. 69
Figure 86. Cross-sections, shown to scale in solid and transparent views, for 4-channel flat-aperture designs with f_0 = 1.0 GHz. Only half of each cross-section (two channels) is shown. Left: FAWSEA. Middle: Previous RAWSEA design. Right: New FRAWSEA. 70
Figure 87. Views of a single-channel FRAWSEA, including a waveguide smooth tapered transition / adapter to facilitate practical connection to a rectangular waveguide. 71
Figure 88. Example four-channel FRAWSEA designed for f_0=1.0 GHz and employing mirror-symmetric feeds. Tapered waveguide transitions/adapters are used to allow practical connection of the antenna to rectangular waveguides. 72
Figure 89. Grill wire diameters and locations along leaky grill. 72
Figure 90. Computed 3D antenna patterns, four-channel FRAWSEA at 3 frequencies. 73
Figure 91. Predicted performance vs. frequency for the 4-channel FRAWSEA (includes waveguide adapters) of Figure 88. 74
Figure 92. FRAWSEA Beam tilt vs. Frequency 75

Figure 93. Polar E- and H-plane pattern cuts at f=f_0 for our recommended 4-channel FAWSEA (left) vs. the new recommended 4-channel FRAWSEA (right). (Same scale.) 75
Figure 94. CAWSEA. Left: Uncompensated. Right: Compensated for aperture curvature. 76
Figure 95. Four channel CAWSEA cross-section (not tapered) for f_0=1 GHz. Units are cm. 76
Figure 96. Half of a 4-channel compensated CAWSEA, sliced along its symmetry plane. 77
Figure 97. Computed Effective VSWR vs. Frequency 77
Figure 98. Computed Gain vs. Frequency 78
Figure 99. Predicted Aperture Efficiency vs. Frequency. 78
Figure 100. Aperture E, uncompensated (left) vs. compensated (right) CAWSEA at f_0. 79
Figure 101. Peak values of E_{max} vs. frequency on exposed exterior window surfaces, for total input power = 1 GW. 79
Figure 102. Principal-plane pattern cuts at f=f_0. 80
Figure 103. Selected 3D far-field patterns for a four-channel *uncompensated* CAWSEA. 81
Figure 104. Selected 3D far-field patterns for a four-channel CAWSEA compensated at f=f_0. 82
Figure 105. Naïve extension of our standard CAWSEA design (left) to a full 180° half-cylinder. (Half models shown above, using symmetry). Phase-correcting feeds are not shown in the right-hand panel, but phase-correction was investigated (see text). 83
Figure 106. Geometry comparison, the "recommended" 4-chan $CAWSEA_{90}$ vs. an alternative 16-chan $CAWSEA_{180}$ 84
Figure 107. 3D gain patterns at f=1.0 GHz. Phase-compensated CAWSEAs. 85
Figure 108. Left: Aperture distribution from 3D RF model of 16-chan $CAWSEA_{180}$. Right: Distribution from an ideal magnitude-preserving plane wave projection. 85
Figure 109. Comparisons of gain, aperture efficiency, VSWR, and beam-tilt vs frequency. 86
Figure 110. Single-channel AAWSEA (design building block) designed for f_0 = 1.0 GHz 87
Figure 111. Grill wire diameters and location along leaky grill. 87
Figure 112. Detail of Upper Region of the Four-channel AAWSEA. 88
Figure 113. Predicted performance plots of the 4-chan AAWSEA (with comparison to 4-chan FAWSEA) 89
Figure 114. Example 3D Antenna patterns for the *single-channel* AAWSEA at three frequencies. The orientation of the antenna is shown at the right. 90
Figure 115. Example 3D Antenna patterns for the *four-channel* AAWSEA at three frequencies. The orientation of the antenna is shown at the right. 90
Figure 116. Comparison of predicted gain vs. frequency for the 4-chan vs. 1-chan AAWSEA. 91
Figure 117. Model-predicted beam tilt (relative to normal at feed end of antenna) for the AAWSEA, vs. the expected curve for a FAWSEA. 91
Figure 118. Derivation of BAWSEA channel-phasing to yield a single high-gain beam. 92
Figure 119. Determination of the required BAWSEA channel effective depths. 93
Figure 120. Non-radiating models to explore constant (left) vs. adjusted (right) depths. 93
Figure 121. Phasing that results from constant (left) vs adjusted (right) depth channels. 94
Figure 122. Example of a Single-channel BAWSEA (views from 3D RF model) 95
Figure 123. Example of a Four-channel BAWSEA (views from 3D RF model) 95
Figure 124. Perspective views of the four-channel BAWSEA example 96
Figure 125. Predicted VSWR (effective) vs Frequency for the example 4-chan BAWSEA. 96
Figure 126. Comparison of Predicted Gain (left) and Aperture Efficiency (right) for the example 4-chan BAWSEA and the 4-chan FAWSEA from Section 4.2.1. 97
Figure 127. Example of a Surface Suitable for a PAWSEA. 97
Figure 128. A Generalized Aperture Waveguide Sidewall-Emitting Antenna (GAWSEA) features multiple channels & curvatures and a distribution of leaky-wave apertures to yield an overall aperture customized for maximizing power delivered against a target. 98
Figure 129. Predicted gain, aperture efficiency, VSWR, and surface $|E|_{max}$ for recommended designs. . 100

Figure 130. E-plane and H-plane polar gain plots at $f = f_0$ for recommended 4-channel designs: FAWSEA (Section 4.2.1), FRAWSEA (Section 4.2.3), AAWSEA (Section 4.4), BAWSEA (Section 4.5.2) and CAWSEA (Section 4.3.1). 101
Figure 131. Over a decade ago, SARA developed "the world's first truly-steerable HPM antenna" leveraging a horn/trans-reflector/twist-reflector combination..... 102
Figure 132. An LWA feed and matching conical-section trans-reflector offer greater peak power handling, while the twist-reflector provides the beam steerabiity..... 103
Figure 133. Model of antenna in Figure 132 with beam in forward "non-steered" position. 103
Figure 134. Beam steered 30° in azimuth (via rotating the twist-reflector 15°). This steering reduces the predicted gain by only 0.18 dB relative to the non-steered case. 104
Figure 135. Example physics-level design (prelim) of an HPM-capable TM_{01}-circular mode driven leaky-wave antenna. (Note: This design is for $f_0 \sim 1.35$ GHz) 105
Figure 136. Predicted behavior of the antenna in Figure 135. 106
Figure 137. Some computed 3D radiation patterns for the antenna in Figure 135. 106
Figure 138. Motivation, problems, and solutions found on the research path that led to this broad-banding concept. 107
Figure 139. A novel antenna combining leaky-wave channels with compensating-path waveguides to drive an array. (L-band, 8x8 array. Other sizes and arrays are possible.) 107
Figure 140. Detail of the coupled paths, which use inductive irises and stubs instead of a wire grill, to leak/couple the traveling-wave's power into eight separate waveguides..... 108
Figure 141. Predicted behavior of this fixed-beam wide-bandwidth antenna is encouraging. 109

1. SUMMARY

The technology of High Power Microwave (HPM) / High Power Radiofrequency (HPRF) sources, whether for purposes of effects-testing or Directed Energy Weapons (DEW) development, has matured greatly in recent years. Similar and perhaps even more dramatic improvements have been seen in high-voltage pulsed power supplies, as well as improved prime power, including batteries. As all of these smaller, more capable, more efficient, lighter weight, and more reliable components have become more available, engineers have sought ways to integrate fieldable DEW packages including them, along with suitable radiators (antennas), and other necessary supporting components (e.g., control electronics). In many cases, the *antenna* is now the bulkiest component of the system. As such, technologists working in the DEW and broader scientific/engineering community have been called upon, repeatedly, to design *more compact* HPM-capable antennas. But this problem remains (and will continue to remain) incompletely solved, since fundamental physics imposes rigorous lower bounds on antenna aperture areas that can deliver the desired gain and peak-power handling. But this is *not* the end of the story. In contrast to aperture *area*, there exists effectively no fundamental physics barrier to reducing aperture *depth* (aka, the "profile") of the aperture. Depth reduction, without prohibitively sacrificing gain, bandwidth, peak power handing, or other desirable antenna performance characteristics is an *engineering* challenge. Genuinely innovative and practical "low-profile" designs can be difficult to prepare, but they are at least possible, given sufficient time and dedication.

The "Flat Aperture, Waveguide Sidewall-Emitting Antenna" (FAWSEA) invented (December, 2004) and advanced (2004-present) by Scientific Applications & Research Associates (SARA), Inc. set a new standard for shallowness-of-depth among gigawatt (GW)-class HPM-capable antennas. The FAWSEA is a Leaky Wave Antenna (LWA) of the *forward-traveling, fast-wave, continuous-aperture* type. This subset of LWAs is especially well-suited to customization for HPM operation. The "FAWSEA family" of designs has grown steadily and now includes several surface-conformal variants with curved apertures, including the "Curved" (CAWSEA), "Arched" (AAWSEA), and "Bent" (BAWSEA) configurations, with the applied name depending on which axis of curvature is involved. In general, these antennas employ multiple evacuated leaky-wave channels arrayed side-by-side and joined in a manner that minimizes breakdown risk, with an aperture covered by a relatively-thin, yet structurally-robust, vacuum window.

This report reviews the principles/theory of operation, explains the analysis methods employed, and presents specific designs of a representative/reference set of HPM-capable LWA antennas of various shapes. In addition to basic theory, two- and three-dimensional Finite Element (FE) based full-wave RF numerical models were used extensively to analyze and characterize these and other designs. More complicated variations, including the "Pinched Aperture, Waveguide Sidewall-Emitting Antenna" (PAWSEA) and "Generalized Aperture, Waveguide Sidewall-Emitting Antenna" (GAWSEA) are also mentioned in this report, but their designs and performance are not addressed in detail.

We also discuss a potentially-important novel design variation that rotates/folds the individual arrayed channels to reduce the antenna depth substantially, albeit at the cost of more complex design/fabrication. In particular, antenna depths can be reduced to as little as ~0.43 λ_0 by such means, with applicability to the flat, curved, arched, and bent variants noted above. An example application of this technique to the FAWSEA (renaming the result as a "FRAWSEA"; the "R" = "Rotated") is analyzed in some detail.

Almost all of the antenna designs described here are built-up using fundamental-mode (TE_{10}) leaky rectangular waveguides. An important exception worth noting is a rather simple-looking long cylindrical LWA fed directly by a cylindrical TM_{01}-mode (typical of some axially-symmetric HPM sources). The predicted performance is surprisingly good and we expect this antenna may have important applications.

The antenna designs presented in this report can, to a large extent, be scaled to nearly-arbitrary frequencies and/or customized across a broad range of aperture aspect ratios by choosing the lengths of individual channels and the number of channels arrayed, and following along with the methods/guidance provided herein. Optimization of designs prepared in this manner may still require use of some 2D/3D RF modeling, but the design time and effort will be greatly reduced compared to starting from scratch. The LWAs featured here exhibit beam-scanning with frequency in the H-plane, with very few exceptions. Beam steering in the E-plane of these antennas is also possible if detailed phase control of multiple channels is available, but this is seldom a practical option using currently-available HPM sources.

Combinations of HPM-capable LWAs with reflectors can provide additional benefits. One simple and convenient gain-boosting configuration is to combine an HPM-capable LWA (acting as a distributed feed) with a conical-sectional reflector. If the reflector's solid surface is replaced with a grill (aka, trans-reflector), then along with the addition of a secondary flat twist-reflector, it becomes possible to steer a GW-class, high-gain beam rapidly through large angles of azimuth and elevation, all without any need for RF phase-control or HPM-capable waveguide rotary joints. An example (and 3D RF numerical model) of such a configuration is included.

Finally, it is sometimes preferable for the beam direction to remain fixed (i.e., not scan) when the frequency is varied. This is not a feature of traveling-wave LWAs generally, however a modified configuration is presented here that combines an LWA with path-compensating waveguide elements to yield a beam that is, in fact, quite stable in its direction as the frequency is varied over substantial bandwidth.

It is important to note that separate, previous, experimental work has validated the VSWR, gain, patterns, and HPM-class peak power capability in full-scale evacuated multi-channel FAWSEAs – with related but not identical designs to those in this report – in laboratory tests at AFRL/RDH (Kirtland AFB, NM). That earlier work increases our confidence in the newer designs presented here, since the latter not only build upon them, but also leverage improved understanding achieved under this program. The "recommended" and other designs presented in this report are based on analyses and numerical models; they have not yet been fully-engineered, built, or tested. Thus, one of the more straightforward "next steps" to advancing the Technology Readiness Levels (TRLs) of these various new designs would be to establish programs to build representative full-power capable hardware and execute laboratory tests.

The investigations performed under this program have expanded the "FAWSEA family" of low-profile LWA-type HPM antennas and have documented new and improved designs and design methods. Some extensions and spinoffs have also been identified, and may themselves prove to be consequential. The future of at least some of these antennas in HPM applications looks bright. We anticipate and look forward to additional opportunities to advance the analyses of some of the less-investigated variants (e.g., the PAWSEA) as well as to further the overall technology of these remarkable antennas.

We are very grateful for ONR's generous support of this research.

2. INTRODUCTION

2.1. Background

Leaky wave antennas (LWAs) have appeared in the literature at least as far back as 1940 (Hansen, 1940). There exist several different important categories of LWAs, of which *only a subset* are discussed in this report. For more general overviews or modern introductions to the well-developed subject of LWAs in general, we refer the interested reader to Oliner and Jackson (2007), Jackson (2012), and/or Xu and Wu (2013). In particular, with few exceptions, we are concerned here only with *forward-traveling*, *fast-wave*, *continuous-aperture* type LWAs. We will further focus our attention on LWAs deemed *one-dimensional,* a potentially-confusing label which means simply that the wave is locally guided in a *single direction*. (Note that for some of the antennas described in this report, this is *not a straight line*.) Needless to say, real-world physical construction of all these antennas is three dimensional and the required *analyses* and *models* of these "1D" antennas may be variously 1D, 2D, or 3D. Of particular motivation and interest here is that the apertures of these antennas can often be made conformable to various flat, singly-curved, or multi-curved surfaces, with some limitations.

Initial research investigating HPM applications of LWAs (Koslover, 2007-2010) was performed by SARA, Inc. under sponsorship of the US Air Force Research Laboratory. SARA's "Flat Aperture, Waveguide Sidewall-Emitting Antenna" (FAWSEA) was the first HPM-capable LWA to be developed and was validated experimentally at AFRL/RDH (KAFB, NM) in operation with an HPM source. This led to increased awareness in the DEW community of the potential benefits offered by LWAs adapted to HPM operation, as well as to additional R&D funding by the Air Force and Navy (NAVAIR and ONR).

Advantages of LWAs adapted/customized to directed energy weapon (DEW) applications include:

- Support for extremely high (e.g., multi-GW) peak power, if evacuated waveguides are employed and the aperture-interface geometries are appropriately customized.
- High gain and aperture efficiency
- Low-profile (thickness $< \lambda_0$ generally; thickness $< \lambda_0/2$ in special "rotated" designs)
- Bandwidth more than sufficient for compatibility with narrowband HPM sources
- Aperture(s) conformable to flat and variously curved surfaces
- Highly customizable to fit various aperture sizes and aspect ratios
- Potential for beam-steering via frequency (in H-plane) or by phasing across multiple channels
- Ruggedizable for harsh operating environments
- No exotic materials or unusual machining tolerances required to fabricate.

2.2. Nomenclature

The following table of "FAWSEA family" antennas (Table 1, next page) gathers together some of the names we now associate with various configurations customized to fit particular aperture shapes and curvatures. An *R* introduced following the first letter (see Table 2) indicates that the individual leaky waveguide channels are *rotated* relative to the aperture. This rotation can significantly reduce the antenna's depth. For example, a "FRAWSEA" is a "Flat *Rotated* Aperture, Waveguide Sidewall-Emitting Antenna."

Table 1. Suggested Nomenclature for the "FAWSEA Family" of HPM-capable Low-profile Forward-traveling Fast-wave Continuous-aperture Leaky-wave Antennas

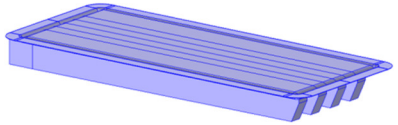
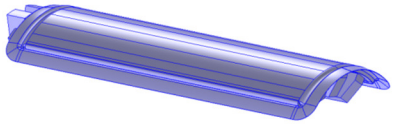
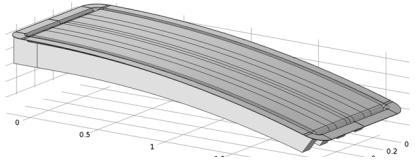
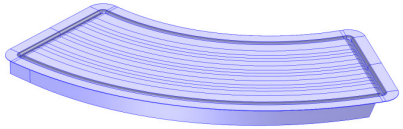
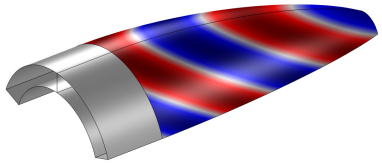
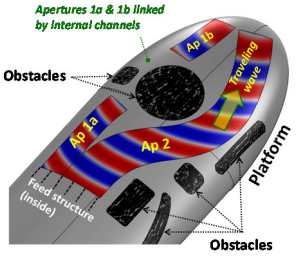
Acronym	Full Name	Identifying Geometry / Feature(s)	Example Appearance
FAWSEA	Flat Aperture, Waveguide Sidewall-Emitting Antenna	Flat linear aperture, parallel straight channels.	
CAWSEA	Curved Aperture, Waveguide Sidewall-Emitting Antenna	Aperture curved in E-plane. Curvature may be compensated via delays introduced at feeds.	
AAWSEA	Arched Aperture, Waveguide Sidewall-Emitting Antenna	Aperture curved in H-plane. Curvature may be compensated via varying β along guides.	
BAWSEA	Bent Aperture, Waveguide Sidewall-Emitting Antenna	Aperture curved in the aperture plane. Curvature compensated via varying β along guides and unequal division of power among channels.	
PAWSEA	Pinched Aperture, Waveguide Sidewall-Emitting Antenna	Double- or triple-curved aperture customized to conform to part or all of an ogive (nose cone). Curvature compensated via delays at feeds and varying β along guides.	
GAWSEA	Generalized Aperture, Waveguide Sidewall-Emitting Antenna	Multiple curvatures, non-contiguous apertures, or otherwise complex geometry. Curvatures and shapes compensated via delays at feeds, varying β along guides, unequal division of power among the channels, etc.	

Table 2. Additional Nomenclature to Indicate Channels Rotated Relative to the Aperture

Original Nomenclature	If channels are rotated	Aperture Curvature (see Table 1)
FAWSEA	FRAWSEA[1]	*Flat*
CAWSEA	CRAWSEA	*Curved*
AAWSEA	ARAWSEA	*Arched*
BAWSEA	BRAWSEA	*Bent*
PAWSEA	PRAWSEA	*Pinched* (to fit an ogive)
GAWSEA	GRAWSEA	*Generalized* (multi-type)

Note: The name "RAWSEA" was used previously to denote an antenna with rotated channels, but this leaves the aperture curvature ambiguous. We encourage using the terms above instead.

In practice, these antennas are normally composed of *multiple* leaky-wave channels, each operating in and supporting only the fundamental waveguide mode. The apertures of these channels are, and must be, joined together cleanly, maintaining a channel-to-channel spacing that simultaneously limits excessive mutual coupling, yields high aperture efficiency, and (in conjunction with a vacuum window interface) supports HPM operation throughout the required bandwidth. Detailed geometries and important features essential to realizing HPM-supporting conditions are discussed in this report. A nearly lossless HPM-capable power divider (i.e., a waveguide corporate feed) is typically combined with such a multi-channel FAWSEA-family antenna if an HPM source with a single output is to be used. In general, multi-output HPM sources can be connected to multi-input antennas by a nearly limitless variety of HPM-capable waveguide combiners and adapters. (Design of those components is beyond the scope of this report, although we may comment on some sub-components here and there.) Regardless, the division of full-aperture width channel LWAs into multiple narrower channels precludes the risk of overmoding. The use of *arrayed* (but carefully seamlessly fused) single-mode-only channels is just one of the important ways that truly HPM-capable designs differ from those in most published literature documenting this subset of LWAs. Of particular relevance here are the works of Honey (1959) and Honey and Shimizu (1960) who reported flat and curved LWAs analogous to the FAWSEA and AAWSEA antennas described herein, but: (1) did not pursue use of multiple channels, instead avoiding overmoding by careful wave-launching, and (2) evidently did not seek to introduce the additional features needed to support HPM operation.

Section 3 presents a brief description of the means by which this research program was executed, which includes both basic theoretical analyses and extensive use of 2D and 3D numerical models. Section 4 is the main body of this report, addressing the theory/analyses applied, the models developed, the designs prepared, and the predicted performance characteristics for suggested embodiments of these antennas. The last few sub-sections of Section 4 present related and novel antenna designs that leverage some of the concepts from this research program. Section 5 and Section 6 present our conclusions and recommendations respectively. Technical papers and literature cited in the body of this report are listed in Section 7.

2.3. Presentations at Meetings/Symposia

Presentations specifically reporting R&D performed under this ONR-supported program include:

- Koslover, R.A., G.R. Raith and S.M. Jalali, "Novel Low-Profile Surface-Conforming Leaky-Wave Antennas for Very High Peak Power Applications," to be presented at URSI/NRSM, UC Boulder, CO, Jan 4–7, 2017.
- Koslover, R.A., G.R. Raith and S.M. Jalali, "Improvements in Low-Profile HPM-Capable Conformable Leaky-Wave Antennas," 18th Annual Dir. Energy Prof. Soc. (DEPS) Symposium, Albuquerque, NM, Mar. 7-11, 2016.
- Koslover, R.A. and G.R. Raith, "Advances in Low-Profile Leaky-Wave Conformable Antennas for HPM Applications," 17th Annual Dir. Energy Prof. Soc. (DEPS) Symposium, Anaheim, CA, Mar. 2-5, 2015.

[1] Section 4.2.3 provides an illustrative example of a FRAWSEA.

3. METHODS, ASSUMPTIONS, AND PROCEDURES

Nearly all of the antennas described in this report leverage geometries where TE_{10} –mode[2] waves are partially transmitted through, and partially reflected by, leaky side-walls. The process can be visualized via decomposition of the TE_{10} mode into two plane waves, as shown in Figure 1. This view provides perhaps the simplest way to understand why the radiated traveling wave always exits at an angle relative to the aperture normal. The leaky wall (or walls, if multiple leaky channels are arrayed together) transition more or less directly to the aperture of the antenna, which generally includes a vacuum-window. The method of computation of the transmitted and reflected amplitudes and phases of the guided waves at the leaky wall depend in detail on the nature of that interface. It is desirable, from the perspective of supporting extremely high peak powers, that the strength of the transmitted wave be as uniform in magnitude as possible as it exits the aperture, to keep |E| well below external air-breakdown thresholds (E_{br}~30 kV/cm) at all locations. This motivates the designer to prefer an aperture that is as *open* and *continuous* as practical.

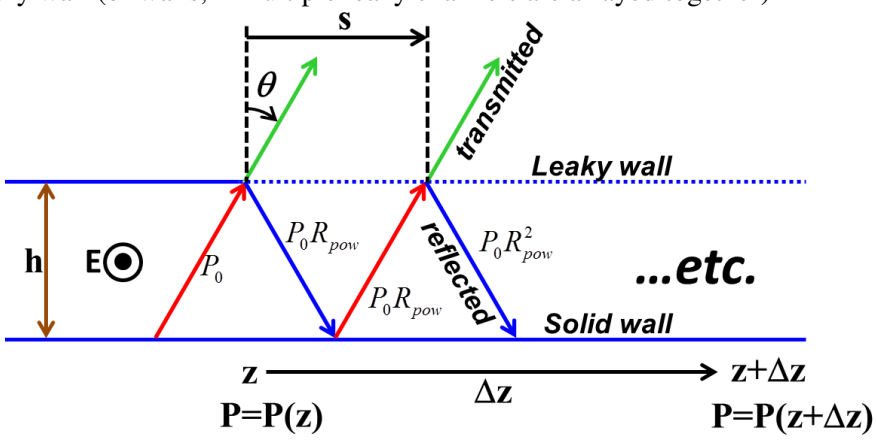


Figure 1. Decomposition of a TE_{10} waveguide mode into a pair of plane-waves.

An especially-practical way (but not the only way) to build such a leaky interface is with a unidirectional wire grill, with its wires aligned parallel to E. Such a grill can completely replace one of the waveguide sidewalls, providing a very substantial "open" area for the emitted radiation. Wires aligned with E (which are also along the waveguide sidewall currents, for a TE_{10} mode) introduce no field enhancements, which is another very desirable feature. The leakage rate can be set via the choice of wire diameters, wire-to-wire spacing, or both. This method provides the designer with the flexibility needed to distribute the radiation along an aperture of highly-customizable length. Uniform wire grills, i.e., those composed of equal-diameter wires uniformly spaced, and subject to plane-wave illumination, have been analyzed in detail and are described in the literature (Lamb, 1898; MacFarlane, 1946; Marcuvitz, 1951) as equivalent to combinations of lumped elements in transmission-line circuits. These treatments can be generalized to grills with *slowly-varying* diameters and/or spacings, providing an analytic basis upon which to establish preliminary configurations of customized leaky walls in waveguides. Such analyses can then be extended further via the Wave Matrix Formalism (Collin, 1991) to include and account for an adjacent dielectric vacuum window as well, although it is not so straightforward to do this correctly if a clean separation of the problem into multiple discrete regions of plane wave-like propagation is difficult. Discussion of analytic methods is provided in Section 4.1. When we found such conventional analyses to be limited, we applied modern numerical models, including many 2D and 3D full-wave RF Finite Element (FE) representations built using Comsol Multiphysics[3] and its associated RF Module, as operated on relatively-powerful scientific workstations.

[2] Section 4.9 presents a notable exception, with an HPM-capable LWA driven by a circular TM_{01} mode.
[3] www.comsol.com

As planned, we developed a number of recommended, reference, or building-block designs for several of the antenna types in Table 1. These designs are presented in this report in some detail. Aside from being more or less usable as-is, the predicted RF performance characteristics of these examples should help the designer to understand just what kind of performance to expect and to endeavor to achieve, when customizing these antennas to various applications.

4. RESULTS AND DISCUSSION

4.1. Theory

4.1.1. Developing an initial understanding of leaky wire grills

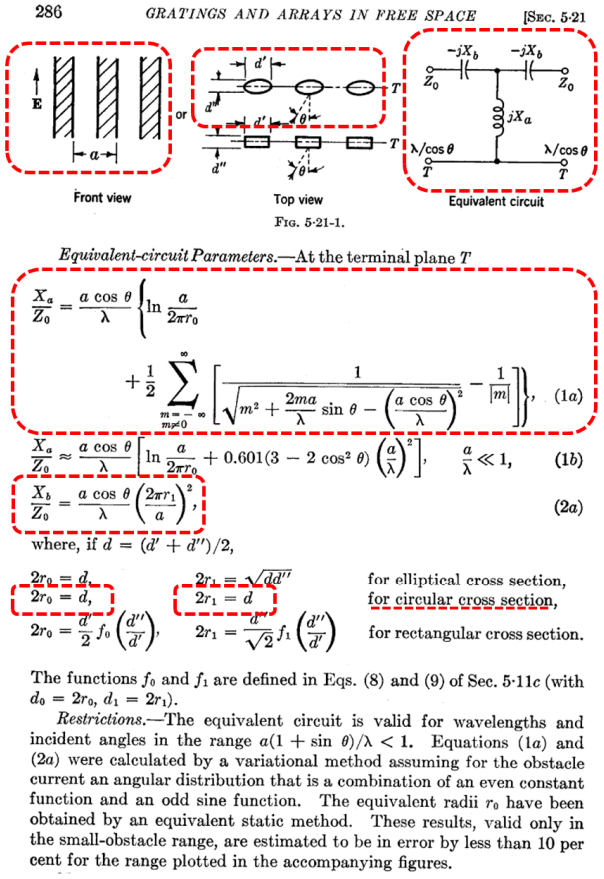
Successful design of leaky-wave HPM antennas depends fundamentally, though not exclusively, upon the designer's ability to engineer well-controlled leaky-wave boundaries (aka, partially reflective surfaces) to replace waveguide sidewalls. Assemblies of waveguide with such boundaries, when appropriately joined/ arrayed, can yield HPM-capable apertures exhibiting high gain and other desirable characteristics. Parallel wire-grills, with wires oriented along **E**, are especially applicable to this objective and thus deserve much attention. The earliest work we have found quantifying reflection and transmission characteristics of wire grills was done more than a century ago (Lamb, 1898). Transmission and reflection of TE and TM-incident plane waves at arbitrary angles of incidence, for infinite, uniform arrays of grill wires, are discussed in the *Waveguide Handbook* (Marcuvitz, 1951), which employs an approximate equivalent-circuit transmission-line (TL) model. Others have since added correction terms and expanded the utility of these kinds of models. R.C. Honey (1959), for example, applied these methods with much success to his "Flush-Mounted Leaky-Wave Antenna," which, despite the fact it was neither intended nor well-suited to HPM operation, sported a leaky-wave aperture that foreshadows SARA's HPM-capable FAWSEA.

Figure 2 shows a page borrowed from Marcuvitz, along with added notes about how to extract the power reflection coefficient from the equivalent circuit representation. This shows us a useful way to compute *plane-wave* reflection and transmission from *uniform grills* in *free space*. But it can also be generalized to *non-uniform* grills and *guided waves*. Perhaps the easiest way to attain this generalization is to recall that a TE_{10} waveguide mode can be written as a superposition of two plane waves, with a characteristic propagation angle. Refer again to Figure 1. The local (as a function of z) reflection and transmission of these waves through a non-uniform leaky-grill can be assessed by the method in Figure 2, provided that: (1) characteristics of the grill vary sufficiently slowly with z, and (2) the leakage rate is sufficiently low that the waveguide mode is well preserved. For the TE_{10} mode: $s=4h^2/\lambda_g$, $\lambda_g=\lambda_0/\sin\theta$, and $\cos\theta = f_c/f$, where f_c is the cutoff frequency, $f_c=c/2h$. The power in the guide remaining at distance $z+\Delta z$ is thus: $P(z+\Delta z)=P(z)R_{pow}^{\Delta z/s}$, since $\Delta z/s$ = the number of bounces between z and $z+\Delta z$. In the limit as $\Delta z \to 0$, this becomes a differential equation:

$$\frac{1}{P(z)}\frac{dP}{dz} = -\alpha(z), \text{ with: } \alpha(z) = -\frac{\lambda_g}{4h^2}\ln\left(R_{pow}\right).$$

Clearly, for a *uniform* grill, R_{pow} would become a constant, and thus α would reduce to a constant as well, leading to the classic solution $P(z)=P_0e^{-\alpha z}$. However, that case is seldom of interest in HPM antenna design. Instead, the optimization of both gain and peak power-handling more-generally mandates that: (1) nearly all the power radiate from the guide within a given length *L*, and (2) that this radiation rate be close to uniform, i.e., that the radiated power per unit length of the aperture be constant. Mathematically, for an aperture spanning from z=0 to z=L, those conditions require:

$$\frac{dP}{dz} = -\frac{P_0}{L} \rightarrow P(z) = P_0\left(1-\frac{z}{L}\right).$$



286 GRATINGS AND ARRAYS IN FREE SPACE [SEC. 5·21

Front view Top view Equivalent circuit

FIG. 5·21·1.

Equivalent-circuit Parameters.—At the terminal plane T

$$\frac{X_a}{Z_0} = \frac{a\cos\theta}{\lambda}\left\{\ln\frac{a}{2\pi r_0} + \frac{1}{2}\sum_{\substack{m=-\infty \\ m\neq 0}}^{\infty}\left[\frac{1}{\sqrt{m^2 + \frac{2ma}{\lambda}\sin\theta - \left(\frac{a\cos\theta}{\lambda}\right)^2}} - \frac{1}{|m|}\right]\right\}, \quad (1a)$$

$$\frac{X_a}{Z_0} \approx \frac{a\cos\theta}{\lambda}\left[\ln\frac{a}{2\pi r_0} + 0.601(3 - 2\cos^2\theta)\left(\frac{a}{\lambda}\right)^2\right], \quad \frac{a}{\lambda} \ll 1, \quad (1b)$$

$$\frac{X_b}{Z_0} = \frac{a\cos\theta}{\lambda}\left(\frac{2\pi r_1}{a}\right)^2, \quad (2a)$$

where, if $d = (d' + d'')/2$,

$2r_0 = d$, $2r_1 = \sqrt{dd''}$ for elliptical cross section,

$2r_0 = d$, $2r_1 = d$ for circular cross section,

$2r_0 = \frac{d}{2} f_0\left(\frac{d''}{d'}\right)$, $2r_1 = \frac{d''}{\sqrt{2}} f_1\left(\frac{d''}{d'}\right)$ for rectangular cross section.

The functions f_0 and f_1 are defined in Eqs. (8) and (9) of Sec. 5·11*c* (with $d_0 = 2r_0$, $d_1 = 2r_1$).

Restrictions.—The equivalent circuit is valid for wavelengths and incident angles in the range $a(1 + \sin\theta)/\lambda < 1$. Equations (1*a*) and (2*a*) were calculated by a variational method assuming for the obstacle current an angular distribution that is a combination of an even constant function and an odd sine function. The equivalent radii r_0 have been obtained by an equivalent static method. These results, valid only in the small-obstacle range, are estimated to be in error by less than 10 per cent for the range plotted in the accompanying figures.

How we are using this:

Step 1. Apply Kirchhoff's laws to extract the impedance this circuit presents to an incident wave on a TL. This yields:

$$Z_{eq} = j(X_a - X_b) - \frac{X_a^2}{-Z_0 + j(X_b - X_a)}$$

Step 2. Compute the power reflection coefficient from the impedance mismatch (with Z_0 normalized to unity.)

$$\Gamma = \frac{Z_{eq} - 1}{Z_{eq} + 1} \qquad R_{pow} = |\Gamma|^2$$

Step 3. Code it into a MatLab function, for convenience.

```
function Rpow = myRpow(AngIn,a,d,freq)
  ct = cos(AngIn);
  st = sin(AngIn);
  c_const = 2.99792458e8; %c in m/s
  lambda = c_const/freq; % free space wavelength
  sum1 = 0;
  sum2 = 0;
  for m = 1:1:1000
     sum1 = sum1+1/sqrt(m^2+2*m*a*st/lambda-(a*ct/lambda)^2)-1/m;
     sum2 = sum2+1/sqrt(m^2-2*m*a*st/lambda-(a*ct/lambda)^2)-1/m;
  end
 % Normalized to Z0 = 1 everywhere
 %  Compute Xa using a detailed sum from Marcuvitz p. 286
  Xa = (a*ct/lambda)*(log(a/(pi*d))+0.5*(sum1+sum2)); % from sum
  Xb = (a*ct/lambda)*(pi*d/a)^2;  % used in either expression
  Zeq = j*(Xa-Xb)-(Xa^2)/(-1+j*(Xb-Xa));
  gam = (Zeq-1)/(Zeq+1);
  Rpow = abs(gam)^2;
end
```

Figure 2. Left: Equivalent-circuit representation (Marcuvitz, 1951) of a uniform, infinite wire grill, for TE plane-wave incidence. Right: Extracting the power reflection coefficient.

But since we also require $\frac{1}{P(z)}\frac{dP}{dz} = -\alpha(z)$, we can combine these expressions and solve for the preferred (or "ideal") value of α(z), which is found to be: $\alpha_{ideal}(z) = \frac{1}{L-z}$.

Now, since we already have an expression for α(z) in terms of R_{pow} from above, setting $\alpha(z) = \alpha_{ideal}(z)$ yields an expression for the "ideal" value of R_{pow}:

$$R_{pow,ideal} = \exp\left(-\frac{4h^2}{\lambda_g(L-z)}\right).$$

This expression is important, because *it is the functional form of the power reflection coefficient that we seek to achieve, to optimize gain and peak-power handling* (at least, at the current level of approximation). We will use this expression to implicitly guide our choices of wire spacing and wire diameters, by means of leveraging the separate expression for R_{pow} (see Figure 2) in terms of those parameters. I.e., choices of wire diameters and spacings for which $R_{pow} = R_{pow,ideal}$, should be considered good choices. Fortunately, modern computers make this optimization very straightforward. Despite the summation and algebraic inconveniences in Figure 2, the root-finding process to find the grill parameters at any given location z executes very rapidly. Figure 3 shows an example computation using a script that leverages Matlab's "fzero" root-finding tool. For this example, we held the antenna length and wire-spacings fixed, and solved for a set of wire diameters that should yield $R_{pow} = R_{pow,ideal}$.

```
% Script to generate ideal Rpow values for a fawsea
% And the wire diameters to go with them.
% R. Koslover
% SARA, Inc.
% October, 2013
% See Marcuvitz, p.286
%
clear
c_const = 2.99792458e8; %c in m/s.
%
L = 5; %length of fawsea aperture in meters.
freq = 1.3e9; %frequency in Hz.
lambda = c_const/freq; % free space wavelength.
AngIn = 30*pi/180; % desired beam angle rel to normal.
fc = freq*cos(AngIn); % cutoff frequency needed to yield AngIn.
h = 0.5*c_const/fc; % H-plane width of guide needed to yield fc.
lambda_g = lambda/sin(AngIn); % Guide wavelength.
%
%
% Compute the 'Ideal' Rpow curve
n = 0;
fac = -4*h^2/lambda_g;
a = 0.030; % Hold a constant for now. Let's find the d values that work!
for z=0:a:0.95*L
   n=n+1;
   RpIdeal(n) = exp(fac/(L-z));
end
%
% Use Matlab's fzero operation and anonymous function to find
% a value (from my MyRpow function) that yields the desired Rpow.
n = 0;
for z=0:a:0.95*L
  n=n+1;
  zlist(n)=z;
  foundd(n) = fzero(@(d) RpIdeal(n)-myRpow(AngIn,a,d,freq), [1e-99 a/2]);
 end
plot(zlist,foundd);
%
[fid] = fopen('d_vs_z.txt','w');
fprintf(fid,'Position , Diameter\n');
for q = 1:n
   fprintf(fid,' %g  %g\n',zlist(q),foundd(q));
 end
fclose(fid);
```

Script generates list of ideal wire diams for a uniform power density aperture.

Compute $R_{pow,ideal}$ here.

Set $R_{pow} = R_{pow,\ ideal}$ & solve for d.

Output list of d values to a file.

```
function Rpow = myRpow(AngIn,a,d,freq)
  ct = cos(AngIn);
  st = sin(AngIn);
  c_const = 2.99792458e8; %c in m/s
  lambda = c_const/freq; % free space wavelength
  sum1 = 0;
  sum2 = 0;
  for m = 1:1:1000
    sum1 = sum1+1/sqrt(m^2+2*m*a*st/lambda-(a*ct/lambda)^2)-1/m;
    sum2 = sum2+1/sqrt(m^2-2*m*a*st/lambda-(a*ct/lambda)^2)-1/m;
  end
  % Normalized to Z0 = 1 everywhere
  % Compute Xa using a detailed sum from Marcuvitz p. 286
  Xa = (a*ct/lambda)*(log(a/(pi*d))+0.5*(sum1+sum2));  % from sum
  Xb = (a*ct/lambda)*(pi*d/a)^2;  % used in either expression
  Zeq = j*(Xa-Xb)-(Xa^2)/(-1+j*(Xb-Xa));
  gam = (Zeq-1)/(Zeq+1);
  Rpow = abs(gam)^2;
end
```

Function that computes theoretical reflected power (R_{pow}) using Marcuvitz' equivalent-circuit model.

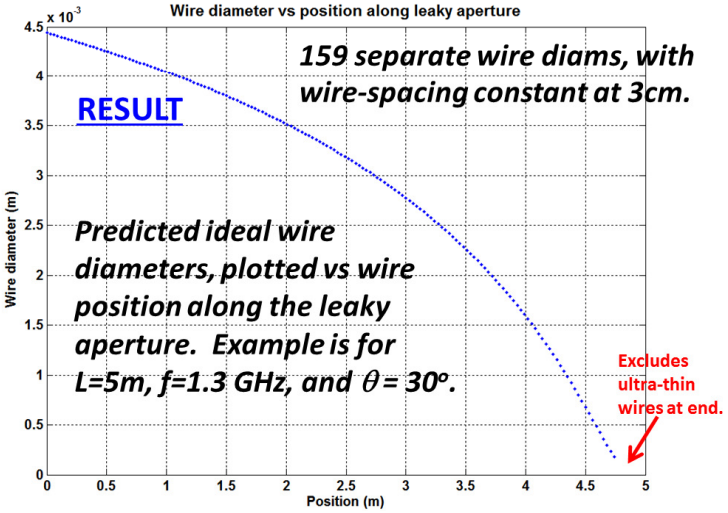


Figure 3. Automated generation of a list of "ideal" wire diameters for an example leaky-wave aperture (L=5m, θ=30°, f=1.3 GHz).

We can test whether or not this algorithm for choosing the wire diameters actually yields a suitable leaky-wave grill via an independent computation, using a full-wave, finite element model, where once again we restrict ourselves (for now) to just the H-plane part of the analyses (setting aside issues such as channel-to-channel coupling). Figure 4 and Figure 5 show the results of a numerical model where the wire grill diameters were chosen in accordance with the guidance from Figure 3. The results are very satisfying. Approx. 98.75% of the input power is radiated (only 1.25% reached the termination) and very good beam uniformity is achieved. This model's -3dB full beamwidth = 3.08°. An ideal uniform aperture of length 5m*cos(30°) would have a -3dB beamwidth of 2.7°, implying that the model's aperture efficiency is 87.7% in terms of projected aperture (4.33m), and 75.9% in terms of geometric aperture (5m). This is respectably-close to, but not fully, optimal.

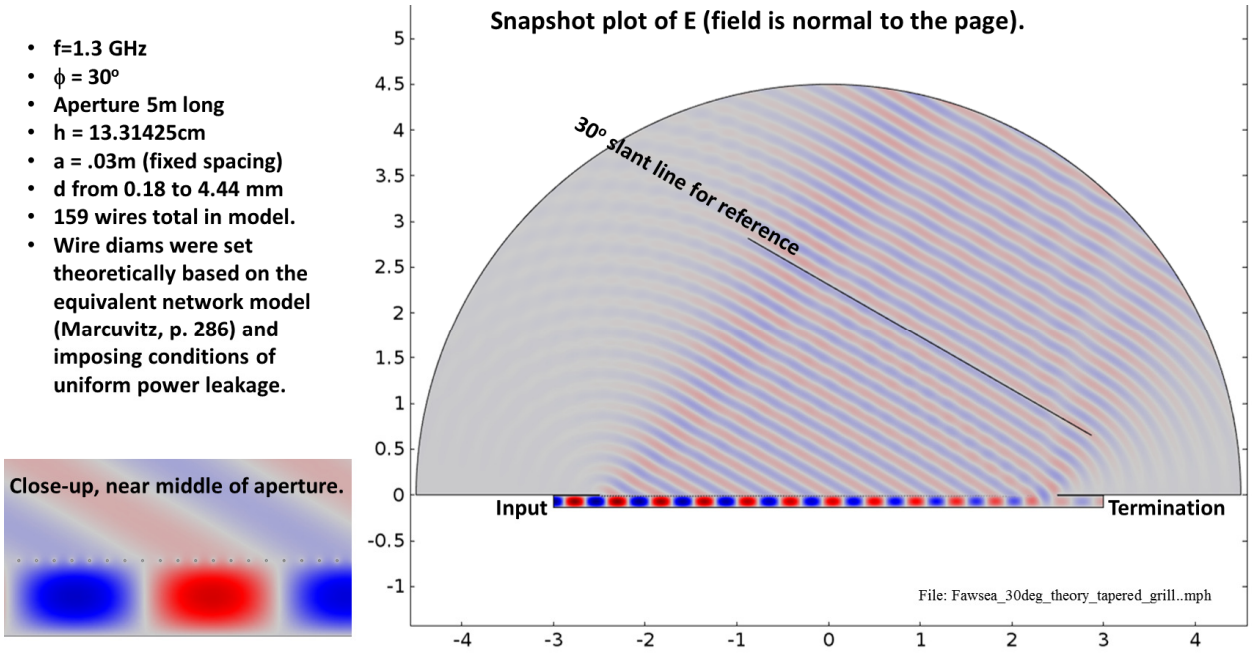


Figure 4. A 2D finite-element model, using the 159 wires generated from the theory and using the scripts described in Figure 3.

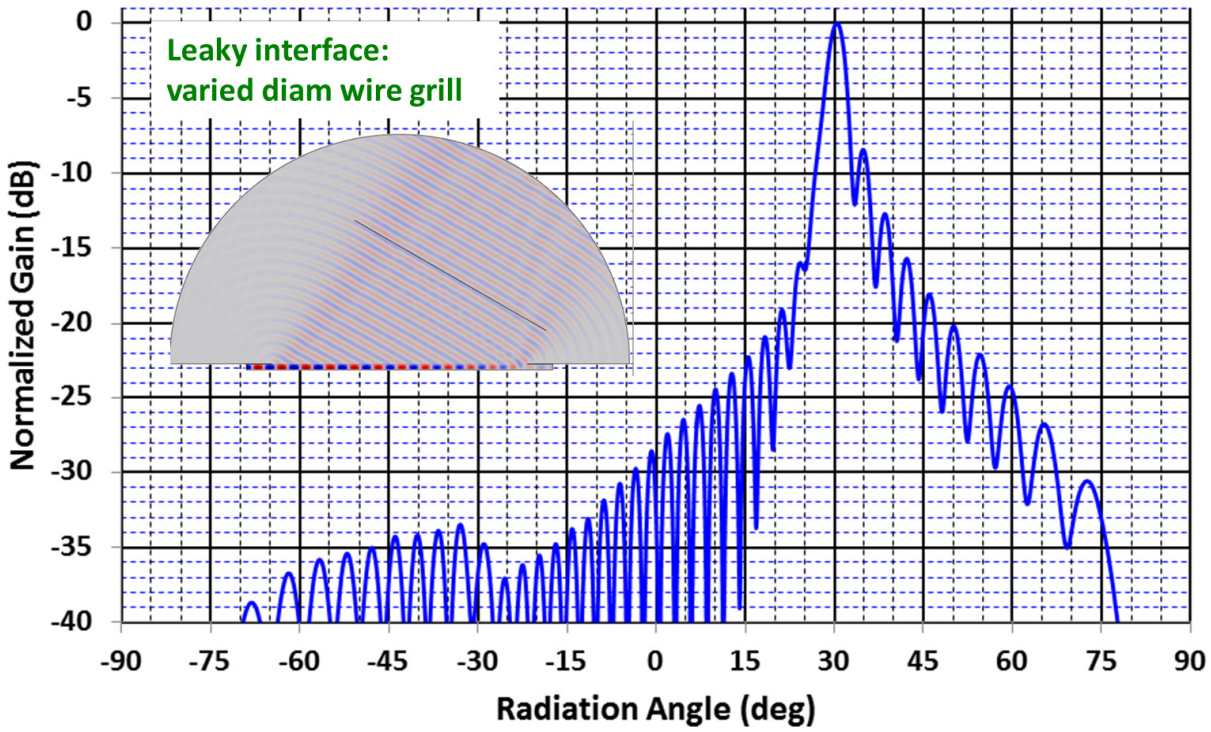


Figure 5. Predicted H-plane pattern, normalized to 0dB, from the 2D finite-element model, using the 159 wires generated from the theory and scripts described in Figure 3.

4.1.2. Developing an initial understanding of leaky dielectric windows

We can understand leaky dielectric windows in a manner fairly similar to that done with wire grills in Section 4.1.1. For example, note the similarity in behavior between a uniform wire grill and a thin window with relatively high-value of ε_r, as shown in Figure 6 (snapshots from 2D FE models). The two arrangements shown yield almost identical results, except for a phase shift in the transmitted wave. So, it makes sense that one should be able to construct, at least in theory, a leaky wave antenna with a graded dielectric window instead of a wire grill.

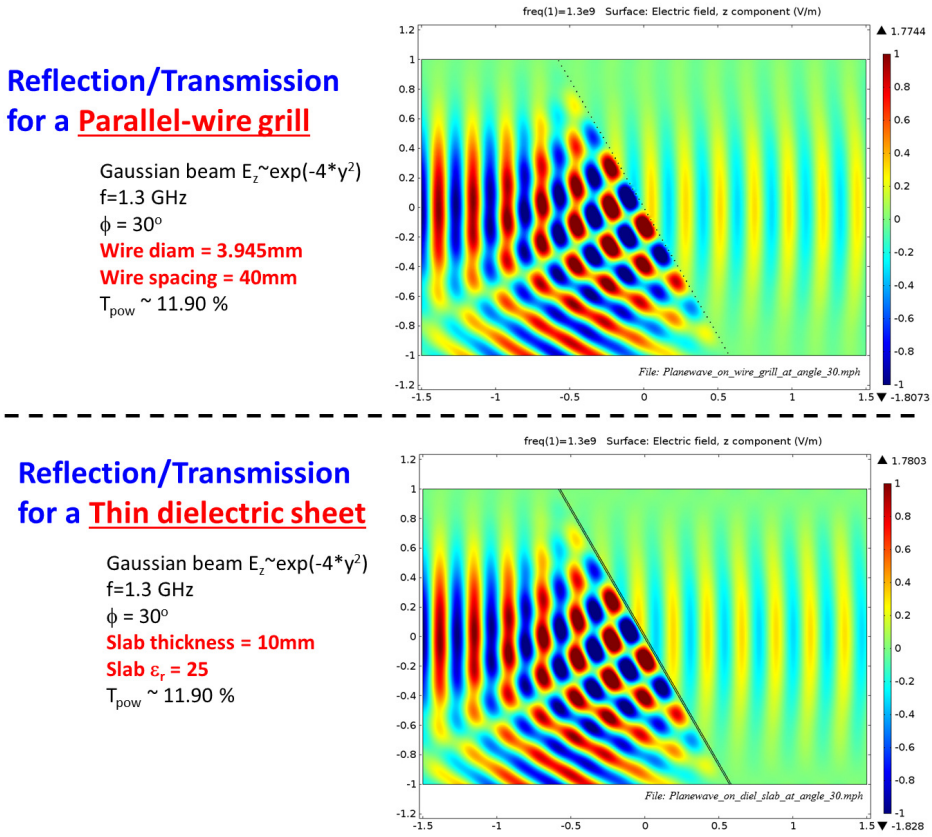


Figure 6. A dielectric window can behave much like a wire grill.

Reasoning in analogy to the development in Section 4.1.1, we first determine an expression for the power reflection coefficient (R_{powD}) of a TE plane wave from a uniform dielectric window, set it equal to $R_{pow,ideal}$ (which was found earlier), and solve for the unknown quantity of interest. For simplicity, we hold the window thickness fixed and allow ε_r to vary as a function of z. Fortunately, R_{powD} for a *uniform* dielectric window with TE *plane-wave* incidence can be expressed in analytic closed form. The following expressions were extracted from a paper by C.E. Baum (2006):

$$R_{powD} = |\rho_D|^2,$$

$$\text{where} \quad \rho_D = \frac{1+\frac{Z_{in}}{Z_1}\cos(\theta_{in})}{1-\frac{Z_{in}}{Z_1}\cos(\theta_{in})} \quad \text{with} \quad \frac{Z_{in}}{Z_1} = \frac{-1}{\sqrt{\varepsilon_r}\cos(\theta_D)}\frac{1-T_2/T_1}{1+T_2/T_1}$$

$$\text{and} \quad \frac{T_2}{T_1} = \frac{1-\sqrt{\varepsilon_r}\cos(\theta_D)/\cos(\theta_{in})}{1+\sqrt{\varepsilon_r}\cos(\theta_D)/\cos(\theta_{in})}\exp\left(-2j\sqrt{\varepsilon_r}k_0 t_D\cos(\theta_D)\right)$$

with $\sqrt{\varepsilon_r}\sin(\theta_D) = \sin(\theta_{in})$ (by Snell's law), and t_D = thickness of the dielectric window.

Armed with this expression for R_{powD}, we can proceed to solve for ε_r (once again, via root-finding) as a function of z, for a window of fixed thickness (chosen here somewhat arbitrarily as 0.5cm) and for an aperture of the same length as our earlier example (L=5m). The predicted distribution of ε_r vs. z is shown in Figure 7.

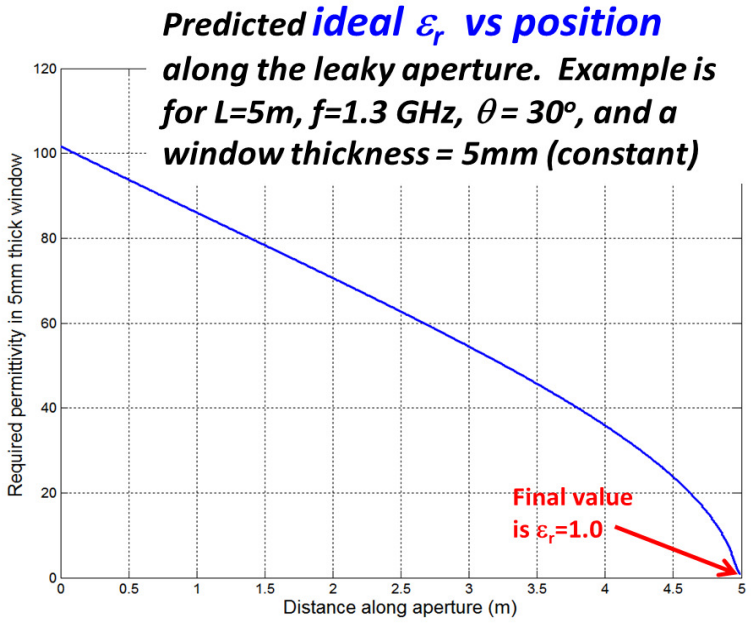


Figure 7. Values of ε_r (z) generated for a dielectric-window designed to deliver ~the same leaky-wave performance as the wire grill defined in Figure 3.

Figure 8 and Figure 9 show the results of a numerical model where the window's ε_r was specified in accordance with the guidance from Figure 7. As before, the results are very satisfying. Approx. 99.9% of the input power is radiated and good beam uniformity is achieved. This model's -3dB full beamwidth = 3.12°. An ideal uniform aperture of length 5m*cos(30°) would have a -3dB beamwidth of 2.7°, implying that this model's aperture efficiency is 86.5% in terms of projected aperture (4.33m), and 74.9% in terms of geometric aperture (5m). As with the earlier wire-grill example, this is respectably-close to optimal.

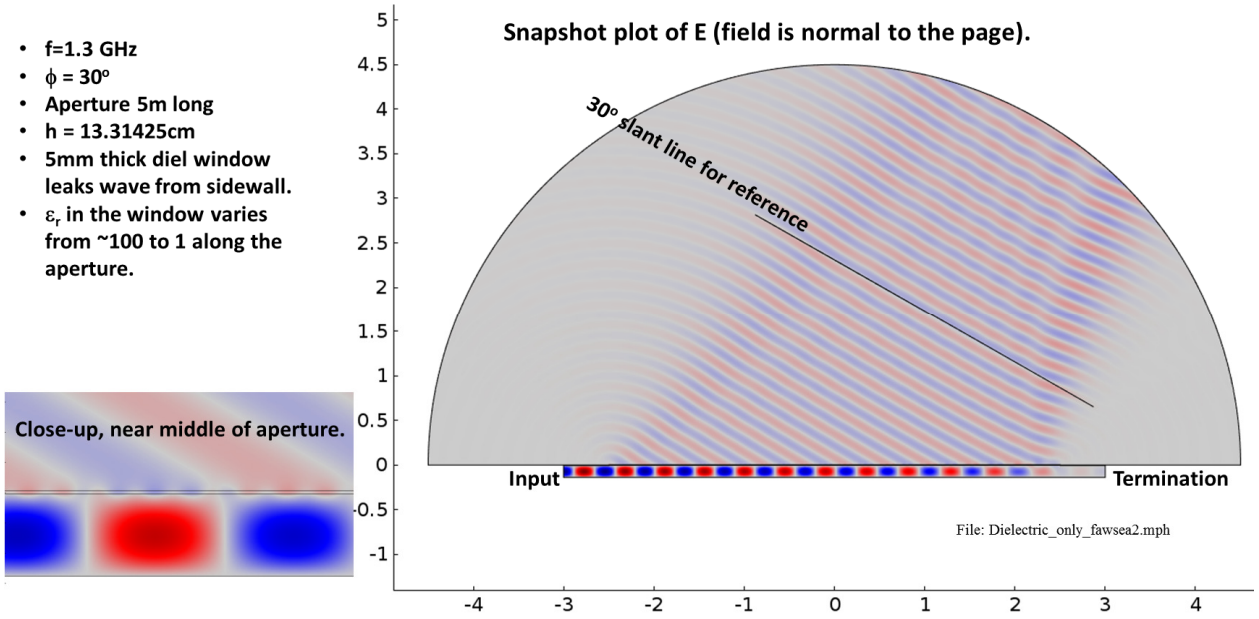


Figure 8. 2D finite-element model using the varied-dielectric window defined in Figure 7.

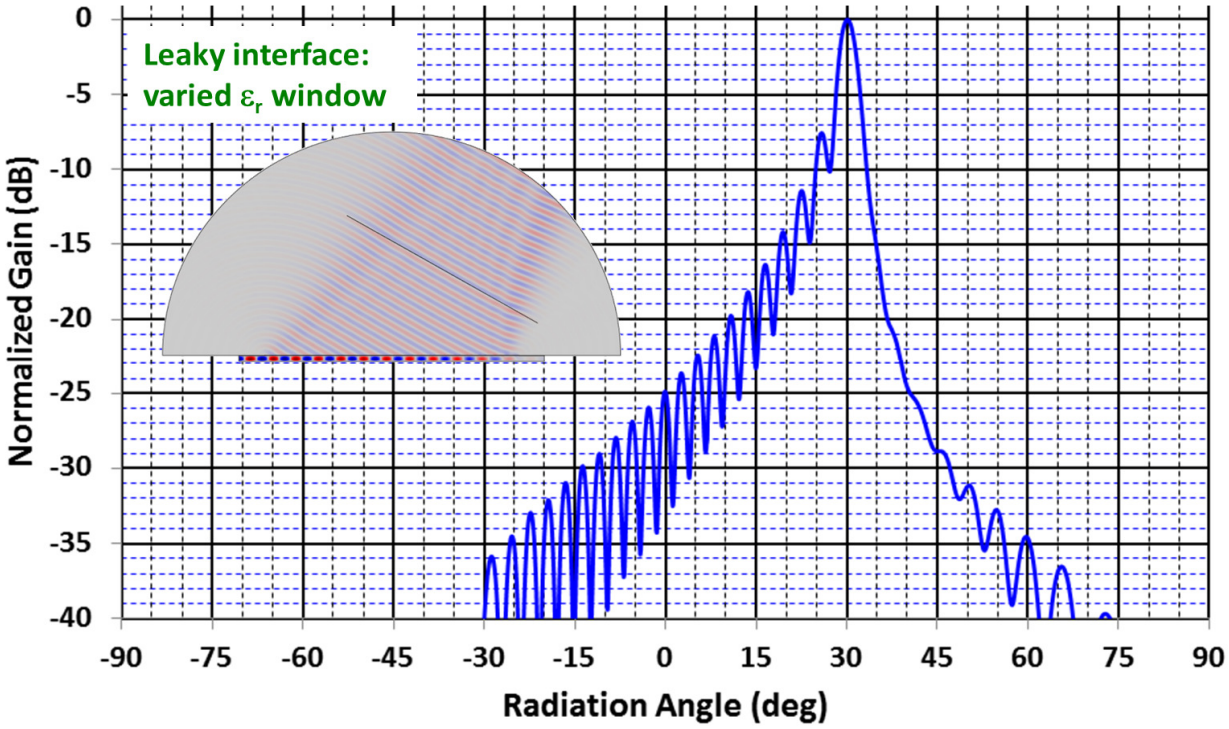
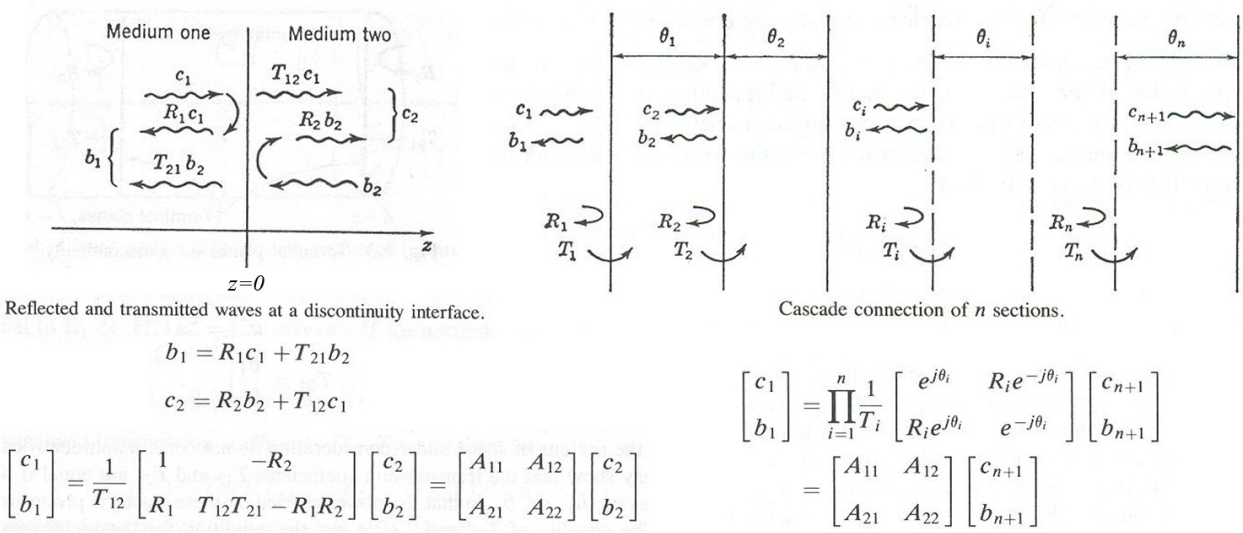


Figure 9. Predicted H-plane pattern, normalized to 0dB, from the 2D finite-element model, using the varied-dielectric window defined in Figure 7.

For both the leaky wire grill and leaky dielectric window, the observant reader may have noted some small departures from optimal beam-forming occurred, which arose due variously to diffraction at the ends of the aperture and to the guided wave transitioning toward an essentially unbound condition as the wave approached the termination (z→ L) region, the latter which obviously violated our earlier simplistic approximation of a constant phase velocity persisting throughout the guide. For leaky wire grills, a nearly-constant phase velocity can be approximately restored to that region by introducing a slight inward tilt of the waveguide wall opposite to the leaky wall, toward the end of the antenna. For additional discussion about how to account for this, see Section 4.1.9.

4.1.3. Generalization of the Approach → Wave Chain Matrix Theory

Wave transmission and reflection properties of wire grills, dielectric windows, and other interfaces between media can all be expressed in the form of *wave matrices* (Collin, 1991). In particular, wave matrix *formalism* is useful to chain together (via matrix multiplication) the behaviors of multiple sequential interfaces in a wave-propagation path. This approach is of interest here, since: (1) we need to understand wave propagation through wire-grills, intermediate spaces, and dielectric windows *in sequence*, and (2) one may eventually be able to extend this to channel-to-channel coupling. We have endeavored to capture some of the ideas in the wave chain matrix formalism in Figure 10 below, which is actually a collage of material pasted from Section 3.4 of Collin's classic book. We refer the interested reader to that text for more detailed information. Note that the θ_i symbols on the right-hand side of Figure 10 refer not to spatial-orientation angles, but to effective electrical lengths ($k_i \cdot z_i$) in each segment of the chain being considered.



Reflected and transmitted waves at a discontinuity interface.

Cascade connection of n sections.

$$b_1 = R_1 c_1 + T_{21} b_2$$

$$c_2 = R_2 b_2 + T_{12} c_1$$

$$\begin{bmatrix} c_1 \\ b_1 \end{bmatrix} = \frac{1}{T_{12}} \begin{bmatrix} 1 & -R_2 \\ R_1 & T_{12}T_{21} - R_1R_2 \end{bmatrix} \begin{bmatrix} c_2 \\ b_2 \end{bmatrix} = \begin{bmatrix} A_{11} & A_{12} \\ A_{21} & A_{22} \end{bmatrix} \begin{bmatrix} c_2 \\ b_2 \end{bmatrix}$$

$$\begin{bmatrix} c_1 \\ b_1 \end{bmatrix} = \prod_{i=1}^{n} \frac{1}{T_i} \begin{bmatrix} e^{j\theta_i} & R_i e^{-j\theta_i} \\ R_i e^{j\theta_i} & e^{-j\theta_i} \end{bmatrix} \begin{bmatrix} c_{n+1} \\ b_{n+1} \end{bmatrix} = \begin{bmatrix} A_{11} & A_{12} \\ A_{21} & A_{22} \end{bmatrix} \begin{bmatrix} c_{n+1} \\ b_{n+1} \end{bmatrix}$$

Figure 10. Some concepts & notation in the wave-matrix formalism (R.E. Collin, 1991).

It is important to recognize that although this formalism provides a tool to compute the combined behavior in the presence of multiple interfaces, it does *not* tell us how to compute the R_i and T_i values themselves[4]. For the latter, we must employ methods akin to those described earlier, such as (but not limited to) those presented in Sections 4.1.1 and 4.1.2. In the subsections below, we endeavor to apply the above formalism to understanding wave transmission and reflection at the combination of a leaky wire-grill, a dielectric window, and the empty space between them.

Our treatment of the dielectric window (in Section 4.1.2) differed from that of the wire grill (in Section 4.1.1) in that we did not invoke an explicit equivalent circuit model, but instead used a solution derived directly from considering a TE-incident wave and the boundary conditions imposed on the fields at the two sides of the window. To manage the grill and window combination, it is helpful to assemble more-consistent methods/notations for these sub-problems. We also need to represent the intervening space via the same formalism. In fact, for the sake of both balance and completeness, *every* interface and propagation region in the problem should have its own matrix. Thus, we will represent the combination of the wire-grill and dielectric window via *five* matrices, corresponding to the following five interfaces or regions: (1) from one side of the wire grill to the other, (2) the intervening empty space between the grill and dielectric window, (3) the boundary between the intervening empty space and the window, (4) the space inside the window, and (5) the boundary between the window and the radiating space. (Note: Once we have prepared the separate matrices, we will *renumber* the individual labels on R_i and T_i as needed. Also, since the vacuum space can be treated as a limiting case of a dielectric window with unit permittivity and permeability, we will do that simple piece last). As before, and for all these interfaces, we first study ideal plane-waves illuminating infinite/uniform interfaces. Later, we will extend/generalize them to apply to forward-traveling, leaky-wave antenna apertures.

4.1.3.1. Representation of the Uniform Wire Grill

Let us consider the left-half of Figure 10 in light of the analyses in Section 4.1.1. First, we can immediately identify the variable R_1 in Figure 10 as identical to Γ in Figure 2. But identifying the correct complex-value for T_{12} is less obvious. Recall that we obtained Γ from: (1) representing both the wire grill and the space to its right as an equivalent-TL impedance, Z_{eq}, and (2) employing the formula for wave

[4] R_i is the complex amplitude reflection coefficient for a wave incident on section *i* from section *i-1*, while T_i is the complex amplitude transmission coefficient for a wave passing from section *i-1* to *i*.

reflection at a transition between two TL of different impedances, i.e., Z=1 on the left and Z = Z_{eq} on the right. That approach worked fine, yet we can see that in the actual space to the right of the wire grill, the wave impedance is the *same* as that on its left. So to better understand what waves actually appear on the right-hand side (both in terms of *amplitude* and *phase*), we need to revisit our circuit model. For convenience, it is shown once again in Figure 11, this time along with a T-network representation.

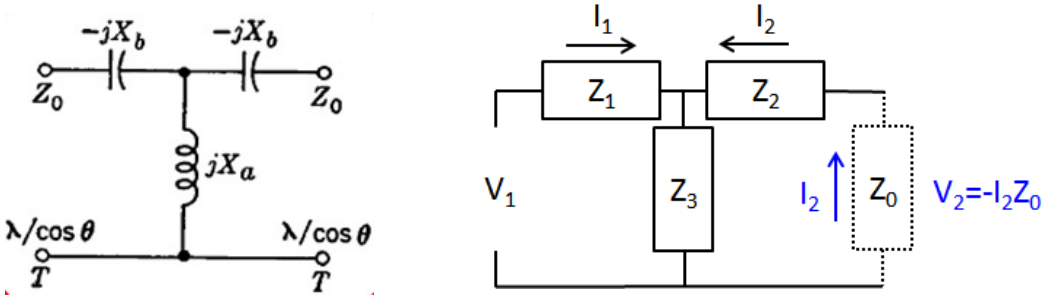


Figure 11. Left: Equivalent circuit of wire grill (from Figure 2). Right: T-network.

Let V_1 be the voltage on the left and V_2 on the right, noting that $V_1 = V_1^+ + V_1^- = (1+\Gamma)V_1^+$, where Γ was previously computed, and $V_2 = V_2^+$ (i.e., *only a right-going wave*). This circuit is of the T-type, as shown in the right-hand panel in Figure 11. For such a network, one can write:

$$\begin{pmatrix} V_1 \\ V_2 \end{pmatrix} = \begin{pmatrix} Z_{11} & Z_{12} \\ Z_{21} & Z_{22} \end{pmatrix} \begin{pmatrix} I_1 \\ I_2 \end{pmatrix}, \quad \text{with } Z_{11} = Z_1+Z_3,\ Z_{12} = Z_{21} = Z_3, \text{ and } Z_{22} = Z_2+Z_3.$$

Specializing to $Z_2 = Z_1$ and noting that $I_2 = -V_2/Z_0$ (due to the sole right-going wave there) this becomes:

$$\begin{pmatrix} V_1 \\ V_2 \end{pmatrix} = \begin{pmatrix} Z_1+Z_3 & Z_3 \\ Z_3 & Z_1+Z_3 \end{pmatrix} \begin{pmatrix} I_1 \\ -V_2/Z_0 \end{pmatrix}$$

or equivalently,

$$V_1 = (Z_1+Z_3)I_1 - V_2 Z_3/Z_0 \qquad \text{[Eq. A]}$$

$$V_2 = Z_3 I_1 - (Z_1+Z_3)V_2/Z_0 \rightarrow I_1 = \frac{V_2}{Z_3}\left(1+\left(\frac{Z_1+Z_3}{Z_0}\right)\right) \qquad \text{[Eq. B]}$$

or $I_1 = \left(\frac{Z_0+Z_1+Z_3}{Z_0 Z_3}\right)V_2$. Substituting Eq. B into Eq. A yields:

$$V_1 = (Z_1+Z_3)\left(\frac{Z_0+Z_1+Z_3}{Z_0 Z_3}\right)V_2 - V_2 Z_3/Z_0 \rightarrow V_2 = V_1\left[\frac{Z_0 Z_3}{(Z_1+Z_3)(Z_0+Z_1+Z_3)-Z_3^2}\right] \qquad \text{[Eq. C]}$$

Now recall that $V_1 = (1+\Gamma)V_1^+$ where $\Gamma = \frac{Z_{eq}-Z_0}{Z_{eq}+Z_0}$. It is also clear from a parallel and series analysis of the network in Figure 11 (with $Z_2 = Z_1$) that

$$Z_{eq} = Z_1 + \left[\frac{1}{Z_3}+\frac{1}{Z_0+Z_1}\right]^{-1} = Z_1+Z_3-\frac{Z_3^2}{(Z_0+Z_1+Z_3)}.$$ Plugging that into our expression for Γ,

$$\Gamma = \frac{Z_1 + Z_3 - \dfrac{Z_3^2}{(Z_0 + Z_1 + Z_3)} - Z_0}{Z_1 + Z_3 - \dfrac{Z_3^2}{(Z_0 + Z_1 + Z_3)} + Z_0} = \frac{(Z_1 + Z_3 - Z_0)(Z_0 + Z_1 + Z_3) - Z_3^2}{(Z_1 + Z_3 + Z_0)(Z_0 + Z_1 + Z_3) - Z_3^2} = \frac{(Z_1 + Z_3)^2 - Z_0^2 - Z_3^2}{(Z_0 + Z_1 + Z_3)^2 - Z_3^2}$$

Thus, we may write: $V_1 = (1 + \Gamma)V_1^+ = \left(1 + \dfrac{(Z_1 + Z_3)^2 - Z_0^2 - Z_3^2}{(Z_0 + Z_1 + Z_3)^2 - Z_3^2}\right)V_1^+$

which can be rearranged to obtain:

$$V_1 = 2V_1^+\left(\frac{(Z_1 + Z_3)(Z_0 + Z_1 + Z_3) - Z_3^2}{(Z_0 + Z_1 + Z_3)^2 - Z_3^2}\right)$$

Finally, inserting this into Eq. C, we obtain:

$$\frac{V_2}{V_1^+} = 2\left(\frac{(Z_1 + Z_3)(Z_0 + Z_1 + Z_3) - Z_3^2}{(Z_0 + Z_1 + Z_3)^2 - Z_3^2}\right)\left(\frac{Z_0 Z_3}{(Z_1 + Z_3)(Z_0 + Z_1 + Z_3) - Z_3^2}\right).$$

On the right-hand side of the equation, the first factor's numerator exactly cancels the second factor's denominator, so this both immediately and conveniently reduces to:

$$T_g \equiv \frac{V_2}{V_1^+} = \frac{2Z_0 Z_3}{(Z_0 + Z_1 + Z_3)^2 - Z_3^2}$$

where we have also noted that this is the *complex transmission coefficient* for the *wire-grill*, T_g. Thus, we now have expressions for *both* T_g and R_g (again, recalling that $R_g = \Gamma$, from before) which are the essential quantities for writing the *matrix representation* describing the reflection and transmission properties of the *wire-grill*. We can also express these in terms of the reactances X_a and X_b in Figure 2 as follows:

$$R_g = \frac{-(X_a - X_b)^2 - Z_0^2 + X_a^2}{(Z_0 + j(X_a - X_b))^2 + X_a^2}$$

$$T_g = \frac{2jX_a Z_0}{(Z_0 + j(X_a - X_b))^2 + X_a^2}$$

where X_a and X_b are given by the expressions in Figure 2. We will now use these to construct the wave matrix to represent the wire grill. To do this correctly, we must recognize that the behavior of the stand-alone wire grill is entirely left-right symmetric, *unlike* a transition between two different dielectric media, for example[5]. Therefore, $T_{12} = T_{21} = T_g$ and $R_2 = R_1 = R_g$. Thus, per Figure 10, the matrix corresponding to a TE-illuminated, uniform, infinite, wire grill, *standing alone*, with zero thickness, becomes:

$$\begin{bmatrix} c_1 \\ b_1 \end{bmatrix} = \frac{1}{T_g}\begin{bmatrix} 1 & -R_g \\ R_g & T_g^2 - R_g^2 \end{bmatrix}\begin{bmatrix} c_2 \\ b_2 \end{bmatrix}$$

where the diagram in the upper left of Figure 10 identifies the wave labels and their directions[6], where R_g and T_g are given just above, and where X_a and X_b are described in Figure 2.

[5] For the latter, $T_{21} = T_{12}$ still holds, but $R_2 = -R_1$.

[6] Note that the wave directions do *not* have to be *normal* to the interface, despite their appearance in Figure 10. For example, the values of X_a and X_b, upon which R_1 and T_{12} depend, are functions of the angle of incidence.

4.1.3.2. Representation of the Uniform Dielectric Window

Again, TE incidence is our primary interest (at least, for now), which is the same as the arrangement shown in Figure 12. Although we actually addressed much of the physics of this problem earlier (in Section 4.1.2), we return to the beginning here, since the approach we seek is slightly different. We want to see the explicit values of the complex reflection and transmission coefficients at each step (so that the overall procedure becomes as clear as possible).

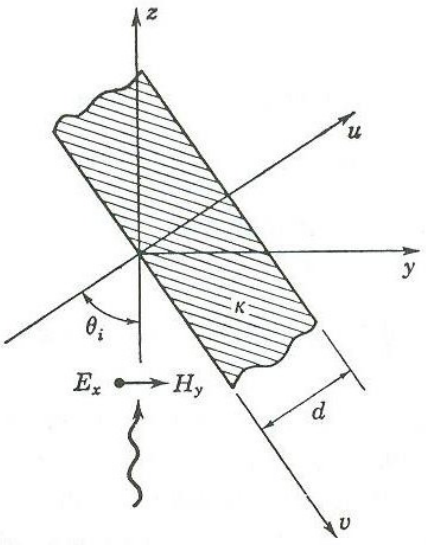


Figure 12. Coordinates used by R.E. Collin [1991] to represent a dielectric window for TE wave incidence.

The plane-wave on the left side of the interface is incident in the +z direction. Although the impedance of this wave in free space is, of course, given by $E_x/H_y = \sqrt{\mu_0/\varepsilon_0}$, it can be recast as an equivalent wave impedance for a wave propagating along the *u* direction, in which case the component of H that matters is its projection along *v*: $H_v = H_y \cos\theta_i$. (E_x remains perpendicular to the plane of incidence in all locations.) In particular, H_v is continuous across the interface. Anyway, the *effective* impedance of the wave on the lower-left side of the dielectric interface *for the component of propagation along u* is thus given by[7]:

$Z_1 = \dfrac{E_x}{H_v} = \dfrac{E_x}{H_y \cos\theta_i} = \sqrt{\dfrac{\mu_0}{\varepsilon_0}} \sec\theta_i$, where θ_i is the incident angle in free space. Similarly, within the slab of thickness *d*, the wave impedance *for the component of propagation along u* becomes:

$Z_2 = \sqrt{\dfrac{\mu_0}{\varepsilon_0 \kappa}} \sec\theta_r$, where θ_r is the angle with the wave normal relative to *u* inside the dielectric and κ is the dielectric constant ($\kappa = \varepsilon_r$). So now we can construct Z_2/Z_1 :

$$\frac{Z_2}{Z_1} = \frac{\cos\theta_i}{\sqrt{\kappa}\cos\theta_r}$$

From Snell's law, $\sqrt{\kappa}\sin\theta_r = \sin\theta_i$, or equivalently, $\cos\theta_r = \sqrt{1-\sin^2\theta_r} = \sqrt{1-\sin^2\theta_i/\kappa}$

Thus, $\dfrac{Z_2}{Z_1} = \dfrac{\cos\theta_i}{\sqrt{\kappa - \sin^2\theta_i}}$. For a simple *single* air-to-dielectric interface, this is sufficient to extract the reflection coefficient there, since: $R_L = \dfrac{Z_2/Z_1 - 1}{Z_2/Z_1 + 1}$. (where our *L* subscript notes the *left* interface.)

Continuity of E_x *at the air-to-dielectric interface* means: $E_x^{trans} = E_x^{inc} + E_x^{ref} = E_x^{inc}(1 + R_L)$

On the other hand, by definition *at that same interface*, $E_x^{trans} = T_L E_x^{inc}$

[7] This approach is useful specifically, and only, because wave transmission-by/reflection-from the window depends *exclusively* on field components *tangential* to the dielectric surface. For TE incidence, these fields are E_x and H_v.

Thus, we may write: $T_L = 1 + R_L$, at this first interface (i.e, the air-to-dielectric interface). And that leads us to the matrix for this (air to dielectric) interface:

$$\begin{bmatrix} c_1 \\ b_1 \end{bmatrix} = \frac{1}{T_L}\begin{bmatrix} 1 & R_L \\ R_L & 1 \end{bmatrix}\begin{bmatrix} c_2 \\ b_2 \end{bmatrix}$$

where R_L and T_L are given immediately above, i.e.,

$$R_L = \frac{\cos\theta_i - \sqrt{\kappa - \sin^2\theta_i}}{\cos\theta_i + \sqrt{\kappa - \sin^2\theta_i}} \qquad \text{and} \qquad T_L = 1 + R_L = \frac{2\cos\theta_i}{\cos\theta_i + \sqrt{\kappa - \sin^2\theta_i}}$$

Next, consider the *intervening space* inside the *dielectric window* of thickness *d*. This matrix is given by:

$$\begin{bmatrix} c_1 \\ b_1 \end{bmatrix} = \begin{bmatrix} e^{j\phi_d} & 0 \\ 0 & e^{-j\phi_d} \end{bmatrix}\begin{bmatrix} c_2 \\ b_2 \end{bmatrix}$$

where $\phi_d = \left(\vec{k}_D \cdot \hat{u}\right)d = k_0 d\sqrt{\kappa}\cos\theta_r = k_0 d\sqrt{\kappa - \sin^2\theta_i}$, is the electrical length along *u* inside the dielectric.

Finally, at the *exiting dielectric-to-air boundary*, we can see that we should have an R_R very much like R_L at the air-to dielectric interface, but with the Z's swapped, which quickly yields

$$R_R = \frac{\sqrt{\kappa - \sin^2\theta_i} - \cos\theta_i}{\sqrt{\kappa - \sin^2\theta_i} + \cos\theta_i}, \text{ (i.e., the } \textit{negative} \text{ of } R_L\text{). Similarly,}$$

$$T_R = 1 + R_R = \frac{2\sqrt{\kappa - \sin^2\theta_i}}{\cos\theta_i + \sqrt{\kappa - \sin^2\theta_i}}$$

And that leads us to the matrix for this (dielectric-to-air) interface:

$$\begin{bmatrix} c_1 \\ b_1 \end{bmatrix} = \frac{1}{T_R}\begin{bmatrix} 1 & R_R \\ R_R & 1 \end{bmatrix}\begin{bmatrix} c_2 \\ b_2 \end{bmatrix}$$

where R_R and T_R are given immediately above.

Now let's combine the above three matrices (i.e., air-to-dielectric, dielectric-propagation, and dielectric-to-air) into a single matrix to represent the dielectric window.

So we can write for the dielectric window (including its interfaces to air or vacuum on each side):

$$\begin{bmatrix} c_1 \\ b_1 \end{bmatrix} = \frac{1}{T_L T_R}\begin{bmatrix} 1 & R_L \\ R_L & 1 \end{bmatrix}\begin{bmatrix} e^{j\phi_d} & 0 \\ 0 & e^{-j\phi_d} \end{bmatrix}\begin{bmatrix} 1 & R_R \\ R_R & 1 \end{bmatrix}\begin{bmatrix} c_2 \\ b_2 \end{bmatrix}$$

where

$$R_L = \frac{\cos\theta_i - \sqrt{\kappa - \sin^2\theta_i}}{\cos\theta_i + \sqrt{\kappa - \sin^2\theta_i}}, \quad T_L = 1 + R_L,\ T_R = 1 + R_R, \text{ and } R_R = -R_L.$$

Putting R_R, T_L, and T_R all in terms of their aforementioned expressions for R_L, this becomes:

$$\begin{bmatrix} c_1 \\ b_1 \end{bmatrix} = \frac{1}{(1+R_L)(1-R_L)} \begin{bmatrix} 1 & R_L \\ R_L & 1 \end{bmatrix} \begin{bmatrix} e^{j\phi_d} & 0 \\ 0 & e^{-j\phi_d} \end{bmatrix} \begin{bmatrix} 1 & -R_L \\ -R_L & 1 \end{bmatrix} \begin{bmatrix} c_2 \\ b_2 \end{bmatrix}$$

which reduces to:

$$\begin{bmatrix} c_1 \\ b_1 \end{bmatrix} = \frac{1}{1-R_L^2} \begin{bmatrix} e^{j\phi_d} - R_L^2 e^{-j\phi_d} & R_L e^{-j\phi_d} - R_L e^{j\phi_d} \\ R_L e^{j\phi_d} - R_L e^{-j\phi_d} & e^{-j\phi_d} - R_L^2 e^{j\phi_d} \end{bmatrix} \begin{bmatrix} c_2 \\ b_2 \end{bmatrix}$$

for the dielectric window of thickness *d*, where

$$R_L = \frac{\cos\theta_i - \sqrt{\kappa - \sin^2\theta_i}}{\cos\theta_i + \sqrt{\kappa - \sin^2\theta_i}} \text{ and } \phi_d = k_0 d \sqrt{\kappa - \sin^2\theta_i} \,.$$

As R.E. Collin notes, the A_{11} term of the matrix is the reciprocal of the window's overall transmission coefficient, T_{win}. Thus, we may write for future reference,

$$T_{win} = \frac{1-R_L^2}{e^{j\phi_d} - R_L^2 e^{-j\phi_d}} \qquad \text{(TE incidence, dielectric window)}$$

where R_L and ϕ_d are given immediately above.

4.1.3.1. Representation of the Intervening Vacuum Space

This is the simplest link in the wave-matrix chain that we are assembling. We take the middle of the three matrices described in Section 4.1.3.2 with $\kappa \rightarrow 1$. Assume a thickness *h* in the *u* direction (in reference to Figure 12). Thus we obtain

$$\begin{bmatrix} c_1 \\ b_1 \end{bmatrix} = \begin{bmatrix} e^{j\phi_v} & 0 \\ 0 & e^{-j\phi_v} \end{bmatrix} \begin{bmatrix} c_2 \\ b_2 \end{bmatrix}.$$

where $\phi_v = \left(\vec{k}_0 \cdot \hat{u}\right) h = k_0 h \cos\theta_i$, is the electrical length along *u* in empty space (subscript *v* = *vacuum*). Now, finally, all we have to do is multiply the matrices together in the correct order.

4.1.3.2. Wire Grill, Vacuum Space, and Dielectric Window – All together

Putting all these terms together and proceeding from left to right, though the grill, vacuum space, and dielectric window, we obtain:

$$\begin{bmatrix} c_1 \\ b_1 \end{bmatrix} = \frac{1}{T_g T_D} \begin{bmatrix} 1 & -R_g \\ R_g & T_g^2 - R_g^2 \end{bmatrix} \begin{bmatrix} e^{j\phi_v} & 0 \\ 0 & e^{-j\phi_v} \end{bmatrix} \begin{bmatrix} e^{j\phi_d} - R_L^2 e^{-j\phi_d} & R_L e^{-j\phi_d} - R_L e^{j\phi_d} \\ R_L e^{j\phi_d} - R_L e^{-j\phi_d} & e^{-j\phi_d} - R_L^2 e^{j\phi_d} \end{bmatrix} \begin{bmatrix} c_2 \\ b_2 \end{bmatrix}$$

where we have defined $T_D = 1 - R_L^2$. This simplifies slightly to

$$\begin{bmatrix} c_1 \\ b_1 \end{bmatrix} = \frac{1}{T_g T_D} \begin{bmatrix} e^{j\phi_v} & -R_g e^{-j\phi_v} \\ R_g e^{j\phi_v} & \left(T_g^2 - R_g^2\right) e^{-j\phi_v} \end{bmatrix} \begin{bmatrix} e^{j\phi_d} - R_L^2 e^{-j\phi_d} & R_L\left(e^{-j\phi_d} - e^{j\phi_d}\right) \\ -R_L\left(e^{-j\phi_d} - e^{j\phi_d}\right) & e^{-j\phi_d} - R_L^2 e^{j\phi_d} \end{bmatrix} \begin{bmatrix} c_2 \\ b_2 \end{bmatrix}$$

with (to summarize most of the various factors in one place):

$$T_g = \frac{2jX_a Z_0}{\left(Z_0 + j\left(X_a - X_b\right)\right)^2 + X_a^2} \quad \text{and} \quad R_g = \frac{-\left(X_a - X_b\right)^2 - Z_0^2 + X_a^2}{\left(Z_0 + j\left(X_a - X_b\right)\right)^2 + X_a^2}$$

where X_a and X_b are given by the expressions in Figure 2,

$$\phi_v = k_0 h \cos\theta_i \qquad \text{and} \quad \phi_d = k_0 d\sqrt{\kappa - \sin^2\theta_i}$$

where h = the vacuum thickness, d = the dielectric window thickness, and κ = dielectric constant, and

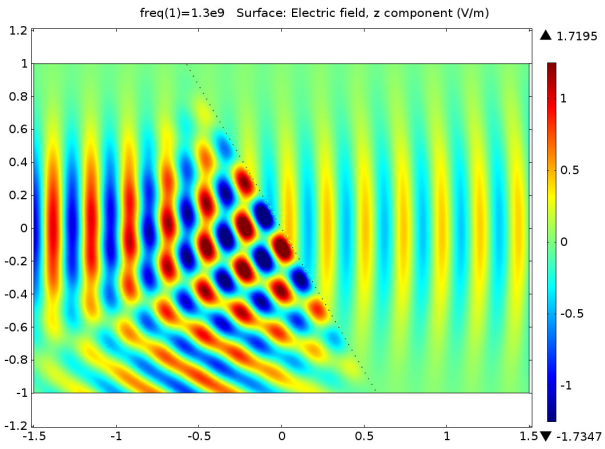
$$R_L = \frac{\cos\theta_i - \sqrt{\kappa - \sin^2\theta_i}}{\cos\theta_i + \sqrt{\kappa - \sin^2\theta_i}} \quad \text{and} \quad T_D = 1 - R_L^2 \ .$$

Again, the A_{11} term of the overall wave-matrix is the reciprocal of the combined wire-grill, vacuum-space, and dielectric window transmission coefficient, which we shall call T_{combo}, and which can immediately be found as:

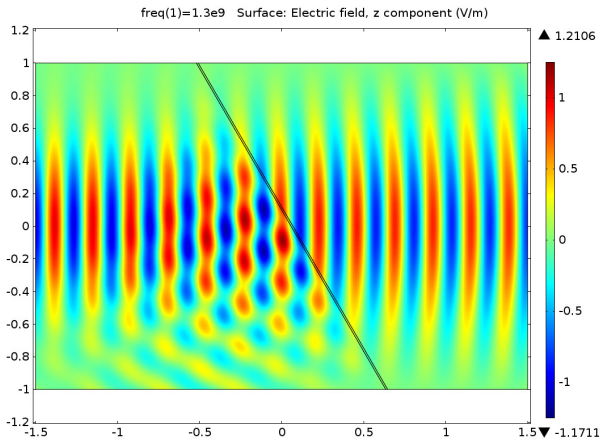
$$T_{combo} = \frac{T_g T_D}{e^{j\phi_v}\left(e^{j\phi_d} - R_L^2 e^{-j\phi_d}\right) + R_g R_L e^{-j\phi_v}\left(e^{-j\phi_d} - e^{j\phi_d}\right)}$$

The resulting *power*-transmission coefficient, T_{pow}, can then be written simply as $T_{pow} = |T_{combo}|^2$, along with $R_{pow} = 1 - T_{pow}$, for lossless media. Of course, expressions for R_{pow} and T_{pow} in terms of the various geometric and material factors are especially useful in the design-process to optimize apertures of FAWSEA-type antennas, as we have shown earlier. Before generalizing the above to non-uniform (slowly-varying) interfaces, it is instructive to compare the above ~analytic expression for T_{pow} to some 2D FE models of combinations of uniform wire-grills with dielectric windows.

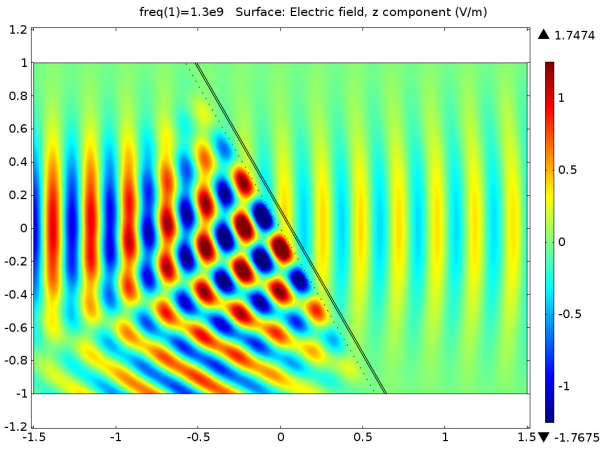
Figure 13 shows the result of a just a few, initial, comparisons. The excellent agreement observed between the above theory and the 2D numerical models is very encouraging.



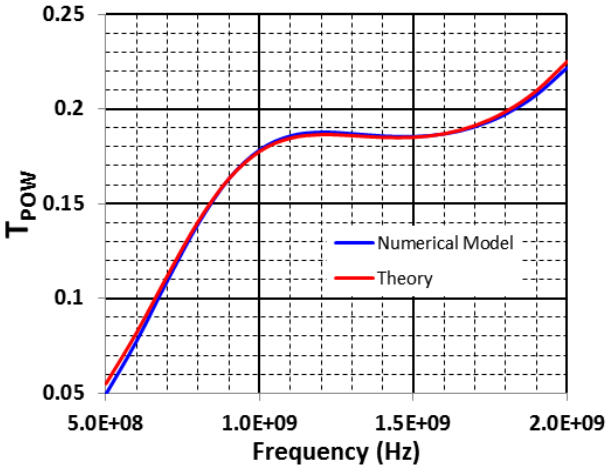
Uniform Grill *Alone* at 1.3 GHz.
Theory T_{pow} = 0.24248. FE model T_{pow} = 0.24285



Uniform Dielectric Window *Alone* at 1.3 GHz.
Theory T_{pow} = 0.91540 FE model T_{pow} = 0.91923



Uniform Window & Grill *Together at* 1.3 GHz.
Theory T_{pow} = 0.18590. FE model T_{pow} = 0.18693



Uniform Window & Grill *Together.*
Predicted T_{pow} vs. freq. Theory vs. FE Model.

Figure 13. Comparison of T_{pow} predictions via Wave Matrix theory and 2D FE models. Example TE wave is incident at 30° relative to the normal. For the wire grill, we have set each wire diameter = 0.2cm and the wire separation = 4cm. The dielectric window is displaced 5cm along the normal from the grill, has a thickness of 1cm, and ε_r = 3.0

4.1.4. Generalization to Finite, Non-uniform (Slowly-varying) Interface Sandwiches

We apply the same approach used in Sections 4.1.1 and 4.1.2 to generalize our calculations to finite, non-uniform, but gradually-varying interfaces. For example, if on the basis of, say, mechanical engineering considerations, we would like to employ a window of a particular material and thickness, at a particular distance from the wire grill, then per Figure 3, we can adjust our design tool by: (1) replacing the call to the "myRpow" function in the script to a call to "myRpowC" instead, where myRpowC is given by the function in Figure 14, while passing along the pre-set values for the window thickness (td), dielectric constant (epr), and distance between the grill and window (h_D). For example, consider again the same input parameters that we used previously for the wire-grill design in Figure 3, but this time with the intent to combine it with an acrylic (ε_r=2.55) window of thickness 1cm at a distance of 2.5cm from the grill.

This then yields a revision to the computation of the ideal wire diameters. It is instructive to compare the values computed in this way to those computed earlier (Figure 3) for which no dielectric window was present. Interestingly, for the example window parameters chosen above, the wire diameters predicted to yield the best performance are larger in diameter than for the no-window case, which may seem counterintuitive[8]. See Figure 15. As before, we can load these predicted wire diameter values into a 2D FE model, and will also include the aforementioned dielectric window, to separately evaluate how well this design-approach appears to work. Figure 16 and Figure 17 show the results.

```
function Rpow = myRpowC(AngIn,a,d,hD,td,epr,f)
    ct = cos(AngIn);
    st = sin(AngIn);
    mysq = sqrt(epr-st^2);
    c_const = 2.99792458e8; %c in m/s
    lambda = c_const/f; % free space wavelength
    k0 = 2.0*pi*f/c_const; %incident k, free space
    phiV = k0*hD*ct;  % electrical length in vacuum gap
    phitd = k0*td*mysq;  % electrical length in window
    RL = (ct-mysq)/(ct+mysq);
    TD = 1-RL^2;
   % Compute Xa and Xb using Marcuvitz's formulas.
    sum1 = 0;
    sum2 = 0;
    for m = 1:1:1000
        sum1 = sum1+1/sqrt(m^2+2*m*a*st/lambda-(a*ct/lambda)^2)-1/m;
        sum2 = sum2+1/sqrt(m^2-2*m*a*st/lambda-(a*ct/lambda)^2)-1/m;
    end
   % Normalized to Z0 = 1 everywhere
   % Compute Xa using a detailed sum from Marcuvitz p. 286
    Xa = (a*ct/lambda)*(log(a/(pi*d))+0.5*(sum1+sum2));  % from sum
    Xb = (a*ct/lambda)*(pi*d/a)^2;  % used in either expression
    Tg = 2.0*1i*Xa/((1+1i*(Xa-Xb))^2+Xa^2);
    Rg = (Xa^2-(Xa-Xb)^2-1)/((1+1i*(Xa-Xb))^2+Xa^2);
    nump1 = exp(1i*phiV)*(exp(1i*phitd)-RL^2*exp(-1i*phitd));
    nump2 = Rg*RL*exp(-1i*phiV)*(exp(-1i*phitd)-exp(1i*phitd));
    Tcombo = Tg*TD/(nump1+nump2);
    Tpow = abs(Tcombo)^2;
    Rpow = 1.0-Tpow;
end
```

Figure 14. A MatLab function to evaluate R_{pow} for TE wave incidence for a wire-grill & window combination.

This *combination* of a grill and window actually performs slightly better than the previous grill alone, possibly due to the combined interface yielding greater constancy of the phase velocity toward the terminating end of the guide (a consideration which was not an explicit part of the computation in the approximation here). About 97.75% of the input power is radiated (~2.25% reached the termination) and very good beam uniformity is achieved. This model's -3dB full beamwidth = 2.79°. An ideal uniform aperture of length 5m*cos(30°) would have a -3dB beamwidth of 2.7° implying that the model's aperture efficiency is 96.7% in terms of projected aperture (4.33m), and 83.8% in terms of geometric aperture (5m). But to be fair, we should discount the beamwidth based performance measures by a factor of 0.9775, due to the 2.25% of the power lost into the termination (as mentioned earlier), implying the aforementioned

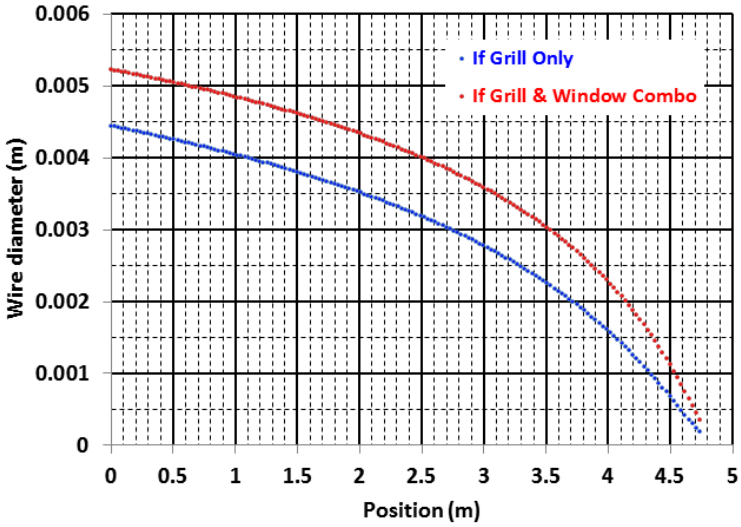


Figure 15. Theory-generated wire-diameters for a high-performance leaky-grill *with* (shown in red) and *without* (shown in blue) the presence of a dielectric window (see text for parameters).

[8] Since a dielectric window introduces additional reflection compared to no window, one might guess that reducing the wire diameters in the leaky grill would be appropriate to compensate. Evidently, this mental picture, which glosses-over such considerations as the phase/interference effects between the grill and window, is overly-simplistic.

efficiencies should be taken as 94.5% and 81.9%, respectively. Finally, the beam direction has shifted nearly a degree (to closer to 29° than 30° relative to the normal), which could call for a minor adjustment to the vertical position of the row of grill wires, if the desired beam angle is 30°. Regardless, the configuration as derived via the above procedure(s) yields an excellent aperture field distribution and radiated beam, in this 2D approximation.

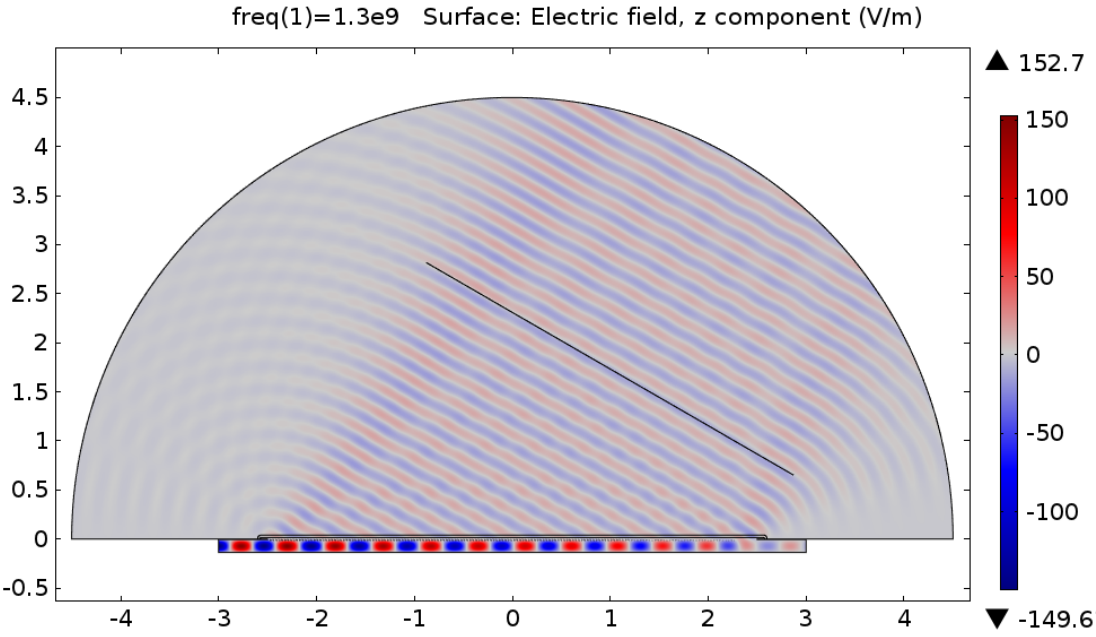


Figure 16. 2D FE model, with 159 wires (see red curve in Figure 15) with diameters set via the combined wave-matrix theory including a dielectric window. (Compare to Figure 4.)

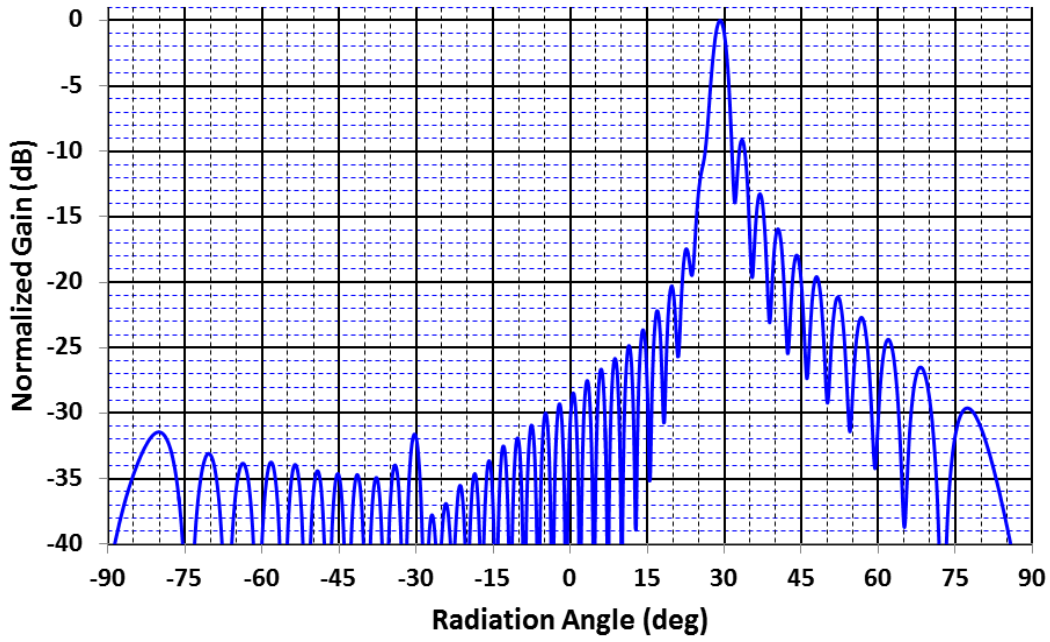


Figure 17. Predicted H-plane pattern, normalized to 0dB, from the 2D finite-element model in Figure 16, using the 159 wires generated via wave-matrix theory and Matlab scripts.

4.1.5. Finite-width Leaky-wave Channels: 2D vs 3D Analyses

The HPM-capable leaky-wave antennas of interest are ultimately 3D structures, most consisting of multiple channels arranged in parallel (or approximately-parallel, for some types of curved apertures). Some important characteristics can be addressed via purely 2D (usually H-plane) analyses and models. Mutual-coupling between neighboring leaky apertures (aka, channel-to-channel coupling) is an example of a true 3D problem. But even with only a *single channel*, a purely-2D theoretical treatment fails to address the impact of the transition geometry in the E-plane, as the wave exits the channel and expands into free space. Consider, for example, Figure 18 and Figure 19, which compare 2D and 3D models of a wire grill-type leaky-wave guide with identical lengths, wire sizes, placements, and channel depths.

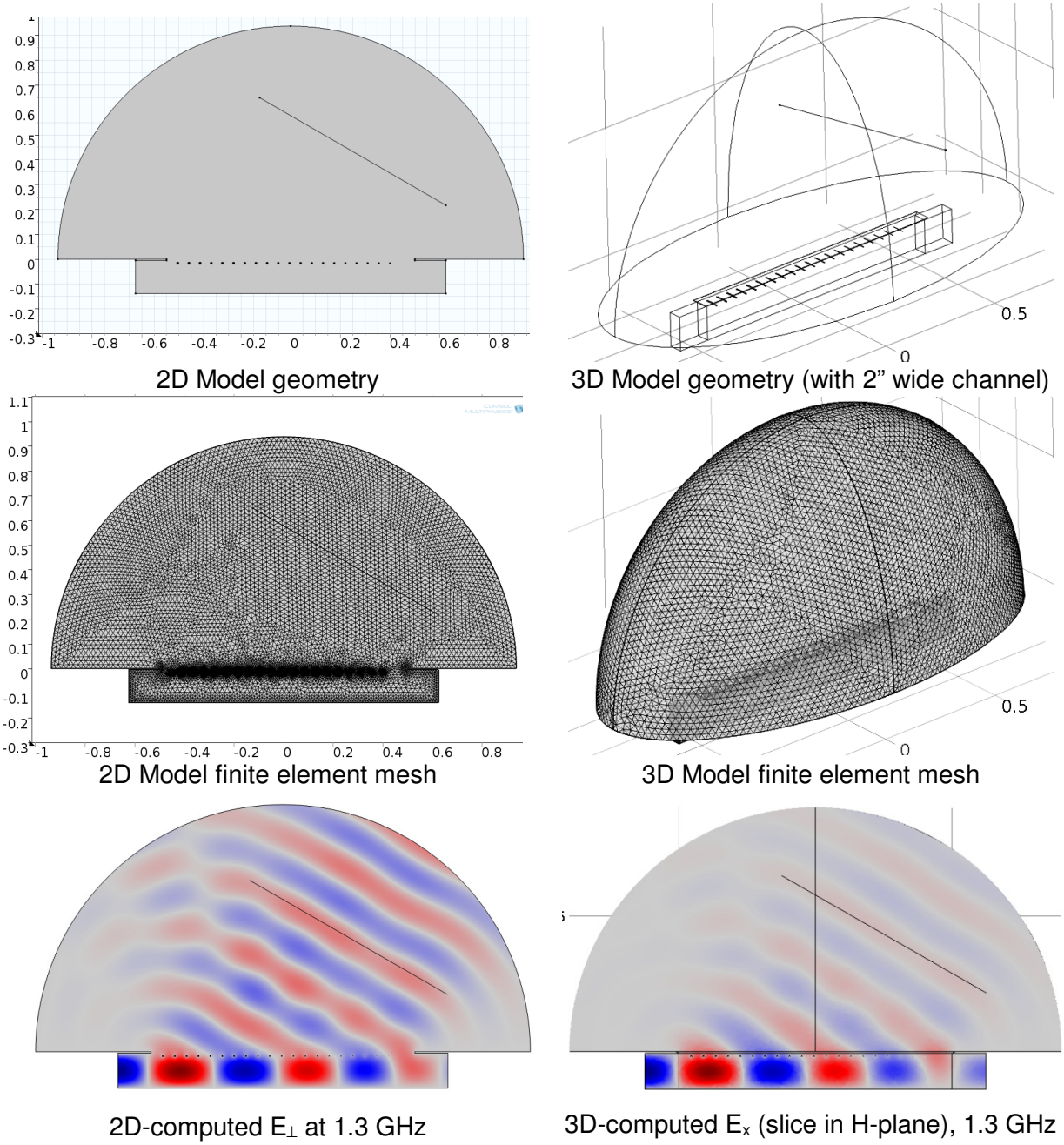
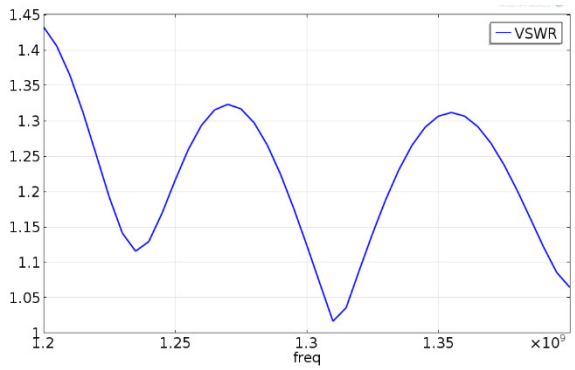
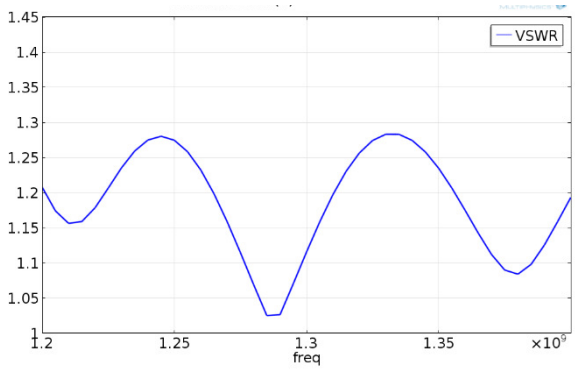


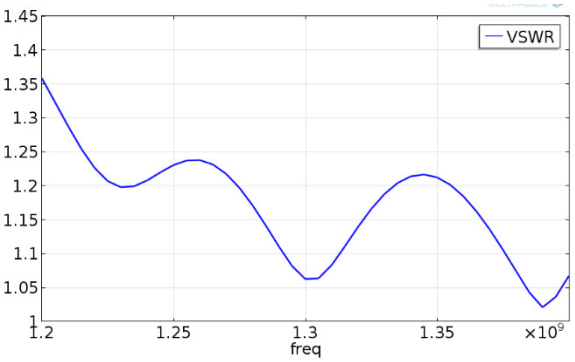
Figure 18. 2D vs. 3D representations of a leaky-wave antenna channel with identical channel lengths, depths, and leaky wire-grill geometries (and no dielectric windows).



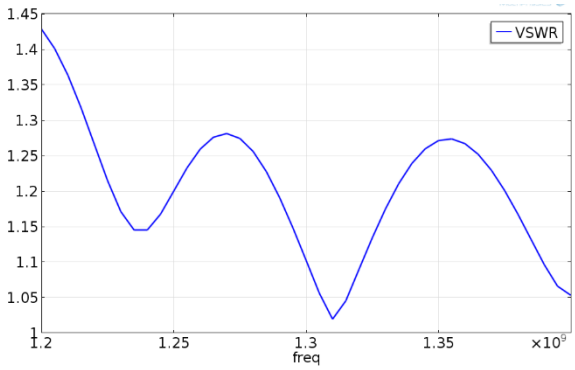
2D-computed VSWR vs. frequency
(equiv. to an *infinitely-wide* channel)



3D-computed VSWR vs. frequency
(for a **2"-wide** channel)



3D-computed VSWR vs. frequency
(for a **4"-wide** channel)



3D-computed VSWR vs. frequency
(for an **8"-wide** channel)

Figure 19. Comparison of computed VSWR vs. frequency, 2D vs. 3D representations. (See Figure 18 for representative model geometries). All four plots on same scale. Top-left: 2D model. Top-right: 3D with 2"-wide channel.→ *Different from 2D results.* Bot-left: 3D with 4"-wide channel.→ *Some similarity to 2D results.* Bot-right: 3D with 8"-wide channel.→ *Very similar to 2D results.*

To avoid obfuscation by window-related effects, we left out dielectrics in the above example. The distributions of wire sizes here were again set via the method[9] described previously, along with f_0 = 1.3 GHz, a desired beam angle relative to normal of 30°, and fixed wire spacing = 4.5cm. A slanted line at 30° in the H-plane is placed in both models for comparison with the computed phase-fronts. The 2D model does not include any of the physics associated with the cross-sectional width of the channel, such as its edges along the aperture and the ground planes on each side. Even so, the predicted H-plane wave fields are about the same[10] and so are the H-plane patterns (not shown here). But comparing computed VSWR vs frequency curves (see Figure 19) shows significant differences between the 2D and 3D models for a narrow channel. *As we make the channel wider* in the 3D model, the disagreement shrinks, indicating that the *channel-width* is the factor that is responsible for the different results.

It is worth noting that *all* our designs of multi-channel FAWSEA-family antennas to-date fall in the regime where the channel widths are sufficiently-narrow that their standalone VSWR vs frequency curves

[9] This method yields a good, but *not fully-optimal* wire grill configuration, since it does not fully account for the impact of the wire grill on the wave propagation constant (β) in the guide. Our purposes *in this section* are to compare 2D vs. 3D representations and understand the physics differences, not (yet) to optimize specific designs.
[10] Note that the weaker amplitude of the radiated waves in the 3D model slice in Figure 18 is due simply to fanning-out of the radiation in the E-plane after leaving the channel. This is absent in the 2D model.

differ significantly from predictions of purely-2D models. And this is likely to hold for future designs as well, since wide channels (such as the 8"-wide example in Figure 19) introduce undesirable support for higher-order modes. (In addition to poor performance, higher-order modes in an HPM antenna can encourage breakdown and even physical damage to the antenna surfaces due to arcs.) So we have little choice but to employ relatively-narrow channels. And thus, it is important to understand their behavior. We can begin to grasp the origin of the 3D vs. 2D differences that appear in Figure 19 by taking a closer look at what happens at the transition from the channel to the open-space in the E-plane.

4.1.6. Transition from a *Finite-width* to *Open Half-space* in the E-plane

Consider first the geometrically-simple problem of a transition from a parallel-plate TEM line[11] into free space, shown via a 2D E-plane model in Figure 20.

This model includes a fine mesh, use of symmetry, and a perfectly-matched-layer (PML) absorbing boundary to improve accuracy. To obtain the effective impedance *at the transition*, we must first *transform* the complex relative impedance (i.e., impedance relative to Z_0) *at the port*. The latter can be found from our model-computed values of S_{11}, i.e.,

$$Z_{in} = \frac{1+S_{11}}{1-S_{11}} \leftarrow \text{Relative impedance } \underline{\textit{at the port}}.$$

The relative impedance <u>*at the aperture*</u> (aka the transition) from the guide to free space is found via[12]:

$$Z_A = \frac{Z_{in} - j\tan\beta\ell}{1 - Z_{in}\, j\tan\beta\ell}, \text{ where } \beta = 2\pi/\lambda$$

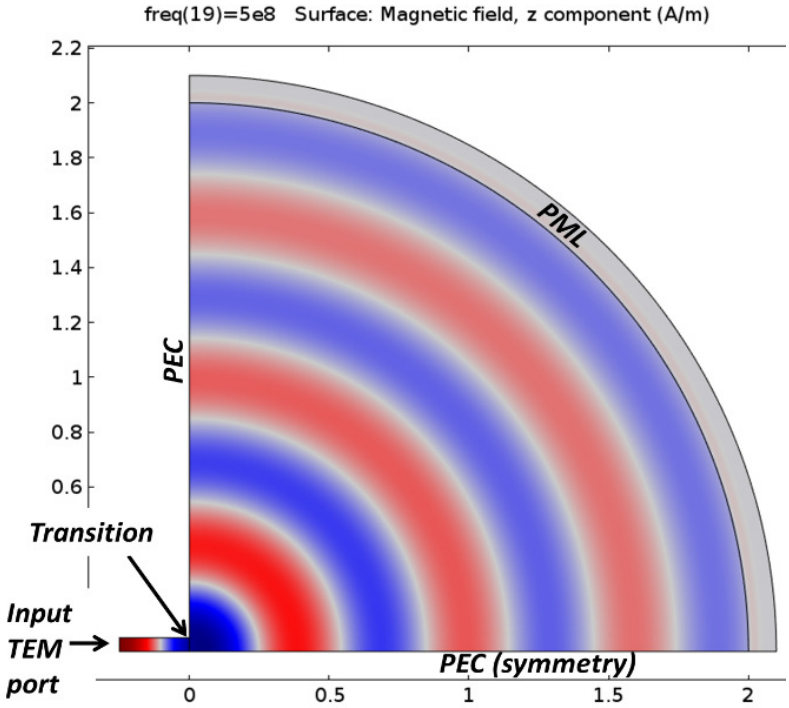


Figure 20. Example channel to free-space transition in 2D, E-plane. (input *E* is vertical.)

where ℓ = transmission line length from the port to the aperture.

Fortunately, the same geometry being discussed here is addressed by Marcuvitz (1951). A snapshot of his description is provided in Figure 21. For comparison purposes it is more convenient to put our calculations in terms of the relative *admittance*:

$$Y_A \equiv \frac{1}{Z_A}, \text{ with } Y_A \equiv G_A + jB_A.$$

where G_A is the *conductance* and B_A is the *susceptance*.

[11] A wave exiting the side of a long channel is similar to one leaving the end of a very-wide parallel plate line, with the exception of the angle relative to the normal. The latter may be included via a factor we will address shortly.
[12] This is the standard formula for transformation of an impedance along a lossless TEM line. See, for example, http://www.antenna-theory.com/tutorial/txline/transmission4.php .

A comparison of our numerical predictions with the plots provided by Marcuvitz is shown in Figure 22. The agreement is best for relatively small channel widths (which is not surprising, in light of the validity restrictions of the equivalent circuit noted in Figure 21). Fortunately, this is the regime of primary interest. Figure 23 compares Marcuvitz's simplest expressions (Eqs. 1*b* and 2*b* in Figure 21) to our FE model in this narrow channel regime.

Bear in mind that to avoid *any* reflection at the aperture, one would seek to have $Z_A \rightarrow Z_0$ (or $Y_A \rightarrow Y_0$) which implies $G_A \rightarrow 1$ and $B_A \rightarrow 0$. It is clear from Figure 22 that this condition never occurs for the narrow apertures of our main interest.

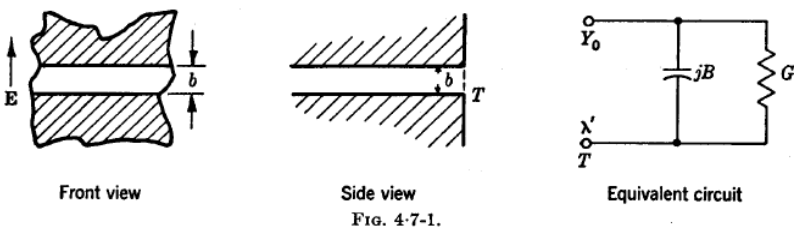


FIG. 4·7-1.

Equivalent-circuit Parameters.—At the reference plane T

$$\frac{G}{Y_0} = \int_0^{kb} J_0(x)\,dx - J_1(kb), \tag{1a}$$

$$\frac{G}{Y_0} \approx \frac{\pi b}{\lambda'}, \tag{1b}$$

$$\frac{B}{Y_0} = \int_0^{kb} N_0(x)\,dx + N_1(kb) + \frac{2}{\pi}\frac{1}{kb}, \tag{2a}$$

$$\frac{B}{Y_0} \approx \frac{2b}{\lambda'} \ln \frac{e\lambda'}{\gamma 2b}, \tag{2b}$$

where

$$k = \frac{2\pi}{\lambda'}, \qquad \lambda' = \frac{\lambda}{\cos\alpha}, \qquad e = 2.718, \qquad \gamma = 1.781.$$

Restrictions.—The equivalent circuit is valid in the range $b/\lambda' < 1.0$. The circuit parameters have been obtained by the variational method assuming a constant electric field in the aperture at the reference plane. No estimate of accuracy is available over the entire range, but the error is no more than a few per cent for $(2b/\lambda') < 1$. Equations (1*b*) and (2*b*) are static results and agree with Eqs. (1*a*) and (2*a*), respectively, to within 5 per cent for $(2\pi b/\lambda') < 1$.

Figure 21. Parallel-plate joining to an open half-space. (Borrowed from N. Marcuvitz, *Waveguide Handbook*.)

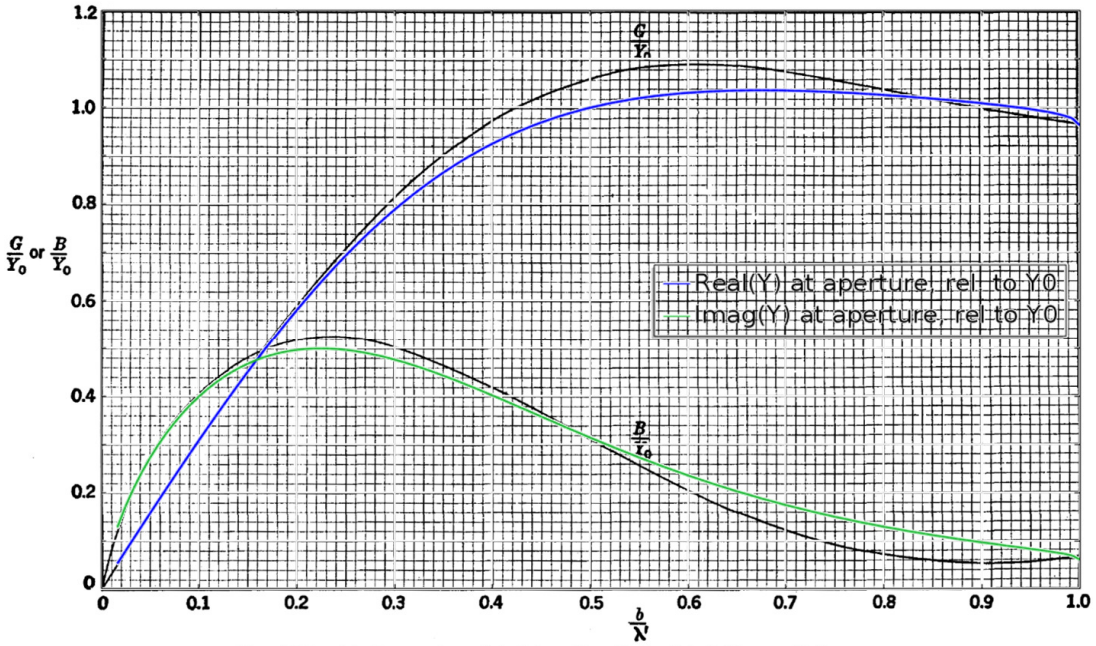


FIG. 4·7-2.—Admittance of parallel plate guide radiating into half-space, *E*-plane.

Figure 22. Overlay of G_A and B_A from our 2D E-plane normal-incidence FE model (the blue and green curves) on the corresponding plots in the *Waveguide Handbook*, for a parallel-plate to free half-space sudden transition in the E-plane.

Figure 24 shows a plot of reflected-wave magnitude (in terms of S_{11} in dB) due to this transition, as predicted by our 2D (E-plane, normal incidence) FE-model. Since the earlier 2D *H-plane* model (left column in Figure 18 and upper left panel in Figure 19) does not include *any* representation of this transition at all, it should not be surprising that the 2D model in Figure 18 gave different results from the 3D model and that the greatest differences observed (see Figure 19) occurred with the narrowest channels.

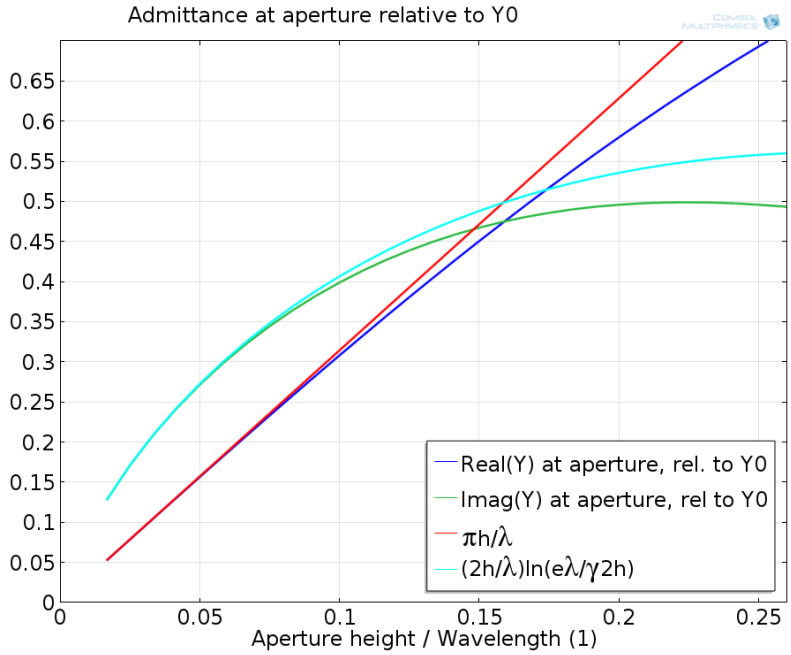


Figure 23. Comparison of G_A and B_A from FE model (blue & green) to Marcuvitz's simplified (narrow-channel) expressions (red & light blue).

The FE model used above shows fairly good agreement with Marcuvitz's expressions for G and B, but in fact our 2D testbed in Figure 20 only checked the case of *normal incidence* (i.e, $\lambda'=\lambda_0$ in Figure 21). To test his circuit model in a non-normal incidence case, we need a 3D FE model. Figure 25 shows[13] a model prepared for this purpose, along with the predicted reflections (S_{11}, in dB) compared to those computed using Eqs. 1b and 2b and the circuit in Figure 21. Note: $\lambda' \equiv \lambda/\cos\alpha'$, with $\alpha' = 30^o$ for all cases in this example. (In the left panel of Figure 25, channel height $b = 2.0$" and f = 1.0 GHz, which corresponds to the case $b/\lambda' = 0.14675$). As hoped, we found that the FE model and equations based on the equivalent circuit in Figure 21 agreed very well for narrow-channel conditions.

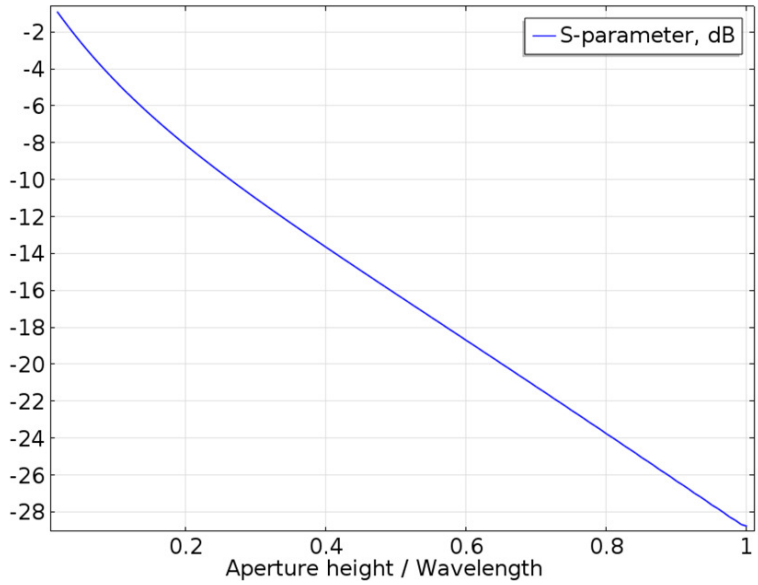


Figure 24. Computed reflection (S_{11}, dB) for E-plane transition, *normal incidence*.

[13] The model shown is for the upper-half volume. The dividing surface is a PEC symmetry plane (parallel to the H-plane and centered in the TL and aperture) This speeds ups the computation and reduces the memory required.

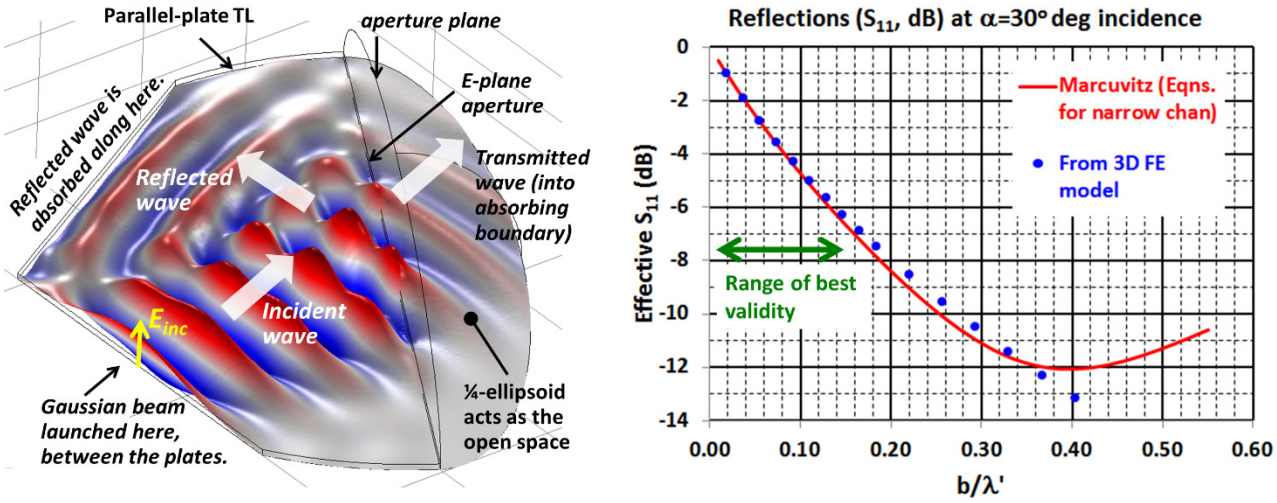


Figure 25. Left: 3D model, E-plane aperture, incidence 30° to normal. Right: Predicted $|S_{11}|$.

Armed with the above, we can now generalize and merge an analyses of the wave reflection associated with this transition into the formalism of *chainable* transitions in the wave-matrix theory discussed earlier Refer again to Figure 10. For purposes of computing wave reflection, the subject transition here is being modeled as *equivalent to* the type of interface on the left in Figure 10, i.e., the matrix mathematics is *analogous* to that of an interface between two media. For *this*[14] interface, we will express the associated wave matrix in the following form:

$$\begin{bmatrix} c_1 \\ b_1 \end{bmatrix} = \frac{1}{T_A}\begin{bmatrix} 1 & R_A \\ R_A & 1 \end{bmatrix}\begin{bmatrix} c_2 \\ b_2 \end{bmatrix}, \text{ where } R_A = \frac{1-Y_A}{1+Y_A}, \text{ with } T_A \equiv \sqrt{1-|R_A|^2} \text{ and with } Y_A \text{ as given earlier.}$$

In principle, we can now drop this into the wave-train expression from before. If we *leave out dielectrics* for now, but include the vacuum-separation (re-interpreting the distance formerly from the grill to the window as the distance from the grill to the E-plane aperture transition), the earlier wave-matrix chain equation becomes:

$$\begin{bmatrix} c_1 \\ b_1 \end{bmatrix} = \frac{1}{T_g T_A}\begin{bmatrix} e^{j\phi_v} & -R_g e^{-j\phi_v} \\ R_g e^{j\phi_v} & \left(T_g^2 - R_g^2\right)e^{-j\phi_v} \end{bmatrix}\begin{bmatrix} 1 & R_A \\ R_A & 1 \end{bmatrix}\begin{bmatrix} c_2 \\ b_2 \end{bmatrix}$$

As before, the A_{11} term of the overall wave-matrix is identified as the reciprocal of the combined wire-grill, vacuum-space, and 3D E-plane transition transmission coefficient, which we will call T_{3D0}. From matrix multiplication it is found immediately as:

$$T_{3D0} = \frac{T_g T_A}{e^{j\phi_v} - R_g R_A e^{-j\phi_v}}$$ (For slot + wire-grill + 3D E-plane transition. No dielectrics.)

where R_A is given above as a function of Y_A, and expressions for T_g, R_g, and ϕ_v were given previously. The resulting *power*-transmission coefficient, T_{pow}, can then be written simply as $T_{pow} = |T_{3D0}|^2$, along with $R_{pow} = 1 - T_{pow}$, for the case of lossless media.

[14] We define T_A here in terms of *magnitude only* (i.e., uncertain phase), due to the single-sided circuit in Figure 21. This incomplete knowledge does not impact computation of predicted power reflection or transfer.

Recall that our expression for T_{3D0}, just as with the term we called T_{combo} previously, was not derived explicitly for a leaky-wave antenna, but rather for an infinitely long aperture with a uniform wire-grill across it. But in this new 3D case, the geometry represented is part of a uniform channel with a *finite width* in the E-plane, transitioning to an open space parallel to the grill-wire plane. In principle, extension and generalization of this expression to apply to a *3D* single-channel forward-traveling leaky-wave antenna can be done in a manner closely-analogous to what we described previously. But before attempting that, let's test the predictive power of the above expression for T_{3D0} with another representative 3D numerical model[15]. Our first selected test-case for T_{3D0} is shown in Figure 26. The reader may notice this is very similar to the model in Figure 25, except that we have now added a *uniform wire grill* parallel to E_{inc} and preceding the aperture. For convenience in setup and to ease management of the boundary conditions on the wave-launching side of the model space, we again employ a Gaussian-bounded TEM wave as the excitation.

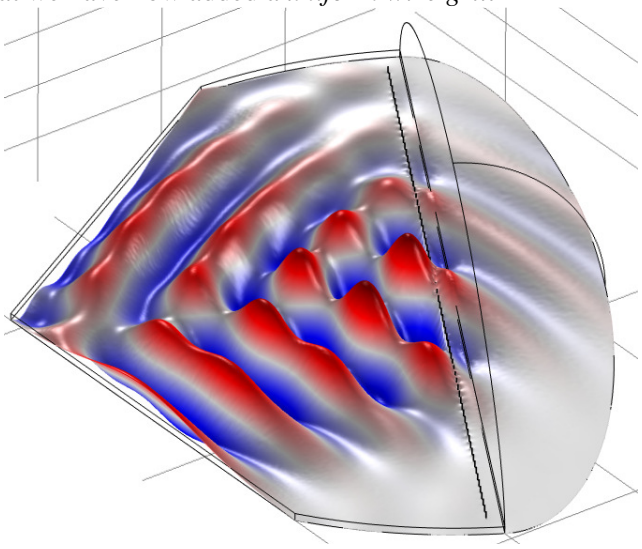


Figure 26. 3D FE model, Test #1 of T_{3D0} expression. f=1.0 GHz. FE model-computed effective S_{11} = -1.882 dB, while S_{11} from wave-matrix theory = -2.018 dB.

The uniform wire grill in Figure 26 has 72 wires of diameter = 0.2 cm, wire spacing = 4.0 cm, and is displaced relative to the E-plane aperture by 5 cm. The aperture height = 2" (5.08cm). Operation in this example is at 1.0 GHz, which yields b/λ' = 0.146748. Now let's assemble the pieces to build T_{3D0}. From Eqs. 1b and 2b in Figure 21, and the value of b/λ', we get Y_A = 0.4610239 + j0.4838804, which in turn yields R_A = 0.2335920 - j0.4085566.

Next, we set $\phi_v = k_0$ * separation * cos30° or $\phi_v = (2\pi/\lambda_0)(0.05m)\sqrt{3}/2 = 0.9075275$ radians.

To compute T_g and R_g, we go back to our MatLab scripts and the equivalent circuits employed there to model the grill. From that: T_g = 0.1552538 + j0.3650053 and R_g = -0.8447299 + j0.3593032. Plugging all these into our expression for T_{3D0}, we find T_{3D0} = 0.6012932 + j0.1005057. It follows immediately that the predicted $T_{pow} = |T_{3D0}|^2$ = 0.3716548 and R_{pow} = 1-T_{pow} = 0.6283452. Thus finally, S_{11} (dB) = 10*log$_{10}$(R_{pow}) = -2.018 dB. This differs from the FE model prediction by ~0.136 dB (about 3.2%). In contrast, if we *ignore* the aperture in the E-plane entirely and consider only reflections from the wire grill, our earlier (2D H-plane) scripts predict an effective S_{11} = -0.743 dB. This differs from the FE-model by 1.14 dB. So our inclusion of the term for the E-plane aperture in the wave-matrix chain yielded superior agreement with the FE model.

[15] If it doesn't work in a simpler model, it's not worth generalizing to a traveling-wave leaky-wave configuration!

As a second test, let's simply increase the wire spacing[16] to 6cm, while holding the other parameters fixed. Using our MatLab scripts, we compute: $T_g = 0.3864008 + j0.4888258$ and $R_g = -0.6135919 + j0.4850244$. Plugging these into our expression for T_{3D0}, we find $T_{3D0} = 0.795477 - j0.1748875$. The predicted $T_{pow} = |T_{3D0}|^2 = 0.663369$, and $R_{pow} = 1-T_{pow} = 0.3366311$. Thus S_{11} (dB) = $10*\log_{10}(R_{pow})$ = -4.728 dB. This differs from the FE model by 0.124 dB, or about 2.9%. In contrast, if we *ignore* the aperture in the E-plane entirely and consider only the reflections from the wire grill, our earlier (2D H-plane) scripts predict an effective S_{11} = -2.134 dB. This differs from the FE-model by 2.47 dB, which is quite a lot. So once again, our inclusion of the term for the E-plane aperture in the wave-matrix chain yielded superior agreement with the FE model.

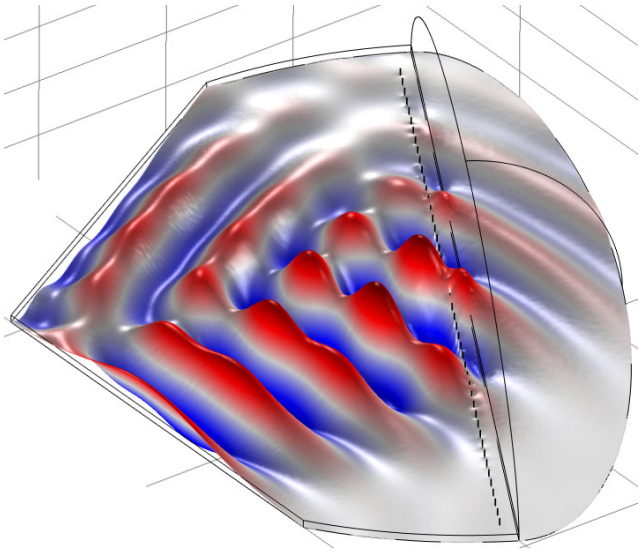


Figure 27. Test #2 of T_{3D0} expression. (Note the more widely-separated wires.) FE model-computed eff. S_{11} = -4.604 dB. S_{11} from wave-matrix theory = -4.728 dB.

Next, we wish to include this interface in computing behavior of a 3D leaky-wave channel, via the same methodology (i.e., leveraging an assumption of slowly-varying properties along the channel) that we used before to address the wire-grill and dielectric window in the H-plane analyses previously. To this end, we prepared a simple Matlab Script to generate a set of wire diameters that optimize the leak-rate (for uniformity of aperture field magnitude) from a *finite-width* leaky-wave channel. For completeness, Figure 28 lists the script and associated function used to compute R_{pow}. (Comments are in green.)

[16] In addition to simply providing another test case, this more transparent grill increases the fraction of the incident wave interacting with the aperture, and thus may constitute a more demanding test of the new term.

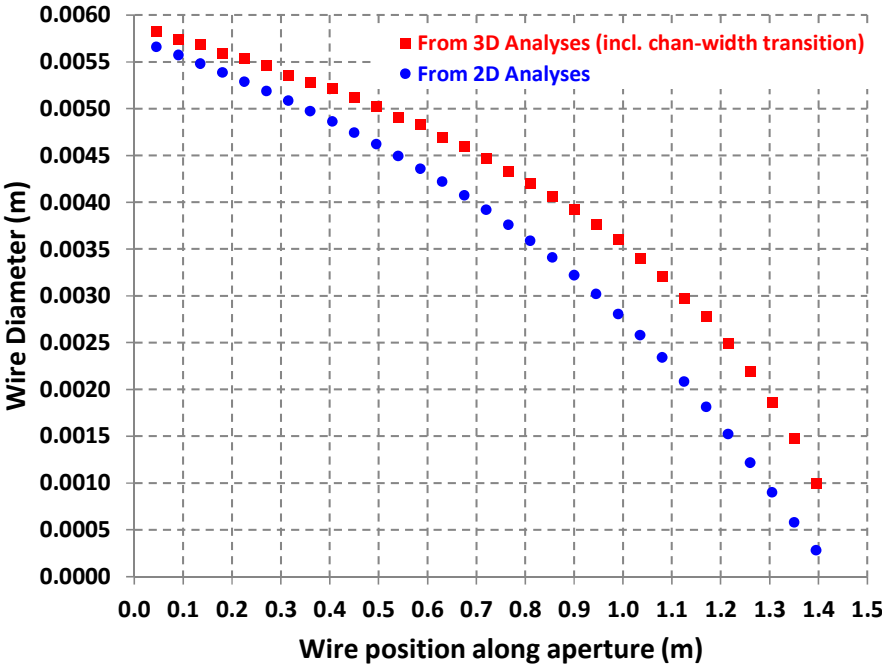
```
% fawsea_script_3D0.m
% Generates wire diameters for a single-channel,
fixed-width, 3D FAWSEA
% Includes sudden E-plane aperture transition into
empty half-space.
% Does not include any dielectric or window.
% See Marcuvitz, Waveguide Handbook, p. 286 and p.
184
% See also 1st and 2nd Quarterly Reports.
% Prepared by R. Koslover, SARA, Inc., Feb., 2014.
clear
c_const = 2.99792458e8; %c in m/s.
% User-specified inputs and derived quantities:
L = 1.5;  % length of desired fawsea aperture in
meters.
f = 1.3e9;  % Preferred frequency of op, in Hz.
lambda = c_const/f; % Free-space wavelength.
AngIn = 30*pi/180; % Desired beam angle rel to
normal.
fc = f*cos(AngIn); % Cutoff frequency needed to
yield specified AngIn.
h = 0.5*c_const/fc; % H-plane depth of guide that
yields fc above
hD = 0.0254; % Distance from wire grill to E-plane
aperture, in meters.
w = 0.0254; % Waveguide E-plane width in meters.
lambda_g = lambda/sin(AngIn);  % Guide wavelength
(ignores leakiness).
a = 0.045;  % Constant wire spacing, in meters.
(Specified by user.)
% Compute the 'Ideal' Rpow (i.e., the ideal power
leak-rate):
n = 0;
fac = -4*h^2/lambda_g;
for z=a:a:0.95*L
    n=n+1;
    RpIdeal(n) = exp(fac/(L-z));  % Ideal leak-rate
for uniform output.
end
% Use Matlab's fminbnd operator with annonymous
function to find set of
% d values (calling MyRpowE function) that best fit
ideal leak-rate.
n = 0;
for z=a:a:0.95*L  %Quits at ~95% of the way. (Drop
too-thin diams later.)
   n=n+1;
   zlist(n)=z;  % z positions of the wires
   foundd(n)=...
     fminbnd(@(d) abs(RpIdeal(n)-
myRpowE(AngIn,a,d,hD,w,f)),1e-99,a/2);
end
plot(zlist,foundd,'.');  % Plot identified wire
diameters vs. positions.
% Store the plotted values to a simple text file.
[fid] = fopen('d_vs_z_3D0.txt','w');
fprintf(fid,'Position , Diameter\n');
for q = 1:n
    fprintf(fid,'  %g   %g\n',zlist(q),foundd(q));
  end
fclose(fid);
```

```
% function Rpow = myRpowE(AngIn,a,d,hD,w,f)
%
% AngIn = angle of incidence rel to normal, in radians
% a = wire spacing in meters
% d = wire diameter in meters
% hD = Distance from wire grill to E-plane aperture, in
meters.
% w = Waveguide E-plane width in meters.
% f = frequency in Hz
%
% Computes plane-wave power-reflection coefficient.
% For a wire grill followed by a vacuum space & sudden
E-plane aperture.
% Analyses based on wave matrix method.
% Does not include any dielectric material or window.
% See Marcuvitz, Waveguide Handbook, p. 286 and p. 184
% See also 1st and 2nd Quarterly Reports.
% Prepared by R. Koslover, SARA, Inc., February, 2014.
% Z0 = 1, Y0 = 1.
function Rpow = myRpowE(AngIn,a,d,hD,w,f)
    ct = cos(AngIn);
    st = sin(AngIn);
    c_const = 2.99792458e8; %c in m/s
    lambda = c_const/f; % free space wavelength
    lambdap = lambda/ct; % lambda prime, for aperture Y
computations.
    k0 = 2.0*pi*f/c_const; %incident k, free space
    phiV = k0*hD*ct;  % electrical length of grill-to-
aperture gap
   % Compute grill Xa and Xb equivalents per Marcuvitz,
p. 286.
    sum1 = 0;
    sum2 = 0;
    for m = 1:1:1000
        sum1 = sum1+1/sqrt(m^2+2*m*a*st/lambda-
(a*ct/lambda)^2)-1/m;
        sum2 = sum2+1/sqrt(m^2-2*m*a*st/lambda-
(a*ct/lambda)^2)-1/m;
    end
    Xa = (a*ct/lambda)*(log(a/(pi*d))+0.5*(sum1+sum2));
% from sum
    Xb = (a*ct/lambda)*(pi*d/a)^2;  % used in either
expression
    Tg = 2.0*1i*Xa/((1+1i*(Xa-Xb))^2+Xa^2);
    Rg = (Xa^2-(Xa-Xb)^2-1)/((1+1i*(Xa-Xb))^2+Xa^2);
   % Compute aperture admittance per Marcuvitz 1b & 2b,
p. 184.
    Ya =
pi*w/lambdap+1i*(2.0*w/lambdap)*log(0.7631026*lambdap/w)
;
    Ra = (1.0-Ya)/(1.0+Ya);  %Reflection at E-plane
aperture
    Ta = sqrt(1.0-abs(Ra)^2); % Effective Ta, Using
magnitude-only.
   % Assemble T3D0.
    T3D0 = Tg*Ta/(exp(1i*phiV)-Rg*Ra*exp(-1i*phiV));
    Tpow = abs(T3D0)^2;
    Rpow = 1.0-Tpow;  %Output the local power reflection
coefficient.
end
```

Figure 28. Left: Script to generate wire diameters vs. position, for a fixed-width channel. Right: Function called by script to compute power-reflection coefficient.

Figure 29 compares wire diameters generated from our previous (2D) analyses and from our new 3D script & function above, for these inputs: L=1.5m, f=1.3 GHz, $\phi_{tilt} = 30^o$, wire spacing = 4.5cm, channel width = 1.0", and grill to aperture[17] dist. = 1.0". The last two parameters are only used in 3D analyses.

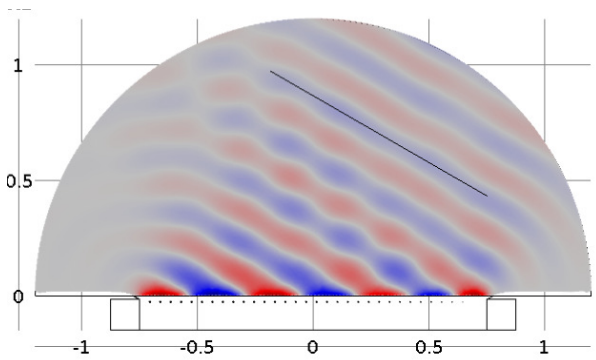
[17] This last value may not be realistic, but it lets us test the models better. We will return to this topic shortly.



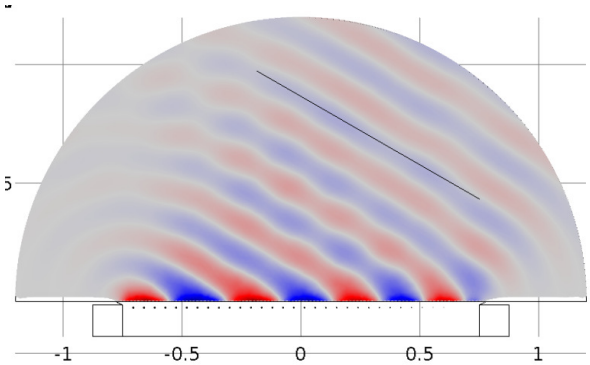
For: L=1.5m, f=1.3 GHz, ϕ_{tilt} = 30°, wire sep. = 4.5cm, chan. width = 1.0", grill to aperture[18] dist = 1.0"

Figure 29. Predicted wire diameters vs. position to yield ~optimum leaky aperture.
Red: Computed via the new 3D script & function listed in Figure 28.
Blue: Computed via earlier 2D script, for same input conditions.

To continue the comparison, we present two 3D FE models corresponding to the above conditions, one with its wire-grill diameters chosen based on the new 3D wave-matrix analysis and the other based on the earlier 2D wave-matrix analysis. Figure 30 and Figure 31 compare the H-plane slices of local radiated fields and predicted far-field (H-plane) patterns[19] for these cases. It is encouraging that the design based on the newer 3D wave-matrix chain is predicted to deliver a narrower (by about 6%) main beam.



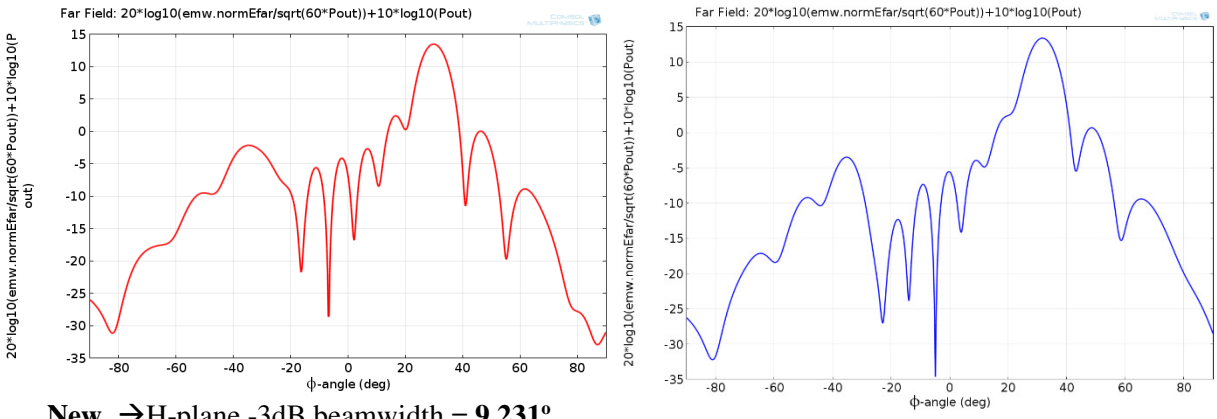
With wire grill based on **3D analyses**.



With wire grill based on **earlier 2D analyses**.

Figure 30. Left: Slice of E_x, 3D model of 1"-wide channel with wire-grill based on new 3D analyses. Right: After replacing wire-grill with one based on earlier 2D analyses.

[18] This last value may not be the most likely value in an actual antenna, but it is useful to test the models.
[19] E-plane patterns and full 3D patterns can also be computed, but are of less interest for a *narrow single-channel* geometry, since the output beam is, of course, very wide in the E-plane. E-plane and 3D patterns of multi-channel configurations are addressed later in this report.



New →H-plane -3dB beamwidth = **9.231º**

Old →H-plane -3dB beamwidth = **9.804º**

Figure 31. H-plane patterns predicted via 3D models of a 1"-wide leaky channel. Left: For antenna with leaky-grill wire diameters derived from the new 3D analyses. Right: For antenna with leaky-grill wire diameters derived from the earlier 2D analyses.

The reader may have noticed that a number of imperfect or potentially-problematic constraints were imposed in our selection and preparation of the test-case examples:

Concern or Question	Comments
The *sharp-step* transition to free-space in the E-plane (see Figure 20) introduces field-enhancements incompatible with HPM. Why wasn't a *rounded edge* considered instead?	A sudden-step is arguably the simplest E-plane transition to analyze theoretically and an equivalent circuit is given in the literature (e.g., Figure 21). But since our approach to generating equivalent admittances via FE-models (e.g., see Figure 22) seems to work, we should be able to *numerically-generate* custom formulas for custom configurations, *including rounded-edge* transitions that are HPM-compatible (see Section 4.1.7).
The 3D examples assumed a 1.0" gap (~λ_0/9) between the wire grill and E-plane transition/aperture. Why? Can the gap be smaller? Can the gap → 0?	Minimizing this gap is usually desirable from the perspective of low-profile design. However, the validity of chaining independent matrices representing independent interfaces (in the wave-matrix method) requires neglecting reactive coupling between the represented stages[20]. Initially, we only sought to determine if we could represent a combined wire-grill and E-plane transition via chaining together matrices for each of them. It appears to work. So now, we are better-prepared to explore the validity of smaller-gap cases.
Surely, we need to include a dielectric window in the 3D version of the analyses. Why was it left out in the 3D test-cases/examples?	Our earlier 2D (H-plane only) analysis with a dielectric window addressed a purely TE-incident plane wave at a fixed angle of incidence and a simple-slab window. In 3D, a dielectric window parallel to a finite-width channel aperture is exposed to a non-planar wave front with both TE and TM components. Curved (not just simple slab) dielectric surfaces are also involved in practical 3D designs. So it is more complicated than in 2D.

[20] If the reactive coupling cannot be neglected, then a new matrix representing the combined coupled stages is required. This new matrix may or may not be straightforward to derive.

4.1.7. E-plane Transitions with Rounded, More HPM-compatible Edges.

If we *round the sharp edge* of the E-plane aperture in Figure 20, we obtain a much more HPM-compatible geometry, but we have not (yet) found equations in the literature for a directly-equivalent circuit. Fortunately, we can build such a model via curve-fitting to predictions from a sufficiently-comprehensive set of numerical models. Figure 32 shows a couple of snapshots from a *single run* (one curvature, one frequency). The full set considered actually spanned a pair of models, the first with 11 radii of curvature (0.0 cm to 5cm, in 0.5cm steps) across 119 frequencies (50 MHz to 3 GHz, in 25 MHz steps), and the second with 10 radii of curvature (5.5 cm to 10cm, in 0.5cm steps) across 59 frequencies (50 MHz to 1.5 GHz, in 25 MHz steps), for a total of 1,899 simulations of unique curvature/frequency pairs.

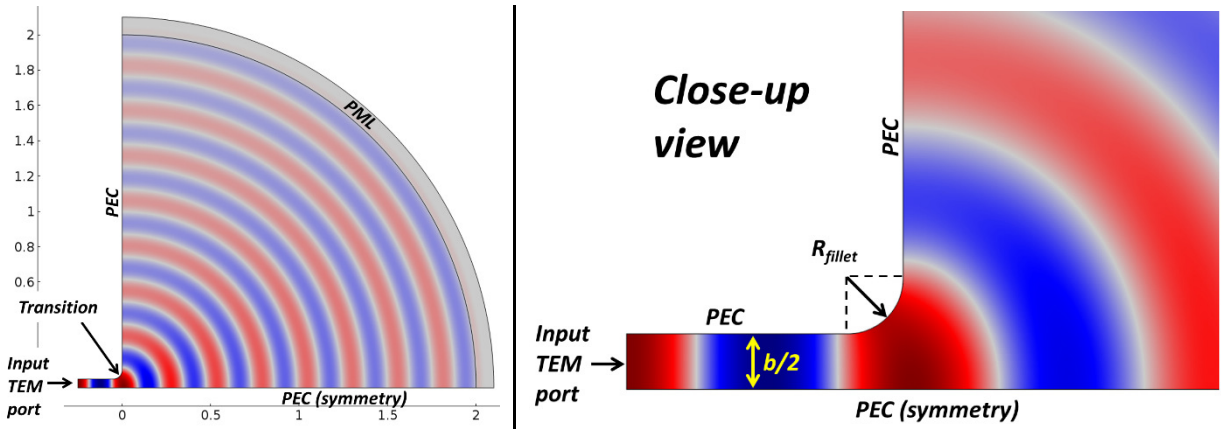


Figure 32. Snapshot from a 2D E-plane model of a channel to free-space transition including a curved edge (input E is vertical.)

Figure 33 shows plots of model-computed real and imaginary parts of the effective extracted Y_A vs. the ratio of plate-separation to wavelength. It is clear that the real part (conductance, G) is only modestly affected by edge-curvature (R_{fillet}), while the reactive component (the susceptance, B) shows a more substantial dependence on it. Based on the left panel of Figure 33, we can see that for narrow enough guides, Marcuvitz's linear approximation for the conductance, $G/Y_0 \approx \pi b/\lambda'$ (for the sharp-edged case) remains applicable here, but we will apply a slightly better approximation shortly.

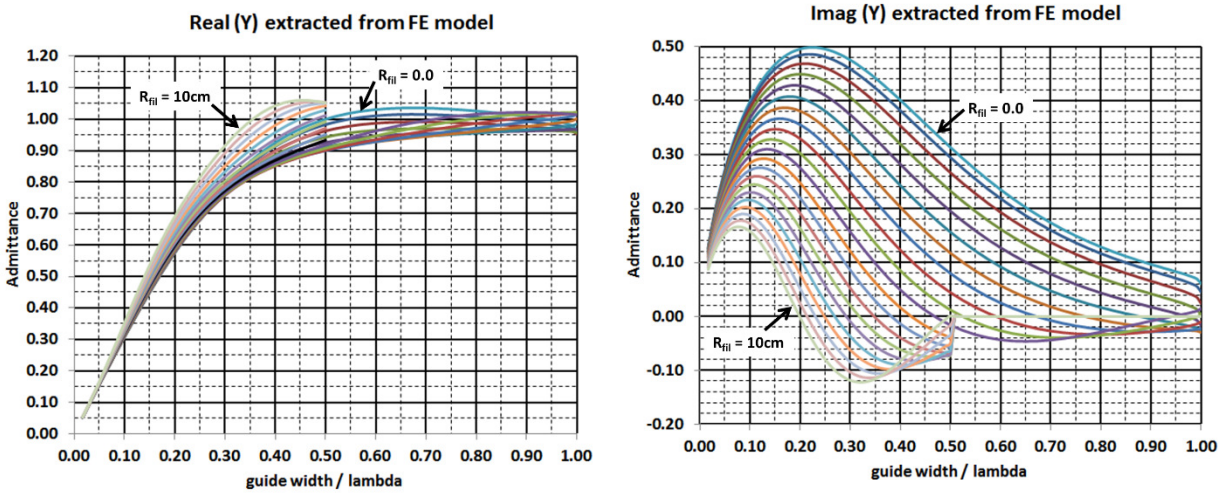


Figure 33. Conductance G (left) and susceptance B (right) parts of Y_A, as extracted from our FE models for a curved-edge, TEM channel to free half-space transition.

We appreciate that Figure 33 may be a bit confusing, since each specific curve plotted corresponds to a particular radius (R_{fil} *not* scaled to λ'). Greater clarity and generality are achieved by representing *all* geometric quantities in terms of wavelengths. This is done for the susceptance (B = imag. part of Y_A) in Figure 34. (The domain spanned consists of two triangular regions when plotted vs. these parameters because the models were stepped linearly in frequency and fillet-radius, holding plate-separation fixed.)

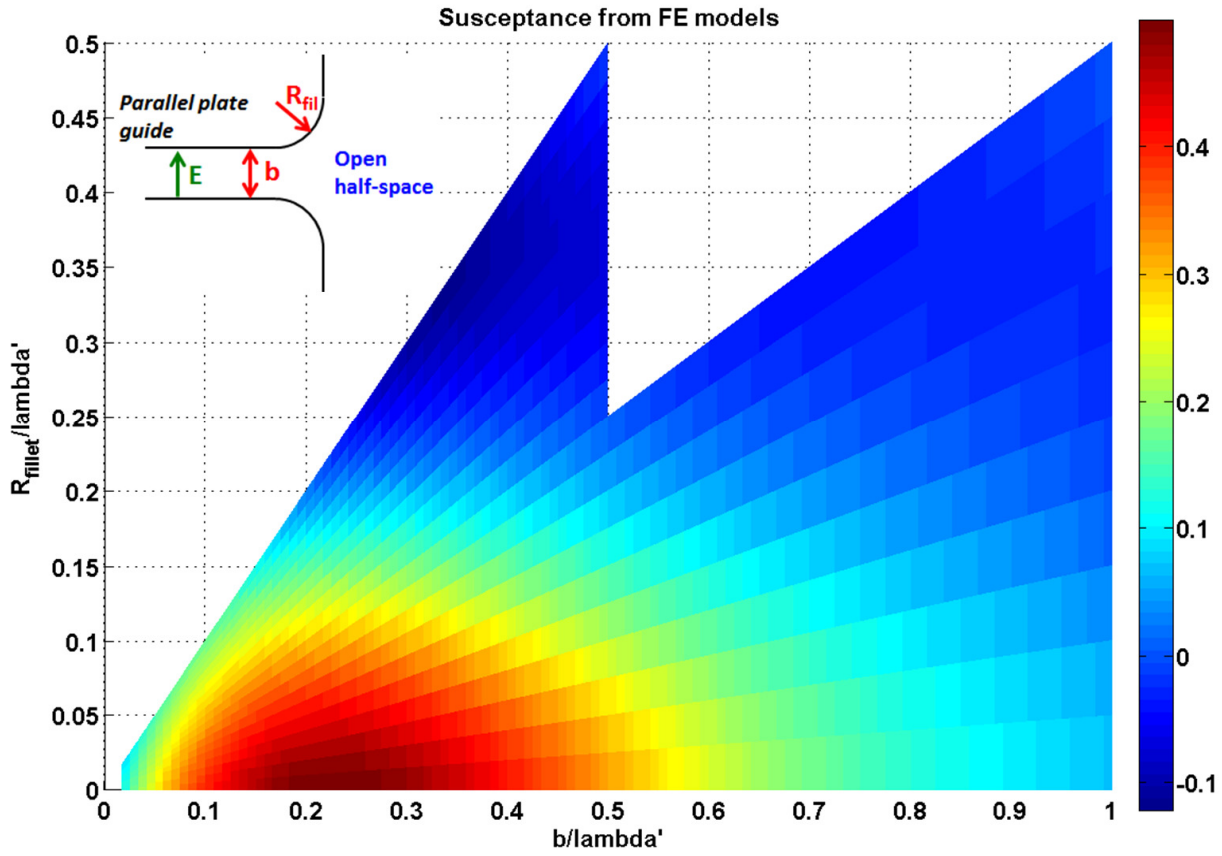


Figure 34. Color-plot of the *FE model-predicted* susceptance vs. both b/λ' and R_{fil}/λ'

Figure 34 helps show B's dependence on wavelength-scaled geometric quantities more-clearly than the right-panel in Figure 33. A reasonably-good fit to Figure 34 is provided by the following[21] expression:

$$\frac{B}{Y_0} \approx 6.2\,\frac{b}{\lambda'}\exp\left(-4.5\,\frac{b}{\lambda'}\right)\left(1-1.4\tanh\frac{3.3R_{fillet}}{\lambda'}\right)$$

A plot of this equation over the *same parametric domain* is shown in Figure 35. We can also improve somewhat upon the linear expression for the conductance (without resorting to Marcuvitz's integral formula) by replacing Marcuvitz's simple $G/Y_0 \approx \pi b/\lambda'$ with a function that more realistically tends toward unity for larger apertures (although we are still ignoring the ~weak dependence of G on R_{fil}/λ'):

$$\frac{G}{Y_0} \approx \tanh\left(\pi\,\frac{b}{\lambda'}+\left(\frac{b}{\lambda'}\right)^2\right)$$

A plot of this expression is given in Figure 36.

[21] If we find later that this is insufficiently-accurate, we may seek a better-fitting expression.

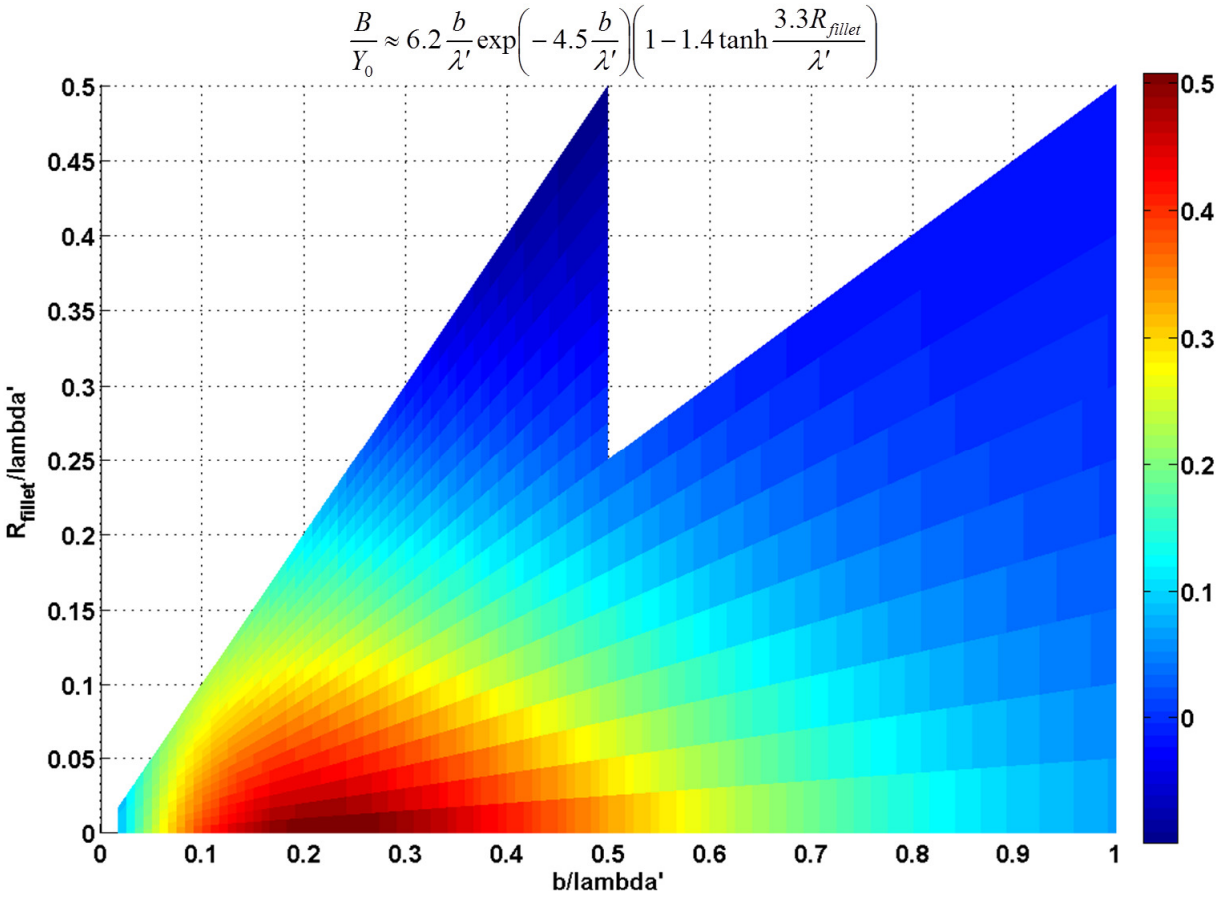


Figure 35. Color-plot of *equation-based approximation* to FE-model data in Figure 34.

In summary, we suggest the following approximate expression for the effective complex admittance at the aperture of a finite-separation, parallel-plate, TEM guide that opens smoothly onto a half-space, with radius of curvature R_{fillet} at the opening edges:

$$\frac{Y_A}{Y_0} \approx \tanh\left(\pi\frac{b}{\lambda'}+\left(\frac{b}{\lambda'}\right)^2\right) + 6.2\,j\frac{b}{\lambda'}\exp\left(-\frac{4.5b}{\lambda'}\right)\left(1-1.4\tanh\frac{3.3R_{fillet}}{\lambda'}\right)$$

As before, our next step is to check this formula, which was derived from wave normal-incidence models, against one or more example 3D apertures with waves at *non-normal* incidence, by (just as before) setting $\lambda' \equiv \lambda/\cos\alpha'$ to compensate.

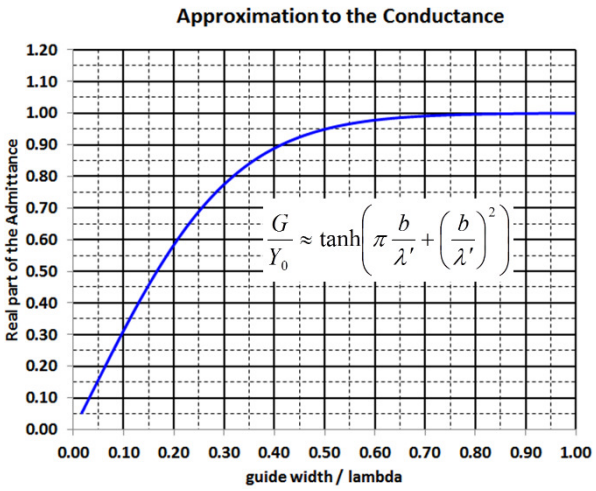
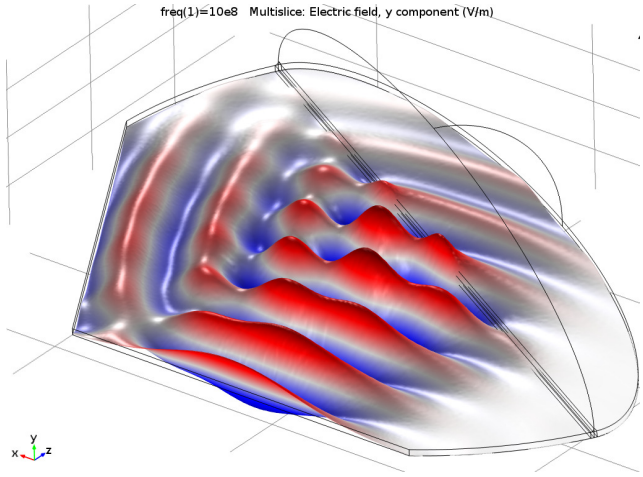


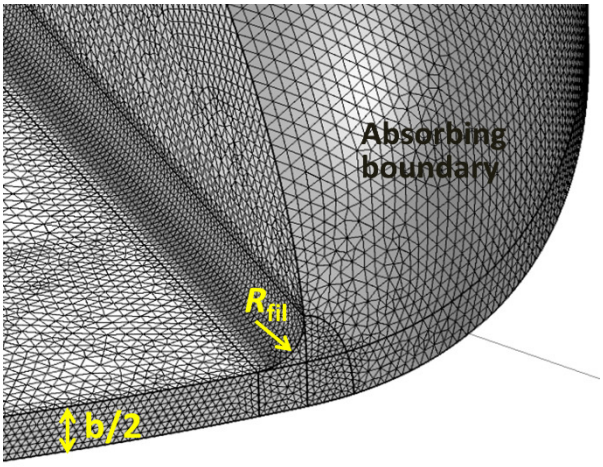
Figure 36. Approx. for the effective conductance term at the aperture, for a finite-width guide (E-plane) at a half-space interface. (Compare to left panel in Figure 33.)

Figure 37 shows the first such test, using a test configuration similar to the one in Figure 25, but with the important difference that we now include a finite-radius transition in the E-plane. The disagreement

between the direct FE-model in Figure 37 and the prediction based on the approximate equation for Y_A above is ~ 0.25dB (~5.6%). To put this in perspective, let's also calculate $|S_{11}|$ assuming a sudden-transition (i.e., $R_{fil} \rightarrow 0$) instead. With the equation for Y_A that we just used, setting $R_{fil} = 0$ yields $|S_{11}| = -7.30$ dB, which differs from the direct FE-model in Figure 37 by ~1.67 dB, or more than 30%. Alternatively, if we used Marcuvitz's narrow-channel sudden-transition formulas (Eqs. 1b and 2b, in Figure 21) to compute Y_A, then we would ultimately get $|S_{11}| = -7.50$ dB, which differs from the direct FE-model in Figure 37 by ~1.47 dB, or more than 28%.



Deformation plot of E_y on the symmetry (PEC) plane



Close-up view, FE mesh near finite-radius transition.

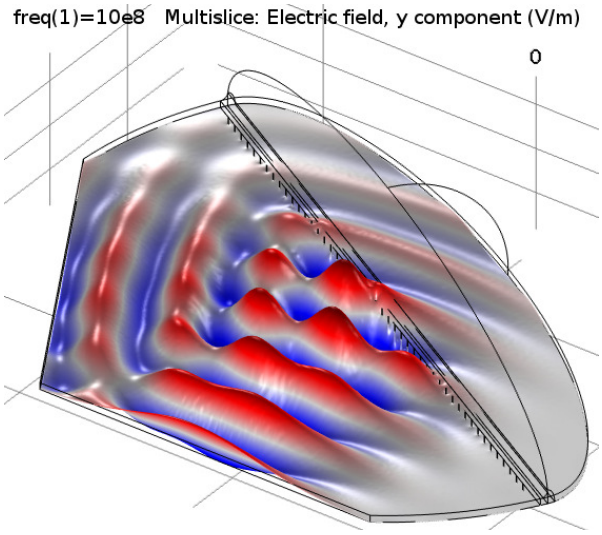
Figure 37. 3D model, E-plane aperture *with finite radius*, R_{fil} = 3.0 cm. Plate separation *b* = 6.0 cm, *f* = 1.0 GHz, and *α'* = 30° rel. to normal. From this FE-model, $|S_{11}|$ = -8.97 dB. A prediction based on our new approx. for Y_A yields: $|S_{11}|$ = -8.72 dB.

Thus, encouraged by our success in accounting for how finite-radius transitions impact the wave reflection process in 3D, let us once again introduce a wire grill analogous to the sudden-transition test cases in Figure 26 and Figure 27, but with a rounded transition (such as in Figure 37) where the channel joins to an open half-space. Our equation for T_{3D0} in Sec. 4.1.6 still applies, but with our new expression for Y_A used to compute $R_A = (1 - Y_A)/(1 + Y_A)$. Of course, a modification to the Matlab function in the

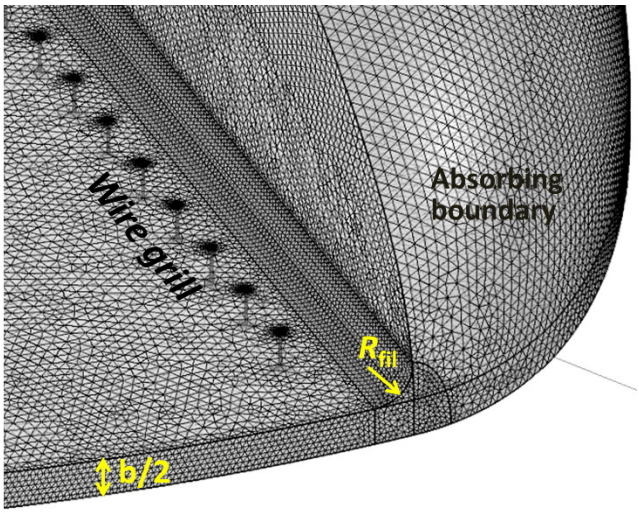
```
function Rpow = myRpowF(AngIn,a,d,hD,w,Rfil,f)
   ct = cos(AngIn);
   st = sin(AngIn);
   c_const = 2.99792458e8; %c in m/s
   lambda = c_const/f; % free space wavelength
   lambdap = lambda/ct; % lambda prime, for aperture Y computations.
   k0 = 2.0*pi*f/c_const; %incident k, free space
   phiV = k0*hD*ct;  % electrical length of grill-to-aperture gap
  % Compute grill Xa and Xb equivalents per Marcuvitz, p. 286.
   sum1 = 0;
   sum2 = 0;
   for m = 1:1:1000
       sum1 = sum1+1/sqrt(m^2+2*m*a*st/lambda-(a*ct/lambda)^2)-1/m;
       sum2 = sum2+1/sqrt(m^2-2*m*a*st/lambda-(a*ct/lambda)^2)-1/m;
   end
   Xa = (a*ct/lambda)*(log(a/(pi*d))+0.5*(sum1+sum2));  % from sum
   Xb = (a*ct/lambda)*(pi*d/a)^2;  % used in either expression
   Tg = 2.0*1i*Xa/((1+1i*(Xa-Xb))^2+Xa^2);
   Rg = (Xa^2-(Xa-Xb)^2-1)/((1+1i*(Xa-Xb))^2+Xa^2);
  % Compute aperture admittance with approx eqs. for radiused transition
   Ga= tanh(pi*w/lambdap +(w/lambdap)^2);
   Ba= 6.2*(w/lambdap)*exp(-4.5*w/lambdap)*(1-1.4*tanh(3.3*Rfil/lambdap));
   Ya = Ga + 1i*Ba;  % Admittance = Conductance + i*Susceptance.
   Ra = (1.0-Ya)/(1.0+Ya);  %Reflection at rounded E-plane aperture
   Ta = sqrt(1.0-abs(Ra)^2); % Effective Ta, Using magnitude-only.
   T3D0 = Tg*Ta/(exp(1i*phiV)-Rg*Ra*exp(-1i*phiV));
   Tpow = abs(T3D0)^2;
   Rpow = 1.0-Tpow;  %Output the local power reflection coefficient.
end
```

Figure 38. Matlab function to compute TEM wave power-reflection coefficient (R_{pow}) for a *wire-grill* across a *fixed-width* channel followed by a short *vacuum-space* and a *rounded transition* to an aperture onto an open half-space.

right-panel of Figure 28 is needed to address R_{fil}. The modified version is shown in Figure 38. Figure 39 and Figure 40 show a couple of examples comparing predicted reflections from an FE-model to those from the wave matrix chain theory embodied in Figure 38.



Deformation plot of E_y on symmetry (PEC) plane



Close-up view, FE mesh near finite-radius transition.

Figure 39. 3D model, wire grill + E-plane aperture *with finite radius,* R_{fil} = 3.0 cm. Plate separation *b* = 6.0 cm, *f* = 1.0 GHz, and α' = 30° rel to normal. Grill wire diams = 2mm. Grill wire spacing = 6cm. Grill is 5cm from aperture. From the FE-model, $|S_{11}|$= -4.19 dB. From the function in Figure 38, $|S_{11}|$= -4.65 dB, for a difference of 0.46 dB or about 11%.

The second example shows considerably better agreement (~3%) between the matrix-chain formalism and the direct FE model than does the first example (~11%). There are limitations to accuracy in these kinds of approximations, when building up the various stages in the wave-matrix chains.

If we assume that the currently-observed level of agreement between the theory and numerical models is sufficient to justify further application, then the next natural step is to apply the above expressions to a single-channel FAWSEA design, in analogy to what we did in Section 4.1.6. Consider a 1.5m long aperture designed for f_0 = 1.3 GHz, a channel width = 5.0 cm, R_{fil} = 2.0 cm, and a preferred wire spacing = 4.5 cm. After modifying our wire-generating script to call the new function in Figure 38 and to include the variable R_{fil}, we can (as we have before) compute a set of

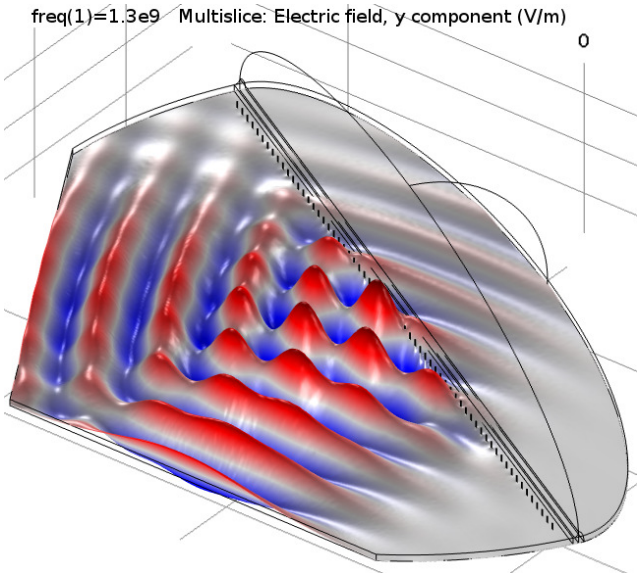


Figure 40. 3D model, wire grill + E-plane aperture *with finite radius,* R_{fil} = 2.0 cm. Plate separation *b* = 5.0 cm, *f* = 1.3 GHz, and α' = 30° rel. to normal. Grill wire diams = 3.0mm. Grill wire spacing = 4.5cm. Grill 5cm from aperture. FE-model→ $|S_{11}|$ = -1.75dB. Function in Figure 38 → $|S_{11}|$ = -1.87 dB, a difference of 0.12 dB, or about 3%.

"optimal" wire diameters intended to yield a uniform (in absolute, not relative terms) leak-rate. That set is plotted in Figure 41. (In this case, all of the wire diameters generated are large enough to be reasonably included in the design.)

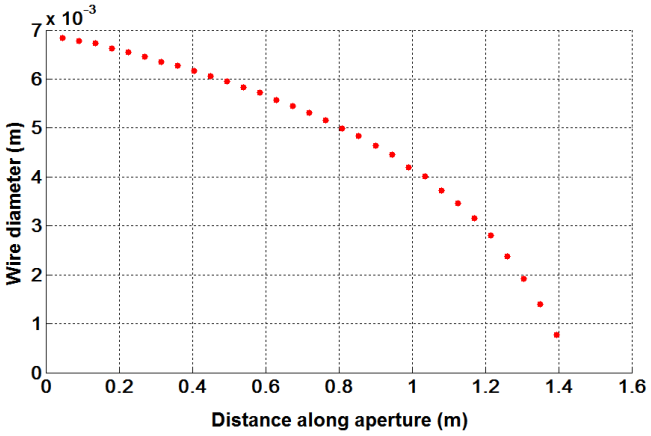
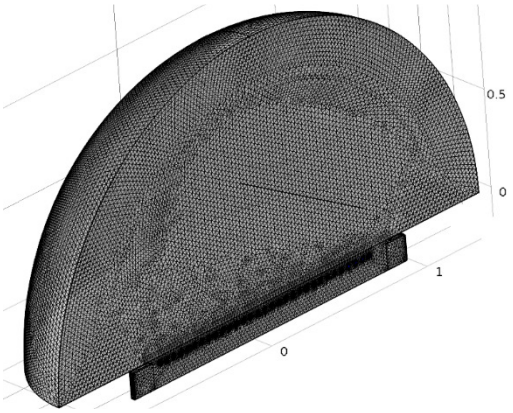


Figure 41. Computed wire diameters vs. position for 3D single-channel 1.5m-long FAWSEA with a flared aperture but no window. See text for more info.

The resulting design could still benefit from some adjustment to the back wall to account for the not quite constant phase velocity in the guide (to be discussed further, shortly). In this example, about 98.4% of the net input power is radiated, with 1.6% absorbed at the termination[22]. See Figure 42. The resulting main beam *direction* is not quite right, again due to our oversimplifying the phase velocity. However, with a mere 2.2% increase to the overall channel depth, and with no change to the wire grill at all, we can shift the beam direction back to ~30°, per our original intent (see Figure 43).



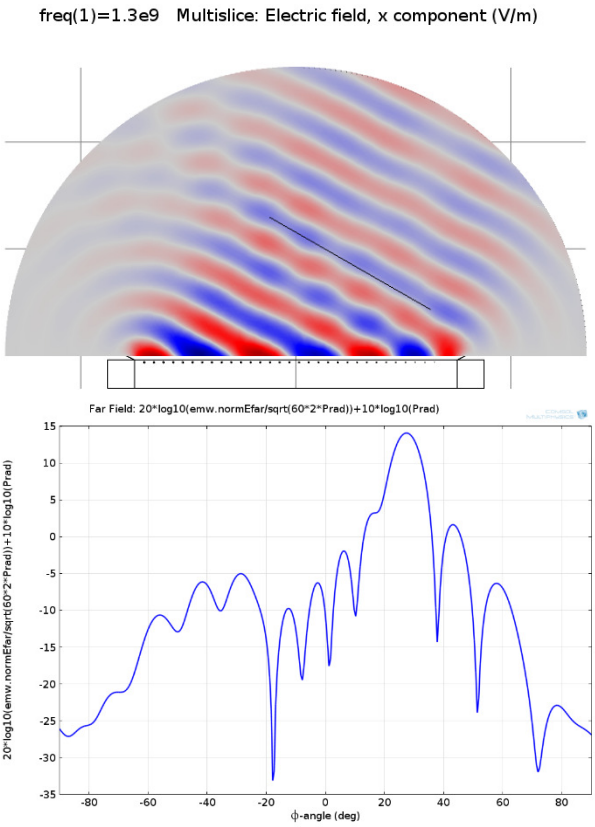


Figure 42. 3D single-channel FAWSEA model for f_0=1.3 GHz, with length =1.5m, chan. width =5cm, R_{fil} = 2cm, and wire-grill based on 3D analyses. No window.

- **Top left: Finite-element mesh used.**
- **Top right: Slice of E_x, above aperture.**
- **Right: Predicted H-plane antenna pattern at 1.3 GHz. Predicted H-plane beamwidth is 9.04°**
- **Beam points ~27.5° (≠ desired 30°).**

[22] In practical HPM FAWSEA designs, we recommend that the termination be a *conducting wall*, not an absorber. This allows the small fraction of power arriving there to simply be reflected and re-radiated as a minor back/side-lobe. This choices also makes for a simpler, more compact, and overall more reliable design.

Comments: More work is needed to improve upon the rough circuit equivalents/admittance expressions given above. In addition, some modification of the design rules presented so far to account for the modified phase velocity of waves in the leaky guides is appropriate. The latter is addressed in Section 4.1.9. Inclusion of dielectric windows into the 3D wave-matrix formalism, even if only approximate, is desirable for the rapid analyses and design of these antennas. But for now, let us discuss another important consideration in leaky-wave HPM antenna design: the effects of unwanted coupling (aka, mutual coupling) between neighboring leaky-wave channels.

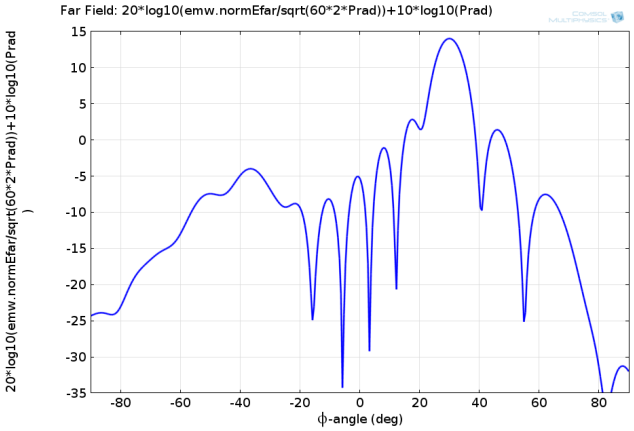


Figure 43. Predicted H-plane antenna pattern after increasing channel depth of model in Figure 42 by 2.2%. The beam now points at 30.0° and the beamwidth = 9.01°.

4.1.8. Mutual Coupling

When two leaky-wave channels are placed in proximity, undesirable coupling between them can cause degradations in antenna performance[23]. Consider the mid-channel field slices in Figure 44. The model shown has two channels, each identical to the channel used earlier to compute Figure 43. In this example, only one channel is driven, but we can see easily that the adjacent channel intercepts some[24] of the power.

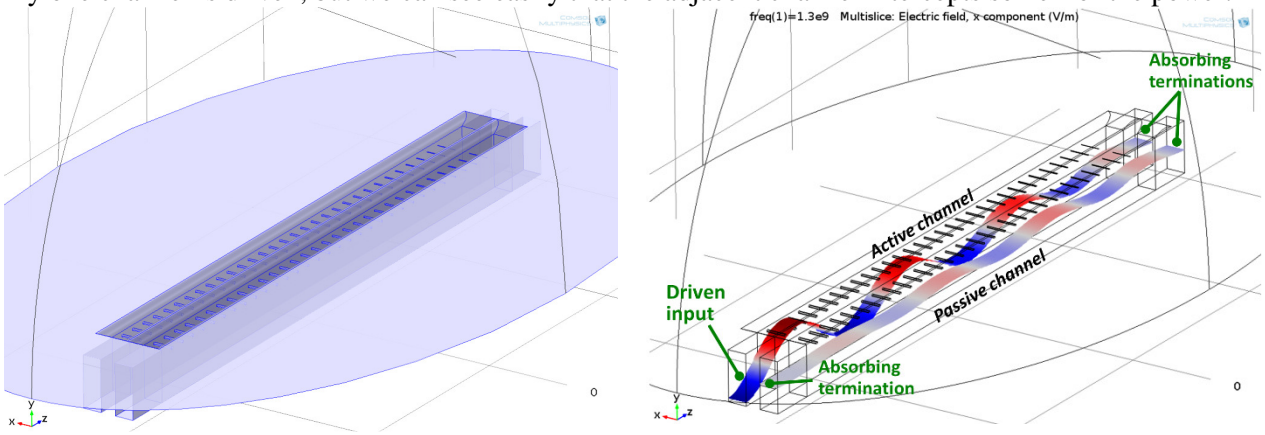


Figure 44. Mutual coupling between two adjacent channels in a leaky-wave antenna. Left: Model geometry. Channel separation (center to center) is 9.0 cm. No window. Right: Mid-channel field-slice at 1.3 GHz (with deformation-style plot to enhance clarity) reveals non-zero coupling from an excited channel to a neighboring passive channel.

As a result of mutual coupling, two channels placed closely together may behave a bit differently than a single isolated channel. This can impact VSWR and the predicted patterns, including gain and beam tilt angle, when compared to that expected from models without any mutual coupling. However, due to symmetry, a pair of identically-driven identical channels will remain locked in phase. So, with some iteration using 3D numerical models if necessary, the performance characteristics of a pair of channels can be re-optimized by adjusting geometric parameters (e.g. the wire sizes and/or spacings).

[23] This concern is not confined to multi-channel *leaky-wave* antennas. A search for the combination of "mutual coupling" and "antenna" among *titles* (not just keywords) of articles in IEEE journals finds hundreds of papers.
[24] In this example, about 2.7% of the power leaving the left channel is captured by the right channel.

In contrast, when *more than two* channels are operated together, the resulting mutual couplings are *not* all identical, so otherwise-identical channels can behave differently, depending on their relative positions. This can sometimes introduce more serious amplitude and phase differences between channels. Fortunately, for channelized apertures that are *neither too closely-packed nor too long*, the undesirable effects of mutual coupling can be controlled. For example, Figure 45 shows five parallel channels, each of the same type as in Figure 44, all driven identically. Despite the differences in mutual coupling seen by the edge vs interior channels, phases and amplitudes remain reasonably well-matched between all 5 channels.

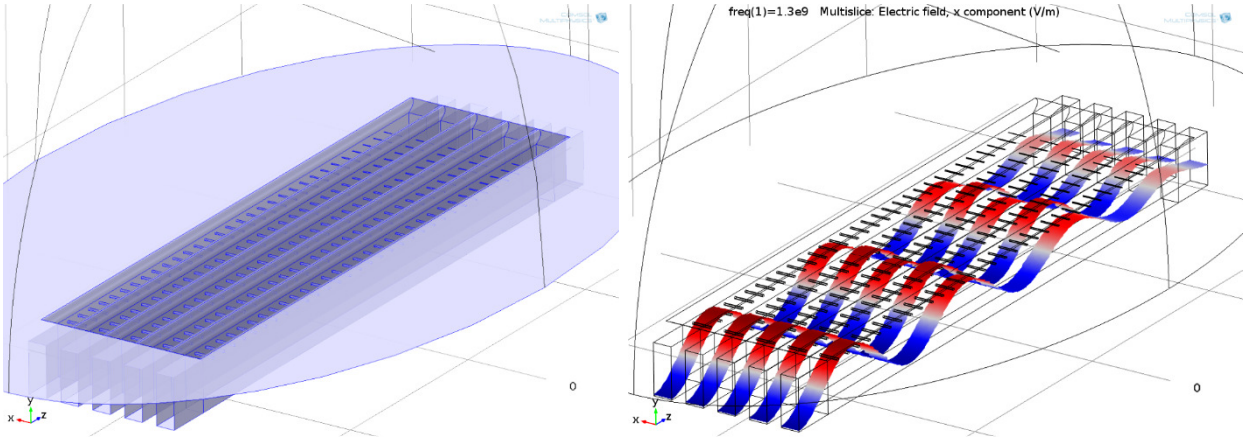


Figure 45. Examining mutual coupling, five neighboring channels *driven identically.*
Left: Model geometry. Channel separation (center-to-center) is 9.0 cm. No window.
Right: Impacts due to mutual-coupling are small[25] in this case; insufficient to generate serious phase or amplitude imbalance, large reflections, or pattern degradations.

Theoretical treatments of mutual coupling between two straight, parallel, infinitely-long, leaky-wave channels with simple constant-width[26] narrow-wall slits are provided by S. Nishida for channels with apertures conformal to a flat ground plane (Nishida, May 1960) or along a cylinder (Nishida, July, 1960). In those papers, Nishida both cited and leveraged the transverse network resonance method and circuit-equivalent admittances tabulated previously (Goldstone and Oliner, 1959 and 1961). Much the same formalism was applied by N. Marcuvitz, R.C. Honey, and others analyzing reflections and transmissions at various leaky-wave interfaces. In principle, Nishida's mutual-coupling analyses should be extensible to *all* FAWSEA-family antennas, provided that appropriate *replacements* for the aforementioned circuit-equivalent admittances of long *constant-width* slots can be established, properly including the leaky wire-grills and dielectric windows. And of course, one would also like the resulting theory to be extensible to more than two parallel channels. For now, we employ a combination of numerical and analytic methods.

It would, of course, be very helpful if the design of forward-traveling leaky-wave HPM-capable antennas could proceed without consideration of the effects of mutual coupling between channels. However, such effects can and do have significant impact on resulting performance, leading to increased design time, uncertainty, and constraints on design choices. Mutual coupling has long received attention in the literature (Oliner and Malech, 1985), but the subject remains theoretically challenging, although simple parallel dipole elements have been analyzed theoretically in much detail. The papers by Nishida are perhaps most relevant to our own work, but do not include essential geometric features (such as rounded edges or dielectric windows) required for HPM-capable designs. In analogy to the numerical study investigating the impact of rounded edges in the E-plane that we described earlier, we performed another

[25] Variations in field magnitudes between channels reach up to about +/-13% in the latter 3rd of the structure.
[26] For a single channel, this yields the classic exponential power loss (constant α) vs. length, which is convenient for analyses but does not optimize gain or peak-power handling.

2D FE-based numerical study, to investigate mutual coupling between radiating openings with rounded (aka, filleted) edges. This study investigated the dependence of mutual coupling on channel separations, choice of fillet radius at the channel openings, and frequency. Figure 46 and Figure 47 summarize the setup of the 2D model.

Parameter	Range	# of cases	
Chan. width:	Fixed at 5.0 cm	1	
R_{fil}:	From 1.0 to 10.0 cm, in 1.0 cm steps	10	→ 100 geometries
Gap:	From 1.0 to 10.0 cm, in 1.0 cm steps	10	
Frequency:	50 to 200 MHz in 25 MHz steps, *plus*	33	
	250 to 1500 MHz in 50 MHz steps	→ 3,300 2D-model runs	

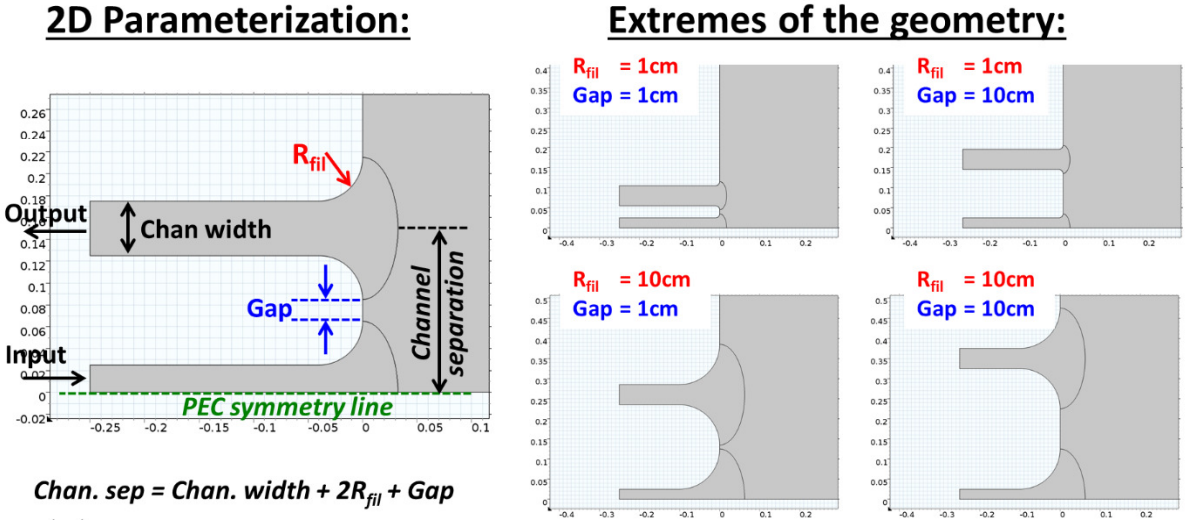


Figure 46. Parameter definitions in 2D E-plane TEM-wave mutual-coupling study.

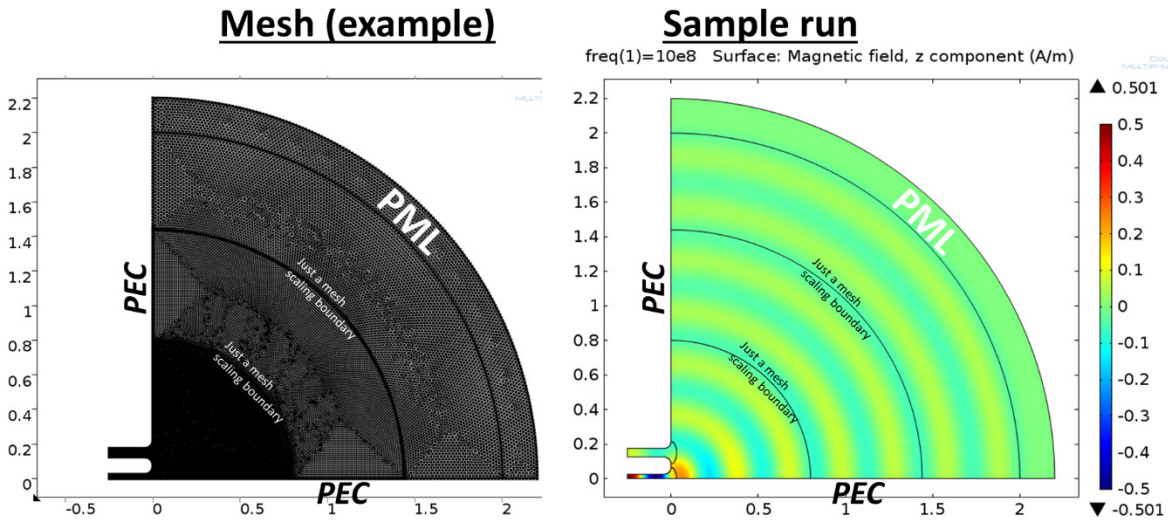
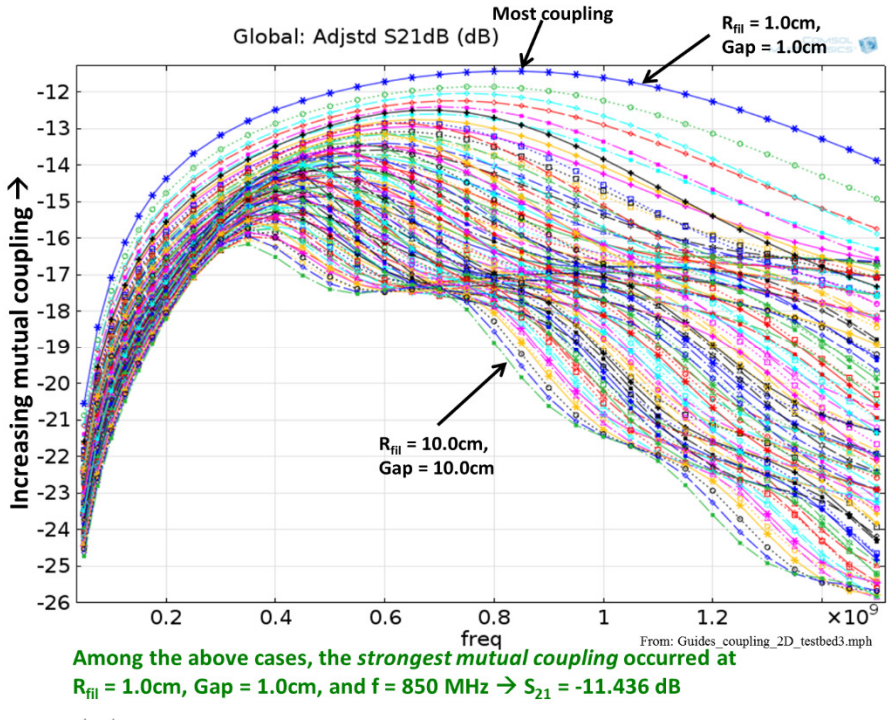


Figure 47. Computation space in 2D E-plane TEM-wave mutual-coupling study.

Intermediate boundaries to gently scale the mesh and a perfectly matched layer (PML) outer boundary were incorporated to improve speed and accuracy, respectively. One hundred geometries were considered at 33 frequency values, for a total of 3,300 runs. A plot showing all 3,330 "raw" values of the

computed magnitude of S_{21} is provided in Figure 48, while projections of these values against some parameters of interest are shown in Figure 49. The closest to a "single-parameter" dependence of S_{21}(dB) is seen for the channel separation/wavelength.



- As expected, strongest mutual coupling occurs when the channels are closest together; weakest coupling when they are farthest apart.
- Coupling becomes *weak at very low frequencies* due to the unavoidably poor impedance match of each channel to its own aperture.
- Coupling also *weakens at sufficiently high frequencies* due to greater *effective* channel separation, rel. to λ.
- Ripples in coupling curves vs. freq are seen in the vicinity of channel separations ~ nλ/2.

Figure 48. Computed S_{21} (dB) vs. frequency (all 3,300 cases)

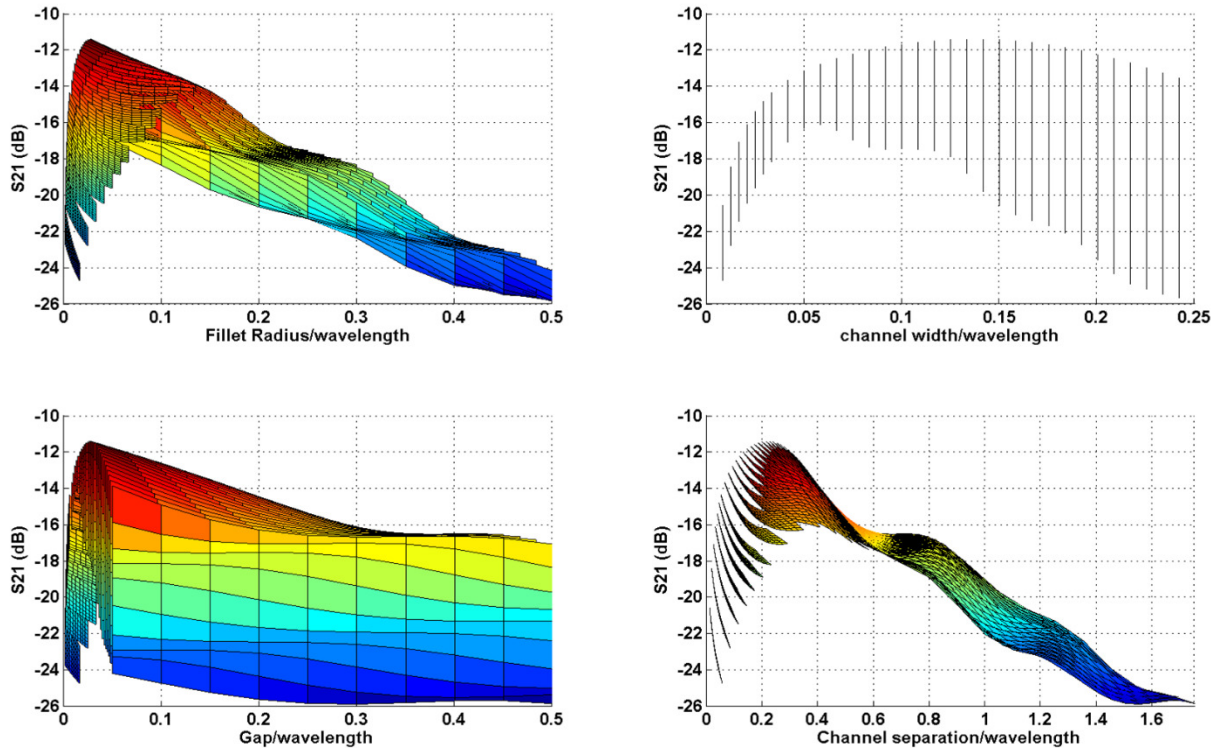


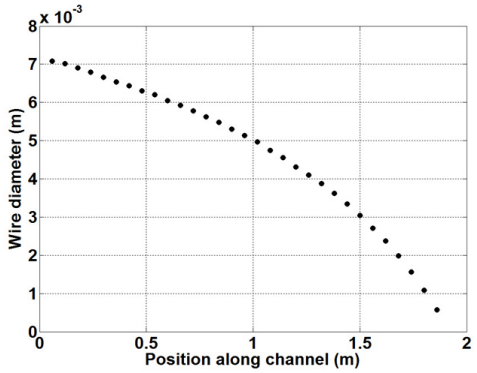
Figure 49. Projections of values in Figure 48 vs. key parameters scaled by wavelength.

Application to 3D

To better understand the implications of the 2D model in a 3D context, we pursued the *following approach* with the help of 3D models:

- Based on the 2D analyses, consider a 3D FAWSEA design likely to exhibit strong mutual coupling, so that any problematic effects of mutual coupling will be easy to observe.
- In particular, noting the highest value of S_{21}(dB) in Figure 48, consider a FAWSEA with f_{TEM} = 850 MHz, with R_{fil} = 1.0cm, Gap = 1.0cm, and channel width = 5cm (yields channel spacing = 8cm).
- Choose the frequency in the 3D model to account for the tilted-wave incidence (vs. normal incidence in the 2D TEM model). I.e., $\lambda_{adj} = \lambda' \cos(\phi_{in})$, where λ' comes from the 2D-model's f_{TEM}=850 MHz. If we choose $\phi_{in} = 30^o$ (a typical value, as noted previously), we obtain f_{3D} = 981.5 MHz.
- Apply the 3D FAWSEA design algorithms & scripts from our previous work, but without a dielectric window (for simplicity), to set the diameters of the grill wires.
- Compare single-channel vs. three-channel 3D configurations, the latter variously with:
  (a) all three channels driven,
  (b) only a single side-channel driven, and
  (c) only the center channel driven.

We selected the following as 3D FAWSEA design parameters (i.e., the *inputs* to our FAWSEA design tools/scripts) : $f_{operating}$ = 981.5 MHz, $\phi_{in} = 30^o$, chan. length = 2.0 m, chan. width = 5.0 cm, R_{fil} = 1 cm, Gap = 1 cm (→ chan. separation = 8 cm), and a constant grill-wire spacing = 6cm. Figure 50 shows the computed wire diameters:



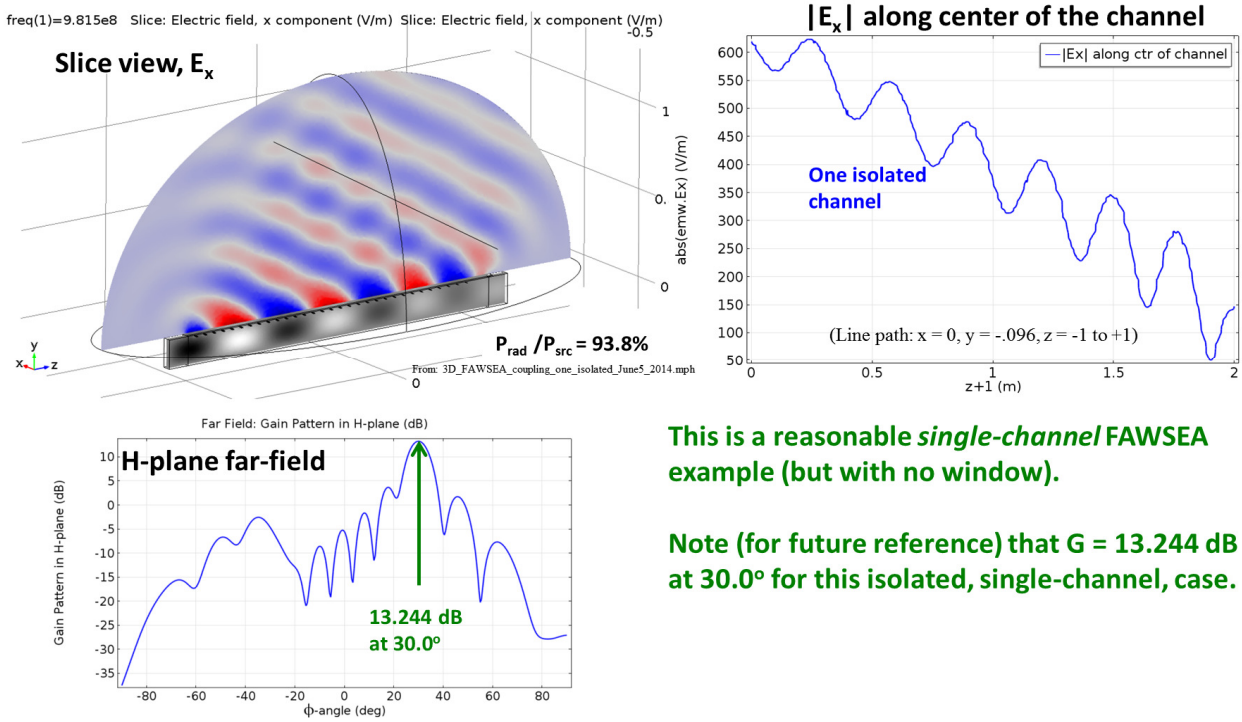
Position	Diameter	Position	Diameter (cont.)
0.06	0.00708204	0.96	0.00513925
0.12	0.00701018	1.02	0.00496521
0.18	0.00690004	1.08	0.00475043
0.24	0.00679323	1.14	0.00455415
0.3	0.0066613	1.2	0.00431537
0.36	0.00654014	1.26	0.00410282
0.42	0.00643618	1.32	0.00387251
0.48	0.00630619	1.38	0.00361951
0.54	0.00620094	1.44	0.00334765
0.6	0.00604983	1.5	0.00303933
0.66	0.00591977	1.56	0.0027051
0.72	0.00577664	1.62	0.00237408
0.78	0.00562465	1.68	0.00198597
0.84	0.00547871	1.74	0.00156414
0.9	0.00530538	1.8	0.00108827
		1.86	0.000577093

*Applied routines: *fawsea_script_3D0_radiused.m* with *myRpowF.m*

With channel depth (initial) = 0.17634777 m.
(Reduced by 2.25% later, to yield clean 30° beam tilt.)

Figure 50. Computed wire diameters vs position for the 3D FAWSEA (with no window) selected for initial use in our mutual-coupling study.

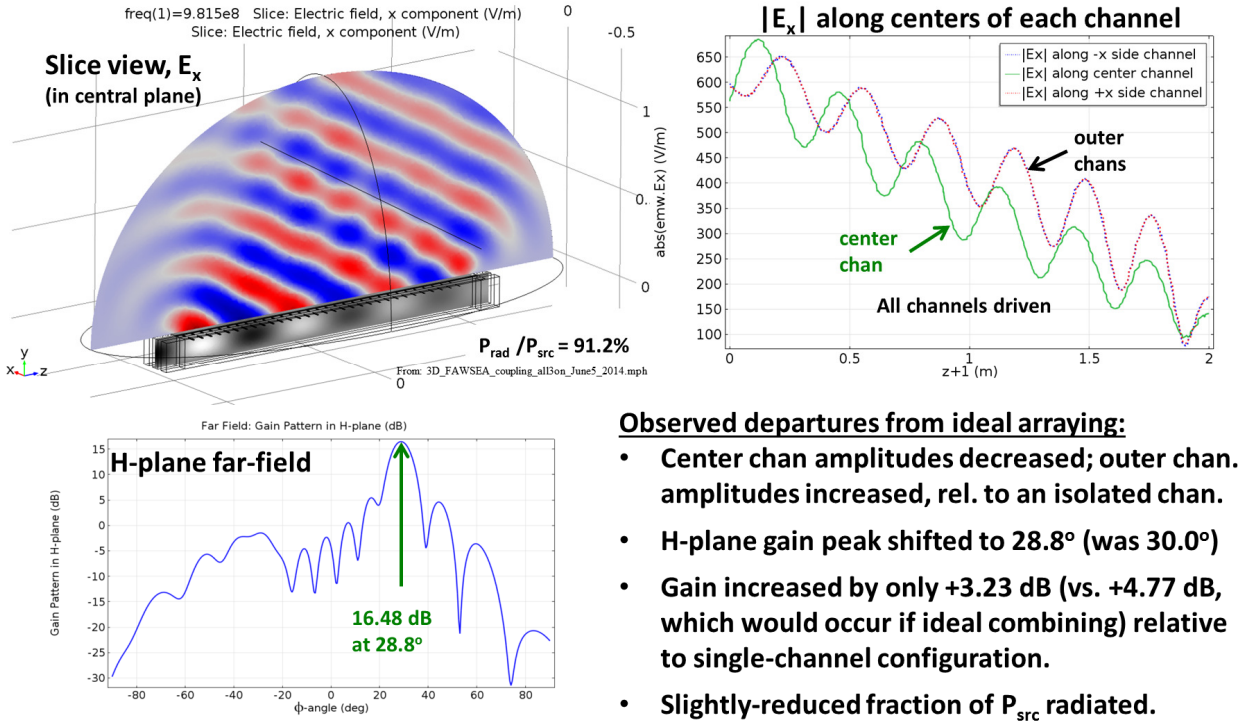
Figure 51 shows a 3D model of a single-channel version of this antenna, including an absorbing termination[22]. Adding two closely-adjacent channels yields the model/results shown in Figure 52. If there was no interaction between the channels, we would expect the gain to increase by $10*\log_{10}(3)$ = 4.77dB. But instead, we find the gain has increased by only 3.23dB, the H-plane peak direction has shifted to 28.8° instead of 30°, and a slightly smaller fraction of the source power is actually being radiated. Thus, mutual coupling in this example has had a deleterious effect.



This is a reasonable *single-channel* FAWSEA example (but with no window).

Note (for future reference) that G = 13.244 dB at 30.0° for this isolated, single-channel, case.

Figure 51. Case of one isolated 3D FAWSEA channel (opening onto a conducting plane).



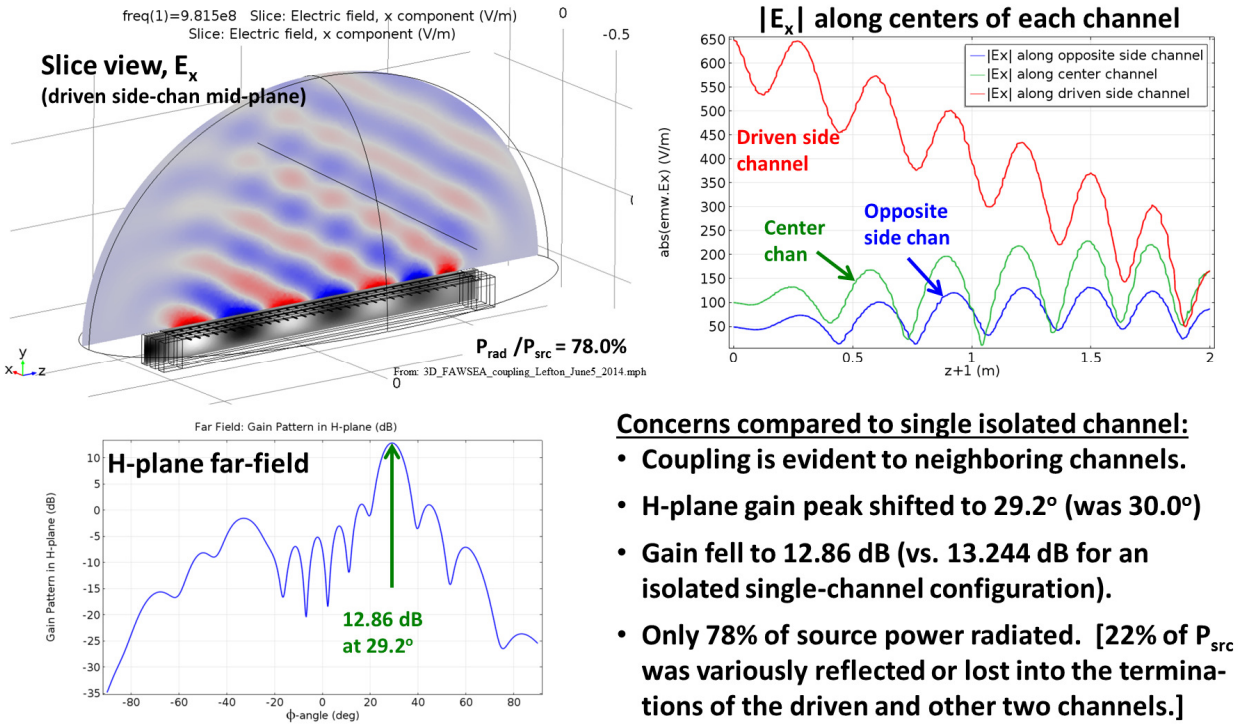
Observed departures from ideal arraying:

- **Center chan amplitudes decreased; outer chan. amplitudes increased, rel. to an isolated chan.**
- **H-plane gain peak shifted to 28.8° (was 30.0°)**
- **Gain increased by only +3.23 dB (vs. +4.77 dB, which would occur if ideal combining) relative to single-channel configuration.**
- **Slightly-reduced fraction of P_{src} radiated.**

Figure 52. Three tightly-spaced channels, all driven. (Channel spacing = 8 cm)

One perspective by which we can partially understand the reduction in gain is as follows: First, recall that the single isolated channel exhibited gain = 13.244 dB (G_N = 21.106). If we associate this with an effective area, we obtain $A_{eff} = G_N \lambda^2 / 4\pi$ = 15.67 cm^2. Since the channel is 2m long, this implies an

effective width W_{eff} = 7.835 cm. However, that ignores the efficiency factor associated with the beam tilt angle. And if we include that term, the effective *length* is reduced to 2m*cos(30°) and the effective width is *increased* to W_{eff} = 9.047 cm. This width is *larger* than the spacing between the channels in the model of Figure 52. So it makes sense that this three-channel configuration is just too closely-packed, i.e., there is insufficient aperture area available (at least, for the middle channel) to deliver the full array gain. Further understanding follows from the models in Figure 53 and Figure 54, which explore the behavior when only a side-channel is driven and when only the center-channel is driven, respectively. From Figure 53, we see that the presence of the two other channels has a moderate impact on the performance of the driven side-channel (e.g., the gain falls to 12.86 dB). But if just the center channel is driven (Figure 54), the channels immediately on either side impact it severely, with the gain falling to 9.04 dB.

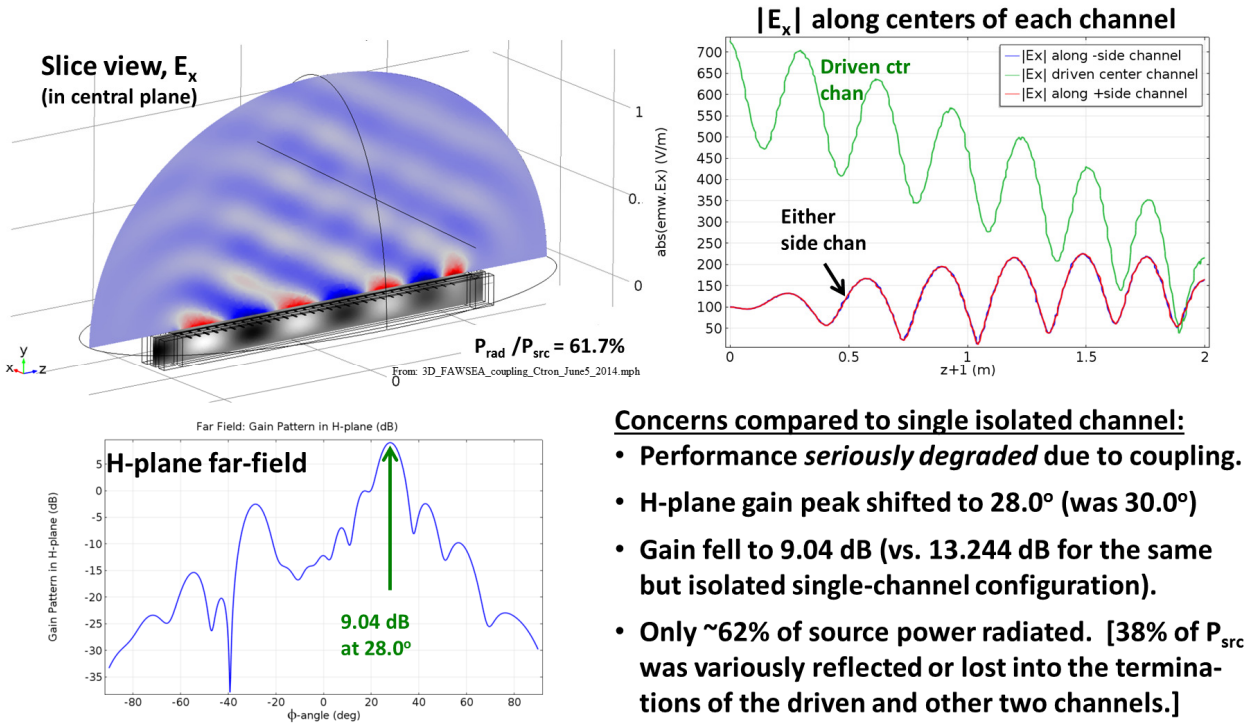


Concerns compared to single isolated channel:

- **Coupling is evident to neighboring channels.**
- **H-plane gain peak shifted to 29.2° (was 30.0°)**
- **Gain fell to 12.86 dB (vs. 13.244 dB for an isolated single-channel configuration).**
- **Only 78% of source power radiated. [22% of P_{src} was variously reflected or lost into the terminations of the driven and other two channels.]**

Figure 53. Three tightly-spaced channels, one side-channel driven. Chan. spacing 8 cm.

To help clarify what to do, Figure 55 revisits some of the curves from Figure 48, highlighting a few of the R_{fil} = 1.0 cm cases with different gaps. Increasing the gap from 1cm to 3cm (which means the channel separation increases from 8cm to 10cm) should reduce the mutual coupling by ~1dB. Is that enough? No. Figure 56 repeats the calculation in Figure 54, but for this modestly-increased spacing. A collapse in gain for the center channel is still there, albeit less dramatic. Clearly, the channels are still too close together. Figure 57 shows the same calculation for a channel-to-channel array spacing of 12cm and Figure 58 shows it for a 14cm spacing. This last case might actually seems pretty good at first look, since the gain of the center channel is very nearly that of the isolated channel case. But a 14cm spacing is well in excess of the "effective width" mentioned earlier, a fact which would *seem* to suggest that the array of three channels, if all operated together, would not produce an appealingly aperture-efficient configuration. But that hypothesis is mistaken, as shown in the model in Figure 59. The gain rises to 18.72 dB! Recall that the *non-interacting* combination of three 100%-isolated channels of this type should have increased to 13.244 dB + $10\log_{10}(3)$ = 18.015 dB. So, where did the *extra* +0.7 dB come from? (continued →)



Concerns compared to single isolated channel:

- **Performance *seriously degraded* due to coupling.**
- **H-plane gain peak shifted to 28.0° (was 30.0°)**
- **Gain fell to 9.04 dB (vs. 13.244 dB for the same but isolated single-channel configuration).**
- **Only ~62% of source power radiated. [38% of P_{src} was variously reflected or lost into the terminations of the driven and other two channels.]**

Figure 54. Three tightly-spaced channels, center-channel driven. Chan. spacing: 8 cm.

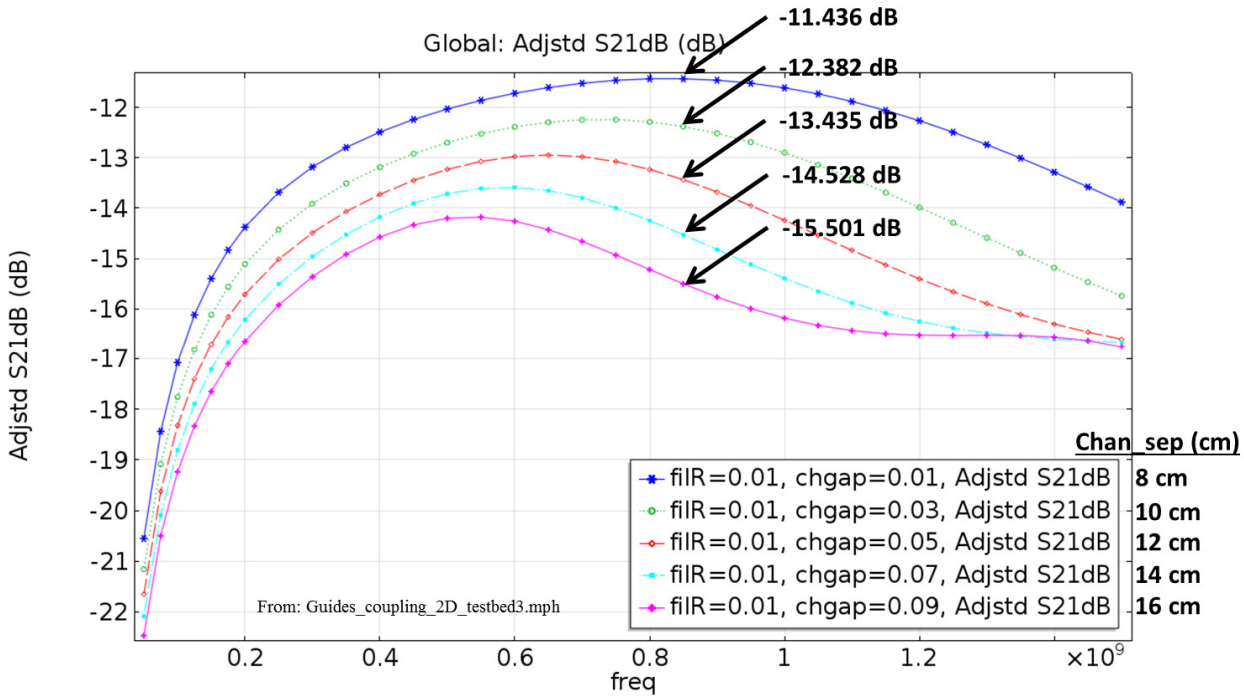
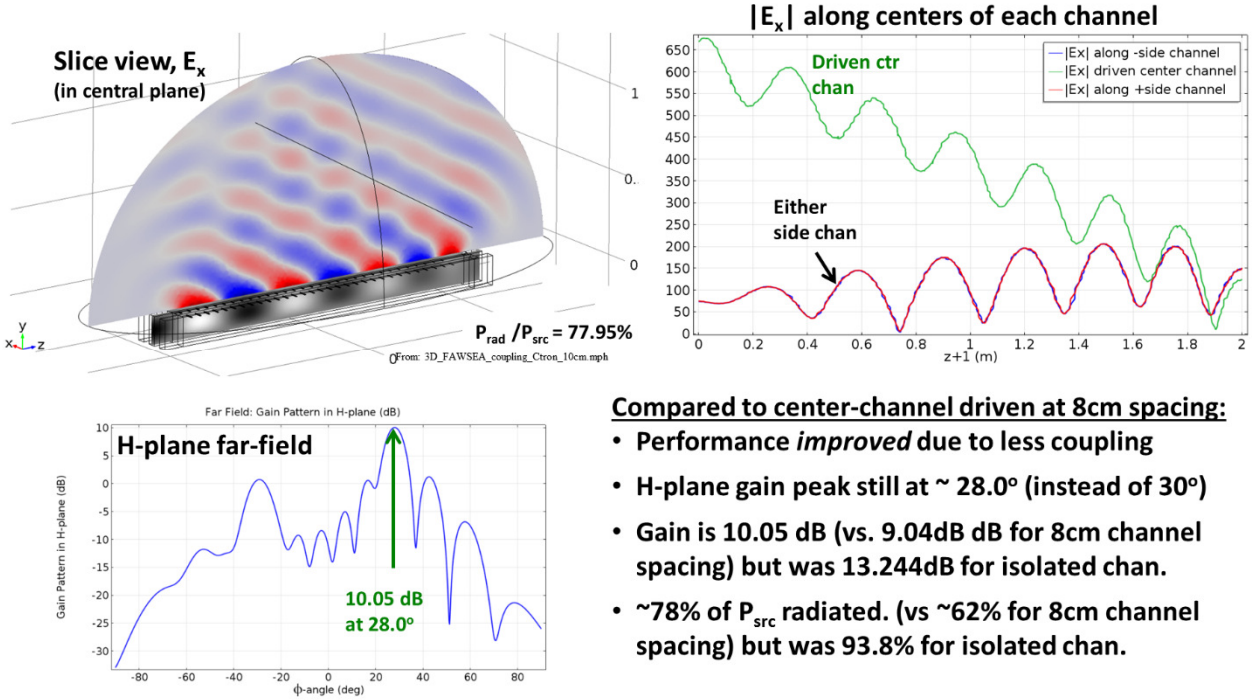


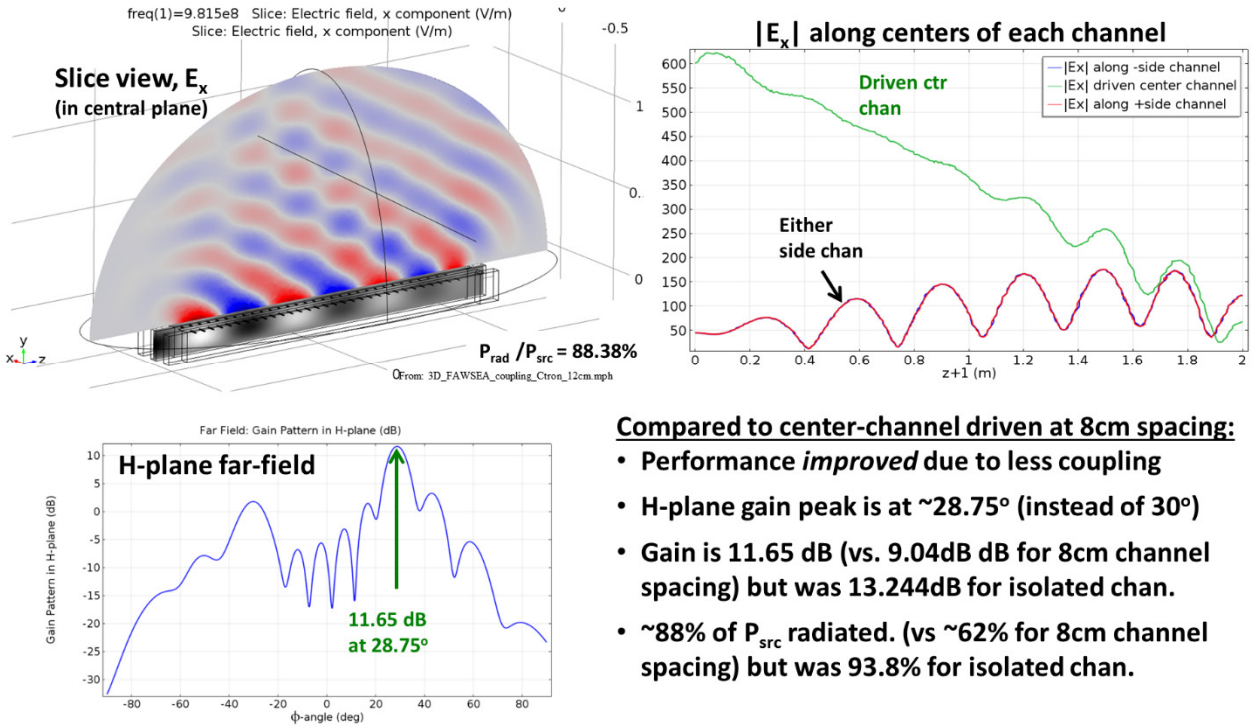
Figure 55. Selected curves from Figure 48, showing falling S_{21} as chan. separation rises.



Compared to center-channel driven at 8cm spacing:

- **Performance *improved* due to less coupling**
- **H-plane gain peak still at ~ 28.0° (instead of 30°)**
- **Gain is 10.05 dB (vs. 9.04dB dB for 8cm channel spacing) but was 13.244dB for isolated chan.**
- **~78% of P_{src} radiated. (vs ~62% for 8cm channel spacing) but was 93.8% for isolated chan.**

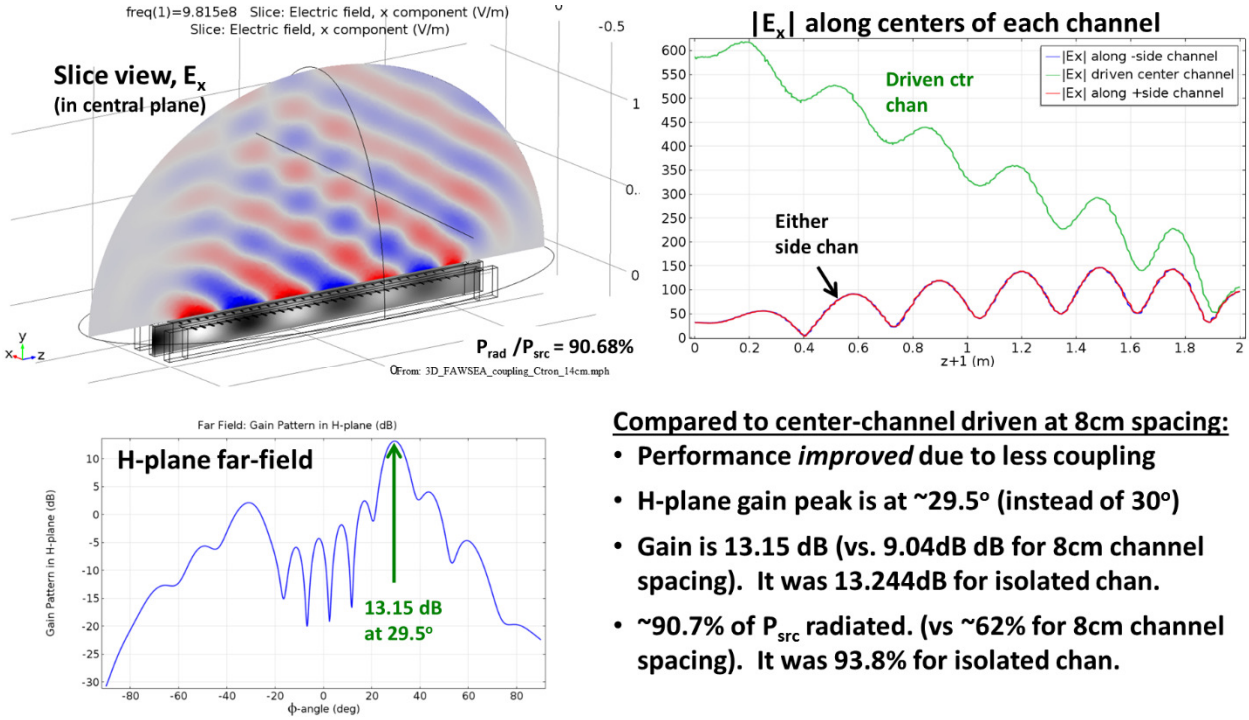
Figure 56. Three channels, with only center-channel driven. Chan. spacing = 10 cm.



Compared to center-channel driven at 8cm spacing:

- **Performance *improved* due to less coupling**
- **H-plane gain peak is at ~28.75° (instead of 30°)**
- **Gain is 11.65 dB (vs. 9.04dB dB for 8cm channel spacing) but was 13.244dB for isolated chan.**
- **~88% of P_{src} radiated. (vs ~62% for 8cm channel spacing) but was 93.8% for isolated chan.**

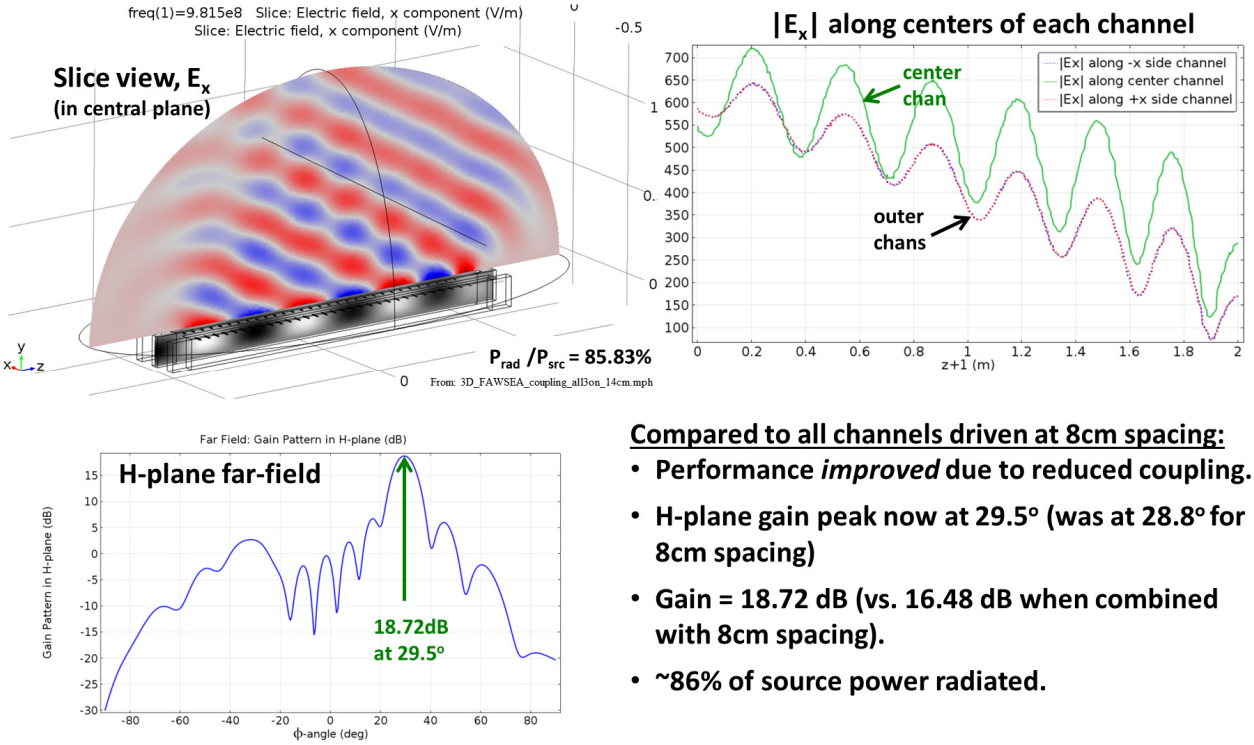
Figure 57. Three channels, with only center-channel driven. Chan. spacing = 12 cm.



Compared to center-channel driven at 8cm spacing:

- **Performance *improved* due to less coupling**
- **H-plane gain peak is at ~29.5° (instead of 30°)**
- **Gain is 13.15 dB (vs. 9.04dB dB for 8cm channel spacing). It was 13.244dB for isolated chan.**
- **~90.7% of P_{src} radiated. (vs ~62% for 8cm channel spacing). It was 93.8% for isolated chan.**

Figure 58. Three channels, with only center-channel driven. Chan. spacing = 14 cm.



Compared to all channels driven at 8cm spacing:

- **Performance *improved* due to reduced coupling.**
- **H-plane gain peak now at 29.5° (was at 28.8° for 8cm spacing)**
- **Gain = 18.72 dB (vs. 16.48 dB when combined with 8cm spacing).**
- **~86% of source power radiated.**

Figure 59. Three channels, all driven. Channel spacing = 14 cm.

The answer is that as we increased the channel-to-channel spacing (and as we observed the center channel gain increasing) the gains associated with the side channels were actually increasing faster, and actually *exceeded* that of the isolated-channel case. In other words, the mutual coupling of each *side channel* to the other two channels *enhanced* the gain. Though initially surprising, this behavior is hardly without precedent in antenna-arrays; it is due to constructive interference from parasitic channels – analogous to the sort of behavior used to advantage in Yagi-Uda antennas, for example. Figure 60 reveals this effect further by modeling the case where the spacing is once again 14cm, but only one side-channel is driven. The gain of this side channel (in interaction with the two parasitic channels off to one side) is 14.4dB, which is about 1.16dB *more* than that from a single channel alone.

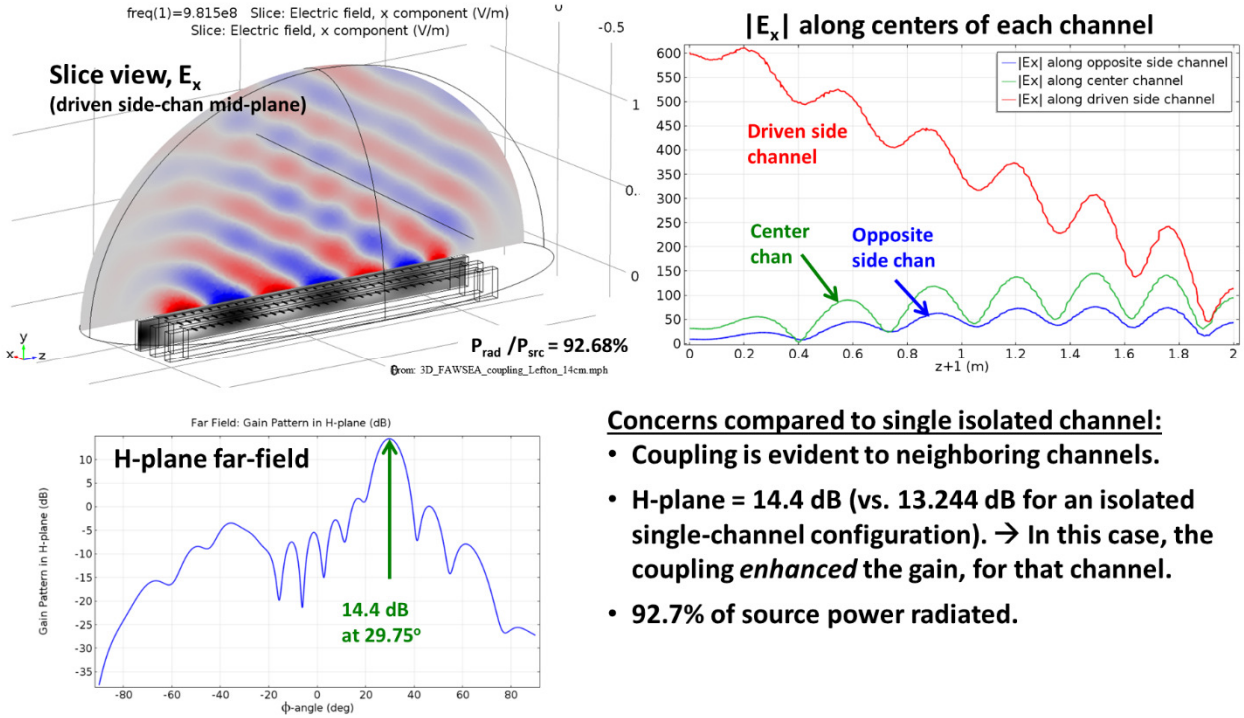


Figure 60. Three channels, only one side channel driven. Channel spacing = 14 cm.

Now, despite the arguably-unexpected 18.72 dB gain computed (per Figure 59) for the all three channels-driven design with 14cm spacing, this design is still somewhat problematic. The *total* aperture width (if we associate +4.5cm extensions on each side, per W_{eff} noted earlier) is ~28+9 = 37cm, yielding a physical aperture area ~0.74m^2. The aperture efficiency corresponding to this 18.72 dB gain at 981.5 MHz for that much area follows immediately, as 74.7%. That's respectable, although we have done somewhat better in other FAWSEA designs. We are more concerned about the imbalanced aperture field distribution. Figure 61 shows slices of |E| at 2, 4, and 6 cm from the aperture. The magnitude of the field is more non-uniform spatially than desirable, a condition which could encourage surface breakdown.

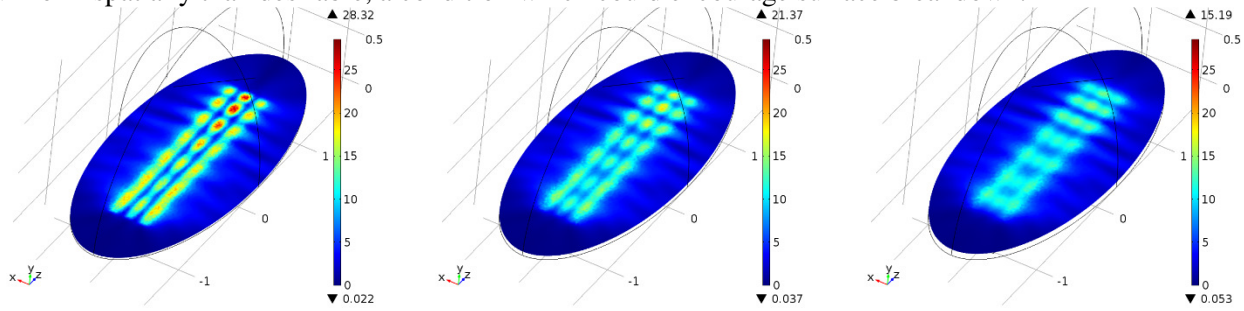


Figure 61. |E| (kV/cm) in vicinity of the aperture for the Figure 59 design, if P_{src} ~1 GW.

Generally, it is desirable to ensure more-uniform aperture surface fields and to reduce the imbalance in the behavior of interior vs exterior channels. For example, consider a design like the one in Figure 59, but with R_{fil} increased to 4cm and the gap reduced to 1cm, again yielding 14cm for the channel-to-channel separation. (Strictly speaking, we should now re-compute the grill wire diameters, but let's just keep them unchanged for now.) Figure 62 shows the predicted performance after this change, which also happens to deliver 0.5 dB more gain than the arrangement in Figure 59.

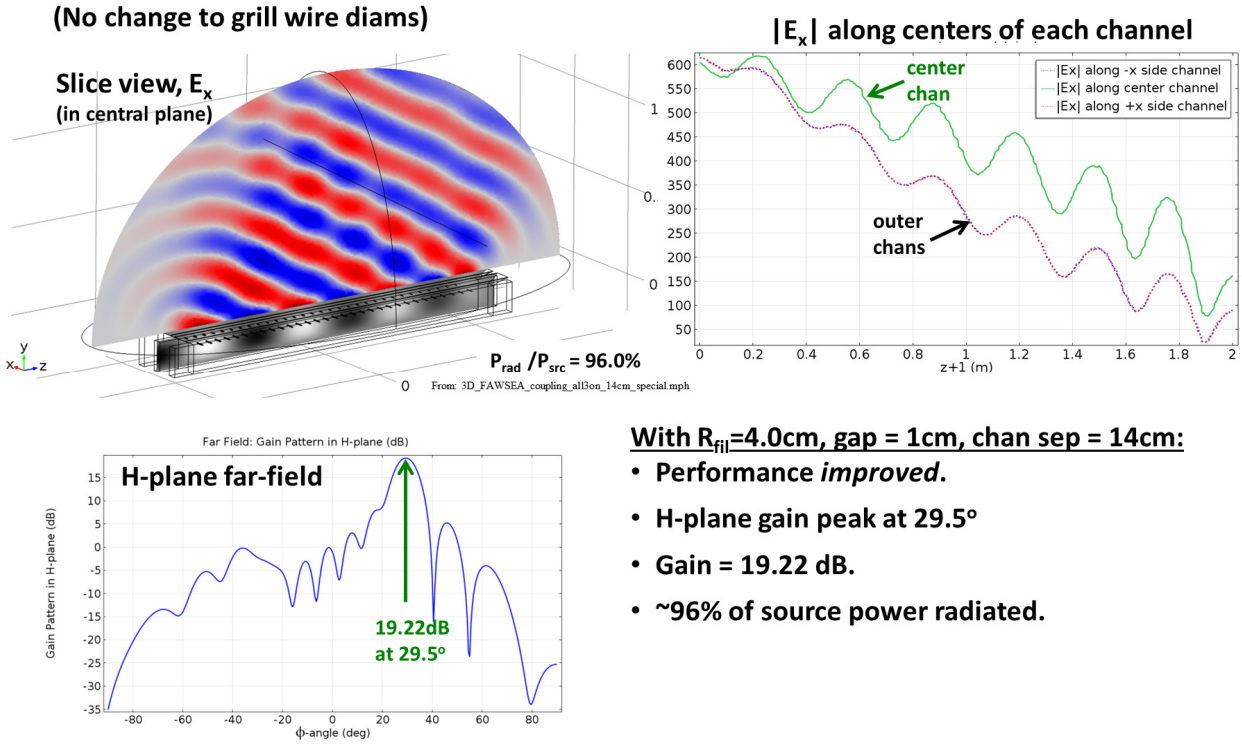


Figure 62. Three channels, all driven, R_{fil} increased to 4cm. Channel spacing = 14 cm.

Also, Figure 63 shows a smoother distribution of |E| near the aperture than that appearing in Figure 61.

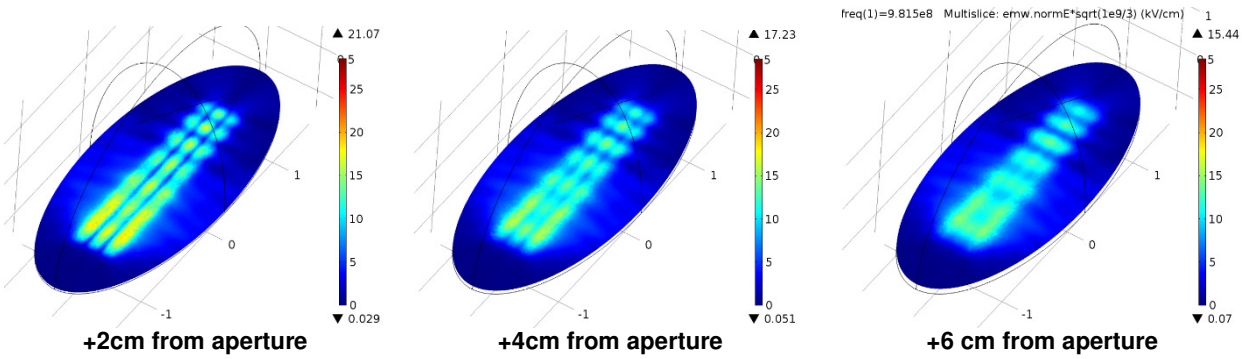


Figure 63. |E| (kV/cm) in vicinity of the aperture for the Figure 62 design, if P_{src} ~1 GW.

4.1.9. Compensating for Modified Phase-velocities in Leaky-wave Channels

Our earlier analyses set-aside the question of explicitly computing the phase velocity of the wave in a leaky-guide, which differs somewhat from that in a closed-wall guide. For only slight leakage the difference is small, but it becomes more pronounced toward the termination end where the leakage is

greater. A corrective adjustment[27] is described below. Recall that for a *uniform* grill and wave incident at angle θ relative to normal, the *complex reflection coefficient* at the grill was given by:

$R_g = \dfrac{-(X_a - X_b)^2 - Z_0^2 + X_a^2}{(Z_0 + j(X_a - X_b))^2 + X_a^2}$, where expressions for X_a and X_b are given by Marcuvitz (1951) and (for his expressions) Z_0 can be normalized to unity. The next step to computing the detailed impact upon the phase velocity within the leaky guide is to recognize that, *in this context*, the grill behaves very much as if it were equivalent to a perfectly-conducting wall moved slightly farther out from the opposite side wall of the waveguide. Figure 64 illustrates this idea. Thus, in practice, all we need to do is compute the value of δ_{xtra} . Once we have that, we can choose where to place the grill wires to match the phase velocity in the feeding waveguide. It is clear that the distance δ_{xtra} corresponds to an equivalent phase factor = $\exp(2jk_0\delta_{xtra}/\cos\theta)$. But since the reflection coefficient at a PEC wall is *real*, the *imaginary* part of R_g (if its magnitude is normalized) must come *solely* from this term. Thus:

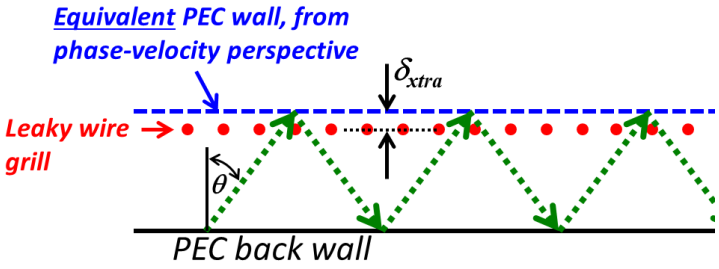


Figure 64. Concept of a *virtual* perfectly-conducting wall for the phase-velocity computation. (Note: this is an H-plane view; E is normal to the page)

$\dfrac{imag(R_g)}{|R_g|} = \sin(2k_0\delta_{xtra}/\cos\theta)$, which immediately yields: $\boxed{\delta_{xtra} = \dfrac{\cos\theta}{2k_0}\sin^{-1}\left[\dfrac{imag(R_g)}{|R_g|}\right]}$

Of course, since R_g varies as a function of position if we change the diameters (or spacing) of the wires as a function of position, then any generalized δ_{xtra} will also vary as a function of position, suggesting (as we have previously-noted) correction methods such as tilting the back-wall and/or otherwise shifting the grill wire positions relative to the back-wall to hold the phase velocity ~constant throughout the channel. For future reference, a custom MatLab function to compute δ_{xtra} via the above rule is provided in Figure 65.

```
% function DeltaXtra = DeltaXtra(AngIn,a,d,freq)
% AngIn = angle of inc. rel to normal, in radians
% a = wire spacing in meters
% d = wire diameter in meters
% freq = frequency in Hz
% Computes distance from grill to equiv PEC wall.
% Used for FAWSEA design.  E is parallel to wires.
% Prepared by R. Koslover, SARA, Inc.
% June, 2014
% See Marcuvitz, Waveguide Handbook, p.286.
% See also Quarterly Report #3.
function DeltaXtra = DeltaXtra(AngIn,a,d,freq)
    ct = cos(AngIn);
    st = sin(AngIn);
    c_const = 2.99792458e8; %c in m/s
    lambda = c_const/freq; % free space wavelength
sum1 = 0;
sum2 = 0;
for m = 1:1:1000
        sum1 = sum1+1/sqrt(m^2+2*m*a*st/lambda-
(a*ct/lambda)^2)-1/m;
        sum2 = sum2+1/sqrt(m^2-2*m*a*st/lambda-
(a*ct/lambda)^2)-1/m;
    end
   % Normalized to Z0 = 1 everywhere
   % Compute Xa using sum from Marcuvitz, p. 286
    Xa = (a*ct/lambda)*(log(a/(pi*d))+0.5*(sum1+sum2));
    Xb = (a*ct/lambda)*(pi*d/a)^2;
    Zeq = j*(Xa-Xb)-(Xa^2)/(-1+j*(Xb-Xa));
    gam = (Zeq-1)/(Zeq+1);
    DeltaXtra =
(ct*lambda/(4.0*pi))*asin(imag(gam)/abs(gam)); % meters
end
```

Figure 65. Listing of custom MatLab function 'DeltaXtra' that computes δ_{xtra}.

A plot of computed δ_{xtra} vs wire diameters at selected wire spacings is provided in Figure 66.

[27] This calculation is only strictly valid in the ideal 2D case (H-plane analyses only) with no dielectric window, but may be generalizable.

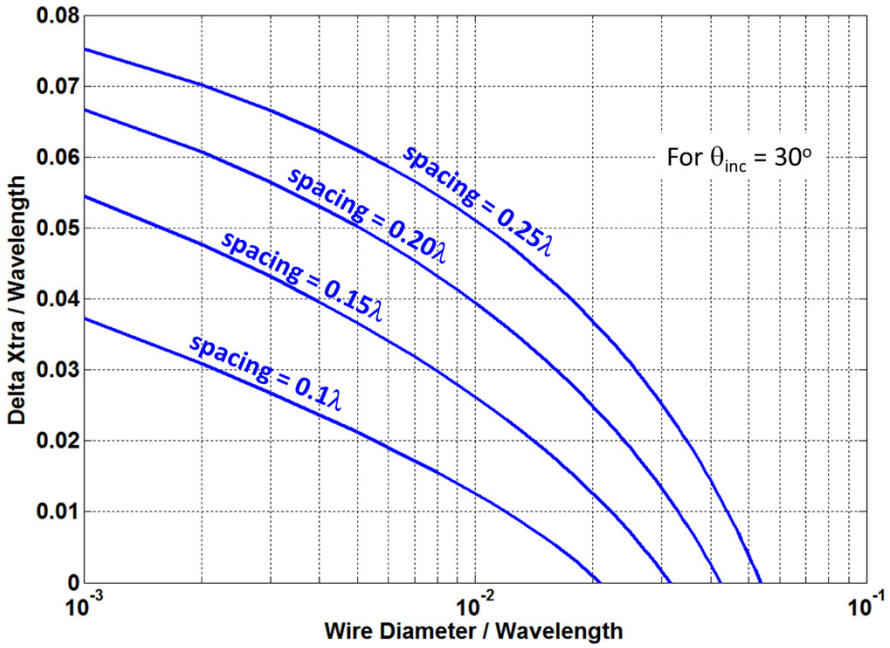


Figure 66. Computed δ_{xtra} vs wire diameter for various wire spacings, scaled to the free-space λ, for θ_{inc}=30°.

Although we have extracted δ_{xtra} from the imaginary component of the wire-grill reflection coefficient R_g, *this could be generalized, in principle,* to use the imaginary component of the *overall* reflection coefficient, the latter found via the wave-matrix formalism, thus effectively accounting for curved channel edges in the E-plane, a dielectric window, and even other factors when positioning the wire grill. However, it is unclear if the additional adjustments to the grill or opposite wall that would follow from doing those more-complete calculations would prove significant and/or improve the resulting designs.

4.1.10. Optimizing Aperture Field Distributions Conformal to Curved Platform Surfaces

The highest peak power-handling for any fixed-size leaky-wave aperture, or most other apertures, is generally realized with the most uniform-magnitude distribution of the aperture electric field. For a flat aperture, this also generally yields the most gain, provided that a linear-phase distribution is maintained. We have explored far-field patterns that can be generated by forward-traveling, leaky-wave field distributions in apertures that are variously flat, curved in the E-plane, curved in the H-plane, curved in the aperture plane, etc. Traveling-wave LWAs cannot deliver uniform phase, but they can deliver fairly-uniform magnitude and polarization, with nearly-linear phase along the aperture. The latter, as already noted, results in a non-zero tilt angle of the beam relative to the aperture normal. Considered separately from other factors, this imposes a factor of cos(ϕ_{tilt}) on the numerical gain, where ϕ_{tilt} is the beam tilt angle. This reduces the effective area: $A_{leaky} = A_{geo}\cos\phi_{tilt}$. Source bandwidths, cutoff considerations, and finite-duration pulse considerations typically lead us to choose ϕ_{tilt} > ~20° or so for practical HPM-capable designs. In particular, selecting ϕ_{tilt} ~25-35° often provides a satisfying tradeoff between bandwidth and gain. Note that within that range, the tilt-related efficiency-factor ranges from cos(25°) = 90.6% to cos(35°) = 81.9%. However, there is more to describing antenna patterns than noting the peak gains achievable, and there are many more apertures of interest than those that are simple and flat.

Curved apertures (e.g., cylinders, ogives, etc.) present field-tangent surfaces that are necessarily oriented in directions other than optimal. As an extreme example, there would not seem to be much point in distributing HPRF power to *shadowed* surface regions (i.e., platform surfaces with lines-of-sight to the target totally blocked either by the platform or by other objects). The more interesting question here is how best to utilize those platform surfaces that are neither shadowed nor particularly well-oriented. From an "antenna-centric" perspective, it makes sense for the designer to concentrate efforts on the most aperture-efficient shapes. But from a "platform-centric" perspective, the more appropriate goal is to make best use of the platform's surface, regardless of shape, so as to maximize both gain and peak power handling. It is these factors (aside from considerations of packaging/integrating HPRF sources and all supporting subsystems) that ultimately constrain the power density deliverable to distant targets. In particular, an antenna delivering somewhat *reduced* aperture efficiency, but which utilizes a *significantly greater fraction* of a curved-platform's surface, may possibly be able to deliver a greater overall power density on a target than a more aperture-efficient, but smaller aperture, antenna.

Field re-distribution schemes to compensate, at least in part, for the gain-degrading effects of aperture curvatures have also been studied. Our computation of far-fields from apertures of potential interest utilized the balanced-form Stratton-Chu aperture-integration approximation formula (Silver, 1949), which we consider to be one of the more practical and convenient[28] expressions for this purpose:

$$\vec{E}_p = \frac{jk}{4\pi}\hat{r}_p \times \iint_s \left[\hat{n}\times\vec{E}_a - \eta\hat{r}_p \times \left(\hat{n}\times\vec{H}_a\right)\right]\exp\left(jk\vec{r}_a\cdot\hat{r}_p\right)dS$$

where $\vec{E}_p$ is the computed electric field at the far-field point *p*, $\vec{E}_a$ and $\vec{H}_a$ are the electric and magnetic complex vector fields on the aperture (or surface *S* enclosing the antenna), $\hat{n}$ is the unit outward normal on the aperture (or surface *S*), η is the impedance of free space (~377 Ohms), k is the free space wave number ($2\pi/\lambda$), $\vec{r}_a$ is the vector from the origin to the aperture field point, $\vec{r}_p$ is the vector from the origin to the radiated field point, with $\hat{r}_p = \vec{r}_p \big/ \left|\vec{r}_p\right|$ = a unit vector along $\vec{r}_p$. In Cartesian coordinates, $\hat{r}_p = \hat{x}\sin\theta_p\cos\phi_p + \hat{y}\sin\theta_p\sin\phi_p + \hat{z}\cos\theta_p$. [Note: for a uniform-field flat aperture in the *xy*-plane, the above surface integral simplifies greatly; it is fairly easy to show that the resulting expression for E_p at θ_p =0 is consistent with on-axis gain $G_{ideal} = 4\pi A_{geo} \big/ \lambda^2$.] Of course, analytic or semi-analytic expressions for E-plane and H-plane cuts of far-field patterns for a variety of idealized aperture antenna distributions can be found in the literature (e.g., Jull, 1988), although most are limited to planar apertures, especially those with rectangular or circular boundaries. (But recall also the works of Honey, Ishimaru, and others in analyzing leaky-wave antennas and apertures conformal to ideal flat or cylindrical surfaces.) For generality, our approach here is numerically-based and applies the aforementioned integral method.

We now consider some examples of simplified representative platform shapes and apply analytic aperture fields with phases that match the desired radiating plane waves. *Ideally*, we would like to fully-match our platform's aperture surface fields (in terms of direction, amplitude, and phase) to a plane wave, however we are constrained (and this is not the only constraint) to choose fields that are *tangent* to the aperture surface. The simplest way to comply with this constraint is to do a vector back-projection of the wave onto the surface and keep only the tangential components. For an aperture surface with a local surface-normal $\hat{n}$, we can simply subtract the normal component of E from the desired plane wave:

$$\vec{E}_{ap} = \vec{E}_{pl} - \hat{n}\left(\hat{n}\cdot\vec{E}_{pl}\right),$$

[28] This expression is convenient numerically because there are no derivatives of the aperture fields involved.

i.e., $\vec{E}_{ap}$ is the component of $\vec{E}_{pl}$ that is tangent to the surface. One consequence of this approach is that for all of the surface, $\left|\vec{E}_{ap}\right| \le \left|\vec{E}_{pl}\right|$. This *magnitude-reducing* mapping puts the strongest E fields in locations where the surface is intuitively best-oriented for launching the desired wave, but weaker fields where the surface would seem to be less-advantageously oriented. Alternatively, we can eliminate that scaling altogether, as follows:

$$\vec{E}_{ap} = \frac{\vec{E}_{pl} - \hat{n}\left(\hat{n}\cdot\vec{E}_{pl}\right)}{\left|\vec{E}_{pl} - \hat{n}\left(\hat{n}\cdot\vec{E}_{pl}\right)\right|} E_0$$

This is a *magnitude-preserving* projection, i.e., $\left|\vec{E}_{ap}\right| = \left|\vec{E}_{pl}\right|$. An immediately-appealing feature of this second mapping option is the expectation of it maximizing peak-power handling. But we should mention that there also exists at least one more option, which is essentially a *reverse* of the initial projection. That is, we can demand that *any* surface field of a contributing aperture region carry a tangent field that would yield the plane wave, if that field were projected into the transverse plane of the desired wave. This scales the aperture fields *oppositely* to that of the direct projection case, yielding the following mapping:

$$\vec{E}_{ap} = \frac{\vec{E}_{pl} - \hat{n}\left(\hat{n}\cdot\vec{E}_{pl}\right)}{\left|\vec{E}_{pl} - \hat{n}\left(\hat{n}\cdot\vec{E}_{pl}\right)\right|^2} E_0$$

This third case is a *magnitude-increasing* projection, i.e., $\left|\vec{E}_{ap}\right| \ge \left|\vec{E}_{pl}\right|$. Its intuitive (but naïve) appeal is that it endeavors to force the local aperture *E* field to generate the desired plane wave point by point. But this is regardless of whether it generates strong (or stronger) radiating waves in other directions as well, and also leads to unbound local aperture field strengths. We include it here primarily for completeness, but will not study it in more detail. Now, for simplicity let us assume, without loss of generality, that the *desired* plane wave is given by:

$$\vec{E}_{pl} = \hat{y}E_0 \exp\left(-jk_0 z\right)$$

For this particular $\vec{E}_{pl}$, the above three expressions become (after just a little algebra):

Direct Projection:	$\vec{E}_{ap} = \left(-n_x n_y \hat{x} + \left(1-n_y^2\right)\hat{y} - n_z n_y \hat{z}\right) E_0 \exp\left(-jk_0 z\right)$
Mag-preserving Projection:	$\vec{E}_{ap} = \frac{\left(-n_x n_y \hat{x} + \left(1-n_y^2\right)\hat{y} - n_z n_y \hat{z}\right)}{\sqrt{\left(n_x n_y\right)^2 + \left(1-n_y^2\right)^2 + \left(n_z n_y\right)^2}} E_0 \exp\left(-jk_0 z\right)$
Mag-enhancing Projection:	$\vec{E}_{ap} = \frac{\left(-n_x n_y \hat{x} + \left(1-n_y^2\right)\hat{y} - n_z n_y \hat{z}\right)}{\left(n_x n_y\right)^2 + \left(1-n_y^2\right)^2 + \left(n_z n_y\right)^2} E_0 \exp\left(-jk_0 z\right)$

The expressions above support convenient representations in Comsol Multiphysics. Figure 67 shows a few examples of simple curved surfaces, along with plots of mapped fields based on the *direct* and *magnitude-preserving* transformations, since we regard these two mappings to be of most interest. The examples include: (1) a 1m-long cylinder with a 25cm radius, with its axis 60° relative to k_0; (2) a sphere with a 25cm radius; and (3) a 75cm-long cylinder with a 25 cm radius, extended by a 75cm-long tangent ogive, with their common axis oriented 60° relative to k_0. All are oriented in a manner such that the aperture fields considered here, though idealized, could potentially be provided by a multi-channel leaky wave antenna. The Snapshots in Figure 67 are all for f=1.0 GHz.

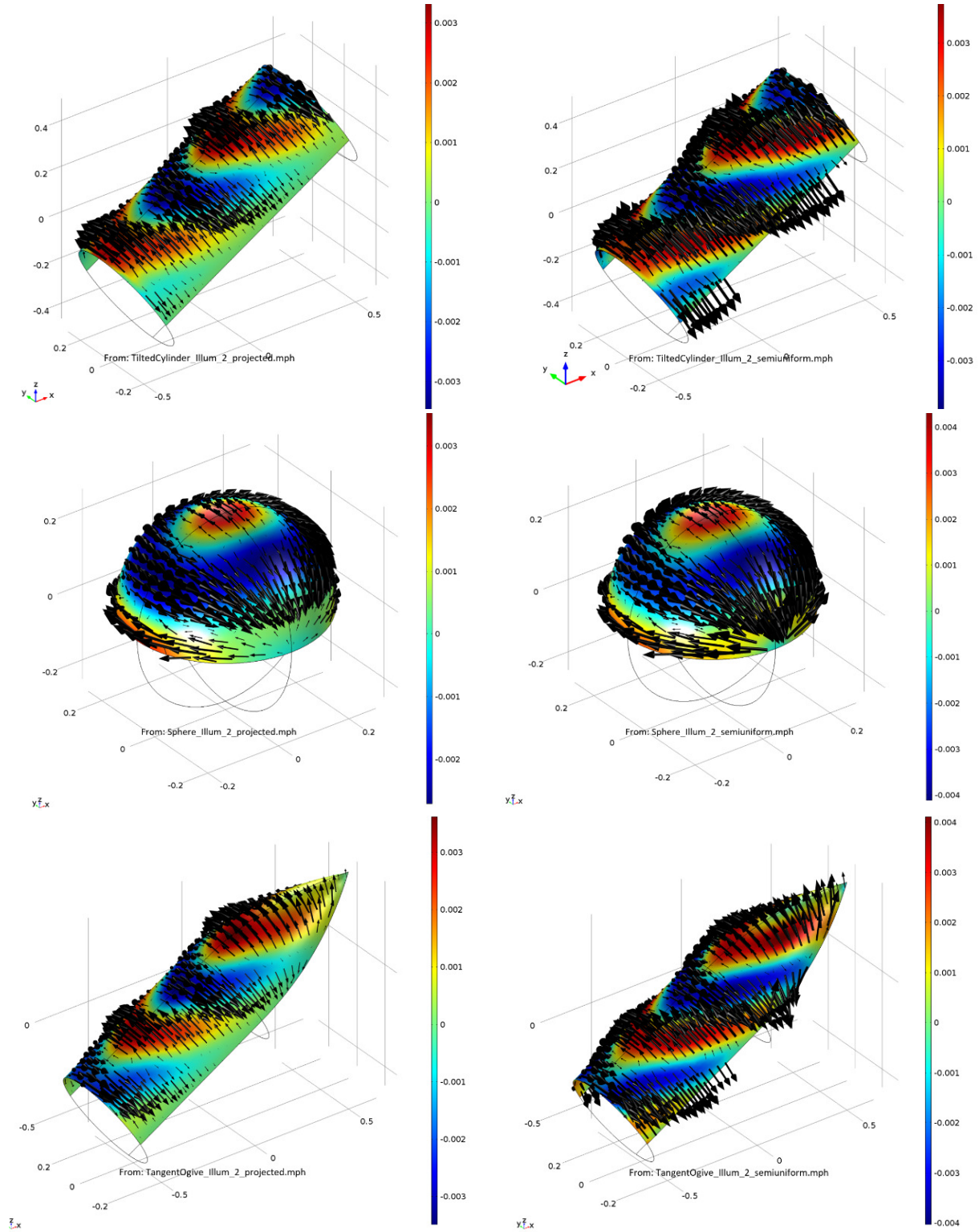


Figure 67. Snapshots, projected plane-waves onto cylinder, sphere, & cylinder + ogive. Left column: *Direct* projection. Right Column: *Magnitude-preserving* projection. Arrows: Electric field. Colors: H_x (reveals the phase). With $f=f_0$ (1 GHz).

Once we have quantified the mapped aperture fields, it is relatively straightforward to compute the far-field patterns and the antenna gain that these surface distributions (if realized) would generate. In Figure 68, we compare the predicted gains for the examples in Figure 67, across a 3-to-1 range of frequencies.

Most interestingly, in all three examples and across all frequencies considered, the *magnitude-preserving* wave *projection yielded higher gain*. It was not obvious to us in advance that this would be the result, but it is a very welcome one, since (as noted earlier) this type of aperture illumination should also provide ~optimal peak power-handling. This analysis motivated us to pursue the design of a "CAWSEA$_{180}$" (see Section 4.3.2) but should also apply to other similar configurations.

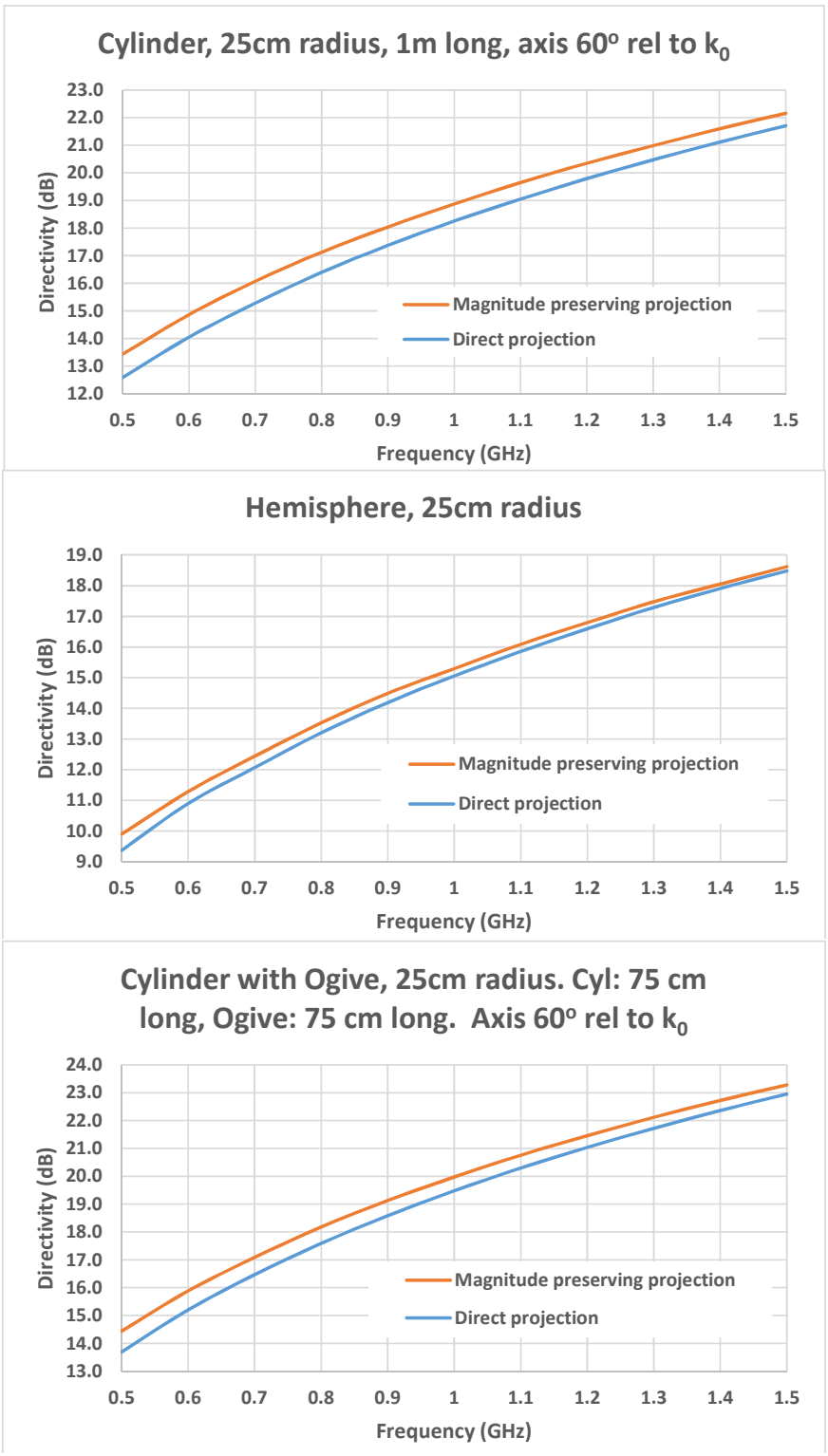


Figure 68. Predicted gains vs. frequency, computed using the projected aperture fields on example surfaces in Figure 67.

4.2. FAWSEA

4.2.1. A Recommended FAWSEA Design

A description of a recommended high-performance FAWSEA design is provided below. The design described here was developed and sized for f_0=1.0 GHz. The dimensions may be scaled linearly (all components) proportional to λ_0, to support other RF/microwave frequencies. Geometries are presented first, in Sections 4.2.1.1-4.2.1.2, in a level of detail sufficient (or nearly so) to guide preparation of fabrication-level drawings by any mechanical engineer possessing basic familiarity with HPM-capable antennas. Key features of the *single-channel* FAWSEA design (channel depth, channel width, wire sizes, wire spacing, and tapering along the length) are also used in both the 4-channel FAWSEA and 4-channel CAWSEA (see Section 4.3). (In the CAWSEA, the channels are arrayed around a circular arc, rather than parallel, and there is additional curvature/shaping to the structures near and in the aperture region that are otherwise not present in the FAWSEA.) The recommended aperture window is polyethylene, with ε_r taken to be 2.26. The window is deliberately-shaped to allow O-rings (silicone recommended, due to microwave compatibility) to be included around the window edges to provide the vacuum seal. Additional O-ring material is placed in strips between the channels, along where the window also makes contact with interior metal parts of the aperture between the channels. High peak power (e.g., GW-class) operation requires that the antenna be evacuated. A vacuum of 10^{-6} Torr or better has been observed to be sufficient to ensure proper insulation. This is readily achievable via modern commercial vacuum pumps and straightforward practices. Predicted performance characteristics of these designs are presented in Section 4.2.1.3. Figure 69 introduces the antenna geometry.

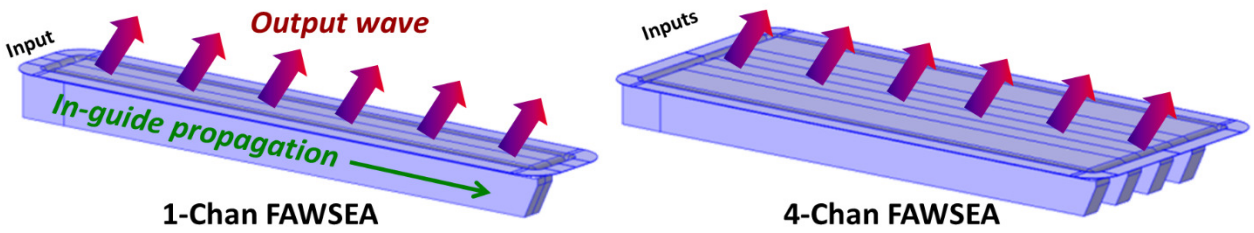


Figure 69. Perspective views of the subject antenna in one- and four-channel variants.

4.2.1.1. Geometry, Single-Channel FAWSEA

Figure 70 shows the cross-section of the single-channel FAWSEA, in a slice just past where the evacuated channel joins to a rectangular waveguide input feed. The geometry can be understood better in conjunction with the side view in Figure 71. In Figure 70, The downward-folds of the window lead into a conducting "well" where they rest on the O-ring channels along the left and right edges. The heavily-rounded edges at the top of the channel and the rising parts of the wings form the sides of this "well", which dramatically suppresses the electric fields at the triple-junction region where air, insulator, and conductors all come together. *This is an important HPM-enabling feature* of the design, since triple-junctions in high-field locations are known to serve as initiation points for surface breakdown. Also, the feet-like projections/supports of the window that rest on O-ring strips *between* the channels (in a multi-channel version, such as in Figure 74) are likewise at regions where the surface |E| is effectively suppressed. But in this case, those regions are in vacuum and the field suppression is due to approximate symmetry between the channels, which necessarily drives the normal component of E toward zero there.

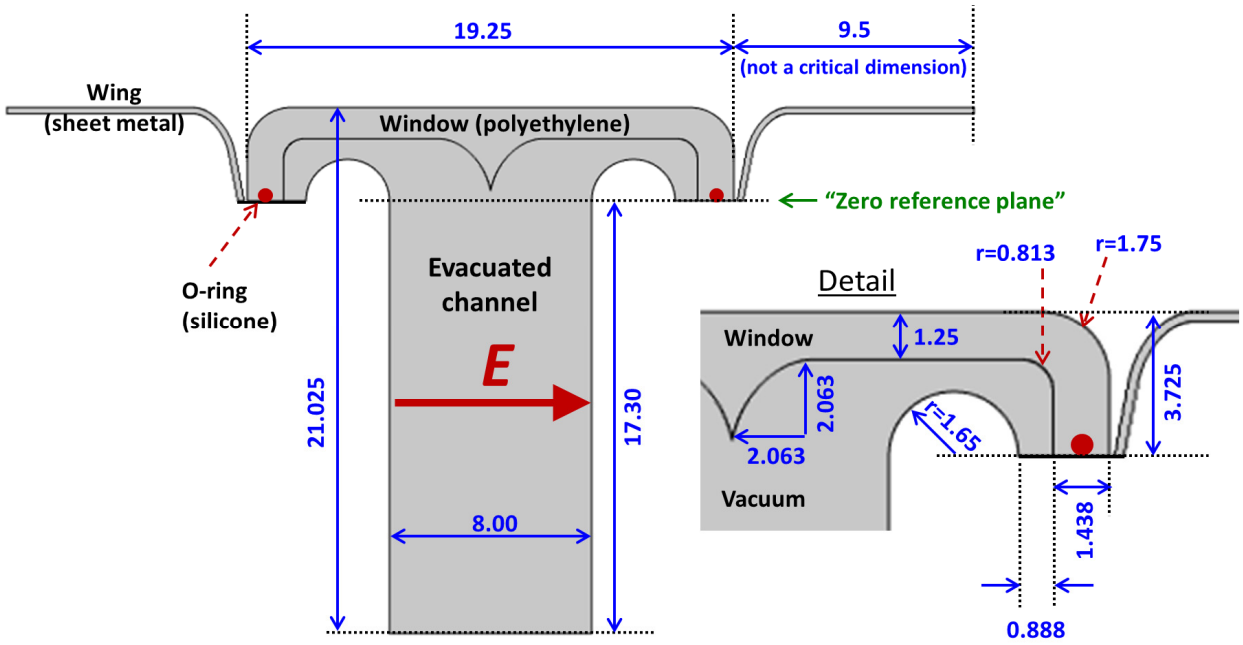


Figure 70. Single FAWSEA channel, cross-section taken at junction to feed. Units are cm.

The leaky-wave grill is a plane-parallel array of 36 wires that are equally-spaced at center-to-center separations of 5.25 cm, beginning (with Wire #1) at 5.25 cm from where the aperture joins to the feeding waveguide. Per Figure 71, this plane of wire-centers is positioned 9.1 mm below the "zero reference plane" noted in Figure 70. The radii of these wires are listed in Figure 72.

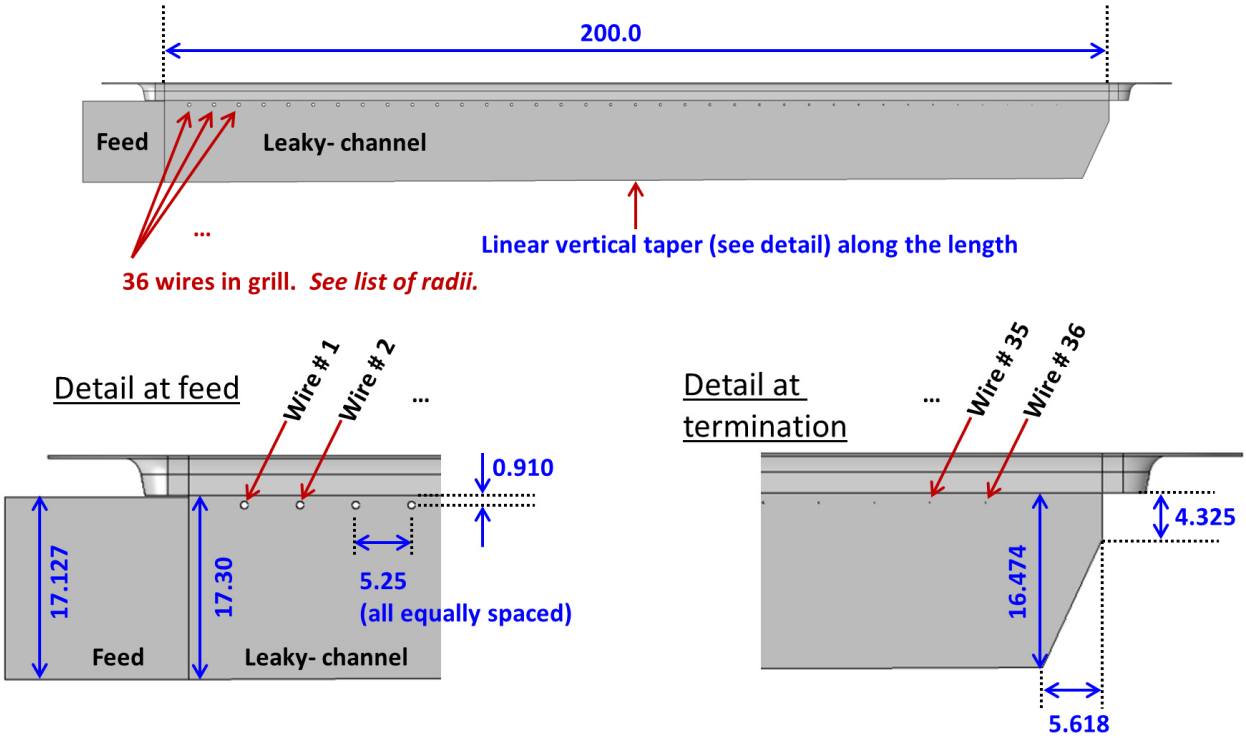


Figure 71. Single channel side view, including wires and tapered backplane. Units are cm.

The wire radii in Figure 72 were derived via the methods described earlier. The last two wires in the list (#'s 35 and 36) are thicker (and match #34) than those that arise from the analyses, to facilitate more practical and rugged fabrication, while ultra-thin wire #'s 37 and 38 (not listed) were simply dropped altogether. The channel is linearly-tapered in depth relative to the "zero reference plane" (note the shallower depth at the termination end vs. at the feed end, as shown in the details in Figure 71) to improve performance by maintaining nearly constant wave phase velocity in the channel, increasing the gain, and reducing the VSWR. The initial taper from feed to termination was based on the estimated effective penetration of a reflected wave from a wire grill (see Section 4.1.9), but subsequently modified based on results of 3D models to yield better performance.

Wire #	Radius (mm)		Wire #	Radius (mm)
1	3.505		19	2.361
2	3.459		20	2.268
3	3.412		21	2.171
4	3.362		22	2.068
5	3.312		23	1.959
6	3.260		24	1.843
7	3.205		25	1.721
8	3.149		26	1.592
9	3.091		27	1.453
10	3.031		28	1.306
11	2.968		29	1.150
12	2.903		30	0.983
13	2.835		31	0.806
14	2.765		32	0.620
15	2.691		33	0.430
16	2.614		34	0.245
17	2.534		35	0.245
18	2.450		36	0.245

Figure 72. List of wire radii vs. position index. Wire spacing is fixed at 5.25 cm, center-to-center. All 36 wires are parallel and lie in the same plane, 9.1 mm below the "zero-reference plane" in Figure 70.

Due to left-right symmetry, full numerical RF models of the antennas in Figure 69 can be made using only half of each antenna, which helps speed-up the computations. Figure 73 shows two views of a half-single channel, from one of our 3D models. Note the wrap-around nature of both the O-ring well and wing, the latter which should generally meld smoothly onto a larger conducting surface, if the aperture is to be mounted on a platform.

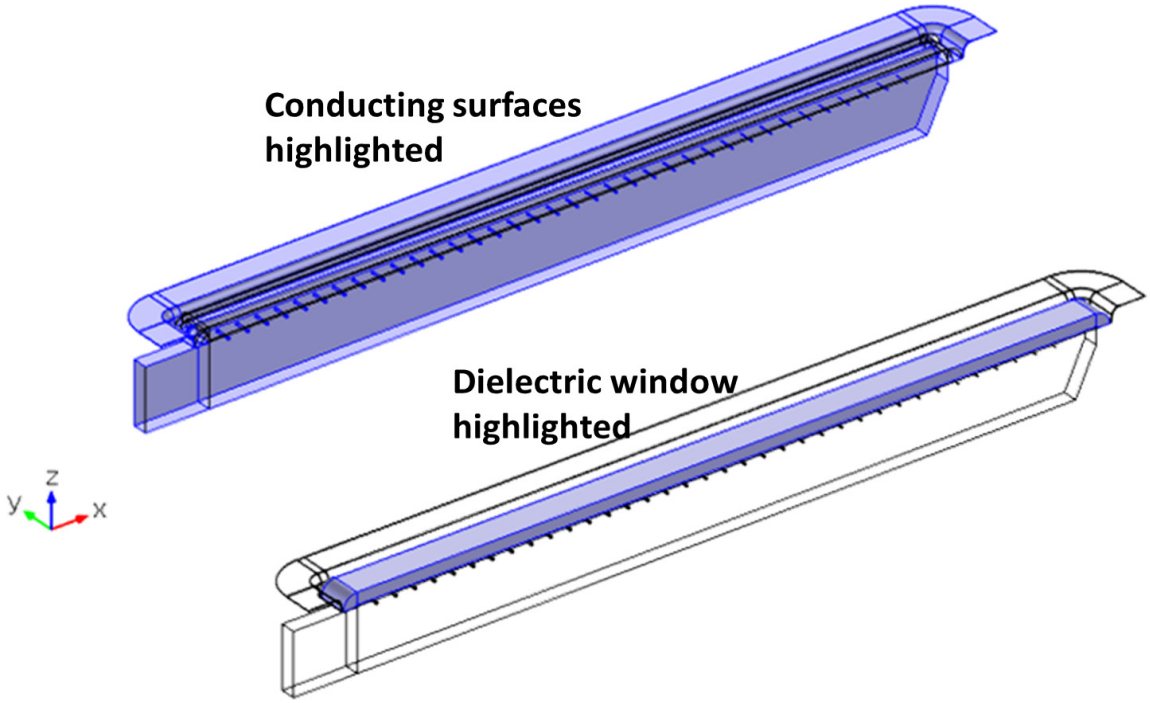
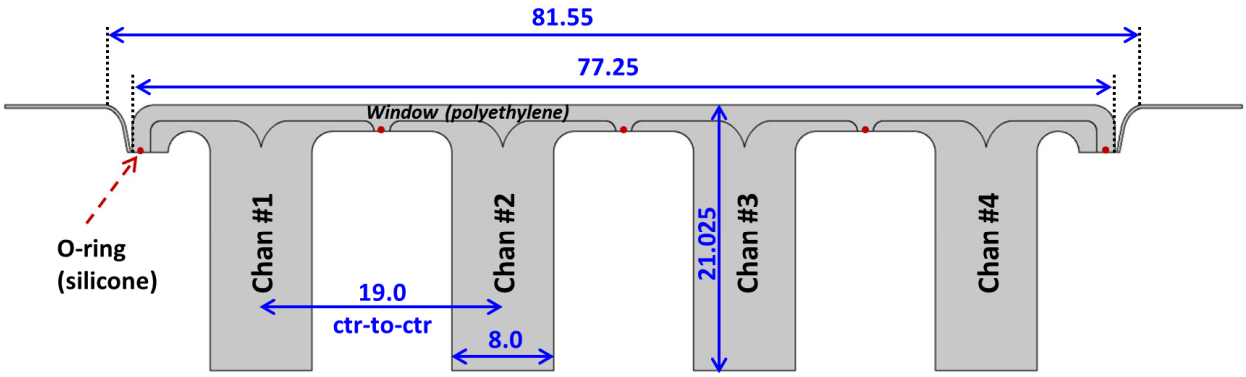


Figure 73. A half-channel, sliced along its symmetry plane for use in 3D RF modeling.

Single-channel FAWSEAs may have some direct applications, but we are more interested in their role as building blocks in constructing more general multi-channel FAWSEA antennas.

4.2.1.2. Geometry, 4-Channel FAWSEA

Figure 74 shows the cross-section of a four-channel FAWSEA based on the single-channel FAWSEA described just above. We have found that four 8cm-wide channels with a c-to-c separation of 19 cm yield very good performance in terms of aperture efficiency, while limiting undesirable cross-channel coupling. Figure 75 shows two views of a half 4-channel FAWSEA, from one of our 3D models.



Refer to the *single-channel* diagram for additional geometric details.

Figure 74. Four channel FAWSEA cross-section (not tapered). Units are cm.

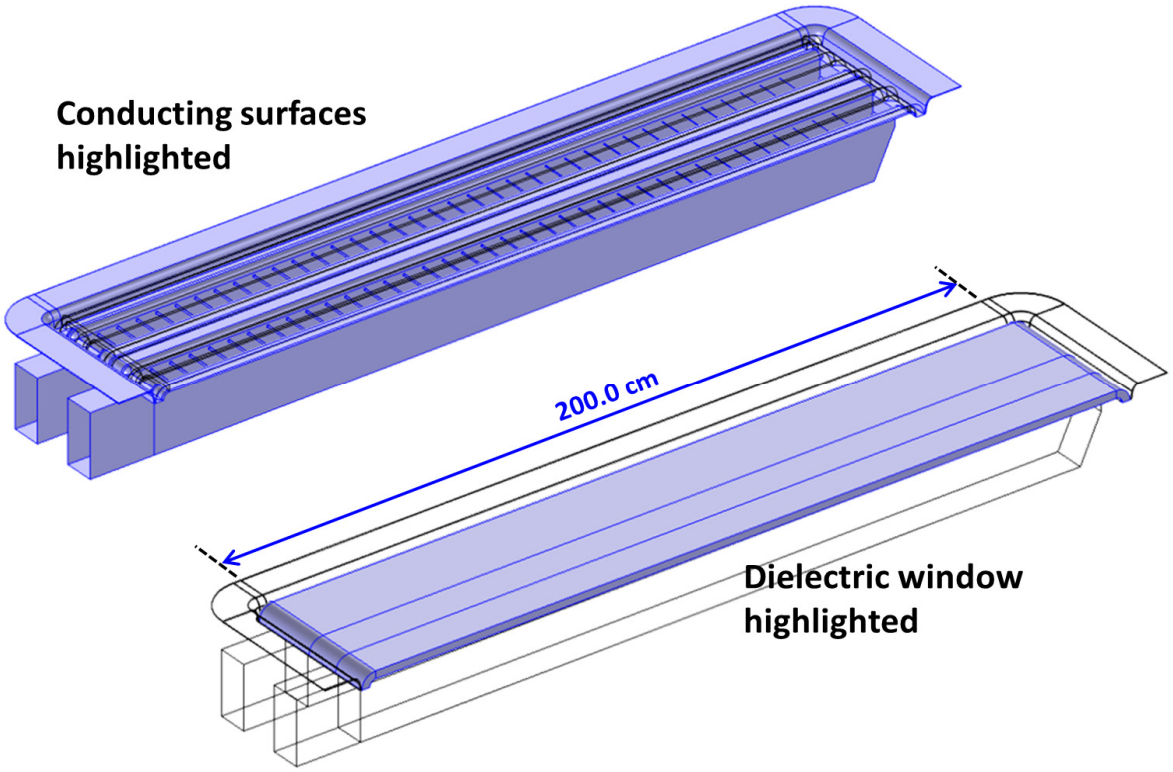


Figure 75. Half of a 4-chan FAWSEA sliced along its symmetry plane, for 3D RF modeling.

4.2.1.3. Predicted Performance Characteristics

Predicted performance characteristics of the aforementioned antennas are shown below. The computed effective[29] VSWR for the aforementioned single-channel and four-channel antennas appear in Figure 76. The VSWR is excellent across a +/-10% bandwidth around f_0. Computed gain is shown in Figure 77.

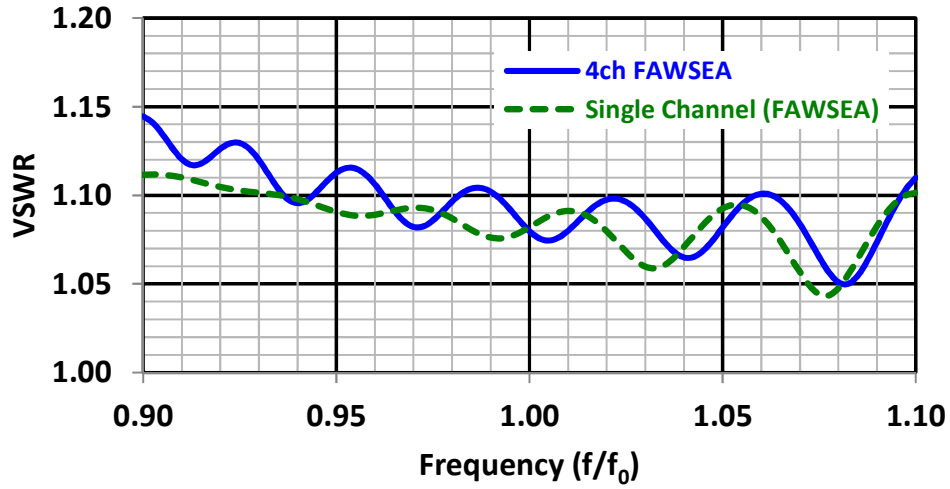


Figure 76. Computed Effective VSWR vs. Frequency

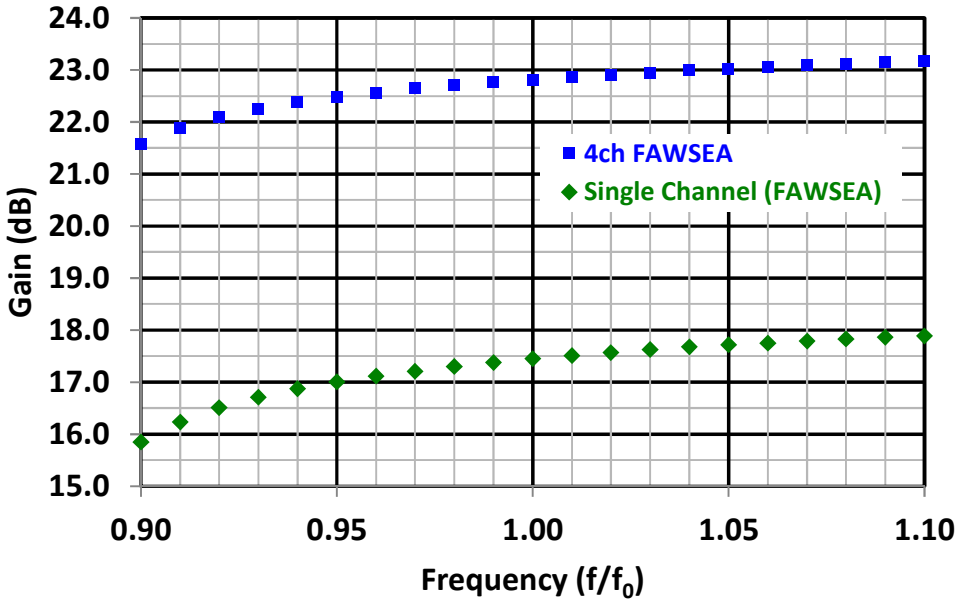


Figure 77. Computed Gain vs. Frequency

The gain may perhaps be better appreciated when considered in the context of *aperture efficiency*. To compute this properly for the 4-channel FAWSEA, we need an *unambiguous* definition of the "geometric area" of the aperture, but this is not immediately obvious by inspection, due to the presence (and helpful impact upon RF performance) of the "wings." Excluding the wings entirely from the assumed geometric area would lead us to overestimate aperture efficiency, but it would also be a mistake to include their *full* extent, since they are of somewhat arbitrary size (and may be considered, at least partially, as surrogate

[29] In the case of multiple channels, the *effective* VSWR is extracted from the overall forward and reflected powers.

extensions of a platform on which such an antenna aperture might be integrated). An unambiguous resolution was attained by defining the "geometric" area of the aperture via a separate 3D numerical RF calculation (not shown here) in which we *replaced* all the FAWSEA channels and window with an *idealized flat rectangular aperture* across which we imposed computationally a 100%-uniform E-field, located in the "zero reference plane," while surrounding it by the *same wings* as shown in Figure 75. This computation allowed us to extract (from the performance of this idealized-aperture case) a value of the geometric area = 1.677 m^2, which (as expected, due to the beneficial effects of the wings) is somewhat *larger* (by ~4.6%) than the window's *physical* projected area (~1.603 m^2). In essence, this way of computing aperture efficiency for the 4-channel FAWSEA compares computed gain to that from an ideal uniform-field aperture *bordered by the same wings*. This definition, in combination with the gains computed earlier, promptly yields Figure 78.

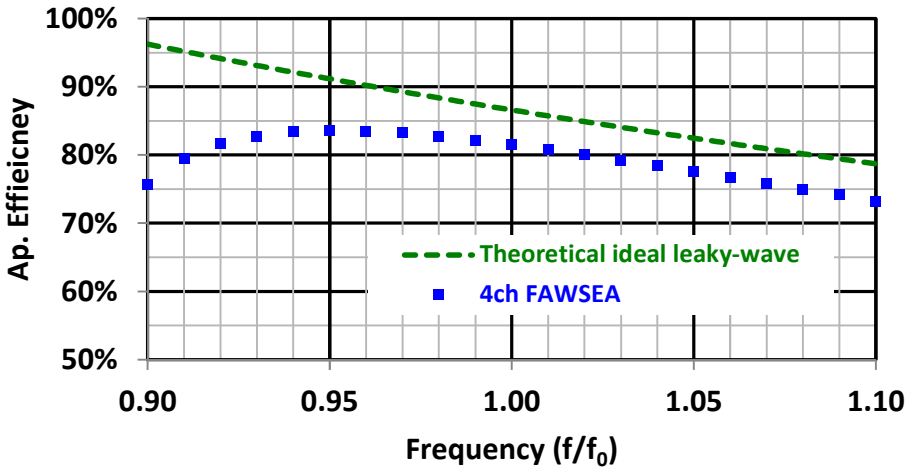


Figure 78. Predicted Aperture Efficiency vs. Frequency.

Note the theoretical upper-bound based on the ideal *leaky-wave* aperture efficiency (shown via the green dotted line) is always less than 100% because the beam is *tilted*. It corresponds simply to $\cos(\theta_b)$, where θ_b is the angle of the beam relative to the aperture normal. The predicted realizable aperture efficiency of the 4-channel FAWSEA (blue squares in Figure 78) is unquestionably excellent. One can also assess the (related) channel arraying efficiency by comparing the curves in Figure 77. *Ideally*, an array of four channels should deliver +6.02 dB more gain than a single channel alone. At $f=f_0$, the 4-channel FAWSEA described here yields an increase in gain of +5.36dB over a single channel, based on the numerical models.

Figure 79 shows[30] predicted peak electric field values on the exterior aperture surfaces for the 4-channel FAWSEA vs. frequency, corresponding to a total input power of 1.0 GW (250MW/channel).

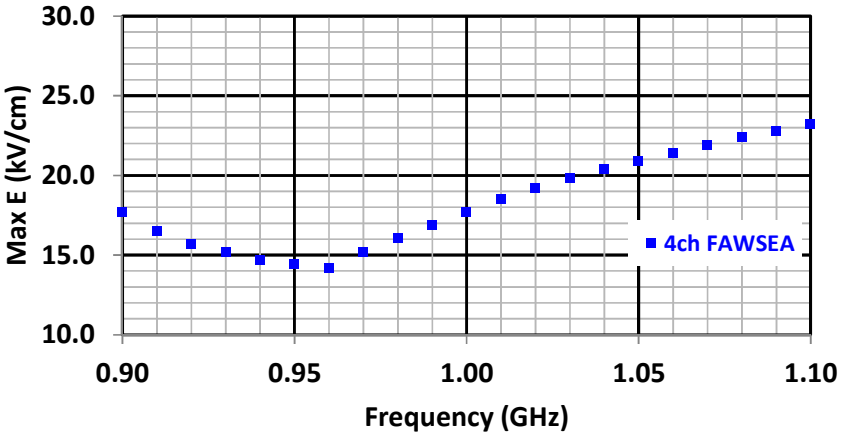


Figure 79. Peak values of E_{max} vs. frequency on exposed exterior window surfaces, for total input power = 1 GW.

[30] If scaling designs presented here to other center (f_0) frequencies, the field values in Figure 79 (with P_{in}=1 GW held fixed) scale proportional to $(f_{0,new}/1.0\ GHz)^2$. In general for HPM, strive to keep E_{max} < 30 kV/cm on the exterior.

The beam tilt vs. frequency follows closely to the theoretical value of $\theta_b = \cos^{-1}(f_c/f)$, where f_c is the effective cutoff frequency of a leaky-wave channel. For the case where f_0 =1.0 GHz and θ_b (by design) is 30°, the value of f_c = 866 MHz. Beam tilt found from a model of the 4-channel FAWSEA vs. this theoretical curve is shown in Figure 80.

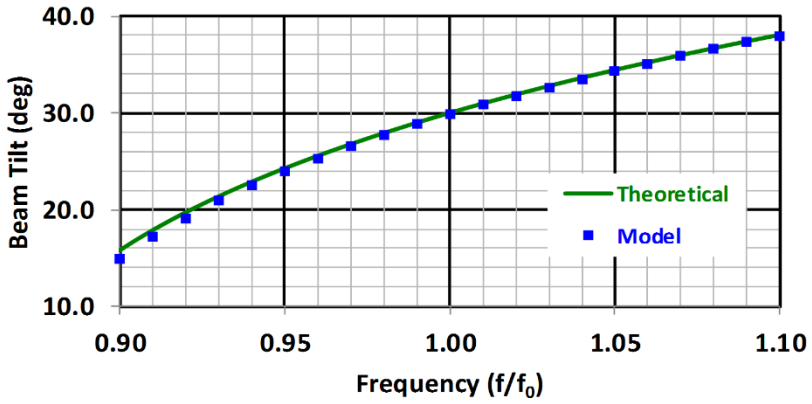


Figure 80. Predicted beam tilt relative to aperture normal, vs. frequency.

Principal-plane polar far-field pattern cuts for the subject antennas at f=f_0 are shown in Figure 81. The E-plane cuts (shown in red) are at a 30° angle relative to the aperture normal, so as to slice through the beam peak, and appear centered on 90° in the figures. The H-plane cuts (shown in blue) exhibit the as-designed beam tilt of 30° relative to the aperture normal. Note how the beamwidths in the H-plane are about the same (corresponding to the in-common aperture length) while the E-plane beamwidths differ markedly due to the different number of channels.

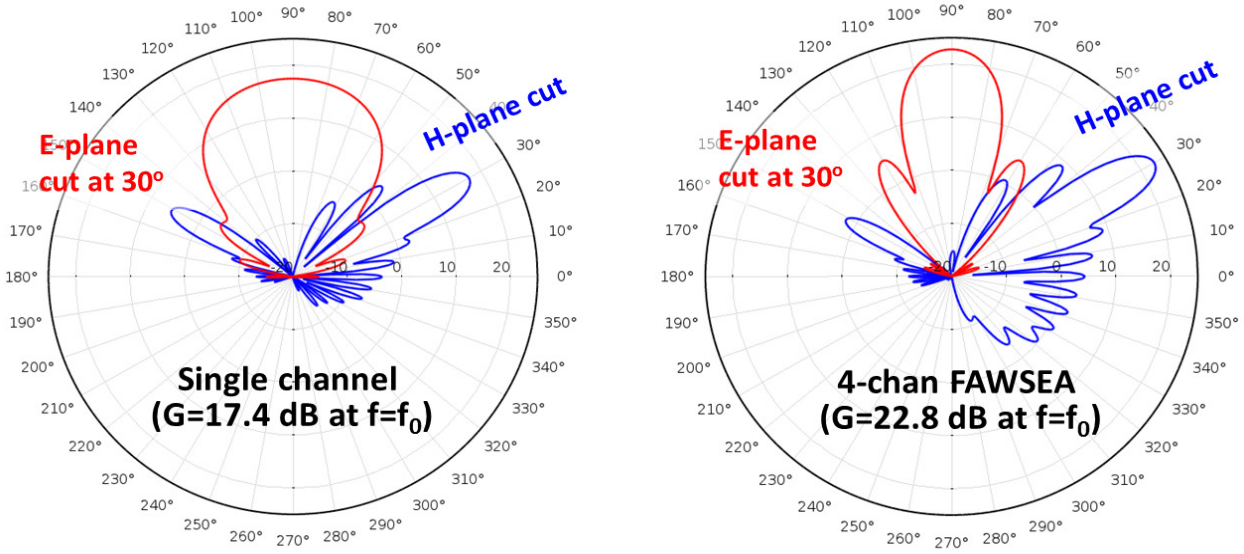


Figure 81. Principal-plane pattern cuts at f=f_0.

To round-out the analyses of these antennas presented so far, we provide images of the predicted 3D far-field patterns, at five frequencies {0.9x, 0.95x, 1.0x, 1.05x, and 1.1x} f_0, for the aforementioned antennas, in the figures to follow. Note that *unlike* the polar patterns in Figure 81, the gain plot ranges (min to max scale) of the 3D patterns that follow are not all the same; the reader is cautioned to use care when comparing different plots.

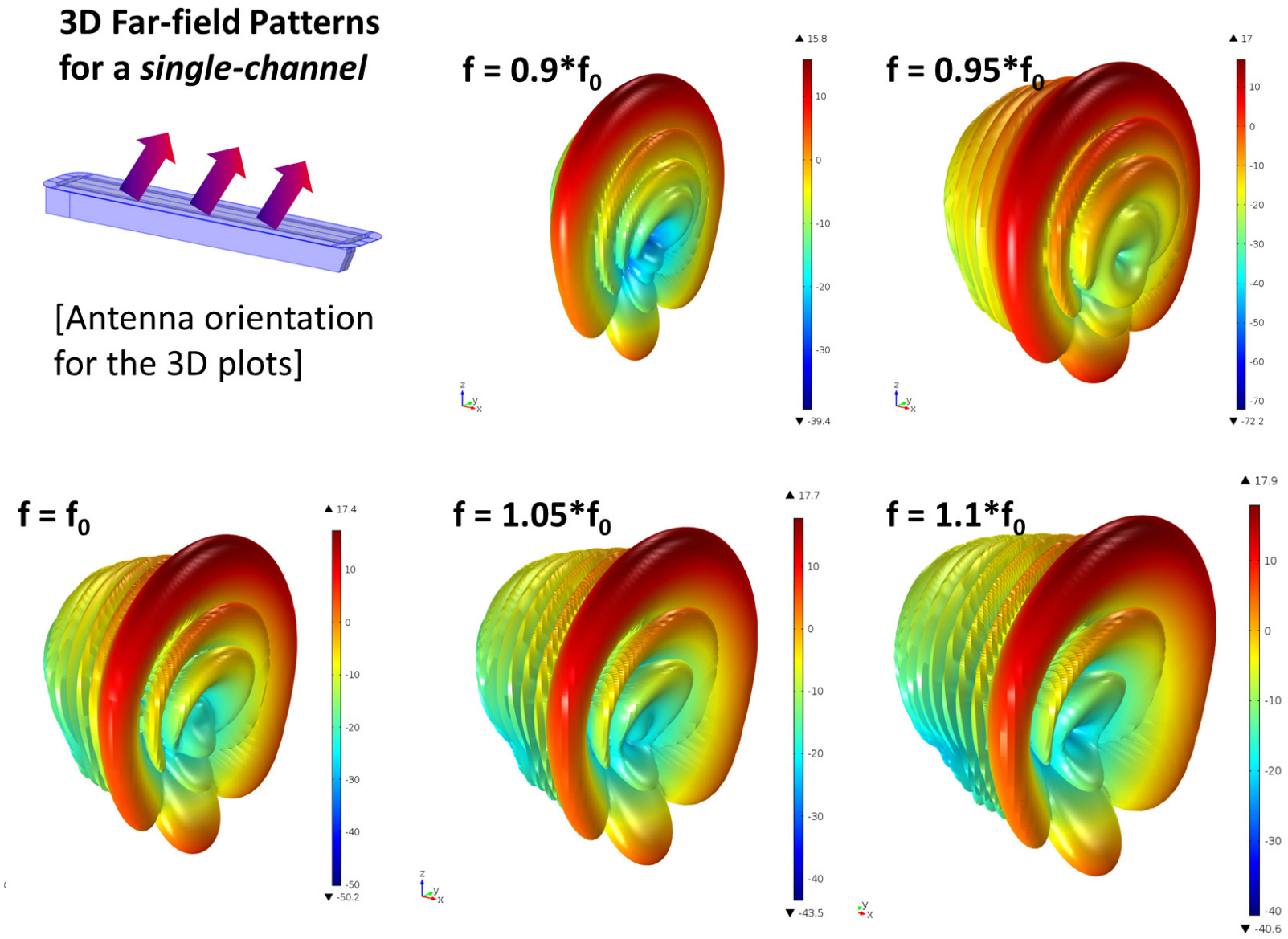


Figure 82. Selected 3D far-field patterns for a single-channel FAWSEA.

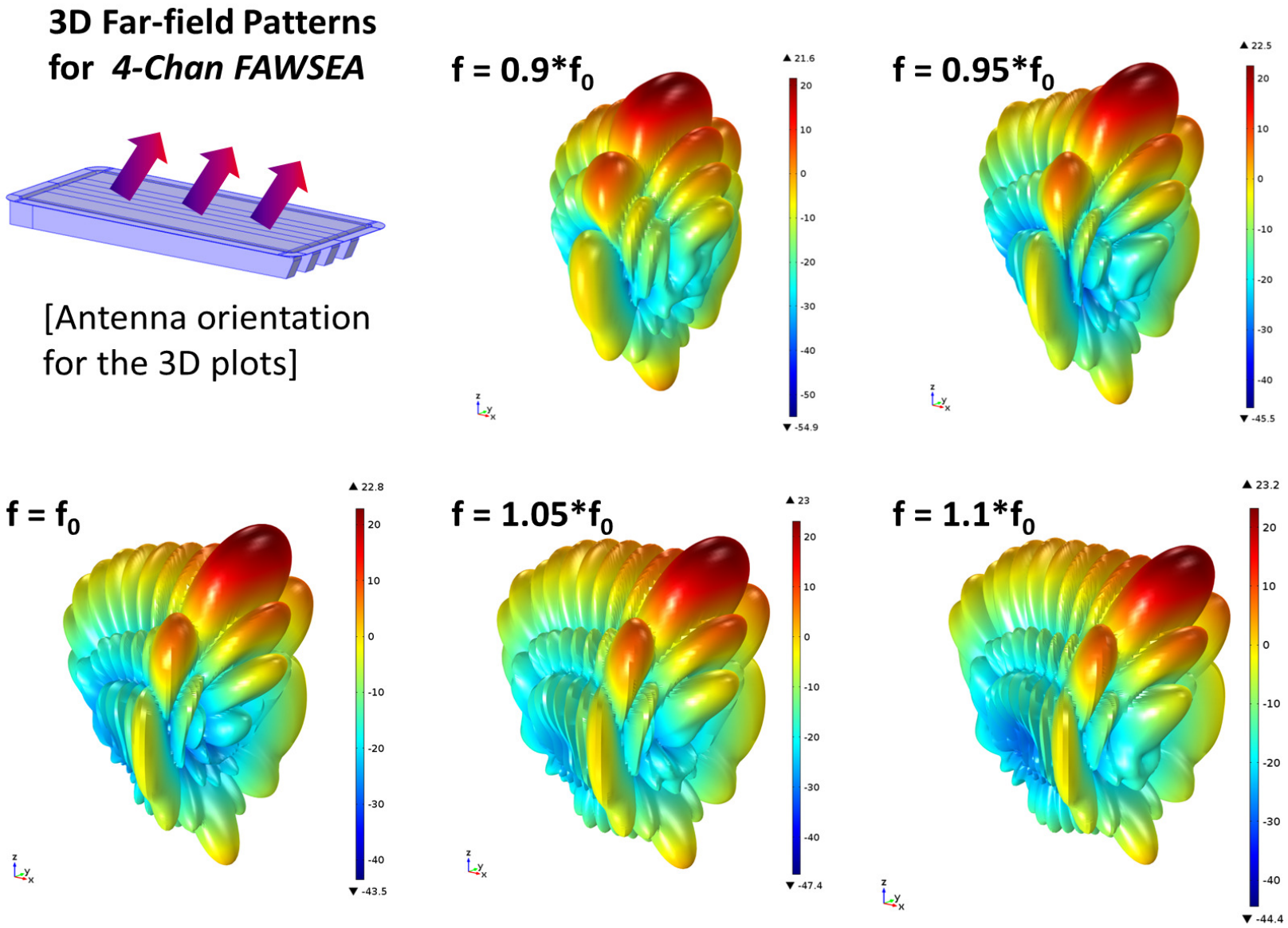


Figure 83. Selected 3D far-field patterns for a four-channel FAWSEA.

4.2.2. Steering a FAWSEA Beam in the E-plane by Phasing Multiple Channels

Although forward-traveling wave LWAs provide frequency-based beam scanning in the H-plane, one can also steer the beam in the E-plane, if individual phase control of multiple channels is available. Although this is not a common capability in the high power sources available today, there are a variety of new devices under development that may provide such capabilities in the future. An *example* concept for such a steerable antenna is shown in Figure 84. Steering with fixed delta-phase is shown in Figure 85.

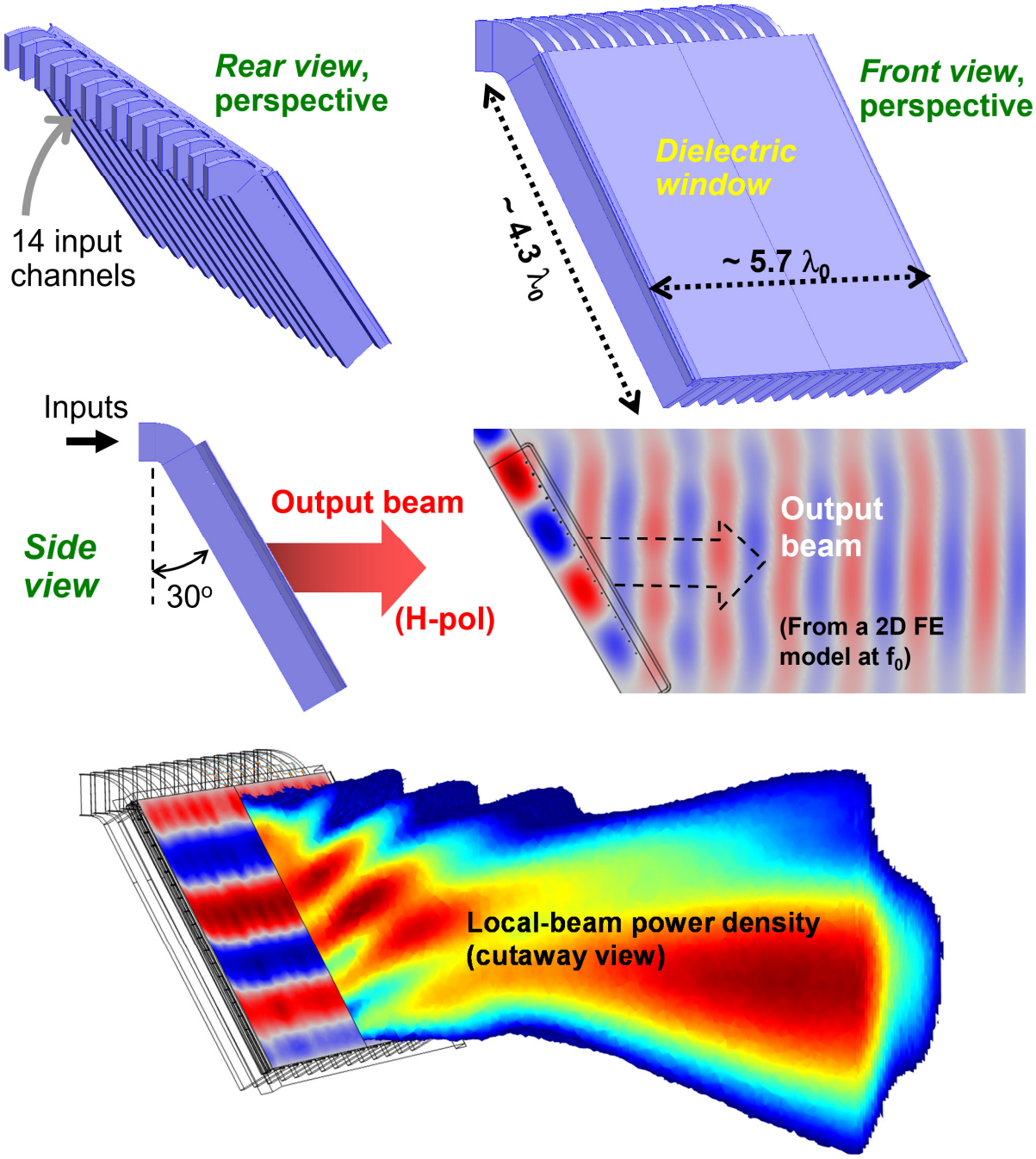


Figure 84. An example 14-channel Phase-Steerable HPM-Capable FAWSEA

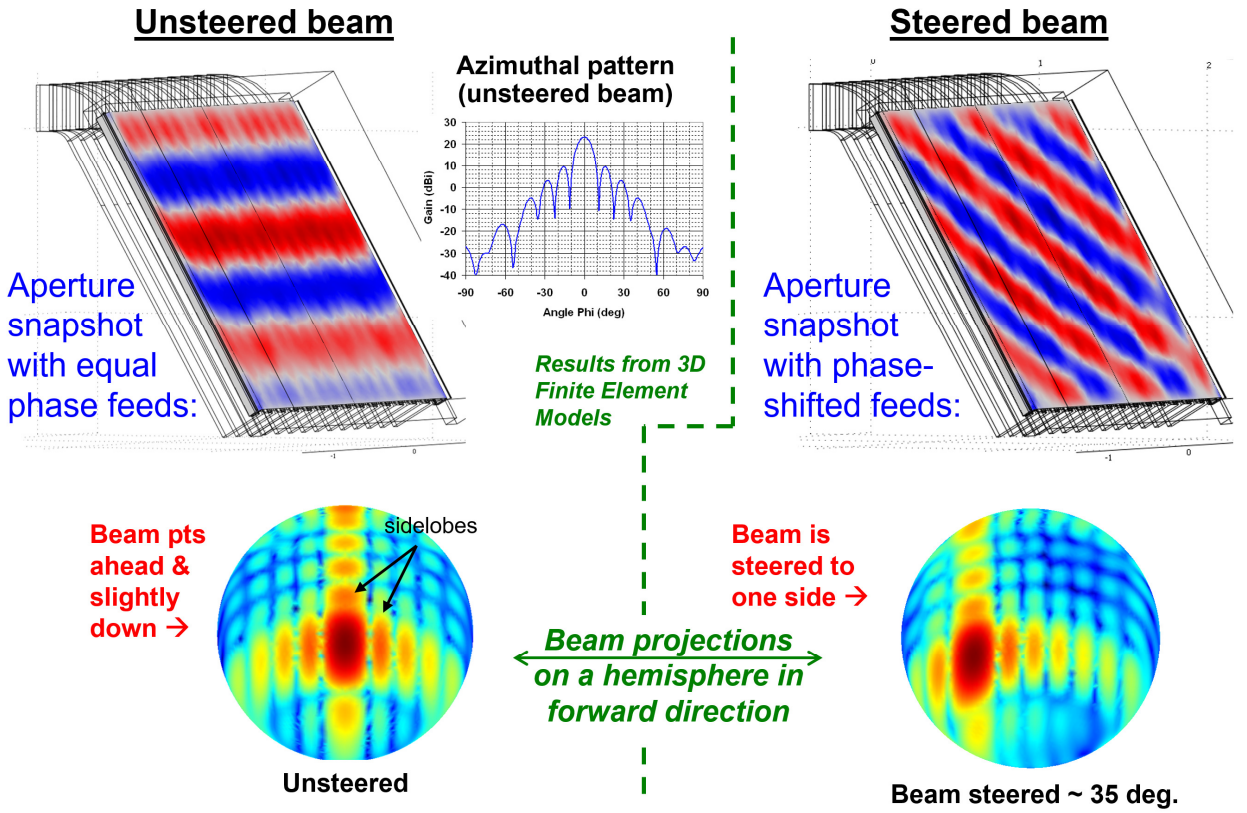


Figure 85. The output beam can be steered effectively via relative phasing the inputs.

Note that if phase-based steering is to be employed, the channel-to-channel spacing of a typical FAWSEA can generally be kept sufficiently tight that grating lobes can be avoided. In this regard, conventional array layout rules apply to the channel spacing; the designer should not allow him/herself to become confused by the presence of the in-common aperture and window region where the fields join together.

4.2.3. Rotation of the Waveguides to Yield a Lower Profile → the FRAWSEA

Although the FAWSEA offers an unusually-low profile for an HPM-capable antenna, it is possible to reduce this profile further, albeit at the cost of additional complexity in fabrication and in the feeding structures. Figure 86 compares cross-sections for three versions of four-channel leaky-wave antennas with flat apertures, all designed to the same center-frequency and shown on the same size scale. The *rotated* channels in the middle and right panels of the figure reduce the depth of the antenna compared to the non-rotated (FAWSEA) version. Our earlier "RAWSEA" concept (middle panel) had its basis in SARA R&D supported by the Air Force (AFRL), in late 2012. At that time, we rotated the leaky grill-wire plane along with the leaky-wave channel (middle panel, bottom). This conveniently maintained the rectangular cross-section of the leaky channel but increased separation between the window interface and grill-wire plane, introducing a quasi-free space transition section (the bend region). This complicated both the theoretical analyses and design[31] of the leaky wire grill. Although the antenna depth was substantially reduced, maintaining high aperture efficiency required placing the channels too close together to achieve a full 90° rotation of the channels. In contrast, the newer "FRAWSEA" configuration, shown in the right-hand

[31] Our *7th Quarterly Report* has the details. See http://www.dtic.mil/dtic/tr/fulltext/u2/a619768.pdf

panel, returns the leaky wire grill to its original FAWSEA-type position very near the window interface, while the bend (curved region) of the channel becomes explicitly part of the leaky waveguide. This allows us to reduce the lateral extension of the rotated channel for a given cutoff frequency.

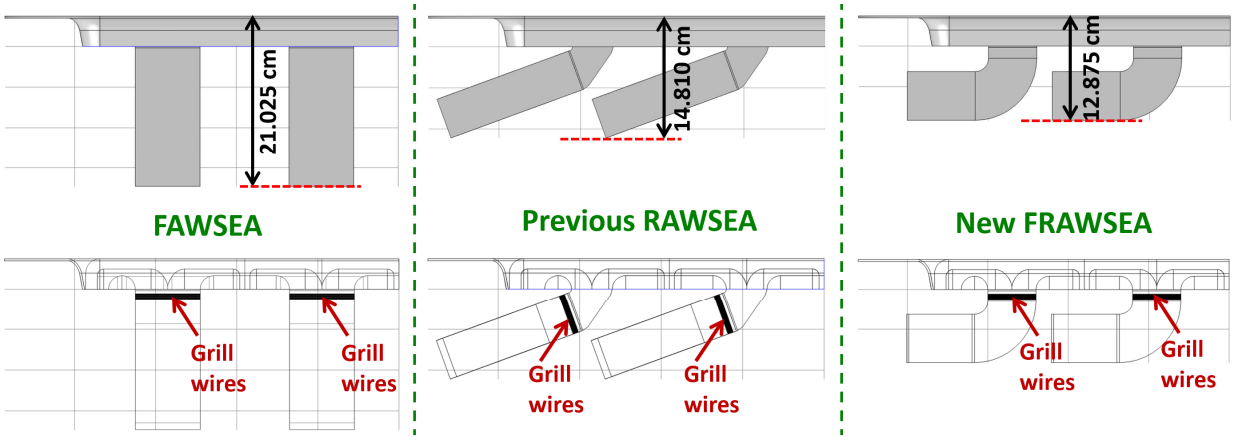


Figure 86. Cross-sections, shown to scale in solid and transparent views, for 4-channel flat-aperture designs with f_0 = 1.0 GHz. Only half of each cross-section (two channels) is shown. Left: FAWSEA. Middle: Previous RAWSEA design. Right: New FRAWSEA.

In fact, this change now means it is small enough to rotate the full 90° without bumping against an adjoining channel. And that yields the *lowest-profile configuration to date*. Not only that, but if the depth of the leaky channel is chosen carefully, the leaky wire grill algorithms used for defining the FAWSEA wire grill can now also be applied here, with minimal modification. The operating mode in the leaky guide is fundamental mode, with the field lines mapped to conform to the new cross-section. The quasi-free space region that complicated the interaction of the grill and window is now eliminated. The new FRAWSEA cross-section in Figure 86 (right), is less than 0.43 λ_0 thick.

In exchange for this packaging advantage, one must address the following: (1) the leaky waveguides do not present simple rectangular cross-sections for connection to the antenna, and (2) there is some new field enhancement internally in the waveguide structure along the smaller radius of the cross-sectional bend. The former can be addressed by means of a custom transition section (which we will discuss shortly) added to the feed, to provide a rectangular guide. The aforementioned field enhancement does not appear to be serious in our candidate configurations; rather, external air breakdown continues to define the upper bound to the overall peak-power handling.

We have prepared 3D RF models and predicted performance curves for our suggested/recommended FRAWSEA design, leveraging this new cross section and are pleased to report that it works fairly well, at least based on numerical models. Figure 87 shows views of an example *single-channel* FRAWSEA, from a 3D RF model. The key parts of this example are usable as building blocks for an array, in much the same way as was done with the FAWSEA designs documented earlier in this report.

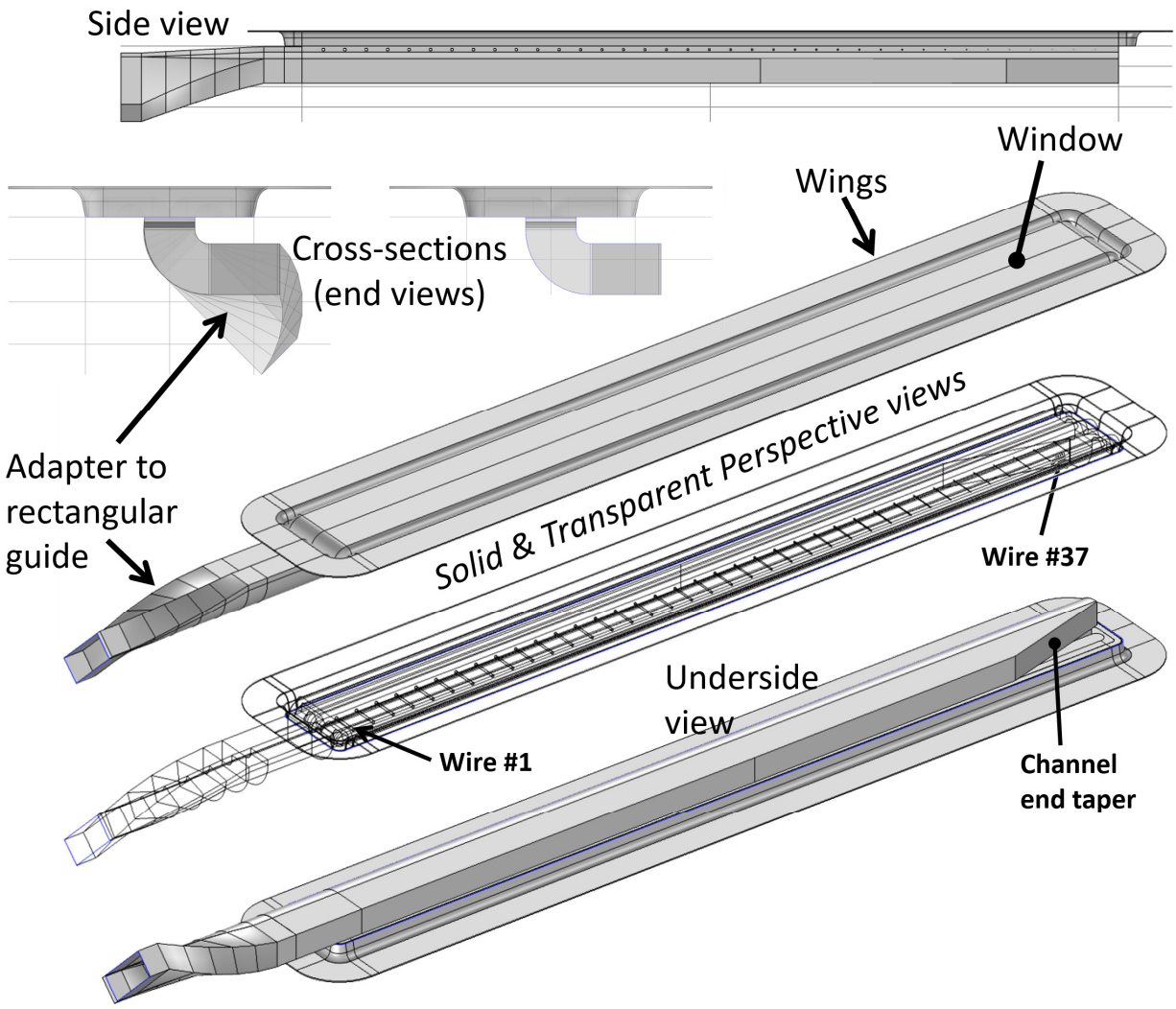


Figure 87. Views of a single-channel FRAWSEA, including a waveguide smooth tapered transition / adapter to facilitate practical connection to a rectangular waveguide.

As with the FAWSEA, an array (a multi-channel FRAWSEA) can be prepared by including appropriate channel-to-channel spacing, joining channels judiciously, extending the aperture window to span multiple channels, and revising the wings to fit around the overall wider aperture. Arrays with either *translational* or *mirror* symmetry employing such rotated channels are possible. The proper choice depends on what is most convenient for packaging and interfacing to the HPM source of interest. It should go without saying that care should be taken in setting the field-orientations at the input, so that the waves at the leaky walls of the individual channels are properly in phase at the aperture; embarrassing errors are easily avoidable by diligently following along the waveguide curves. A four channel FRAWSEA (with mirror symmetry, in this case) is shown in Figure 88, and is hereby denoted a "suggested/recommended" design. Just as with the other antennas described in this report, a wide variety of sizes and aspect ratios are realizable.

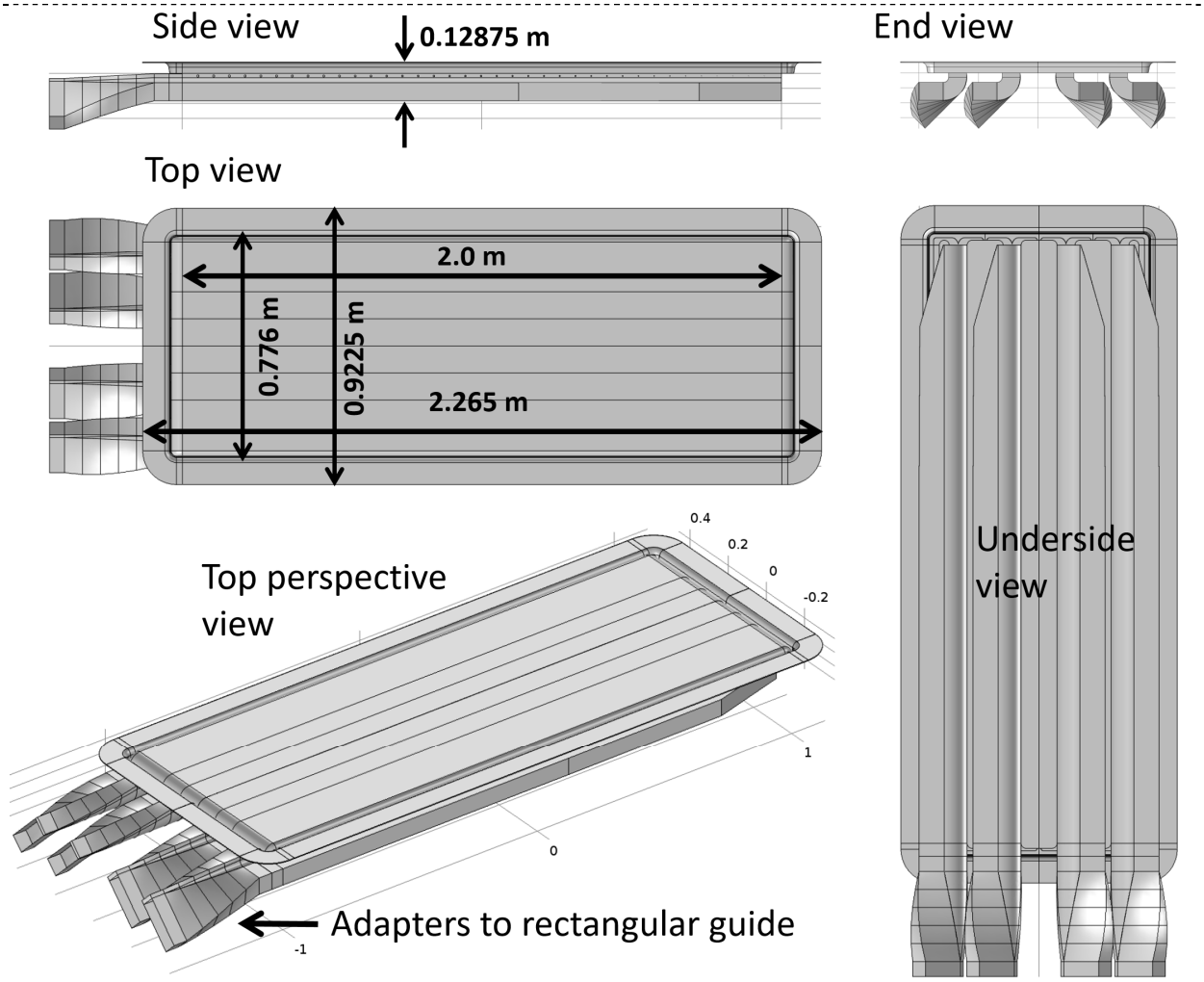


Figure 88. Example four-channel FRAWSEA designed for f_0=1.0 GHz and employing mirror-symmetric feeds. Tapered waveguide transitions/adapters are used to allow practical connection of the antenna to rectangular waveguides.

Figure 89 tabulates diameters and positions for the 37 wires comprising the leaky-grills of the FRAWSEAs in Figure 87 and Figure 88. Wire sizes were derived from the FAWSEA wire-grill generation routines, but the last few values (#s 35-37) were replaced with those from wire #34. This helped to reduce (but

FRAWSEA wire grill info. Grill wire centers are at -.91 cm vert from top of chan.

Grill wire index	Distance along the aprtr (cm)	Grill wire dia (mm)	…continued: Grill wire index	Distance along the aprtr (cm)	Grill wire dia (mm)	…continued: Grill wire index	Distance along the aprtr (cm)	Grill wire dia (mm)
1	5.25	7.010	14	73.50	5.530	26	136.50	3.183
2	10.50	6.918	15	78.75	5.382	27	141.75	2.907
3	15.75	6.823	16	84.00	5.229	28	147.00	2.613
4	21.00	6.725	17	89.25	5.068	29	152.25	2.299
5	26.25	6.624	18	94.50	4.899	30	157.50	1.966
6	31.50	6.519	19	99.75	4.723	31	162.75	1.612
7	36.75	6.411	20	105.00	4.537	32	168.00	1.240
8	42.00	6.299	21	110.25	4.341	33	173.25	0.859
9	47.25	6.182	22	115.50	4.135	34	178.50	0.489
10	52.50	6.062	23	120.75	3.917	35	183.75	0.489
11	57.75	5.937	24	126.00	3.687	36	189.00	0.489
12	63.00	5.806	25	131.25	3.443	37	194.25	0.489
13	68.25	5.671						

Figure 89. Grill wire diameters and locations along leaky grill.

did not eliminate) a tendency to form a hot spot (high E) on the aperture near the termination end of the channel. We found it helpful to use a more aggressive taper at the channel end (see underside view in Figure 87) than would normally apply for a comparable FAWSEA. Computed patterns for the antenna in Figure 88 at f = 0.95 f_0, 1.0 f_0, and 1.05 f_0, are given in Figure 90. This model includes the custom feeds.

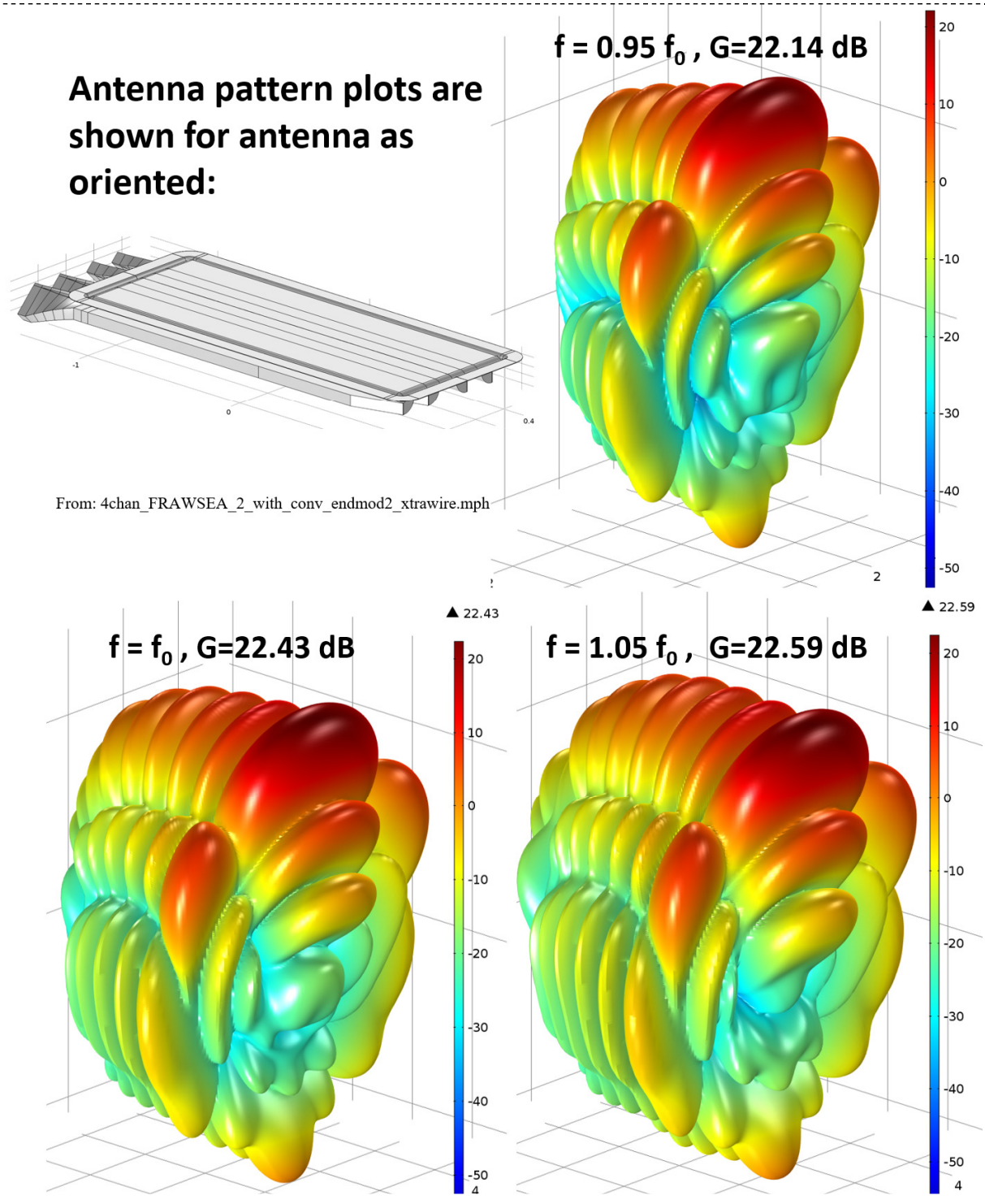


Figure 90. Computed 3D antenna patterns, four-channel FRAWSEA at 3 frequencies.

Some important performance characteristics for this FRAWSEA vs. frequency are shown in Figure 91.

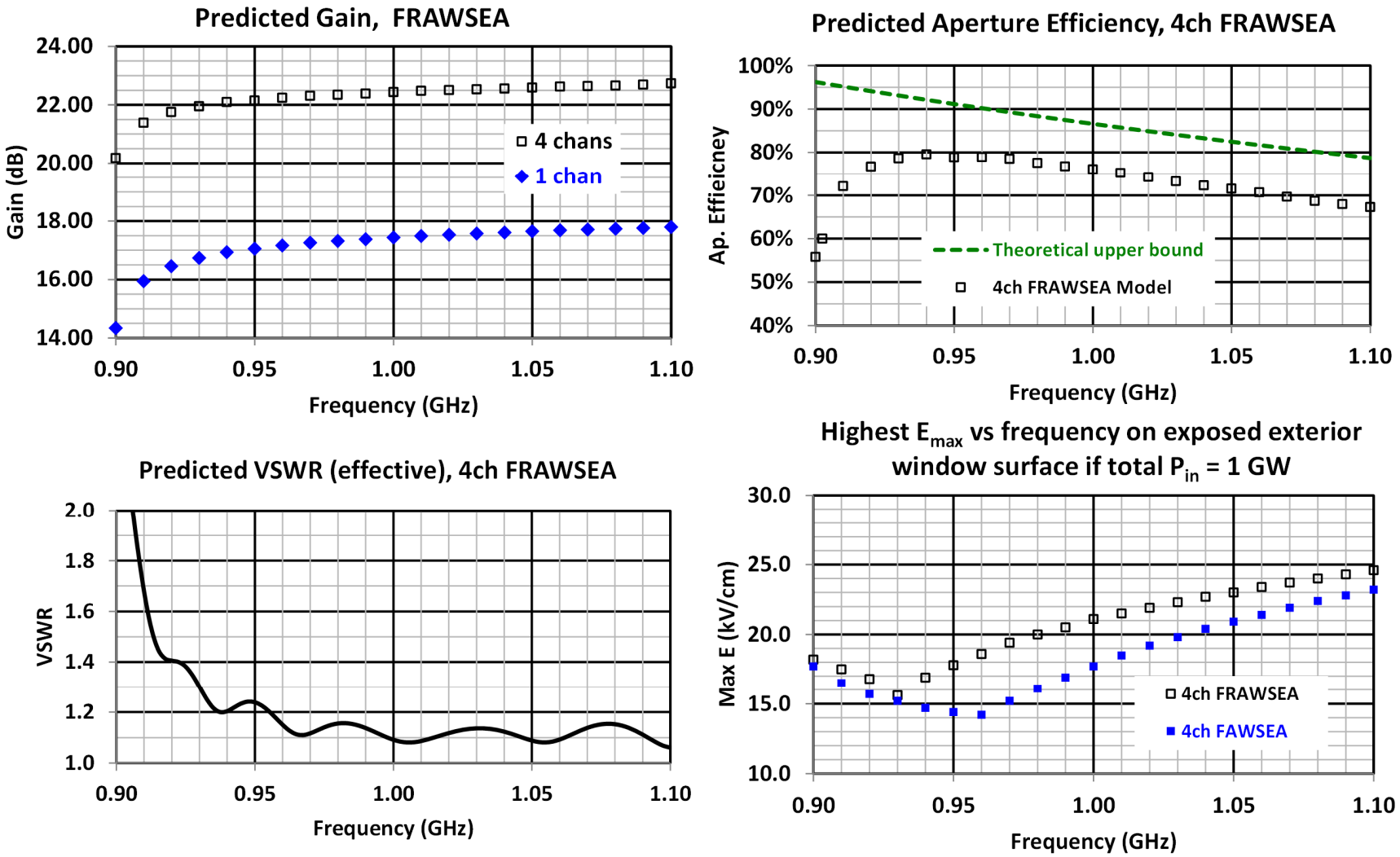


Figure 91. Predicted performance vs. frequency for the 4-channel FRAWSEA (includes waveguide adapters) of Figure 88.

The curves in Figure 91 compare respectably to those of the other suggested/recommended leaky-wave designs in this report, in terms of gain, bandwidth, and more. The beam tilt angle relative to the aperture normal likewise follows the theoretical curve fairly well (see Figure 92), though not quite as perfectly as our standard/ recommended FAWSEA. Figure 93 provides a comparison of polar plots taken in the E and H planes at $f=f_0$, for a FAWSEA and FRAWSEA of essentially the same aperture dimensions. The pattern differences are very small. Although it is subtle to see from these plots, the FRAWSEA beam is tilted at a 29.37° angle relative to the normal, rather than at 30.0° like the FAWSEA, and the FRAWSEA delivers ~0.37dB less gain.

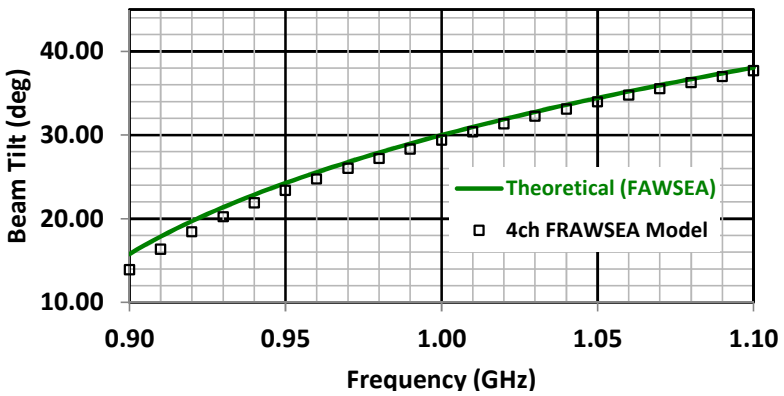


Figure 92. FRAWSEA Beam tilt vs. Frequency

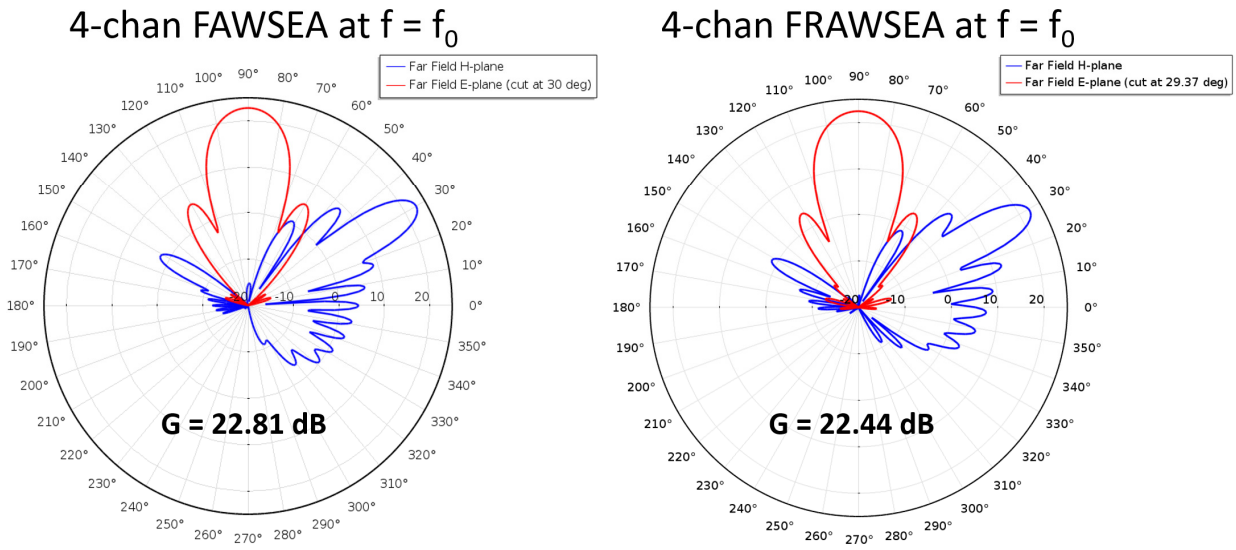


Figure 93. Polar E- and H-plane pattern cuts at $f=f_0$ for our recommended 4-channel FAWSEA (left) vs. the new recommended 4-channel FRAWSEA (right). (Same scale.)

Some, but not all of the predicted performance differences between the FAWSEA and FRAWSEA arise from the waveguide adapter/transition sections added to the FRAWSEA. The rest we attribute mostly to the field distributions in the FRAWSEA leaky waveguide incident at the wire-grill being somewhat less than ideal, due to the wave passage around the bend immediately adjacent to that wire-grill interface. Regardless, given its excellent predicted performance overall, the new FRAWSEA represents an option to be seriously considered wherever an especially low-profile high-gain HPM-capable antenna is needed.

4.3. CAWSEA

4.3.1. A Recommended CAWSEA Design

A recommended 4-channel CAWSEA design is described below. As with the FAWSEA, this design was developed and sized for f_0=1.0 GHz and dimensions may be scaled linearly with λ_0 to support other RF/microwave frequencies. The four-channel CAWSEA in Figure 94 and Figure 95 is derived from the single-channel and four-channel FAWSEA design. Key features such as channel depth, width, wire sizes, wire spacing, and channel tapering along the length (see Section 4.2.1) are reused in the recommended 4-channel CAWSEA. However, in the CAWSEA, the channels are oriented radially rather than parallel, and there is additional curvature/shaping in the aperture region otherwise not present in the FAWSEA. The aperture window is again polyethylene, with $\varepsilon_r = 2.26$ assumed. Extending the feed guides to the center channels (see Figure 96) compensates, in part, for aperture-curvature induced phase error (and the decrease in gain) that would otherwise occur. Since *uncompensated* CAWSEA configurations offer significantly reduced performance we do not recommend their use, but some of their characteristics are also documented here.

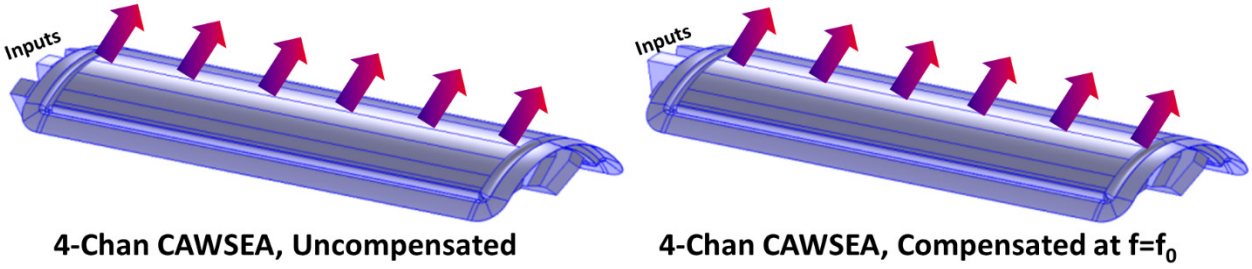


Figure 94. CAWSEA. Left: Uncompensated. Right: Compensated for aperture curvature.

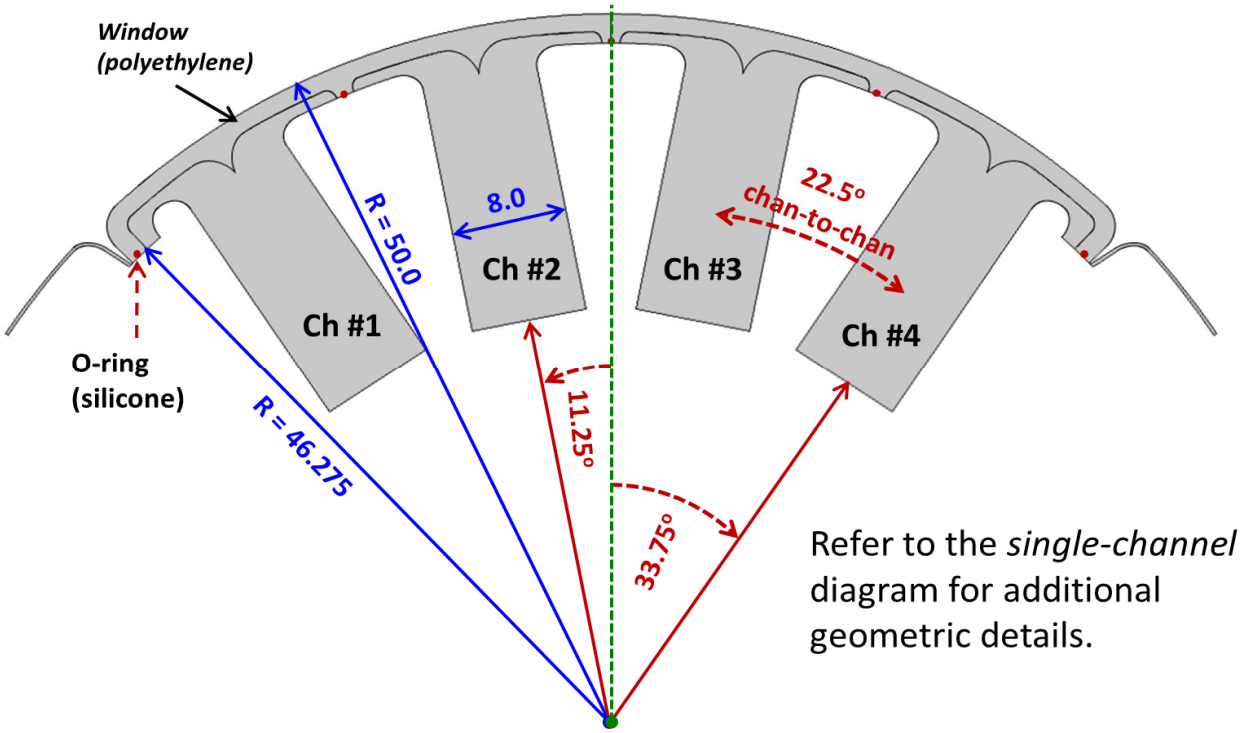


Figure 95. Four channel CAWSEA cross-section (not tapered) for f_0=1 GHz. Units are cm.

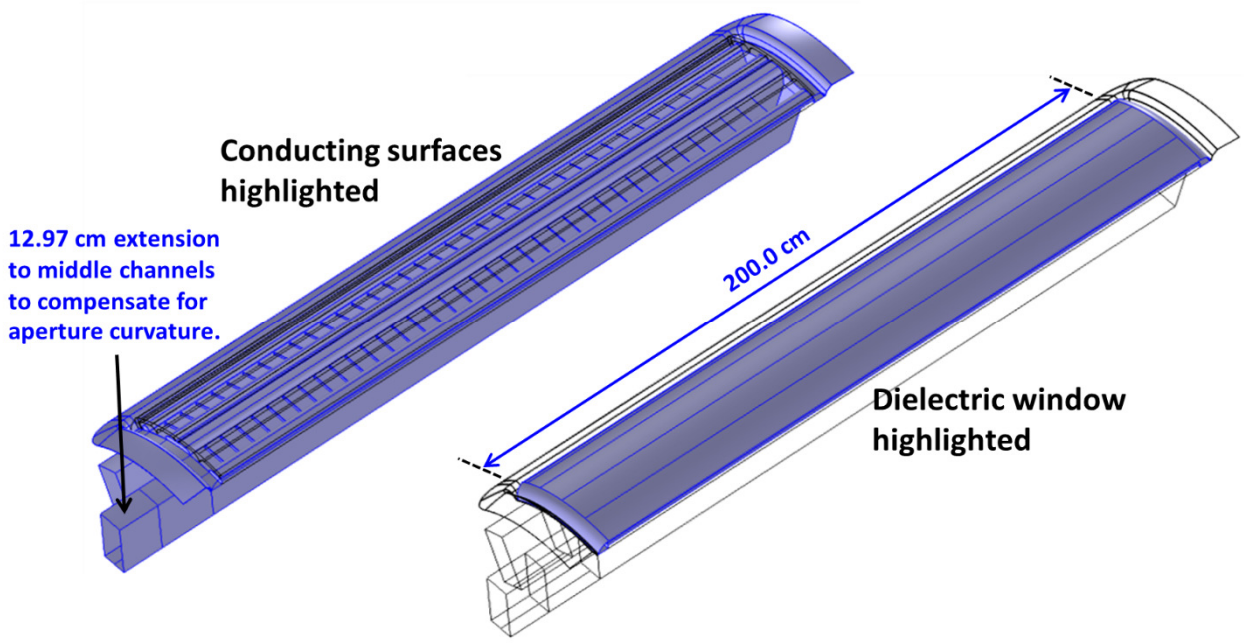


Figure 96. Half of a 4-channel compensated CAWSEA, sliced along its symmetry plane.

4.3.1.1. Predicted Performance Characteristics

Predicted performance characteristics are described below. In addition, we will contrast some of the performance characteristics of the compensated CAWSEA (i.e., including the waveguide extension in Figure 96) with an uncompensated version. The computed effective VSWR for the aforementioned antennas is plotted in Figure 97. In this case, since we found minimal differences in comparing VSWRs of the compensated and uncompensated versions of the CAWSEA, only the former is shown in Figure 97. In contrast, substantial differences are observed in the gains, as noted in Figure 98.

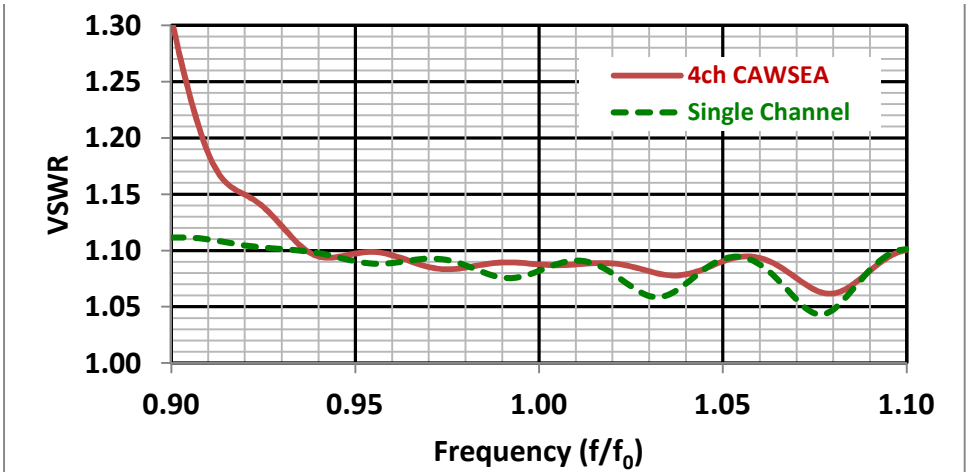


Figure 97. Computed Effective VSWR vs. Frequency

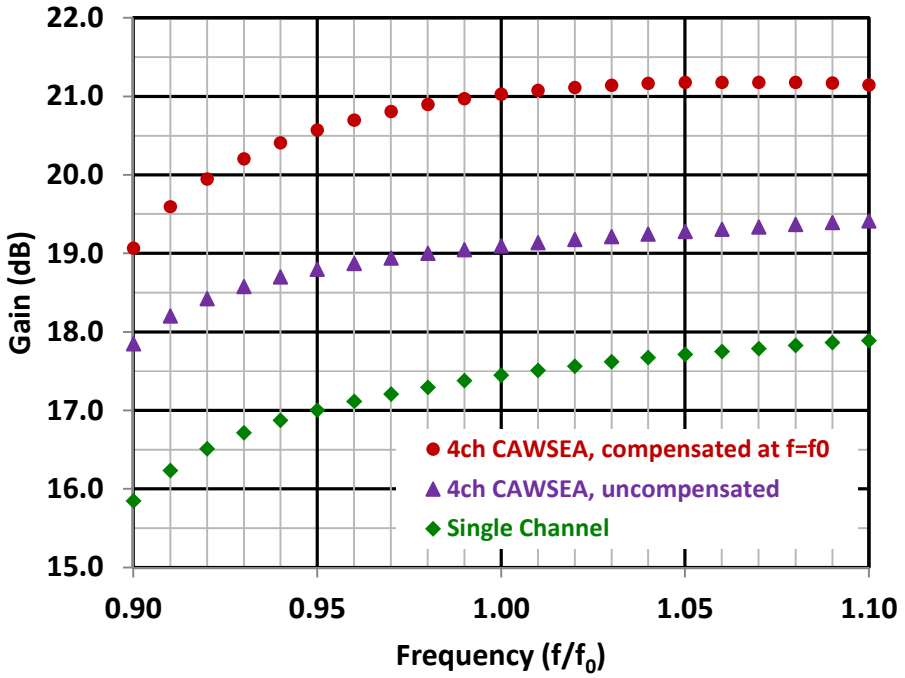


Figure 98. Computed Gain vs. Frequency

A comparison of predicted aperture efficiencies of the CAWSEA and FAWSEA is shown in Figure 99.

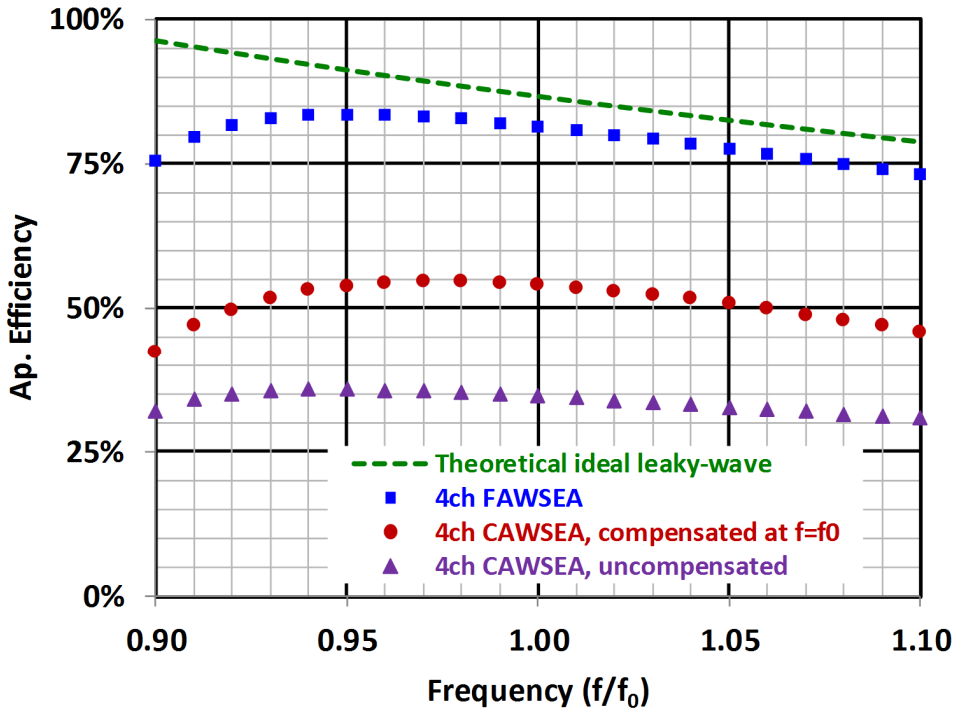


Figure 99. Predicted Aperture Efficiency vs. Frequency.

The aperture efficiency of the *compensated* CAWSEA is not as high as that of the FAWSEA, but is still respectable, and exceeds 50% over a considerable bandwidth. In contrast, the aperture efficiency of the *uncompensated* CAWSEA suffers all the classic consequences of entirely-uncorrected aperture curvature. One can assess the channel arraying efficiency by comparing the curves in Figure 98. *Ideally*, arraying four channels would deliver +6.02 dB more gain than a single channel alone. At $f=f_0$, the uncompensated

and compensated CAWSEAs yield increased gain of +1.64 dB and +3.58dB, respectively, vs. that of a single channel. Figure 100 shows phase-snapshots of surface electric fields on the windows of uncompensated and compensated CAWSEAs (half-models shown).

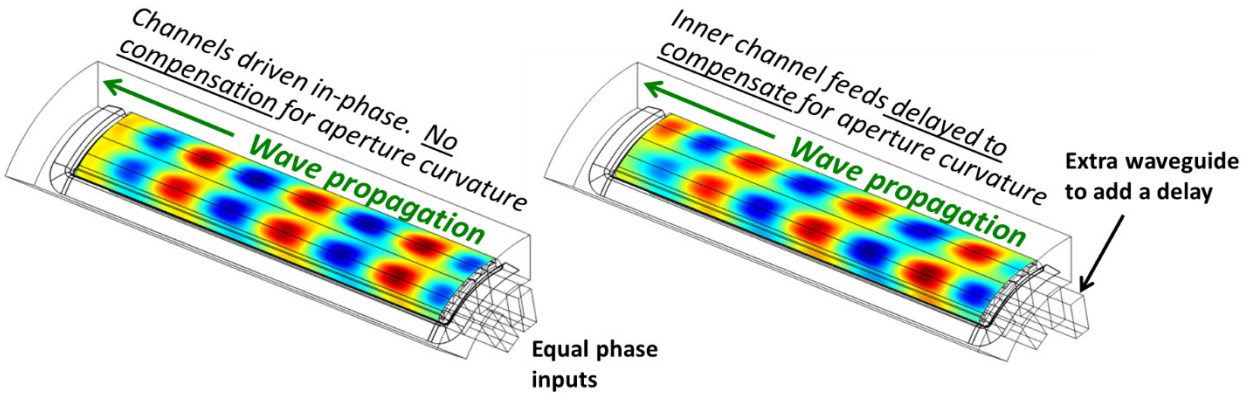


Figure 100. Aperture E, uncompensated (left) vs. compensated (right) CAWSEA at f_0.

Fortunately, the "shear" introduced to the aperture field distribution on the surface of the compensated CAWSEA does not appear to yield troublesome "hot-spots" that might encourage breakdown. Figure 101 shows[32] predicted peak electric field values on the exterior aperture surfaces for the 4-channel CAWSEAs vs. frequency, corresponding to a total input power of 1.0 GW (i.e., 250MW per channel) For more than half of the frequency range, the compensated CAWSEA's peak surface fields are actually less than those in the uncompensated configuration. The CAWSEA beam tilt is similar to that of the FAWSEA and is not reproduced here.

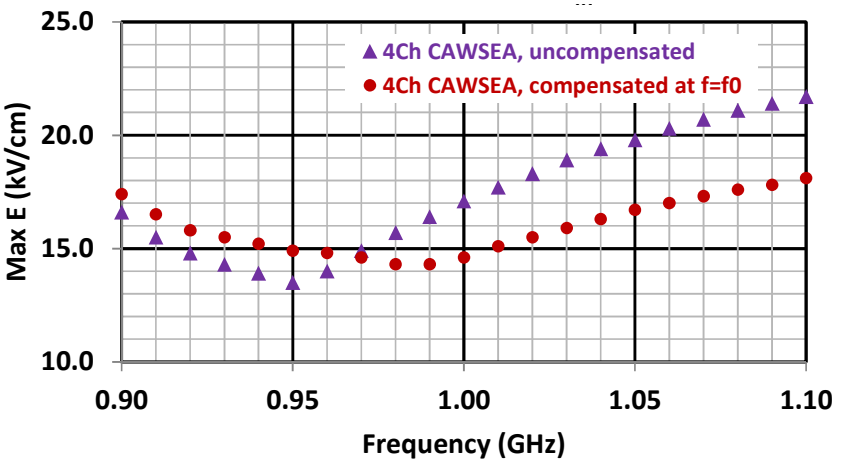


Figure 101. Peak values of E_{max} vs. frequency on exposed exterior window surfaces, for total input power = 1 GW.

Principal-plane polar far-field pattern cuts for the subject antennas at $f=f_0$ are shown in Figure 102. The E-plane cuts (shown in red) are at a 30° angle relative to the aperture normal, so as to slice through the beam peak, and appear centered on 90° in the figures. The H-plane cuts (shown in blue) exhibit the as-designed beam tilt of 30° relative to the aperture normal. Again, note how the beamwidths in the H-plane are about the same (corresponding to the in-common aperture length) while the E-plane beamwidths vary markedly, in this case due to the relative effective phase uniformity in the plane-projected aperture field distribution as looking across the narrower dimension of the antenna. The advantage of including the compensation (extra delay to the middle feeds) is clear.

[32] As before, if scaling to other center (f_0) frequencies, the field values in Figure 101(with P_{in}=1 GW held fixed) scale proportional to $(f_{0,new}/1.0\ GHz)^2$. In general for HPM, strive to keep E_{max} < 30 kV/cm on the exterior.

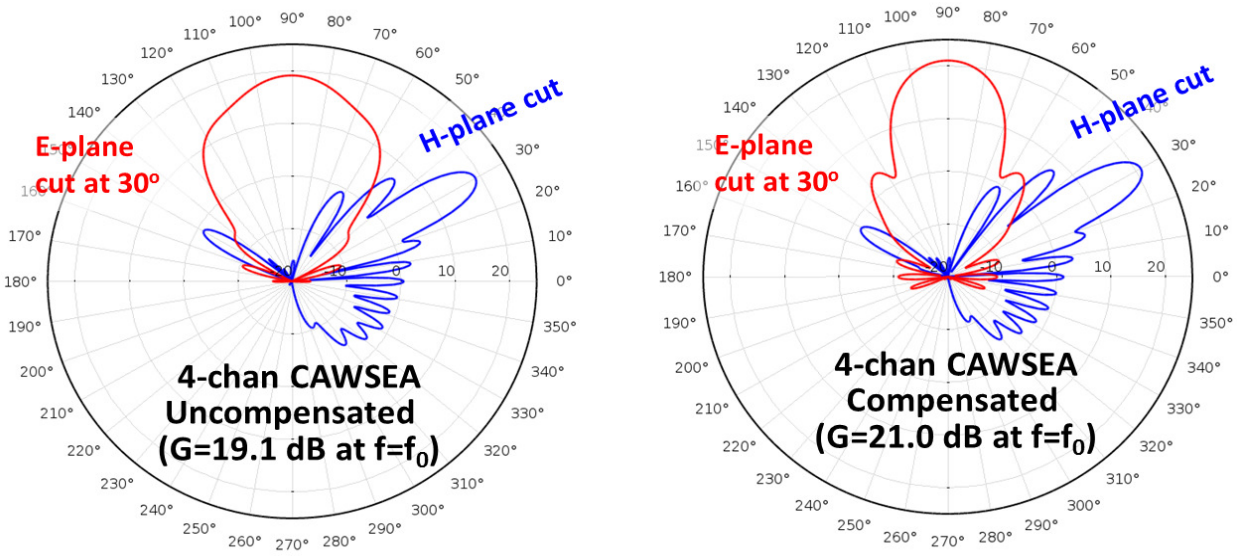


Figure 102. Principal-plane pattern cuts at $f=f_0$.

To round-out the analyses, we provide images of the predicted 3D far-field patterns, at five frequencies {0.9x, 0.95x, 1.0x, 1.05x, and 1.1x} f_0, for the uncompensated and compensated antennas, in Figure 103 and Figure 104, respectively. Note that *unlike* the polar plots in Figure 102, the gain plot ranges (min to max scale) of the 3D patterns that follow are not all the same; the reader is cautioned to use care when comparing different plots.

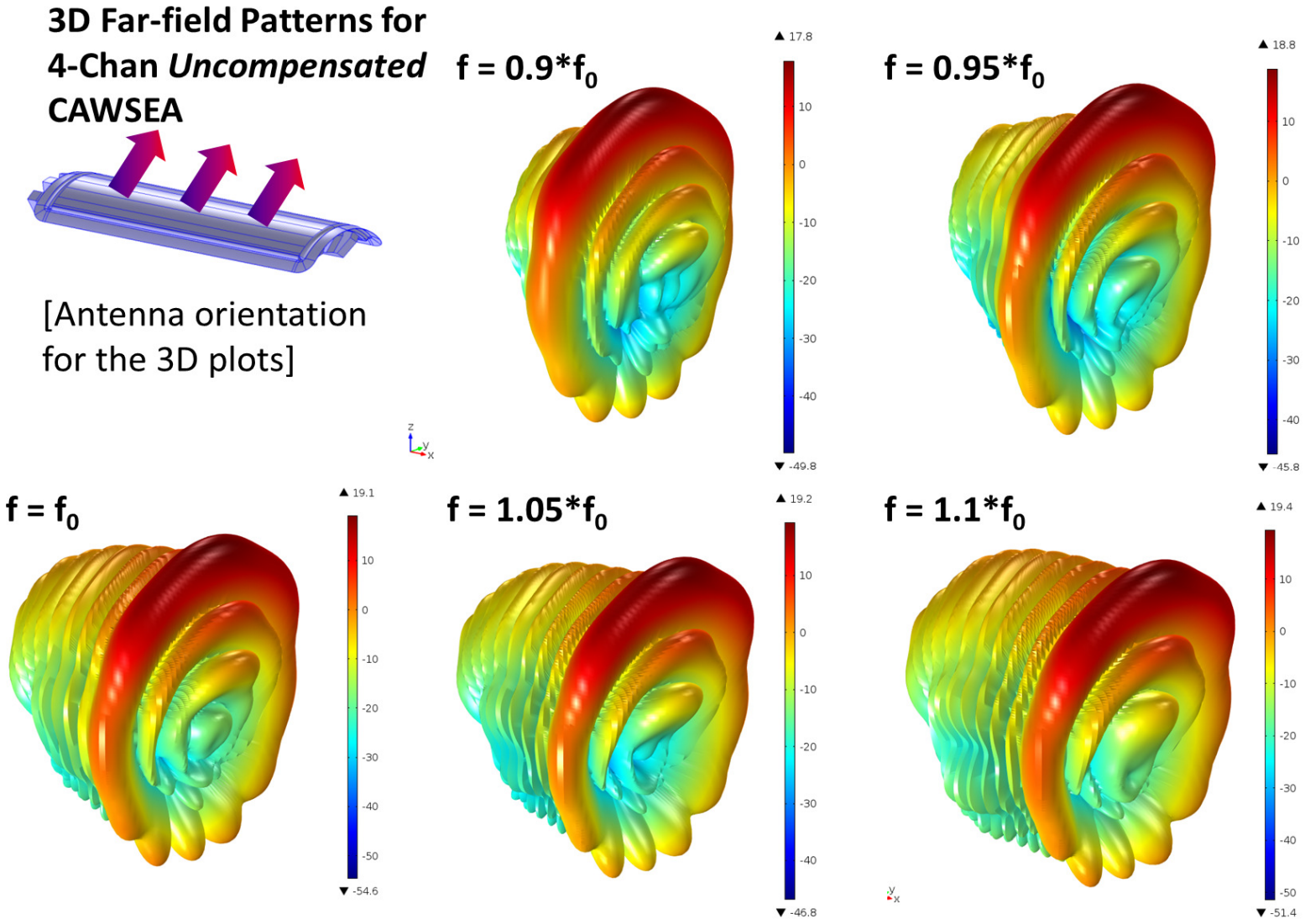


Figure 103. Selected 3D far-field patterns for a four-channel *uncompensated* CAWSEA.

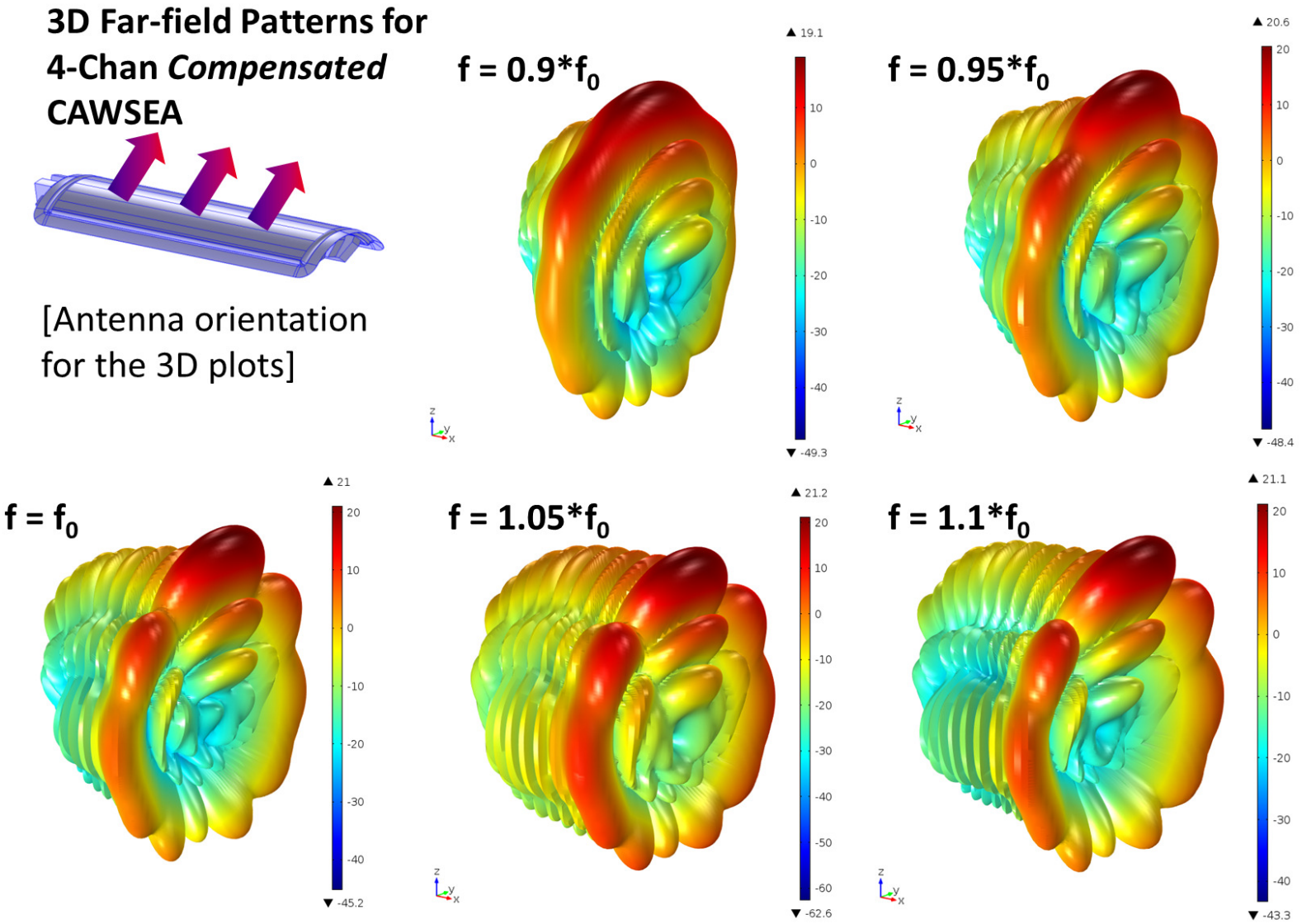


Figure 104. Selected 3D far-field patterns for a four-channel CAWSEA compensated at $f=f_0$.

4.3.2. Taking Advantage of a Greater Fraction of a Cylindrical Surface → CAWSEA$_{180}$

Recalling the noticeable improvement in gain due to better-utilization of the non-shadowed half of a cylinder (Section 4.1.10, top rows of Figure 67 and Figure 68) suggests that our recommended/standard CAWSEA design in Section 4.3.1 does not take full advantage of the available[33] surface of a complete cylinder. So let's revisit that design and consider extending the cross-sectional arc-length to a full 180^o wrap. The *simplest* way to attempt this is to merely add more channels, as shown in Figure 105.

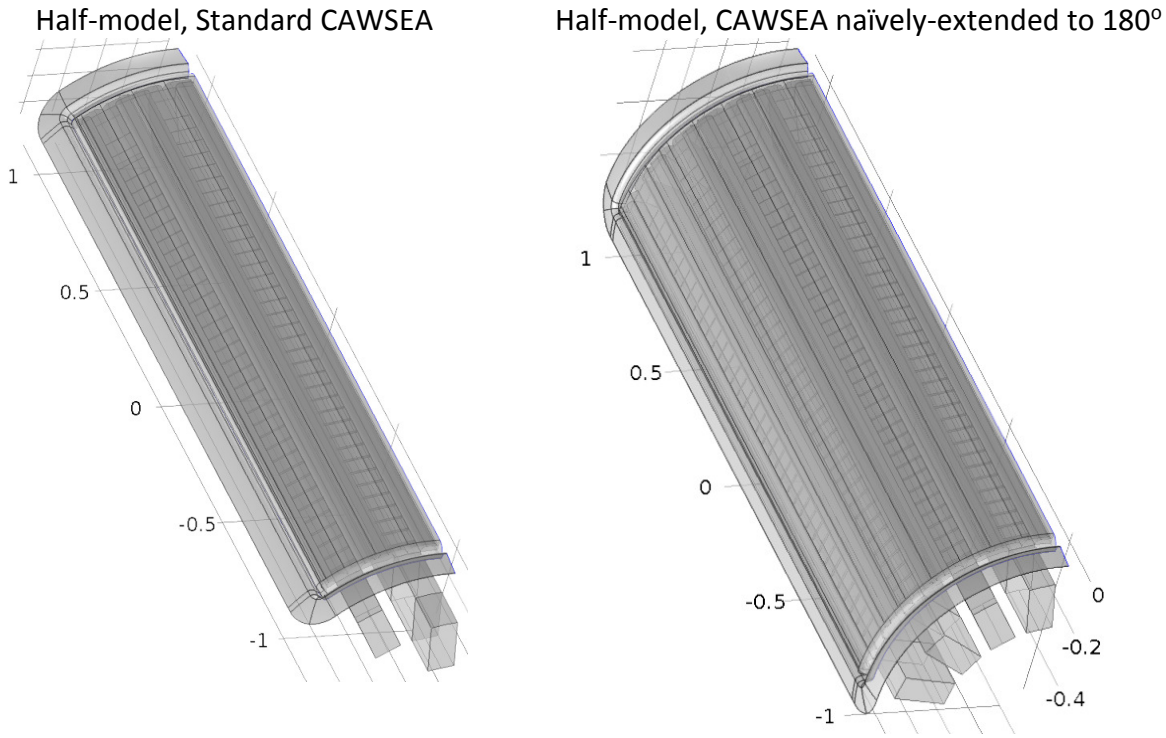


Figure 105. Naïve extension of our standard CAWSEA design (left) to a full 180^o half-cylinder. (Half models shown above, using symmetry). Phase-correcting feeds are not shown in the right-hand panel, but phase-correction was investigated (see text).

This naive approach *fails*. The aperture-phase correction required in our recommended CAWSEA is small enough that it can be moderately-approximated via the channel-discretization shown above/left. But that approximation fails for the aperture on the right in Figure 105; there does not appear to be any way to phase these eight discrete channels (four in each half) to compensate adequately. Regardless of phasing, the gain resulting from this aperture is actually *less,* despite its 2x-larger physical surface area.

Fortunately, there is a solution. Figure 106 shows a version of a "16-chan CAWSEA$_{180}$," where we employ channels half as wide and twice as densely-packed as in the "4-chan CAWSEA$_{90}$." Wire sizes and spacings in the narrower channels were unchanged (not re-optimized) to reduce design time for this configuration. The more closely-packed channels suffer in terms of increased cross-channel coupling and greater VSWR, but the purpose here was merely to see if there can exist a buildable configuration with enhanced performance (more gain, in this case) relative to the earlier design, yet conform to the same diameter cylinder. The simple channel layout in Figure 105 fails in that regard, but the layout in Figure 106 is a success worthy of additional study and optimization. Since the phase corrections required in the feeds are large, and optimized at only one frequency, a design like this offers reduced bandwidth (e.g., +/- 5% vs. +/- 10%) compared to the design in Section 4.3.1, but may still be useful in many circumstances.

[33] In practice, integration of other platform hardware, including waveguide plumbing, may also limit aperture sizes. But it is still valuable to understand limits imposed by the platform exterior, independent of other packaging issues.

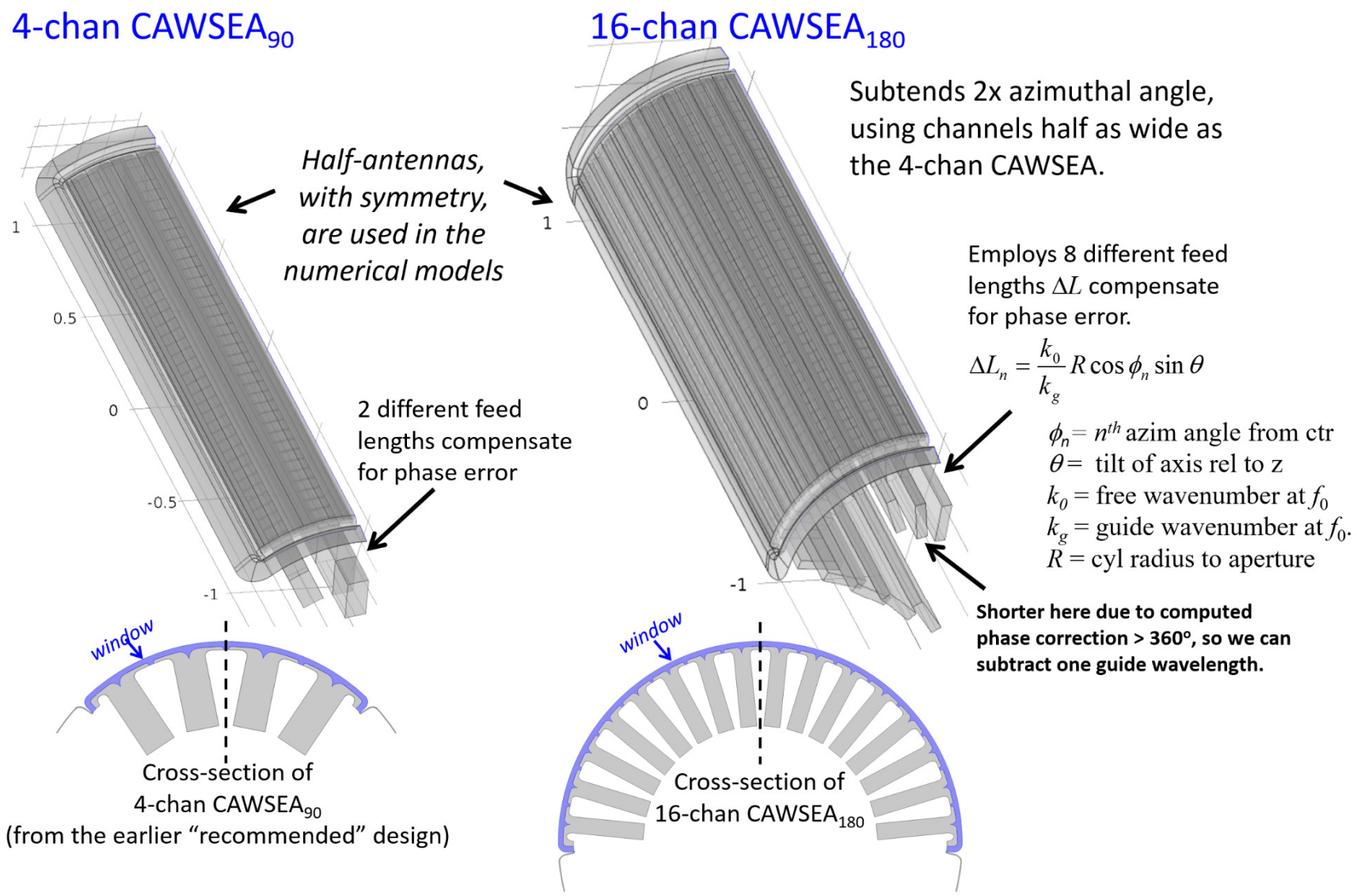


Figure 106. Geometry comparison, the "recommended" 4-chan CAWSEA$_{90}$ vs. an alternative 16-chan CAWSEA$_{180}$

Figure 107 compares computed 3D gain patterns at f=f_0 (1 GHz). The 16-chan CAWSEA$_{180}$ delivers about 2.6 dB more gain, which is a *major improvement* (i.e., >80% more power density on a distant target, for a given source power). The E-plane pattern is narrower, corresponding to the higher gain. There is a more prominent, but not too severe, rear sidelobe due to greater reflections from the terminating end. We suspect this reflection can be reduced via some design adjustments.

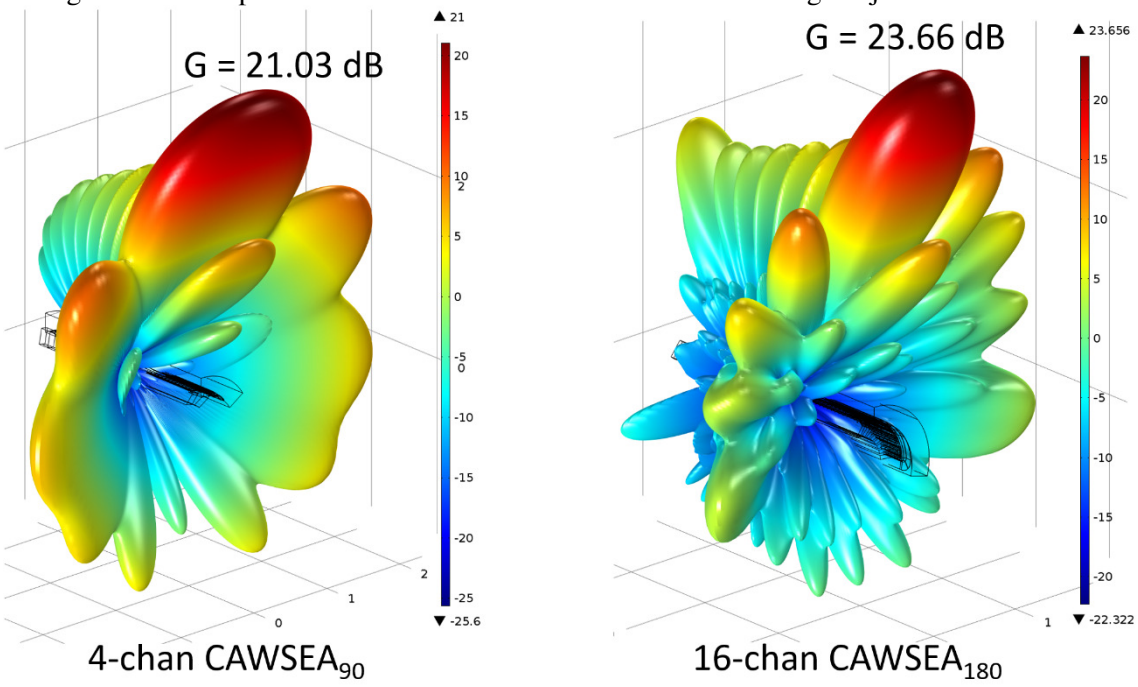


Figure 107. 3D gain patterns at f=1.0 GHz. Phase-compensated CAWSEAs. (RF model outlines are included in the images, to clarify the antenna orientation.)

Figure 108 compares the computed achieved aperture phase distribution vs. the ideal one. There is clearly room for improvement in several spots, but the aperture distribution overall is a fair match.

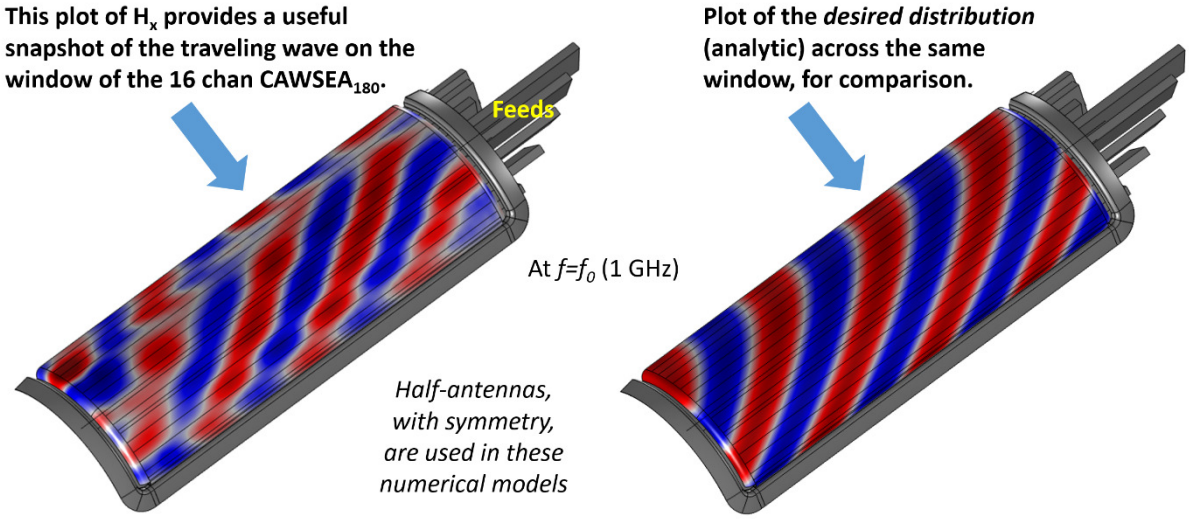


Figure 108. Left: Aperture distribution from 3D RF model of 16-chan CAWSEA$_{180}$. Right: Distribution from an ideal magnitude-preserving plane wave projection.

Figure 109 summarizes some of the more important predicted performance characteristics vs frequency. Note especially the improvement in gain.

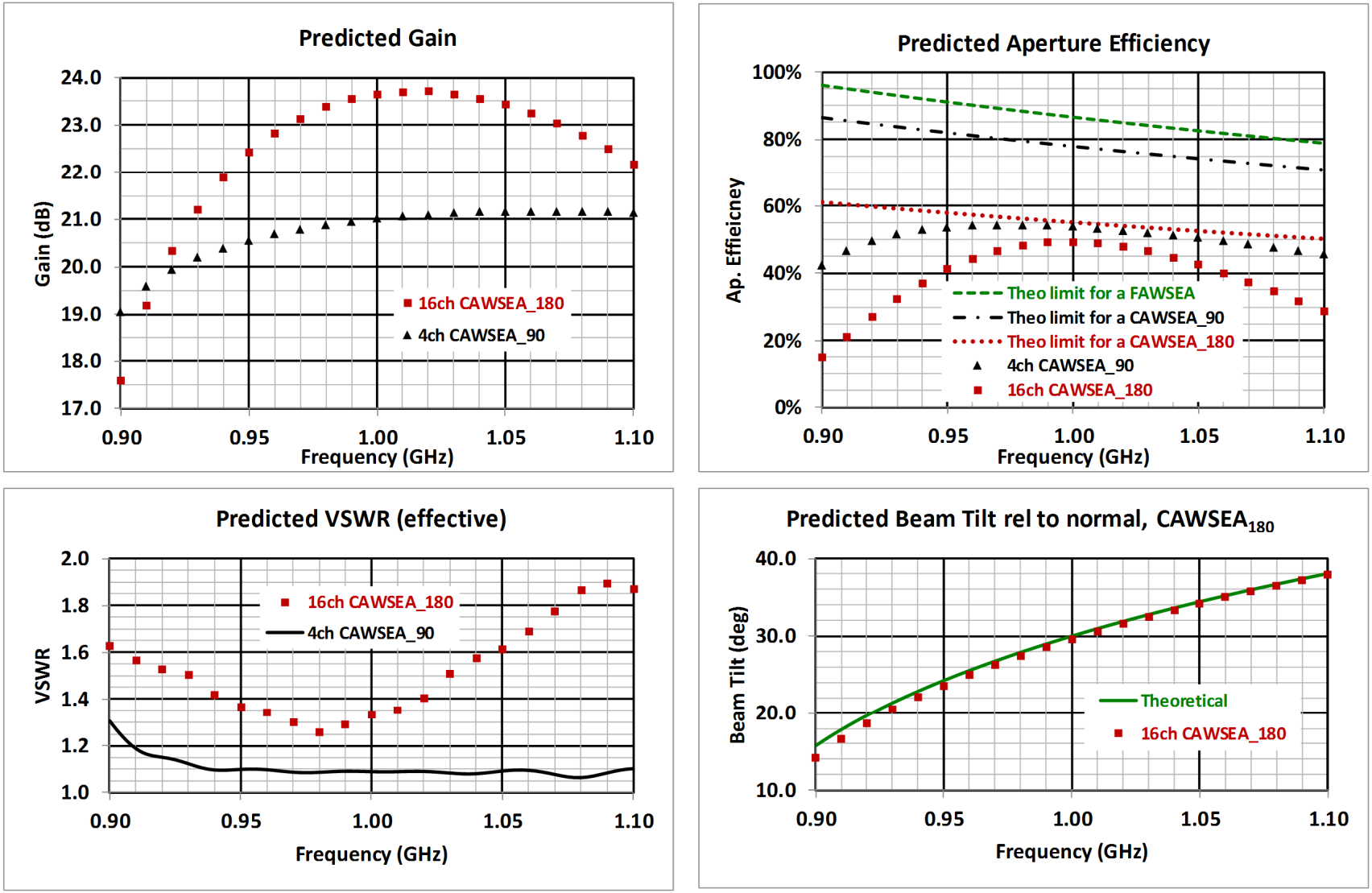


Figure 109. Comparisons of gain, aperture efficiency, VSWR, and beam-tilt vs frequency.

4.4. AAWSEA — A Representative Design Example

The H-plane aperture curvature of the "arched" variant of this antenna (AAWSEA) is apparently more complicated to address quantitatively than either the E-plane curvature of the CAWSEA (Section 4.3) or the in-aperture curvature of the BAWSEA (Section 4.5). Considerable effort was expended during this research program to formulate a detailed analytic/recipe-type approach to the AAWSEA design process, so as to reduce reliance on numerical models. That work remains incomplete[34]. In this section, we focus primarily on an AAWSEA design example that we evolved with the aid of both analyses and models. This example demonstrates that aperture-efficient configurations (via full-wave 3D numerical models) are indeed realizable, even if the design process itself still entails much iteration and 3D modeling.

Figure 110 shows a *single-channel* AAWSEA just over 2m long, with its input cross-section very similar to that of the standard/recommended FAWSEA design described earlier.

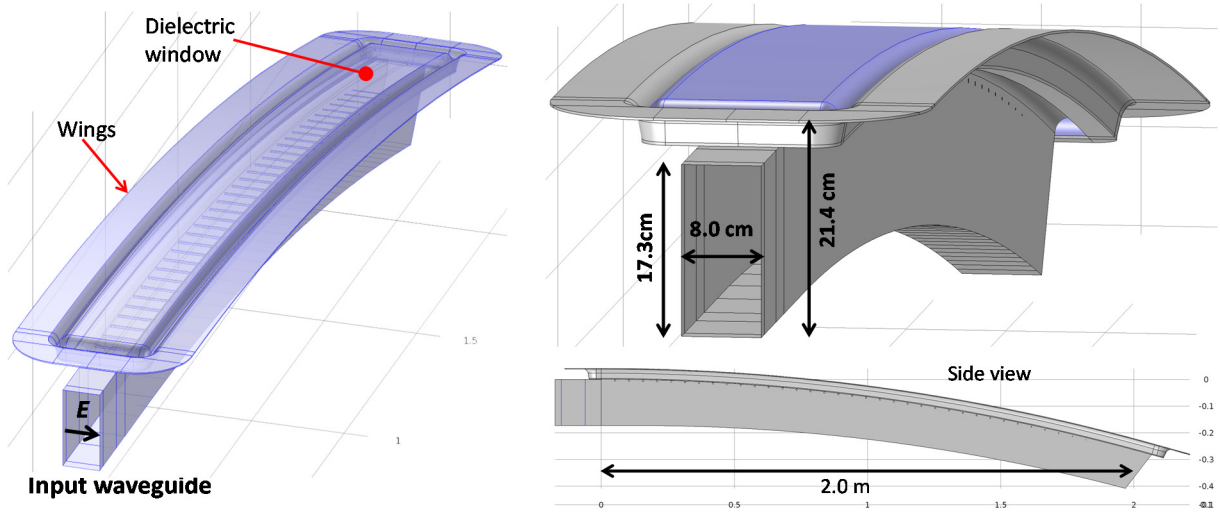


Figure 110. Single-channel AAWSEA (design building block) designed for f_0 = 1.0 GHz

The shape of the curved wall opposite the leaky grill is represented by a many-polygon model. Figure 111 provides a table of diameters vs. placement for the 35 wires composing the grill in the AAWSEA of Figure 110.

Grill wire index	Distance along the arc (cm)	Grill wire dia (mm)	...continued: Grill wire index	Distance along the arc (cm)	Grill wire dia (mm)	...continued: Grill wire index	Distance along the arc (cm)	Grill wire dia (mm)
1	5.25	6.007						
2	10.50	5.995	14	73.50	5.644	25	131.25	4.656
3	15.75	5.980	15	78.75	5.591	26	136.50	4.496
4	21.00	5.964	16	84.00	5.533	27	141.75	4.316
5	26.25	5.945	17	89.25	5.469	28	147.00	4.112
6	31.50	5.924	18	94.50	5.399	29	152.25	3.879
7	36.75	5.900	19	99.75	5.322	30	157.50	3.612
8	42.00	5.873	20	105.00	5.238	31	162.75	3.301
9	47.25	5.844	21	110.25	5.144	32	168.00	2.937
10	52.50	5.811	22	115.50	5.041	33	173.25	2.504
11	57.75	5.775	23	120.75	4.926	34	178.50	1.987
12	63.00	5.735	24	126.00	4.798	35	183.75	1.365
13	68.25	5.692						

Figure 111. Grill wire diameters and location along leaky grill.

Figure 112 shows a four-channel AAWSEA based on the above one-channel building block, and with a channel-to-channel spacing the same (i.e., 19 cm) as was used in our standard/recommended 4-channel FAWSEA (also for f_0 = 1.0 GHz, which aids in convenient geometric scaling to other frequencies).

[34] We refer the interested reader to SARA's periodic reports submitted previously to ONR under this program. For other relevant theoretical background, see Honey and Shimizu (1960) and also Ichimaru and Beich (1962).

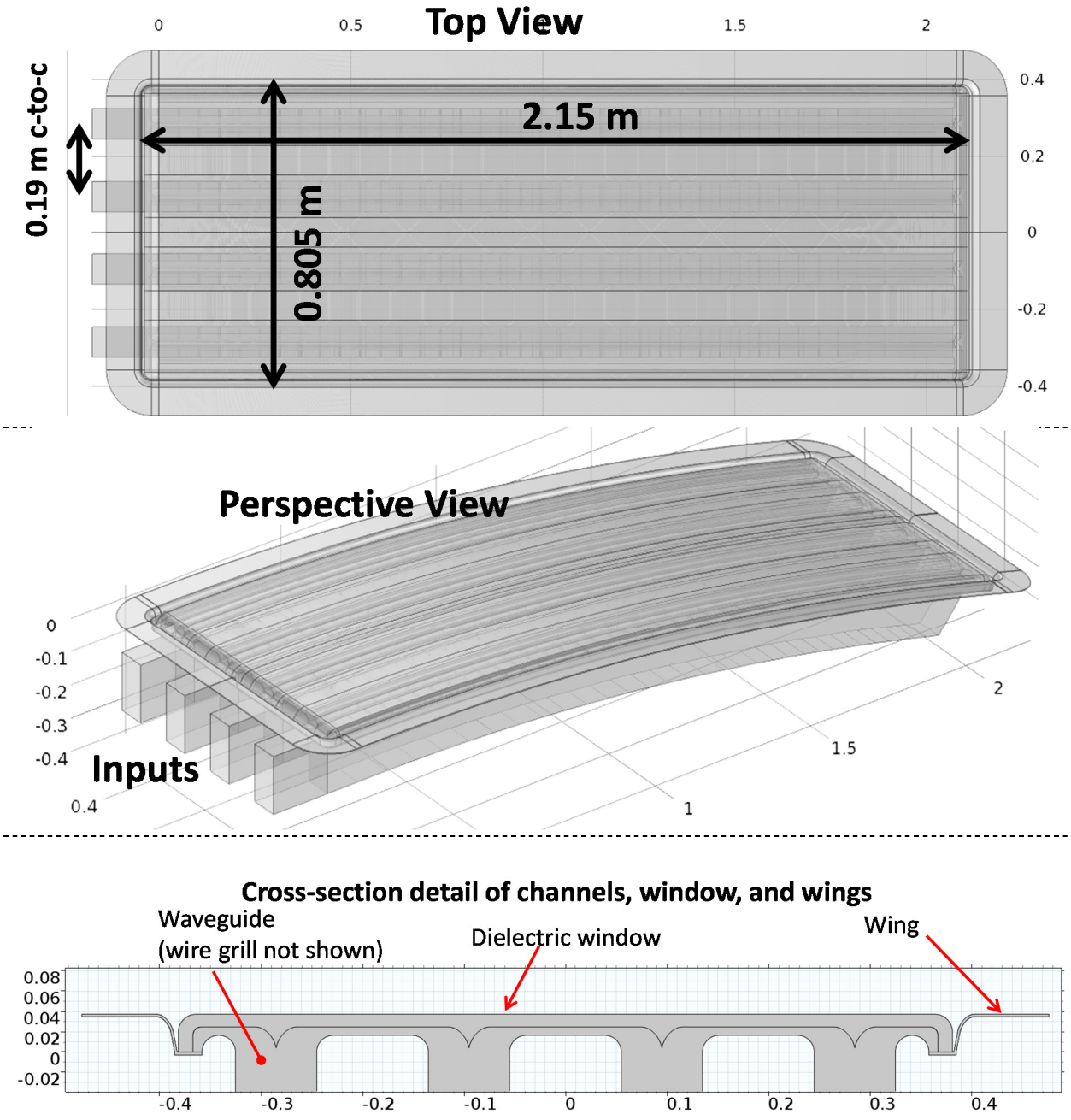


Figure 112. Detail of Upper Region of the Four-channel AAWSEA.

Figure 113 (next page) compares the predicted performance of the 4-channel AAWSEA with the FAWSEA. The relatively high gain of the AAWSEA is partly due to our use of a slightly larger aperture; a more apples-to-apples comparison is revealed in the aperture efficiency plot. The effective VSWR of the AAWSEA is increased at the low-frequency end, which is largely a consequence of the termination section becoming close to cut-off (necessary to compensate for the curvature). The surface-field magnitude for a given input power is encouragingly low. This suggests that AAWSEAs are well-suited to extremely high peak power operation.

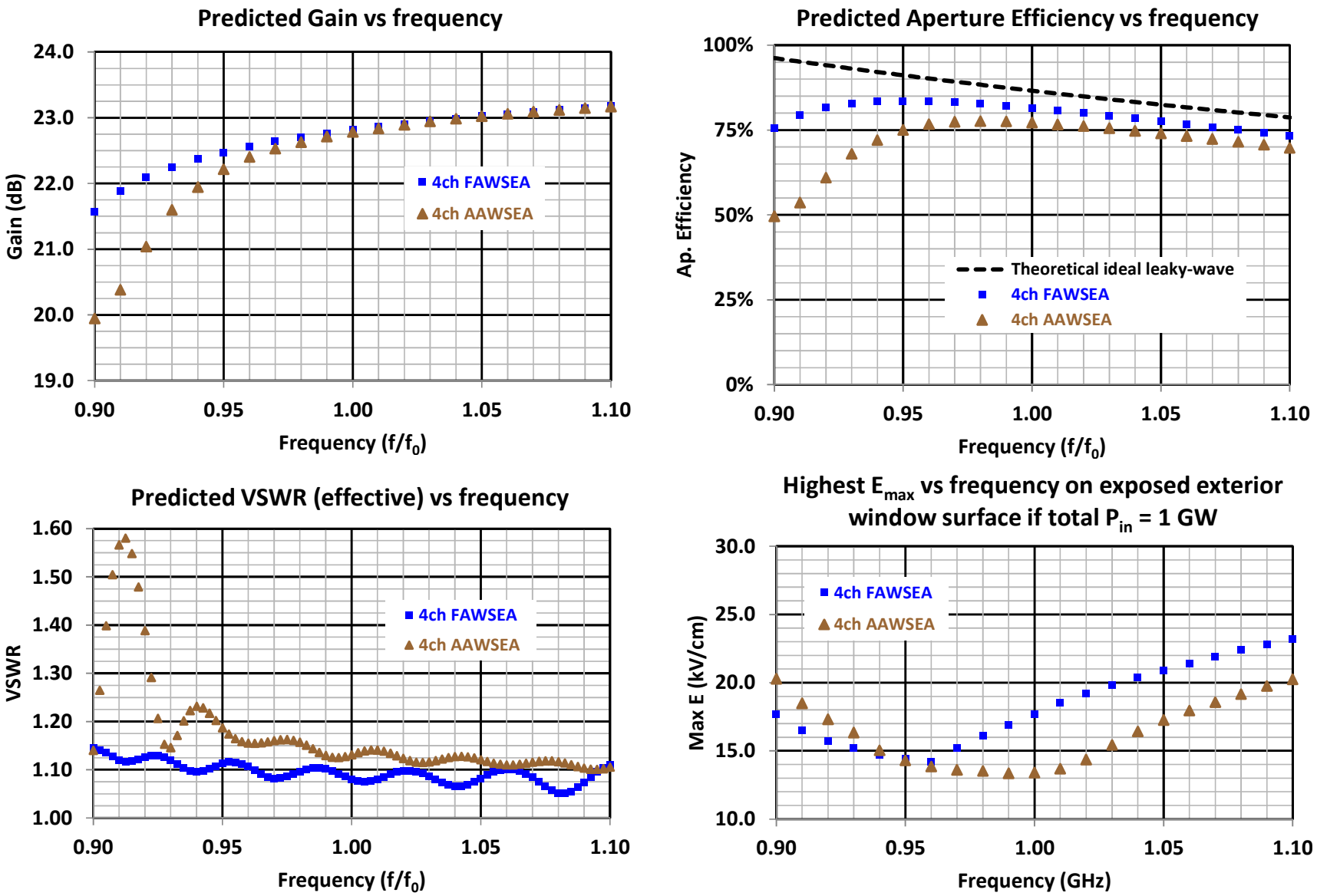


Figure 113. Predicted performance plots of the 4-chan AAWSEA (with comparison to 4-chan FAWSEA)

Sample 3D antenna patterns are shown for three frequencies ($0.95f_0$, f_0, and $1.05f_0$) for single-channel and four-channel AAWSEAs in Figure 114 and Figure 115, respectively. Note again how the beam pattern becomes narrowed in the E-plane as additional channels are added, while the H-plane beamwidth is not noticeably affected. This is as expected.

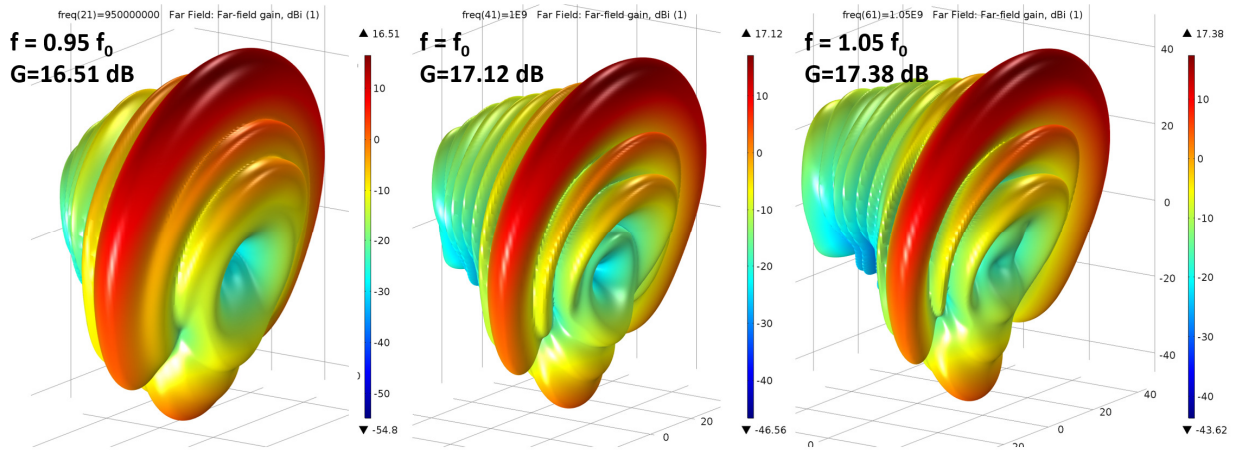
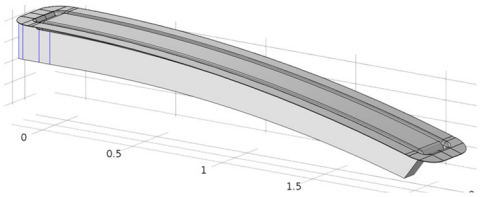


Figure 114. Example 3D Antenna patterns for the *single-channel* AAWSEA at three frequencies. The orientation of the antenna is shown at the right.



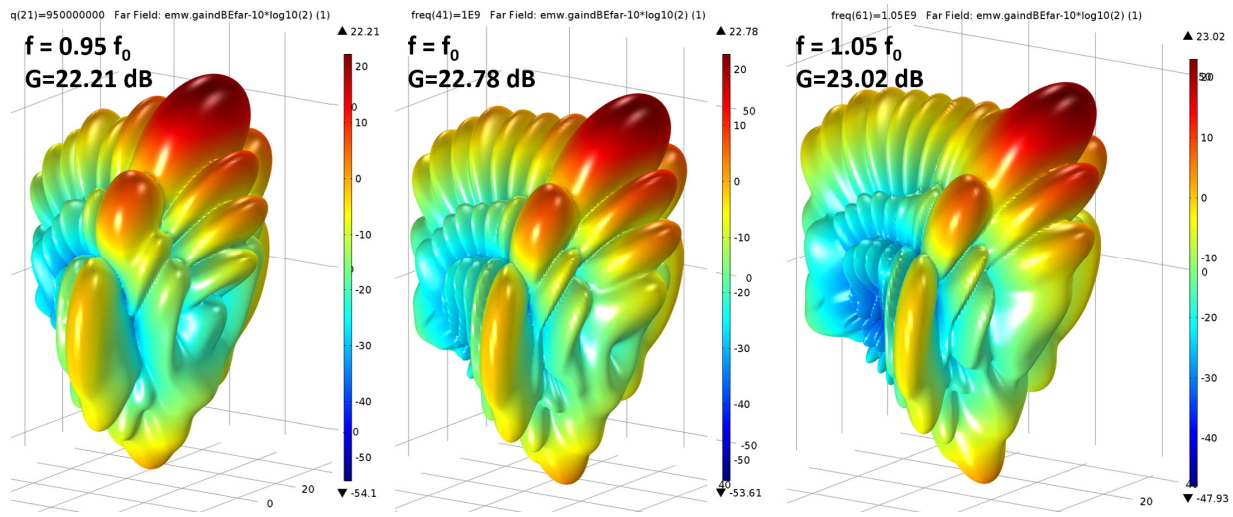
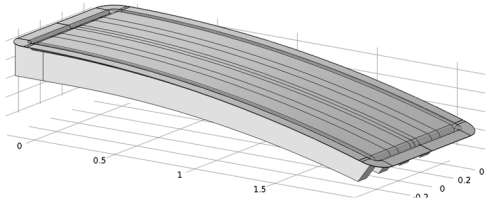


Figure 115. Example 3D Antenna patterns for the *four-channel* AAWSEA at three frequencies. The orientation of the antenna is shown at the right.



The gain exhibited by the 4-channel design is about half a dB less than the ideal +6.02dB above that of the single channel. This is due to the proximity of the channels and is necessary to maintain a compact package (and high aperture efficiency). Figure 116 provides a more detailed comparison from $0.9f_0$ to $1.1f_0$.

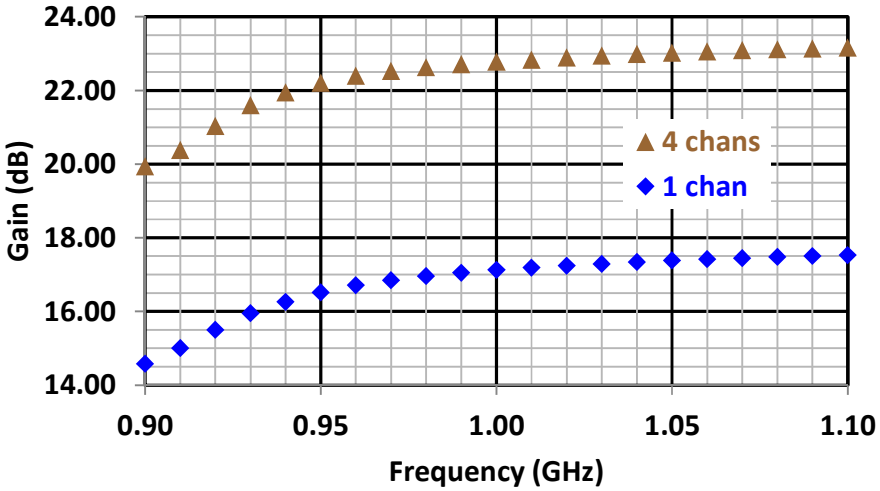


Figure 116. Comparison of predicted gain vs. frequency for the 4-chan vs. 1-chan AAWSEA.

To pre-design the beam pointing direction of the AAWSEA without resort to a full-wave 3D model requires some iteration and is thus more complicated than with the other antenna types. For the example design here, the realized beam direction departed from our planned design value (30°) at f_0 by roughly 3°, which is a rather substantial amount. In addition, the behavior vs. frequency is not just a simple offset from the customary (non-arched LWA) curve. Figure 117 compares the observed (in the numerical model) beam angle vs. frequency of what one would expect (and which we do see) in a FAWSEA vs. that observed in our 3D numerical model of the AAWSEA. We look forward to opportunities to both improve our currently imperfect understanding of this variant, as well as to streamlining the AAWSEA design process in the future.

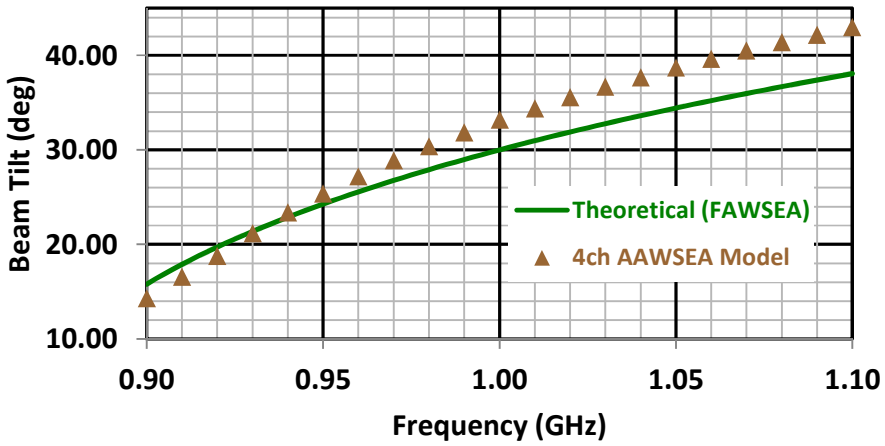


Figure 117. Model-predicted beam tilt (relative to normal at feed end of antenna) for the AAWSEA, vs. the expected curve for a FAWSEA.

4.5. BAWSEA

4.5.1. BAWSEA Principles

Curving a FAWSEA type aperture around an axis normal to it (curvature within the aperture plane) yields the "bent" or BAWSEA configuration. To be most useful, just as with the CAWSEA and AAWSEA, we seek to generate conditions across the aperture such that, *despite the curvature*, the fields match up with a single radiated plane wave at a single well-defined angle. Consider a simple circular-arc bend, such as shown in Figure 118, viewed here looking normal to the aperture Note: With the feeds at the bottom of the figure, we seek to launch a wave heading outward from the page and tilted upwards.

Consider channels bent in an arc.
To get a high-gain beam, we require:

$$\beta_n r_n d\theta_n = \beta_T dy$$

for all *n*, where β_n is the wavenumber *along the n^th curve*, and β_T is the desired traveling wavenumber *along y*.
Since $y = r_n \sin\theta_n$, we promptly obtain

$$\beta_n = \beta_T \cos\theta_n$$

as the required behavior of the wavenumber in the n^th channel.

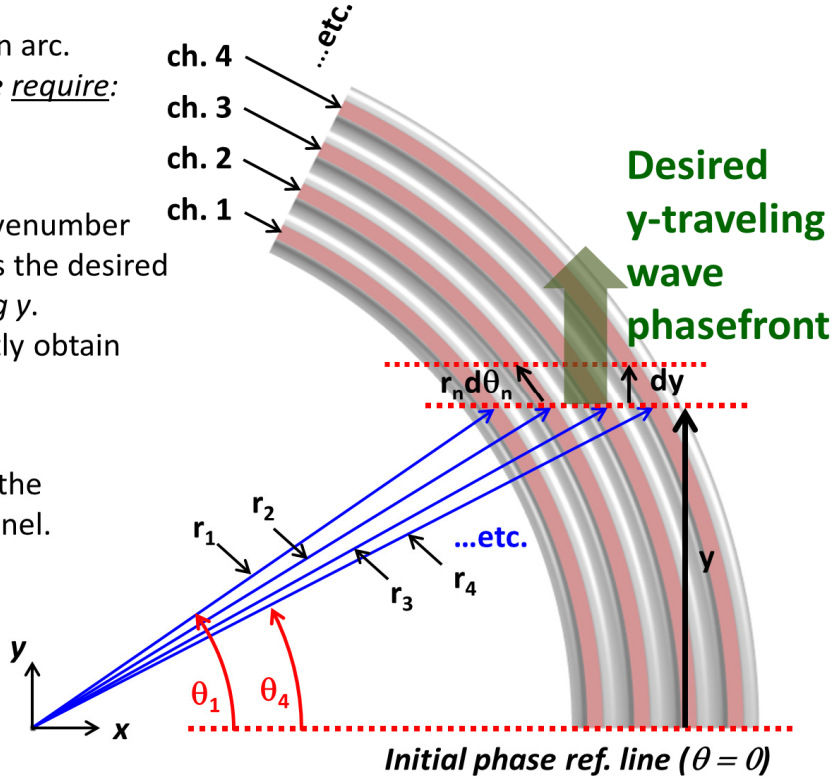


Figure 118. Derivation of BAWSEA channel-phasing to yield a single high-gain beam.

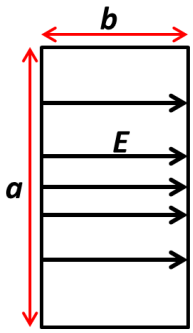
We can see that to maintain the radiated-wave direction and tilt, we must gradually reduce the wave-number β (and thus, increase the phase velocity) in each channel vs angle, as the traveling waves go around the bend. Figure 119 shows how to set the waveguide depths (actually *effective* depths, when adding leaky interfaces later) to deliver this required phasing. As θ increases (i.e, as the wave goes around the bend) a_{eff} must decrease to compensate. Cutoff occurs when $a_{eff} = a_{cut} = \lambda_0/2$, imposing a practical limit. Wave matching at the aperture is *only possible if* $\beta_T < k_0$. From Figure 118, this implies $\beta < k_0 \cos\theta$. Combining with the expressions in Figure 119, we obtain the limiting curvature-angle to the BAWSEA:

$$\theta_{max} = \cos^{-1}\left(\sqrt{1-\left(\frac{f_c}{f}\right)^2}\right)$$

Again, recall that we are trimming the structure (adjusting f_c, via a_{eff}). To apply the above equation properly, one holds the value of f fixed while varying f_c. Recall that $f_c = (1/2)c/a_{eff}$. Tapering a_{eff} to the extent that f_c rises to ~ $0.9f$ is about as far as practical, due to resulting bandwidth limitations and wave reflection issues. Plugging that in suggests θ_{max} ~65° for a good, practical, BAWSEA.

The wavenumber β for propagation of the fundamental mode in a rectangular cross-section evacuated waveguide of dimensions (a,b) is:

$$\beta = \frac{2\pi}{c}\sqrt{f^2 - \left(\frac{c}{2a_{eff}}\right)^2}$$



(For a *leaky-sidewall* waveguide, we have replaced a with a_{eff}, since the leakage modifies that effective dimension slightly.) Solving for a_{eff} in terms of β, we obtain:

$$a_{eff} = \frac{\pi}{\sqrt{\left(\frac{2\pi f}{c}\right)^2 - \beta^2}} = \frac{\pi}{\sqrt{k_0^2 - \beta^2}}$$

where k_0 is the free-space wavenumber.

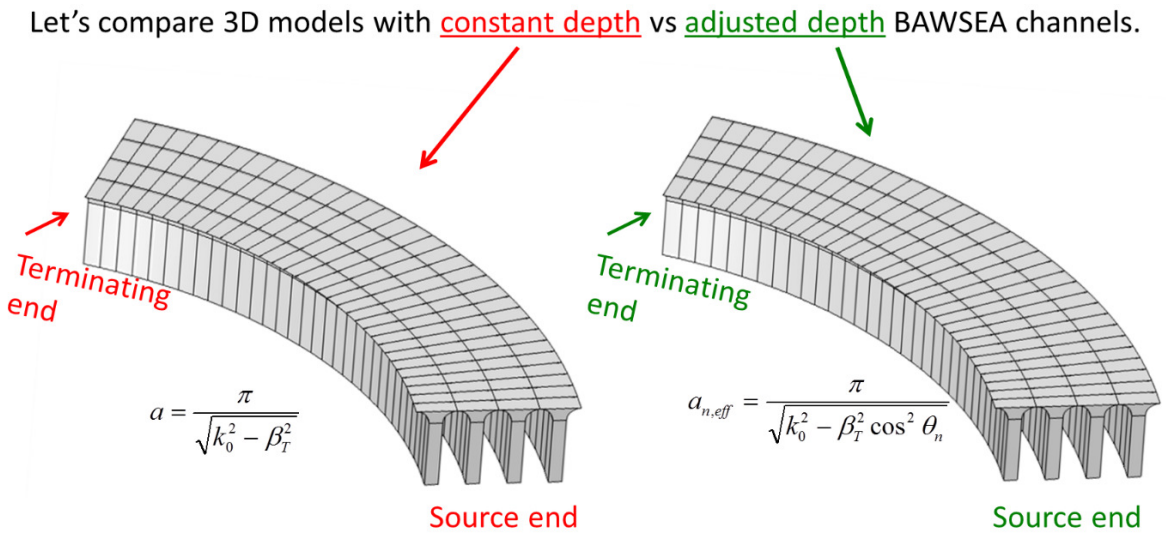
From before, if we now apply this rule to the n^{th} channel, we obtain:

$$a_{n,eff} = \frac{\pi}{\sqrt{k_0^2 - \beta_n^2}} \quad \rightarrow \quad \boxed{a_{n,eff} = \frac{\pi}{\sqrt{k_0^2 - \beta_T^2 \cos^2\theta_n}}}$$

This equation tells us **how to set the (effective) depth** of each channel in the BAWSEA **as a function of angle**, if the channel is to be bent along a circular arc.

Figure 119. Determination of the required BAWSEA channel effective depths.

Figure 120 shows a couple of initial (non-radiating) numerical model geometries set up to simply confirm the resulting wave-alignments under this BAWSEA-phasing plan.



{Note: It is easiest to see the geometric difference if you compare the structures near their terminating ends.}

Figure 120. Non-radiating models to explore constant (left) vs. adjusted (right) depths.

Figure 121 shows the wave phasing that results from the fundamental-mode waves propagating around the bends in the waveguides in the models from Figure 120. It is clear that making proper adjustments to the depths of the guides is essential to compensate for significant angular bends.

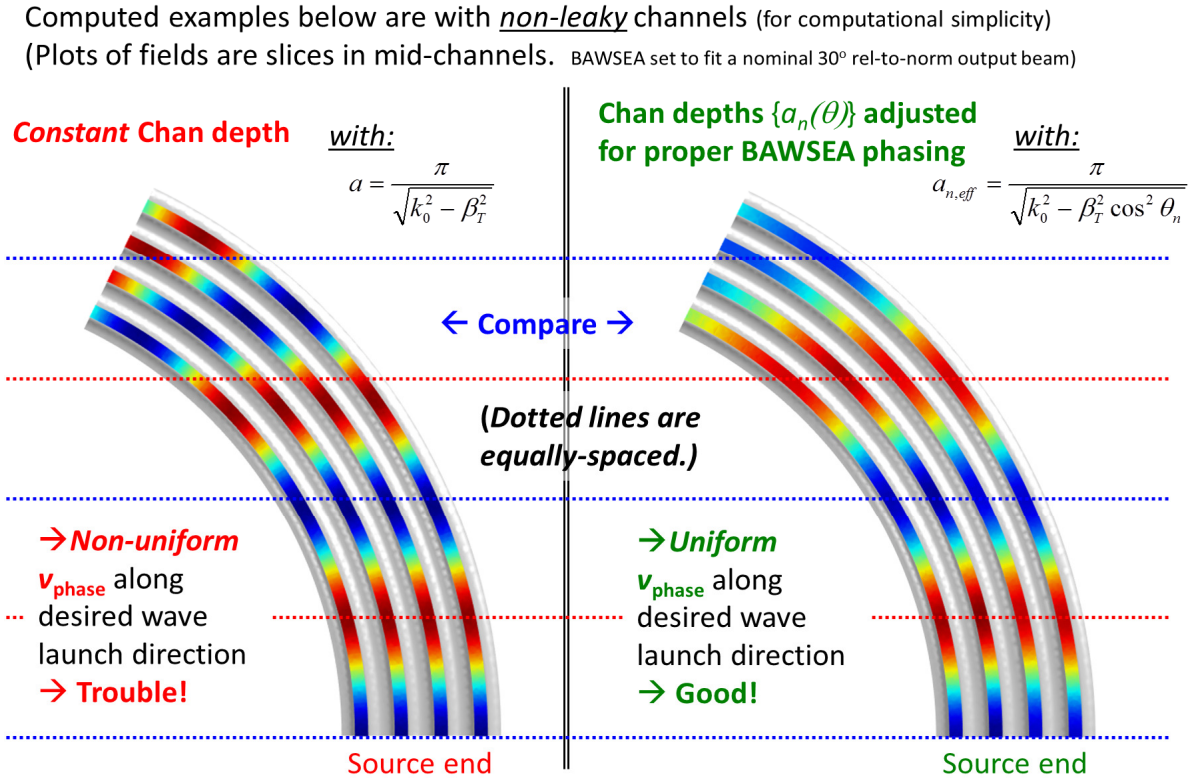


Figure 121. Phasing that results from constant (left) vs adjusted (right) depth channels.

4.5.2. A Recommended BAWSEA Design (Preliminary)

Two-dimensional numerical models do not capture important details of the BAWSEA design process, while a 3D model does not present a convenient symmetry plane. This makes the design/optimization process for a BAWSEA somewhat more computationally-intensive. For a BAWSEA terminated as indicated earlier[35], the neighboring channels will (in the most general case) have different curvatures and lengths. Despite these challenges, we have achieved some success in the examples below.

Figure 70 shows a single-channel BAWSEA with a 60° bend, while Figure 123 shows a more ambitious example: a four-channel BAWSEA. We will focus on the latter here. The 4-channel version has wire grills for each channel that are *different*. The wire spacings are fixed, but the number and diameters of the wires are customized to each channel in accordance with the different channel lengths, and to meet the phasing criteria set forth in Section 4.5.1. A couple of perspective views of this 4-channel example are provided in Figure 124. These four channels should, ideally, *not* be fed by identical power inputs, but rather (in this particular BAWSEA) be scaled as follows in overall input power, from innermost to outermost guides: 21.27%, 23.76%, 26.24%, and 28.73% (from scaling by path lengths). For *idealized* leaky grills in this geometry, this uneven distribution leads to an aperture with the ~most uniform |E|.

[35] A BAWSEA composed of ~identical parallel channels (including with identical radii of curvature) should also be both possible and practical. Its design is left as an exercise for the reader.

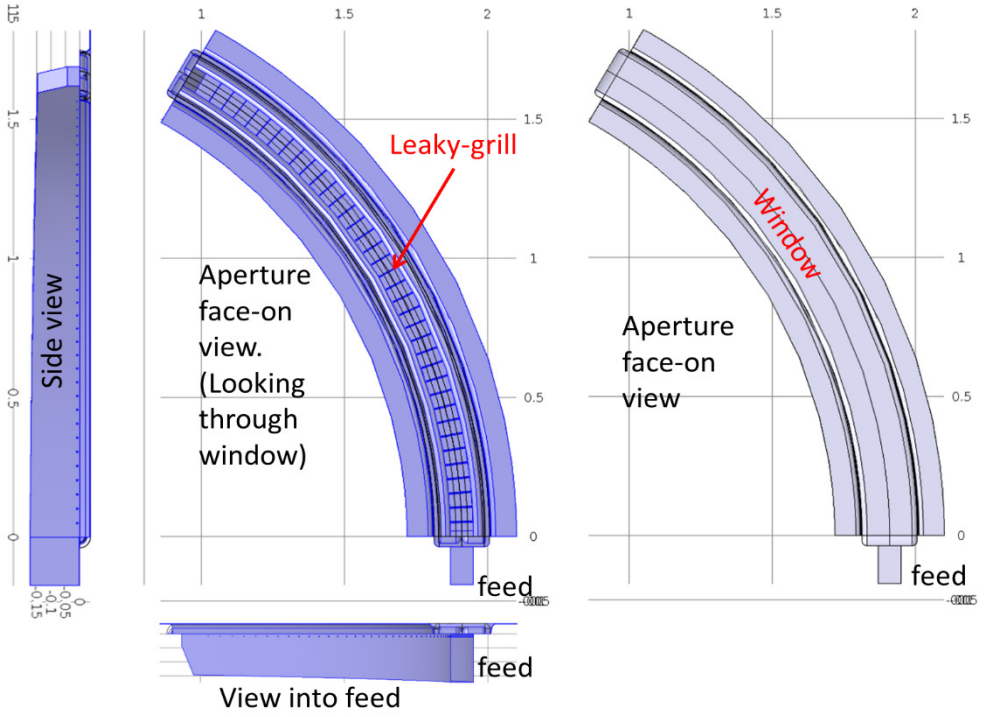


Figure 122. Example of a Single-channel BAWSEA (views from 3D RF model)

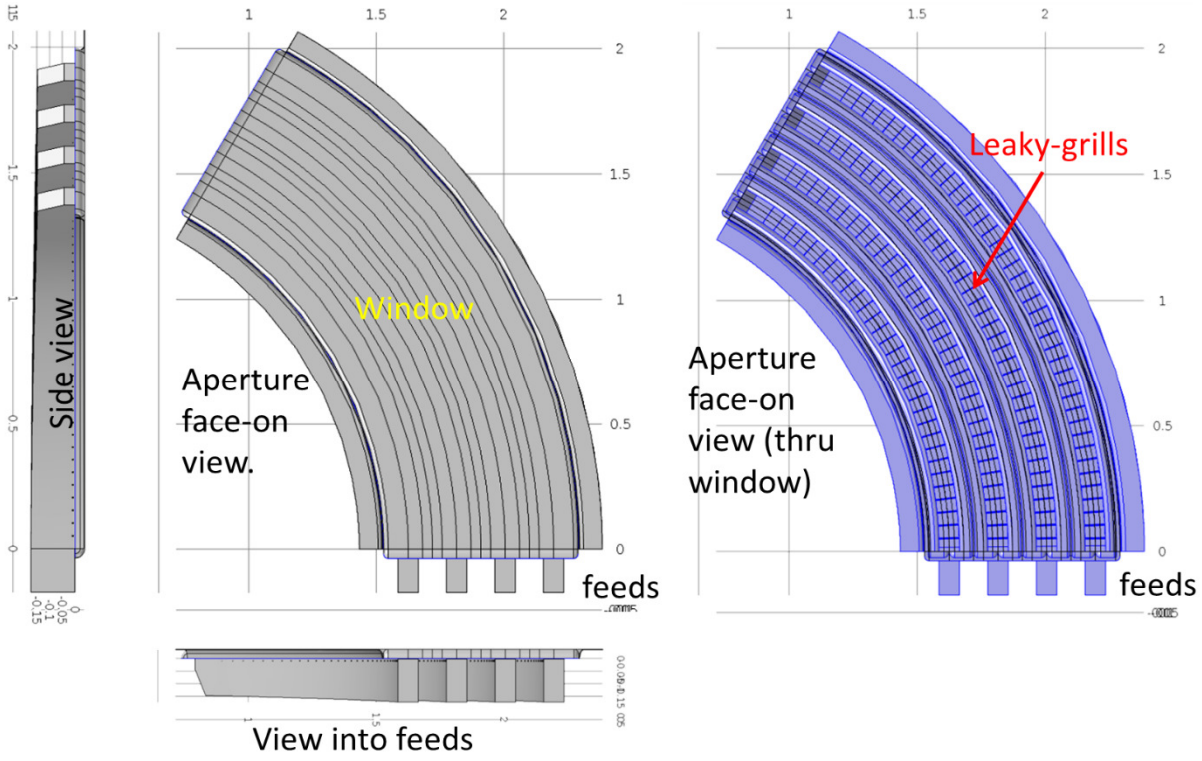


Figure 123. Example of a Four-channel BAWSEA (views from 3D RF model)

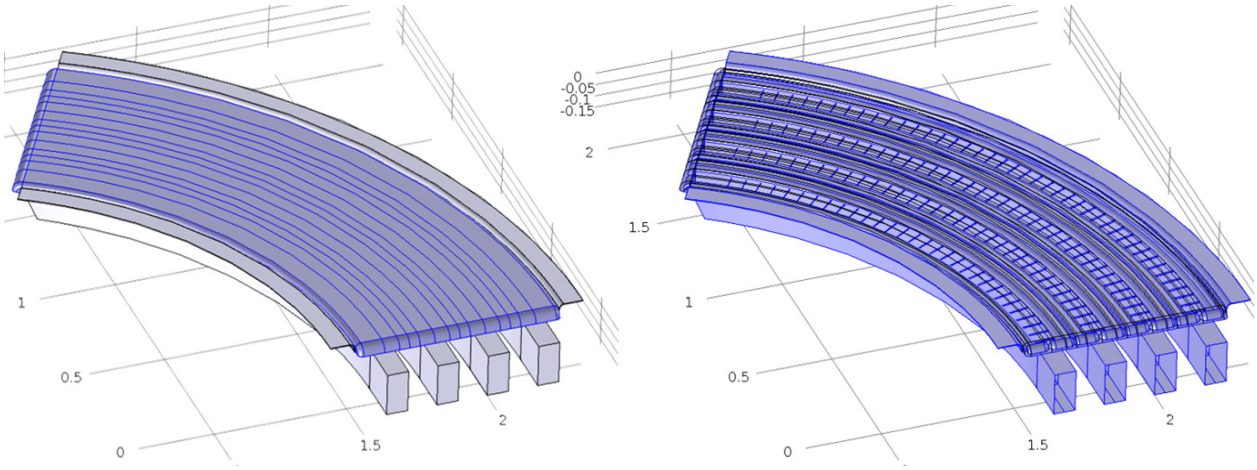


Figure 124. Perspective views of the four-channel BAWSEA example.

Predicted effective VSWR (derived from overall reflected vs. incident power) vs frequency for this BAWSEA is shown in Figure 125. (As with most of the other forward traveling-wave, leaky-wave antenna designs, this one likewise offers excellent VSWR bandwidth.)

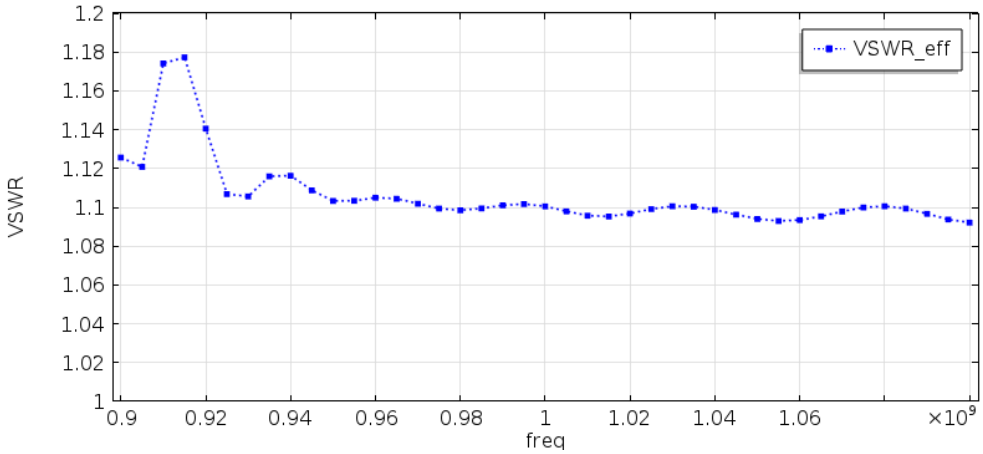


Figure 125. Predicted VSWR (effective) vs Frequency for the example 4-chan BAWSEA.

Of course, it is especially useful to compare the predicted gain of the example 4-channel BAWSEA to that of our earlier "recommended" design for a 4-channel FAWSEA. In fact, the example 4-chan BAWSEA shown here was designed to exhibit nearly the same aperture area and to operate at the same center frequency specifically to ease such a comparison. The channel widths and center-to-center separations are also the same (although this does not guarantee comparable channel-to-channel coupling) and the window cross-section is also very similar. Figure 126 provides a comparison of 3D model-predicted gain and aperture efficiency, from $0.9f_0$ to $1.1f_0$. At the center design frequency (f_0), we see that this BAWSEA should deliver only about 1dB less gain than the (very high performing) FAWSEA. This corresponds to a BAWSEA aperture efficiency of about 65%. Needless to say, that is very respectable. Indeed, it is *better* than that of the 4-chan, compensated CAWSEA that we recommend to fit typical cylindrical apertures. We are thus persuaded that BAWSEAs represent practical and potentially platform-conformal options for HPM antenna designers. Finally, it is worth noting that this particular example BAWSEA design has not been fully optimized; better performance than shown here may be attainable.

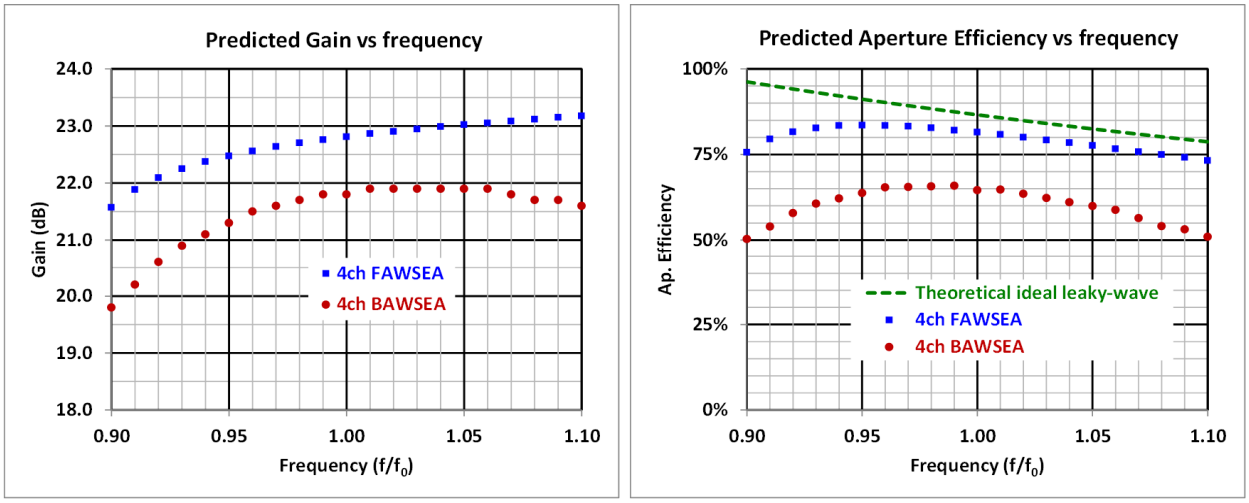


Figure 126. Comparison of Predicted Gain (left) and Aperture Efficiency (right) for the example 4-chan BAWSEA and the 4-chan FAWSEA from Section 4.2.1.

4.6. PAWSEA and GAWSEA

The concept of a "Pinched Aperture, Waveguide Sidewall-Emitting Antenna" (PAWSEA) to fit an ogive-type surface (e.g., Figure 127) was identified at the start of this research program, but since it combines multiple curvatures, its design is challenging. We did not prepare a representative "recommended" design for this antenna type under the subject program. At this stage, we recommend that ambitious PAWSEA designers make use of the other designs presented in this report as helpful starting points in regard to consideration of features such as the channel widths, separations, window designs, grill wire sizes and spacings, etc. Consuming a full 180° (or more, if a nearer to end-fire configuration is desired) of azimuthal angular extent in a PAWSEA may be appropriate, in light of the findings in Sections 4.1.10 and 4.3.2 of this report.

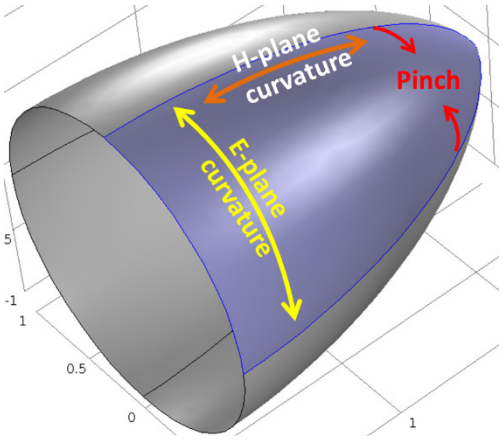


Figure 127. Example of a Surface Suitable for a PAWSEA.

Subject to practical constraints, it is possible to define an even more general family of forward-traveling, fast-wave, leaky-wave, HPM-capable apertures that support customization to suit very complex surfaces. Greater design flexibility follows from considering the inclusion of non-leaking waveguide connections to link separated leaky-wave structures, thereby supporting multiple apertures; introducing delays if/as needed at locations other than just the initial feeds, and even to rebalance or resynchronize phases at the midpoints as might become necessary. One could introduce other variations in propagation (wavenumber) along the paths to compensate for modest changes in leaky-waveguide direction, on a per channel basis if needed, once again to better fit to the required plane-wave boundary-matching conditions. Multiple channels comprising such an antenna need not necessarily be always adjacent to one another. For example, one could define an overall aperture such that it splits apart and then smoothly surrounds the sides of an obstacle or opening on a platform (e.g., a window, landing gear, fuel-port, vent, etc.) that would otherwise prohibit placement of an aperture there, such as illustrated notionally in Figure 128.

It is this perspective that motivates what we term the "Generalized Aperture Waveguide Sidewall-Emitting Antenna" (GAWSEA).

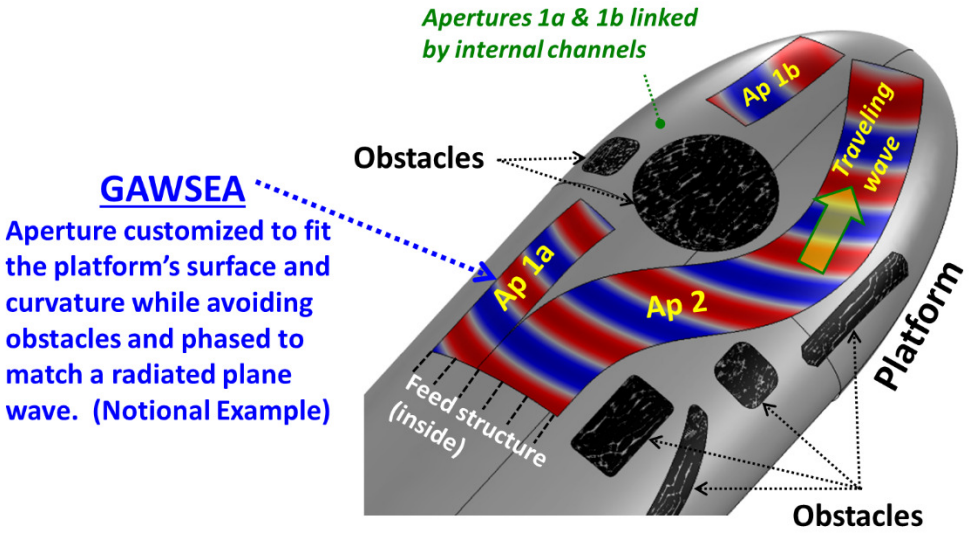


Figure 128. A Generalized Aperture Waveguide Sidewall-Emitting Antenna (GAWSEA) features multiple channels & curvatures and a distribution of leaky-wave apertures to yield an overall aperture customized for maximizing power delivered against a target.

Interestingly, the most serious design constraint of a BAWSEA or AAWSEA – that channel curvatures must not be so extreme that the wave propagation would need to pass through cutoff conditions to compensate – can potentially be *relaxed*, if the trouble-making sections are *replaced* by non-radiating waveguide connections. Admittedly, this represents at least a partial extension into consideration of *discrete aperture* LWA's (which incidentally include periodic-aperture LWAs). A discrete array concept presented later in this report (see Section 4.10) might arguably be claimed to belong in that category. In any case, the application of field distributions across what may appear (at the platform surface) to be entirely disjoint apertures (as envisioned in the GAWSEA concept) offers increased flexibility to the designer, despite the additional engineering challenges it entails.

If the disjointed apertures of the GAWSEA seem a bit radical, remember that there is *no fundamental theoretical requirement* that physical antenna apertures, whether used individually or as arrays, exhibit simple, symmetric, contiguous, or attractive cross-sectional shapes or be uniformly-spaced. This is true despite the fact that the majority (but not all) of aperture antennas (horns, reflectors, lenses, etc.) invented, designed, engineered, and/or built during the last 100 years or so have exhibited rectangular, circular, elliptical, or similarly-appealing cross-sections, and that most commonly-employed arrays (but not all) are uniform. Yes, such choices stem from direct or indirect application of established design principles, can be specified using well-documented rules and simplifications, often provide elegant amenability to both analytics and aesthetics, and possess symmetries and uniformities that ease fabrication and keep manufacturing costs reasonable. And yet, most of the time, those antenna apertures *do not actually need to be those particular shapes*[36] *to do their jobs*. It may never be possible to shape HPM antennas truly arbitrarily, but powerful computers and modern 3D full-wave RF modeling tools aid the designer in pushing the limits and may soon bring real-world GAWSEA designs to reality.

[36] When aperture shape is critical, it is most often due to relative phasing requirements. If there exists sufficient flexibility to control phase in the design, geometric constraints are more relaxed. The CAWSEA, AAWSEA and BAWSEA provide examples of this flexibility, enabling conformance to curved surfaces. The GAWSEA concept combines and generalizes the approach to achieve even greater design flexibility.

4.7. Summary of Performance Characteristics for Recommended 4-Channel Designs

For convenient comparison and reference, Figure 129 gathers together and compares the predicted gain, aperture efficiency, VSWR, and surface E_{max} (for P_{in} = 1GW at $f = f_0$ = 1.0 GHz) for the major recommended *4-channel designs* in this report. Representative E- and H-plane polar plots at $f = f_0$ are then provided in Figure 130.

For more details about these individual antennas, and for information about the other types of antennas also discussed in this report, we refer the reader to the specific report sections devoted to them.

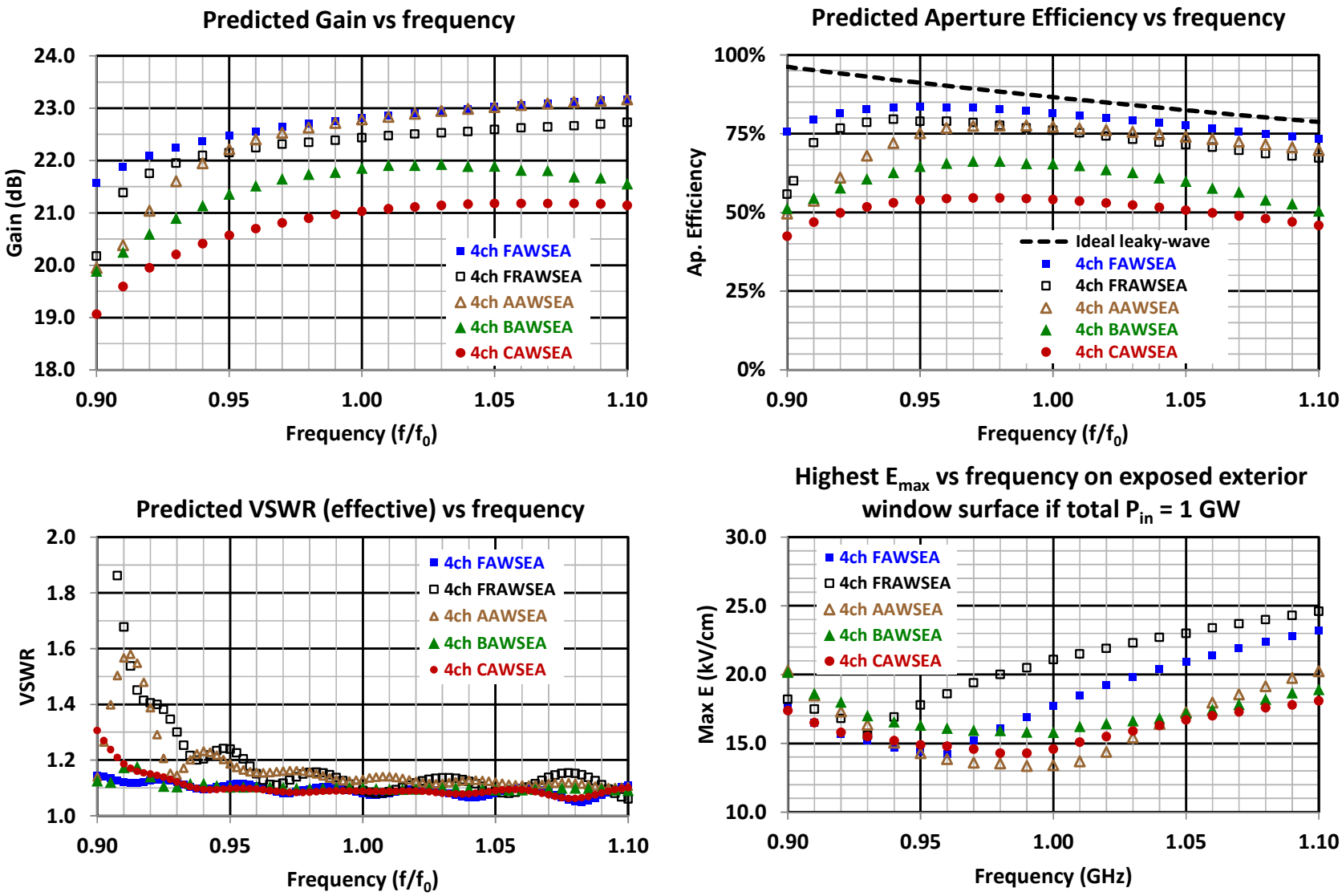


Figure 129. Predicted gain, aperture efficiency, VSWR, and surface $|E|_{max}$ for recommended 4-channel designs.

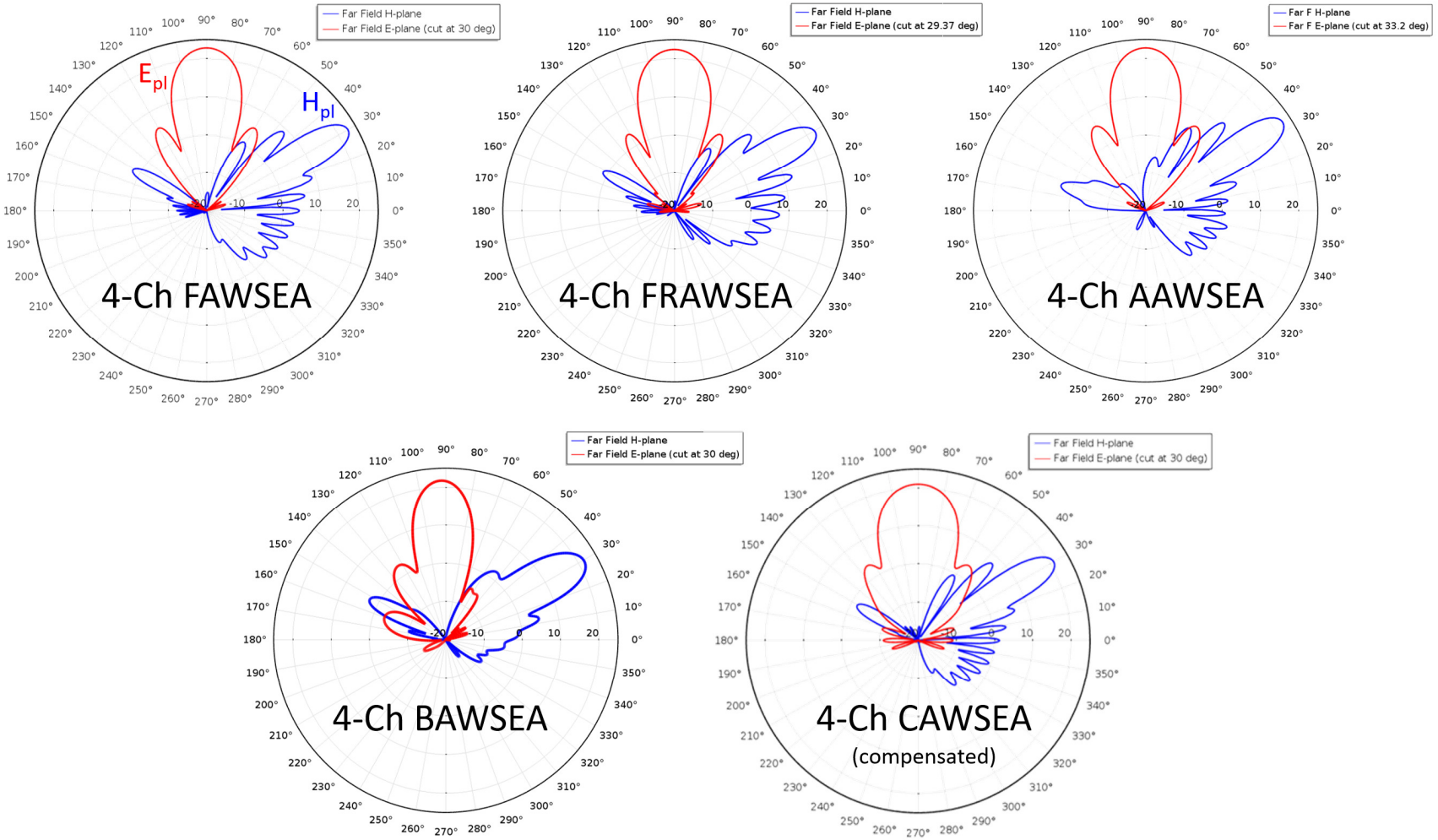
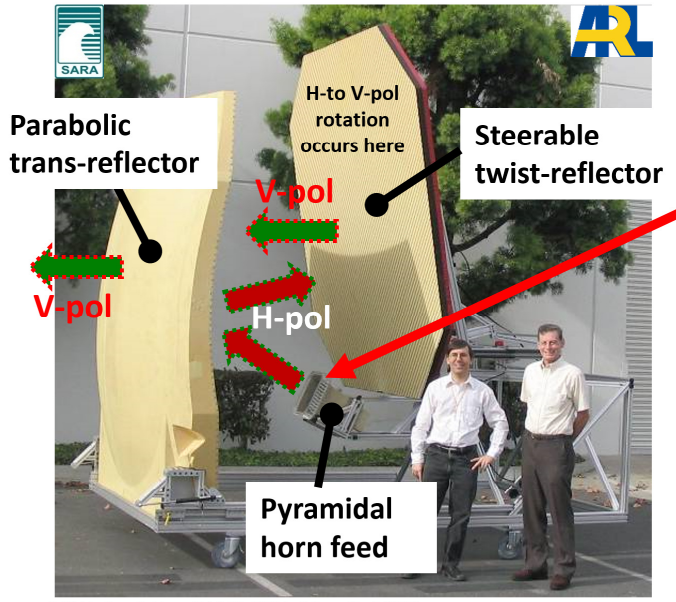


Figure 130. E-plane and H-plane polar gain plots at $f = f_0$ for recommended 4-channel designs: FAWSEA (Section 4.2.1), FRAWSEA (Section 4.2.3), AAWSEA (Section 4.4), BAWSEA (Section 4.5.2) and CAWSEA (Section 4.3.1).

4.8. Combinations with Novel Reflectors → High-Gain, Rapid HPM Beam Steering

Beam-steering of HPM antennas has long been problematic. Phase-based multi-channel steering (e.g., see Section 4.2.2) is ideal, but is seldom an option, since the technology of HPM oscillators based on relativistic electron beams is seldom compatible with the continuous rigorous phase control of multiple high power outputs. Employing waveguide rotary joints is also inconvenient, as they tend to be bulky, are more difficult to work with when pressurized or evacuated, and even then can become power-handling bottlenecks. To address some of those difficulties, SARA introduced an alternative mechanical-based steerable HPM antenna leveraging a combination of a pyramidal feed horn, a paraboloidal trans-reflector, and a flat twist-reflector (Koslover, 2003). This eliminates the need for rotary joints and yields a high gain beam that can be steered rapidly and over large angles in both elevation and azimuth. Downsides of this approach, however, include considerable antenna volume and reduced aperture efficiency (topping out at about 60%, in more recent designs) compared to other antennas. Finally, feed aperture-area is a key limiting factor to peak power-handling in all conventional point-focus, parabolic reflector antennas.

We present here a new way to *overcome* that peak-power handling limitation by taking advantage of an HPM-capable LWA. To see how this works, first consider the aforementioned horn/trans-reflector/twist-reflector antenna (Figure 131). We can keep the steerability offered by the twist-reflector, but replace the feed-horn by an LWA, and the *paraboloidal* section trans-reflector by a *conical* section trans-reflector (Figure 132). The peak power handling is thereby increased to that provided by the LWA.



US Patent No. 6,559,807, May 6, 2003.
Work supported by US Army/ARL Contract # DAAD17-01-C-0071.

- **G~29dB (L-band).**
- **Very widely-steerable in azimuth and elevation.**

Risk of air/surface breakdown at the feed constrained operation to about 100-200 MW peak.

So… what if you want to operate at P_{pk} > 1 GW?

Figure 131. Over a decade ago, SARA developed "the world's first truly-steerable HPM antenna" leveraging a horn/trans-reflector/twist-reflector combination.

1. **Replace the pyramidal horn feed with a suitable GW-class FAWSEA or CAWSEA.**
2. **Replace the offset *parabolic* trans-reflector with suitable offset *conical* trans-reflector.**

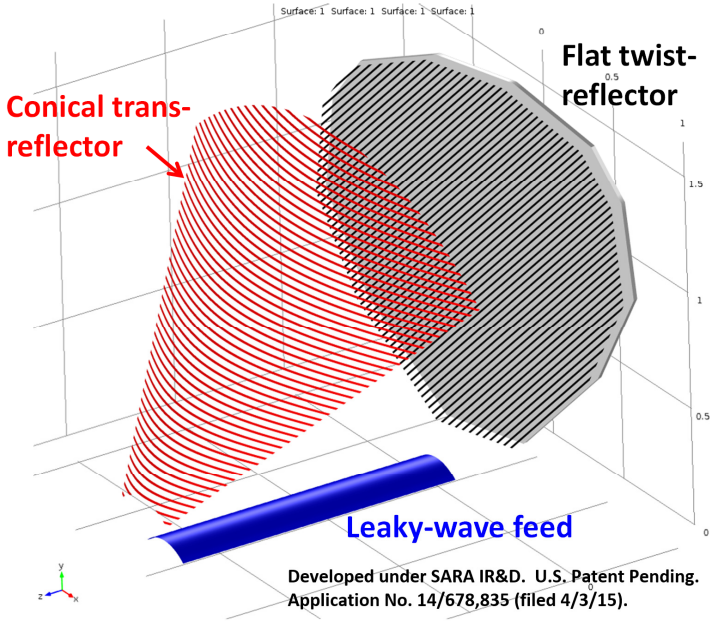


Figure 132. An LWA feed and matching conical-section trans-reflector offer greater peak power handling, while the twist-reflector provides the beam steerabiity.

Figure 133 and Figure 134 show the above antenna represented in 3D FE-based full-wave RF models.

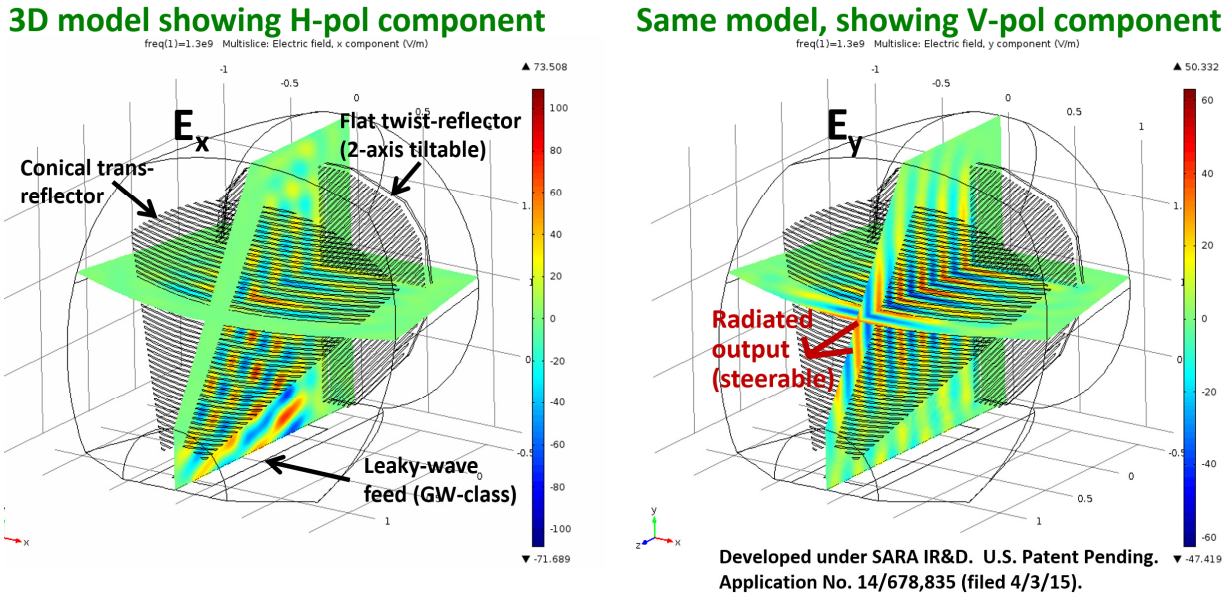


Figure 133. Model of antenna in Figure 132 with beam in forward "non-steered" position.

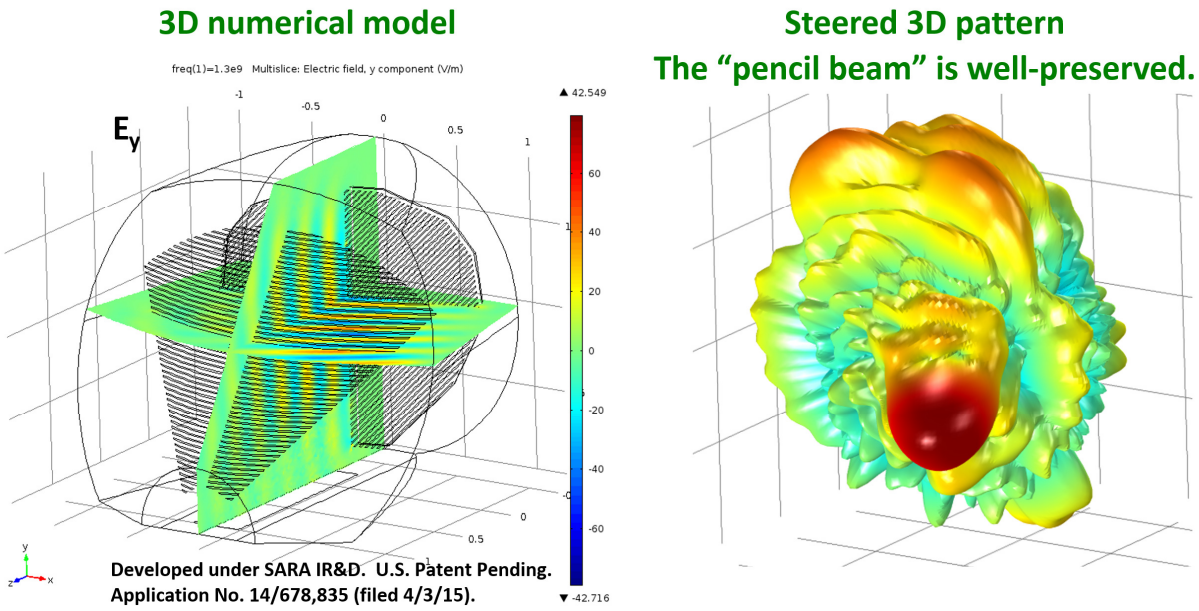


Figure 134. Beam steered 30° in azimuth (via rotating the twist-reflector 15°). This steering reduces the predicted gain by only 0.18 dB relative to the non-steered case.

4.9. An HPM-Capable Cylindrical TM_{01}-driven Leaky Wave Antenna

A number of important cylindrically-shaped HPM sources generate outputs directed along their axes of symmetry, in the circular-waveguide TM_{01} mode. Direct radiation (such as by a conical horn antenna, as was commonly done in the 1980s) yields a low-gain pattern with a null on the axis. This is inconvenient for both effects testing and weaponization. A single-peak beam is much preferred. Fortunately, there exist means for converting from the TM_{01} circular mode to fundamental mode of either circular TE_{11} (Koslover et al., 1991) or rectangular TE_{10} (Harrington and Mautz, 1991), either of which becomes much more convenient for driving an antenna to yield a high-gain beam. Nevertheless, such mode-converting components increase bulk, while potentially also reducing bandwidth and/or efficiency. Some alternative options for managing microwave sources with circular TM_{01} outputs are to employ asymmetric apertures (Vlasov and Orlova, 1975; Haworth et al., 1998) or asymmetric reflectors (Courtney and Baum, 2000) to compensate for the circularly-symmetric TM_{01} mode, yielding an acceptable moderate- or high-gain beam. There also exists some discussion in the literature of leaky-wave antennas driven by *non-fundamental* waveguide modes, including circular TM_{01} modes (Goldstone and Oliner, 1961) but there appears to have been little if any analyses published regarding the suitability of these kinds of antennas for high peak power (e.g., GW-class) operation. We decided to explore this possibility.

Our investigations using numerical models convinced us that there is indeed value in using circular-waveguide TM_{01}-based forward-traveling leaky-wave HPM-capable antennas with TM_{01}-output HPM sources. Like SARA's FAWSEA-family of antennas, the subject antenna is of the continuous-aperture, forward traveling-wave type. However, the leaky "wire grill," to the extent it can be said to exist at all, is now aligned with the antenna axis and is far simpler. The resulting antenna appears to be especially well-suited to long, narrow-diameter, cylindrical packages.

The leaky aperture(s) employed here can be made to span various fractions of the full azimuthal-angle around the guide. The example shown in Figure 135 has two apertures, together spanning less than 180°. A curved dielectric window (polyethylene, in this example) provides the vacuum-to-air interface. This interface is similar in geometry to a window suitable for one of our CAWSEA designs. As such, its curvature provides structural support without needing to be excessively thick. We have also found that the addition of modest-extension fins, as a sort of back-plane, help to increase the gain. The aperture length is, of course, customizable, but relatively-long lengths appear to work better, allowing for a more gradual leakage of the radiation. The output beam direction depends on the frequency just as with other types of forward traveling-wave, leaky-wave antennas.

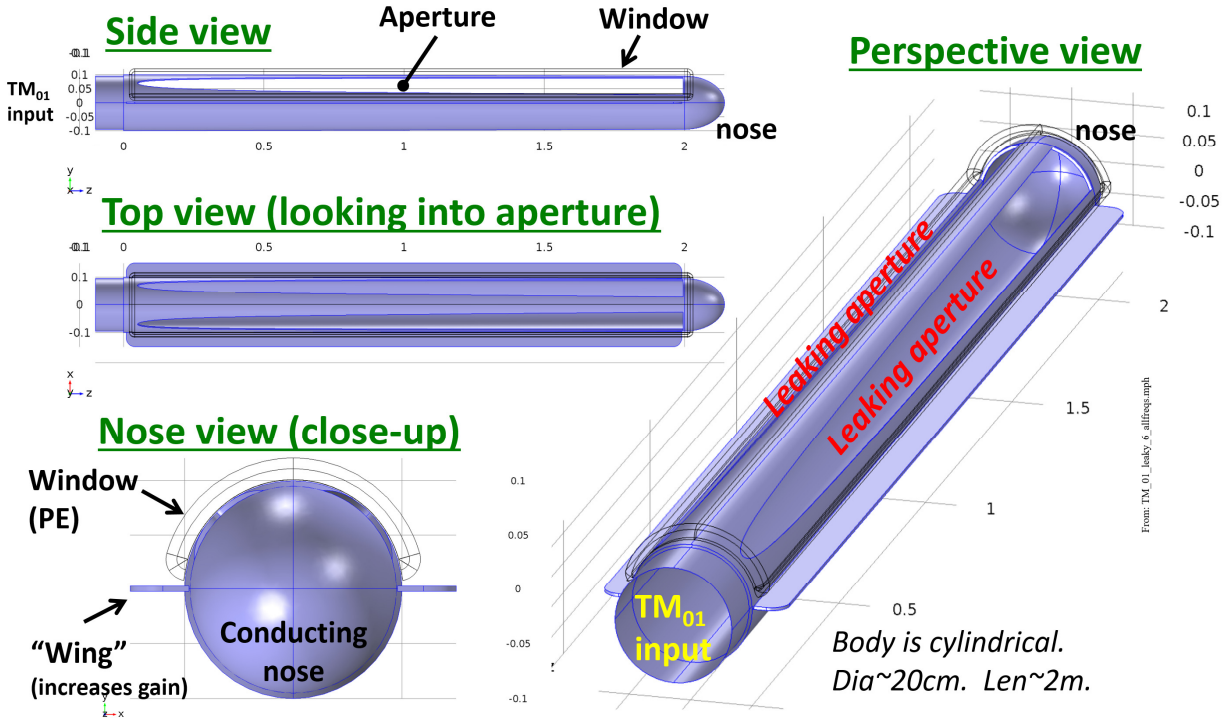


Figure 135. Example physics-level design (prelim) of an HPM-capable TM_{01}-circular mode driven leaky-wave antenna. (Note: This design is for f_0 ~ 1.35 GHz)

Predicted performance (see Figure 136 and Figure 137) in regard to VSWR and gain vs. frequency, while ensuring that |E| does not exceed breakdown, are all very respectable. We conclude that this antenna deserves both attention and consideration by anyone interested in integrating TM_{01}-circular output HPM sources into DEW systems.

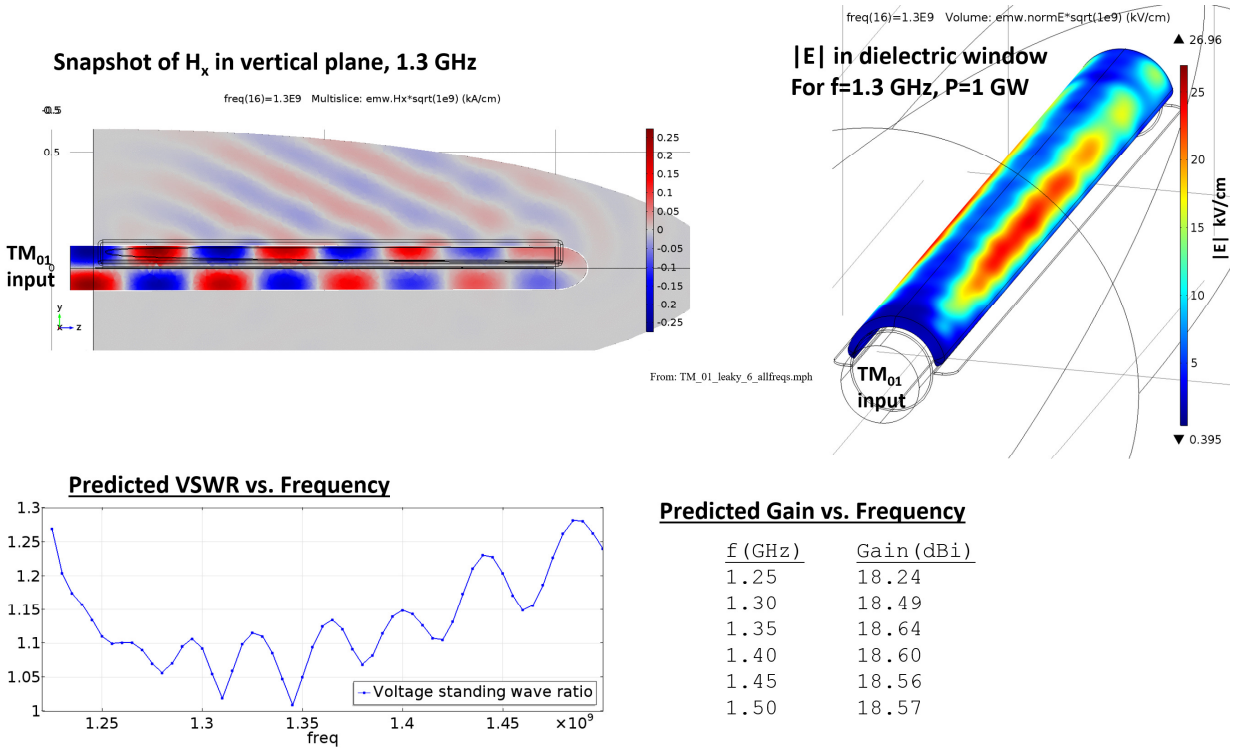


Figure 136. Predicted behavior of the antenna in Figure 135.

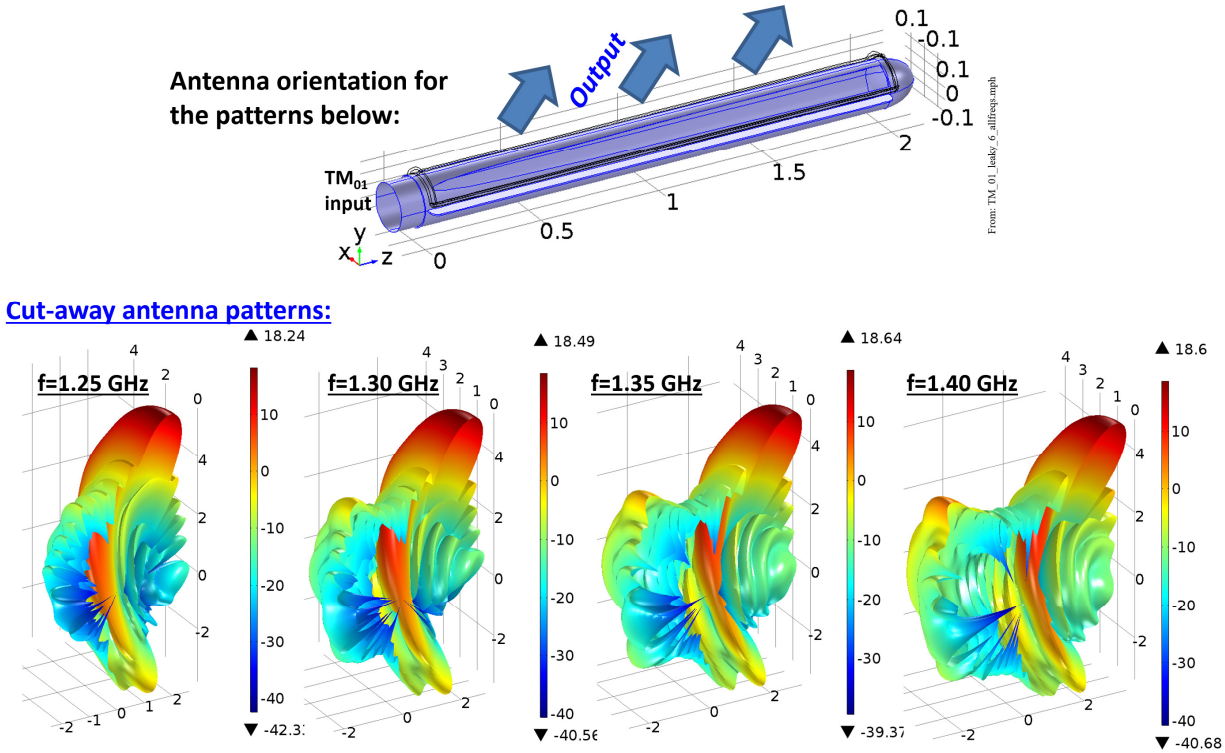


Figure 137. Some computed 3D radiation patterns for the antenna in Figure 135.

4.10. Beam Stabilization: Compensation/Suppression of Scanning with Frequency

We report here a means to combine leaky-waveguides, comparable to those in the FAWSEA-family of LWAs, with added waveguides and apertures to compensate for frequency-dependent beam scanning. A recent investigation[37] along these lines is summarized in Figures 138-141. Note how each "path compensating" waveguide is shorter in length than its predecessor, since the corresponding path to reach its feed point along the leaky channel increases. Despite dielectric-filling, which is necessary partly to decrease the array spacing to avoid grating lobes, the overall antenna is not as shallow as the evacuated, more-purely leaky-wave antennas described earlier in this report. It remains to be seen if some of the narrow structures required by the novel arrangement shown here will limit will peak-power handling prohibitively. However, this configuration does yield a *fixed-direction beam*, potentially expanding the applicability of this technology to broader bandwidth HPM sources.

Motivation: **Leaky-wave narrowband HPM antennas (e.g., FAWSEA, CAWSEA, RAWSEA, BAWSEA…) offer *superior* P_{pk}-handling in *compact* packages.**

Issue for *broadband* application: **Dispersion in the waveguide steers the leaked beam vs. frequency, effectively limiting usable antenna bandwidth during a macro-pulse to much less than the waveguide operating range.**

Idea: ***Compensate*** **by attaching multiple waveguide channels of different lengths along the leaky-waveguide wall, then route them all to a form a new aperture (e.g., array of horns) to yield direction ~independent of frequency.**

Complications: **(1) Could greatly-increase size and volume, (2) the discrete waveguides produce new reflections → grill-wires design algorithm *fails*, and (3) resulting array spacing is too-large → generates grating lobes.**

Solutions: **(1) Fold/arrange compensating waveguides judiciously and fill with dielectric to reduce size & volume, (2) use individually customized inductive irises instead of wire-grill to couple power into compensating channels, and (3) using dielectric-filled horns → tighter array spacing→ avoids grating lobes.**

Figure 138. Motivation, problems, and solutions found on the research path that led to this broad-banding concept.

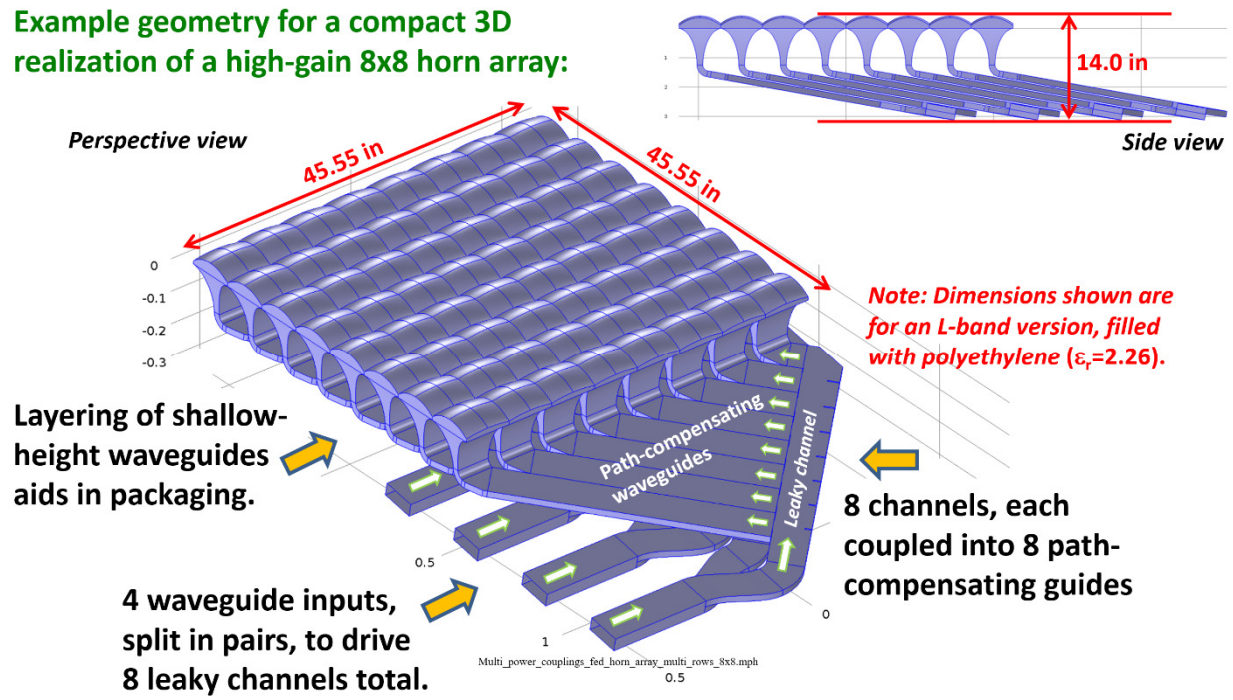


Figure 139. A novel antenna combining leaky-wave channels with compensating-path waveguides to drive an array. (L-band, 8x8 array. Other sizes and arrays are possible.)

[37] Work supported under a subcontract to SARA from Leidos, Inc.; AFRL prime Contract: FA9451-13-D-0210.

Figure 140 shows how an approximately-balanced 1-to-8 power coupling geometry can be achieved. Each output channel, as we step successively along the leaky-path from the input, must extract a greater fraction of the remaining power in the traveling wave. Ideally, the 1st channel couples exactly 1/8th of the input power, or $P_{in}/8$. For the 2nd channel to extract the same absolute power, it must couple 1/7th of the *remaining* power, i.e., $(1/7)*(P_{in} - P_{in}/8) = P_{in}/8$. The 3rd channel must couple 1/6th of the power remaining in the leaky channel, and so on, with the final (8th) channel extracting *all* of the remaining power in the guide. As noted in Figure 140, the achieved balance in our example here is imperfect, but it may be close enough to do the job (and can likely be improved with some additional effort).

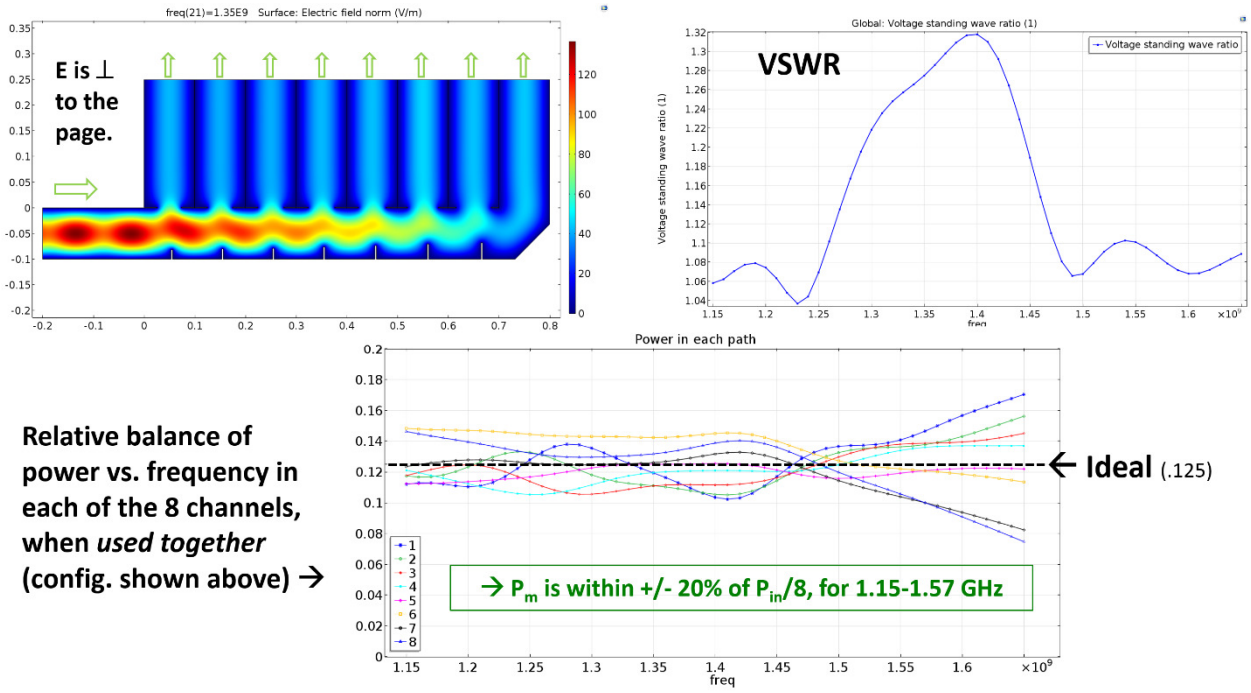


Figure 140. Detail of the coupled paths, which use inductive irises and stubs instead of a wire grill, to leak/couple the traveling-wave's power into eight separate waveguides.

Figure 141 shows predicted performance based on a 3D full-wave RF model of an L-band version. The predicted bandwidth and impressively-high aperture efficiency are encouraging.

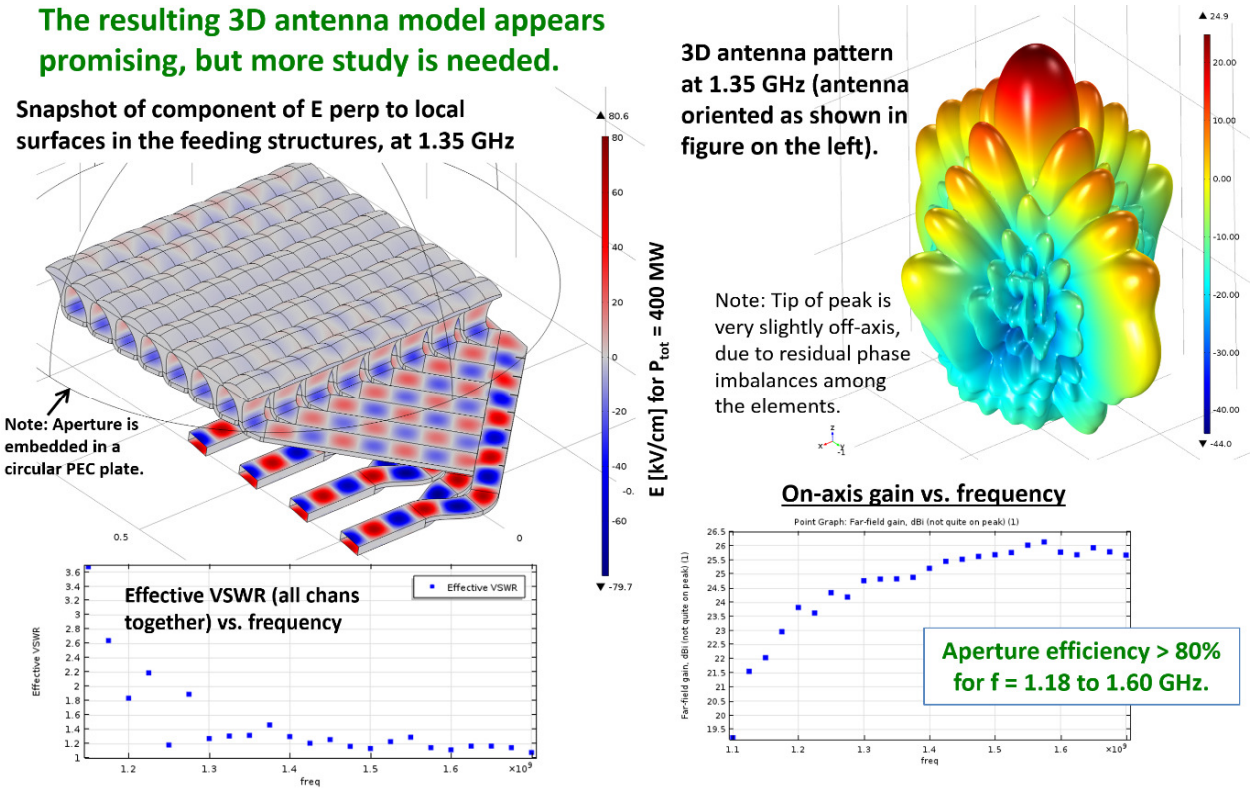


Figure 141. Predicted behavior of this fixed-beam wide-bandwidth antenna is encouraging.

5. CONCLUSIONS

As demonstrated by the results of this work and of other related investigations, it is clear that *forward-traveling, fast-wave, continuous-aperture* type Leaky Wave Antennas (LWAs) offer a very compelling mix of excellent performance capabilities and system-integration/packaging advantages in High Power Microwave (HPM) Directed Energy Weapon (DEW) applications. These include:

- Support for extremely high (e.g., multi-GW) peak power, if evacuated waveguides are employed and the aperture-interface geometries are appropriately customized.
- High gain and aperture efficiency
- Low-profile (thickness < λ_0 generally; thickness < $\lambda_0/2$ in special "rotated" designs)
- Bandwidth more than sufficient for compatibility with narrowband HPM sources
- Aperture(s) conformable to flat and variously curved surfaces
- Highly customizable to fit various aperture sizes and aspect ratios
- Potential for beam-steering via frequency (in H-plane) or by phasing across multiple channels
- Ruggedizable for harsh operating environments
- No exotic materials or unusual machining tolerances required to fabricate.

The work done under this ONR-sponsored program has substantially strengthened the knowledge base upon which this technology can and will continue to build. It includes an improved understanding of LWA design practices for HPM applications and guides the designer toward configurations that can both support extreme peak power handling and deliver high gain beams, in a variety of low-profile geometries. The "recommended" designs documented by this work serve not only as valuable, scaleable, and usable design options, but also serve as examples of the achievable performance, thereby contributing to more accurate and realistic system-integration assessments. In addition to the various flat and curved aperture geometries that were the primary focus of this work, we identified feature-rich capabilities achievable via combination of these antennas with additional components (e.g., reflectors, to yield rapid high-gain beam-steerable configurations). We also identified a configuration compatible with non-fundamental mode HPM sources (specifically, circular TM_{01}-mode output sources). It would not be surprising to us if these alternatives and technology extensions lead to real-world DEW applications.

6. RECOMMENDATIONS

Opportunities exist in at least two areas: (1) to continue and expand-upon the analyses and modeling performed to date, to further mature the designs of the identified antenna variants and to document other potential valuable configurations and improvements; and (2) to pursue hardware engineering/fabrication and experimental validation of the antenna types already identified, especially concentrating resources upon configurations judged variously by Government and DEW-community experts to be of the most interest and value to potential end users. Following either (preferably, both!) of these paths will no doubt advance and mature this technology.

We thank ONR for supporting this research.

7. REFERENCES

Baum, C.E., "Transmission/Reflection at a Dielectric Slab," *Sensor and Simulation Notes* No. 521, Dec. 2006. [Note: Typesetting errors found in the equations therein were corrected prior to use.]

Bodnar, D.G. and D.T. Paris, "New Variational Principle in Electromagnetics," *IEEE Trans. Antennas & Propagat,* vol. AP-18, pp. 216-223, 1970

Courtney, C.C. and C.E. Baum, "The Coaxial Beam-rotating Antenna (COBRA): Theory of Operation and Measured Performance," *IEEE Trans. Antennas Propag*., vol. 48, no. 2, pp. 299–309, Feb. 2000.

Collin, R.E., *Field Theory of Guided Waves*, *Second Edition*, IEEE Press, NY, 1991.

Goldstone, L.O. and Oliner, A.A., "Leaky-Wave Antennas I: Rectangular Waveguides," *IRE Trans. Ant. and Propagat*., Oct., 1959, pp. 307-319.

Goldstone, L.O. and Oliner, A.A., "Leaky-Wave Antennas II: Circular Waveguides," *IRE Trans. Ant. and Propagat*., May., 1961, pp. 280-290.

Guglielmi, M. and D.R. Jackson, "Broadside Radiation from Periodic Leaky-Wave Antennas," *IEEE Trans. Antennas & Propagat,* vol. 41, no. 1, pp. 31-37, Jan 1993

Hansen, W.W., "Radiating Electromagnetic Wave Guide, US Patent No. 2,402,622. Filed Nov. 26, 1940, issued June 25, 1946.

Harrington, R.F. and J.R. Mautz, "A High Power TM_{01} Circular to TE_{10} Rectangular Waveguide Mode Converter," Seventh International Conference on Antennas and Propagation, (IEE), York, 1991, pp. 125-128 vol.1.

Haworth, M.D., G. Baca, J.N. Benford, T. Englert, K. Hackett, K.J. Hendricks, D. Henley, M. LaCour, R.W. Lemke, D. Price, D. Ralph, M. Sena, D. Shiffler, and T.A. Spencer, "Significant Pulse-lengthening in a Multigigawatt Magnetically Insulated Transmission Line Oscillator," *IEEE Trans. Plasma Sci.,* vol. 26, no. 3, pp. 312-319, Jun 1998.

Honey, R.C., "A Flush-Mounted Leaky-Wave Antenna with Predictable Patterns," *IRE Trans. Antennas and Propagat*., 7, pp. 320-329, 1959.

Honey, R.C., and J.K. Shimizu, "A Leaky-Wave Antenna with a Curved Aperture," Scientific Report # 5, Stanford Research Institute (SRI) Project 2605, Air Force Cambridge Research Center, Air Research and Development Command, Laurence G. Hanscom Field, Bedford, MA, Feb. 1960. DTIC AD236085.

Ishimaru, A.K. and Beich, F.R., "Pattern Synthesis With a Flush-Mounted LeakyWave Antenna on a Conducting Circular Cylinder," *J. of Res. of the Nat. Bureau of Standards-D. Radio Propagat* Vol. 66D, No.6, Nov- Dec. 1962, pp. 783-796.

Jackson, D.R., C. Caloz and T. Itoh, "Leaky-Wave Antennas" *Proceedings of the IEEE,* Vol. 100, pp. 2194-2206, 2012.

Jull, E.V., "Radiation from Apertures," Chap. 5 of *Antenna Handbook: Theory, Applications, and Design,* Ed. by Y.T. Lo and S.W. Lee, Van Nostrand Reinhold, NY, 1988.

Koslover, R.A., C.D. Cremer, W.P. Geren, D.E. Voss, and L.M. Miner, "Compact, Broadband, High Power Circular TM_{01} to TE_{11} Waveguide Mode Converter," US Patent No. 4,999,591, March 12, 1991.

Koslover, R.A., "Compact, Lightweight, Steerable High-Power Microwave Antenna," US Patent No. 6,559,807, May 6, 2003.

Koslover, R.A., S.P. Catanzariti, R.F. Anderson, G.R. Raith, and B.G. Flores, "The Flat Aperture Waveguide Sidewall-Emitting Antenna (FAWSEA)," AFRL-DE-PS-TR-2007-1097, May 17, 2007.

Koslover, R.A., "Flat Aperture Waveguide Sidewall-Emitting Antenna," US Patent 7,528,786, May 5, 2009.

Koslover, R.A., S.P. Catanzariti, R.F. Anderson, G.R. Raith, N.P. Bloomhardt, M.C. Griskey, and K.S. Fine, "Advances in Flat and Curved-Aperture Waveguide Sidewall-Emitting Antennas for Airborne HPM Platforms," USAF Technical Report AFRL-RD-PS-TR-2010-1033, June 14, 2010.

Lamb, H., "On the Reflection and Transmission of Electric Waves by a Metallic Grating," *Proc. London Math. Soc*., v. 29, pp. 523-544; 1898.

Lewin, L., "Theoretical analysis of the junction discontinuity between a straight and a curved section of rectangular waveguide," *Proc. IEE,* Vol. 124, pp. 511-516, 1977.

Lewin, L., "The E-plane Taper Junction in Rectangular Waveguide," *IEEE Trans. Microwave Theory and Techniques*, vol. MTT-27, pp. 560-563, 1979.

Macfarlane, G.G., "Surface Impedance of an Infinite Parallel-Wire Grid At Oblique Angles of Incidence," *J. Inst. of Electrical Engineers - Part IIIA: Radiolocation*, Vol. 93, No. 10, pp. 1523–1527, 1946.

Marcuvitz, N., *Waveguide Handbook*, McGraw-Hill, NY, 1951.

Nishida, S., "Coupled Leaky Waveguides I: Two Parallel Slits in a Plane" *IRE Trans. Ant. and Propagat*., May, 1960, pp. 323-330.

Nishida, S., "Coupled Leaky Waveguides II: Two Parallel Slits in a Cylinder," *IRE Trans. Ant. and Propagat.,* July, 1960, pp. 354-360.

Oliner, A.A. and R.G. Malech, "Radiating Elements and Mutual Coupling," "Mutual Coupling in Infinite Scanning Arrays," and "Mutual Coupling in Finite Scanning Arrays," -- Chaps. 2, 3, and 4 respectively of *Array Theory and Practice*, Vol. II of *Microwave Scanning Antennas*, Ed. by R.C. Hansen, Peninsula Publishing, Los Altos, CA, 1985.

Oliner., A.A, and D.R. Jackson, "Leaky Wave Antennas," Chap. 11 of *Antenna Engineering Handbook*, 4th Ed., Edited by J.L. Volakis, McGraw-Hill, NY, 2007.

Schwinger, J., and D.S. Saxon, *Discontinuities In Waveguides - Notes on Lectures by Julian Schwinger*, Gordon and Breach Science Publishers, NY, 1968.

Silver, S. *Microwave Antenna Theory and Design.* 1st Ed, publ. by office of Scientific Research and Development, National Defense Research Committee, NY, 1949. [Sec. 5-11, "The Aperture Field Method," and Sec. 5-12, "The Fraunhofer Region."] See: http://www.jlab.org/ir/MITSeries/V12.PDF .

Vlasov, S.N. and I.M. Orlova, "Quasioptical Transformer which Transforms the Waves in a Waveguide Having Circular Cross-Section into a Highly Directional Wave Beam," *Radiophys. Quantum Electron.* , vol. 17, pp. 115–119, 1975.

Xu, F. and Wu, K., "Understanding Leaky-Wave Structures," *IEEE Microwave Magazine*, pp.87-96, July/August, 2013.

SUGGESTED DISTRIBUTION LIST

Official Record Copy
Mr. Lee Mastroianni
E-Mail: lee.mastroianni@navy.mil
Code 30
Office of Naval Research
875 North Randolph St.
Arlington, VA 22203-1995 1 cy

Dr. Joong H. Kim
E-Mail: joong.kim@navy.mil
Code 30
Office of Naval Research
875 North Randolph St.
Arlington, VA 22203-1995 1 cy

Director, Naval Research Lab
E-mail: reports@library.nrl.navy.mil
Attn: Code 5596
4555 Overlook Avenue, SW
Washington, D.C. 20375-5320 1 cy

Defense Technical Information Center
E-mail: tr@dtic.mil
8725 John J. Kingman Road
STE 0944
Ft. Belvoir, VA 22060-6218 1 cy

Dr. Donald Shiffler
AFRL/RDH
Kirtland AFB, NM 87117-5776 1 cy

Dr. Kyle Hendricks
AFRL/RDHP
Kirtland AFB, NM 87117-5776 1 cy

Dr. Andrew D. Greenwood
AFRL/RDHE
Kirtland AFB, NM 87117-5776 1 cy

Dr. Susan Heidger
AFRL/RDH
Kirtland AFB, NM 87117-5776 1 cy

Mr. Matthew McQuage
Naval Surface Warfare Center
Dahlgren Division, Q07
Dahlgren, VA 22448 1 cy

Michael Wagaman
Advanced Technology Directorate
PEO Strike Weapons and Unmanned Aviation
Patuxent River, MD. 1 cy

Dr. Frank E. Peterkin
Director
Directed Energy Technology Office
17320 Dahlgren Road
Naval Surface Warfare Center
Dahlgren, VA 22448 1 cy

LTC Charles Ormsby
Chief
Directed Energy Requirements
Langley AFB, VA 1 cy

Patrick Randeson
Science, Technology and Weapons Analyst
Central Intelligence Agency
Washington, D.C. 1 cy